Characterisation and high-temperature sensing potential of fibre Bragg gratings in specialised optical fibres

A thesis submitted

by

Suchandan Pal

for the degree of

DOCTOR OF PHILOSOPHY

at

CITY UNIVERSITY, LONDON

School of Engineering and Mathematical Sciences

October 2004

Table of contents

List of Tables

List of Figures

Acknowledgements

Many people have helped me personally and academically since the starting of my PhD and it is very difficult to acknowledge them only by saying- 'thank you'. Still this is the only way to do this. First of all, I would like to express my sincere gratitude to Prof. K. T. V. Grattan for giving me the opportunity to research in this fascinating area and for his supervision throughout the whole period of my research at City University, London. Sincere gratitude is also extended to Dr. T. Sun for her valuable suggestions during the whole time of my research, and to Prof. B. M. A. Rahman for his timely advice at various stages of my work.

I am grateful to the Commonwealth Scholarship Commission in the UK for providing me a Commonwealth Scholarship to pursue my PhD in the UK and the Central Electronics Engineering Research Institute (CEERI), Pilani, India for approving my study-leave during my PhD project.

Thanks are due to Dr. Wade, Dr. Collins, Dr. Baxter (all from Victoria University, Australia), Dr. Dussardier and Dr. Monnom (both from Université de Nice, France) for providing me various types of photosensitive fibres, and Dr. Fokine, Dr. Carlsson and Dr. Fonjallaz (all from ACREO, Sweden) for providing me several chemical composition gratings during my research. I am thankful to Jharna, Jackson, Venu, Kajan, Dr. Zhao, Dr. Shen and all other co-researchers of Optical Fibre Sensor Research Group at City University for their co-operation and various helps during my research time. I also acknowledge the encouragement from my colleagues at CEERI, India, during the time of my research in the UK.

Most of all, I would like to acknowledge the continuous encouragement from my parents, uncle-aunt and other relatives, in-laws, brothers and sister- whose sincere wishes, even from a far distance, made my academic abroad-life easier. Lastly, it would not be possible to complete my PhD so smoothly without my wife's continuous support in all aspects during various ups and downs of my stay in London; thanks Nandini. I was inspired and back to my work with full of energy and fresh mind for several times to complete my PhD by seeing my daughter's energetic activities all along the day and her fresh look; so, it is just for you- Ananya.

Copyright Declaration

Abstract

Starting with a brief, yet comprehensive review of optical fibre Bragg gratings (FBGs) and their various sensing applications, this thesis covers the characterisation and high-temperature sensing potential of fibre Bragg gratings written in specialised optical fibres. Following work done to optimise the grating-writing system set-up, different types of FBGs (type I and type IIA) were written in various photosensitive fibres (germanium and boron-germanium doped fibres) including in several specially fabricated photosensitive fibres (tin-erbium-germanium, erbium-high germanium and antimony-erbium-germanium doped fibres). The gratings were fabricated through a phase-mask technique by using 248 nm ultra-violet (UV) light from a krypton-fluoride (KrF) excimer laser. The photosensitivity of the fibres and the on-line growth of the gratings during the fabrication process were studied and compared. The thermal sustainability of the gratings written in various photosensitive fibres, including a chemical composition grating (CCG), were tested and thus the operational ranges of temperature measurement, using these FBGs, were determined and compared.

The thermal stability (reflected in the decay) of the gratings was studied and analysed both in terms of the refractive-index modulation (correlated to the reflectivity of the grating) and the effective refractive index (depending on the blue-shift in the Bragg wavelength of the gratings). Type I uniform gratings written in one of the most UV-photosensitive fibres (boron-germanium doped fibre) and one of the most promising fibres for high temperature sensing applications (tin-erbium-germanium doped fibre) were used in this thermal stability analysis, by adopting the *power-law* and the *master aging curve* approach. The operational lifetimes of the gratings at relatively lower temperatures were predicted by the *accelerated-aging* test.

To extend the work further, the thermal response of the pre-annealed gratings was studied over a wide range of temperatures. Linear and non-linear regressions were fitted to the experimentally measured data and the deviation between the regression and the actual data was compared for each grating. Non-linear fittings were found to reflect the optimised regression for the grating calibration for temperature measurement.

Finally, following a brief introduction to the simultaneous measurement of strain and temperature, a new development is applied for the measurement of both parameters over wider ranges (temperature: 20-600°C, strain: 0-2000$\mu\varepsilon$). The scheme is based on a combined fluorescence and grating based technique and thus, gratings were written in specially fabricated tin-erbium-germanium and antimony-erbium-germanium doped fibres to demonstrate the technique. A scheme for a strain-independent temperature measurement is also demonstrated by writing type I and type IIA gratings in the same fibre (erbium-high germanium doped fibre).

The significance of the work is considered and the suggestions for future work are made.

Symbols and Abbreviations

ASE	Amplified Spontaneous Emission
CCG	Chemical Composition Grating
CFBG	Chirped Fibre Bragg Grating
CW	Continuous Wave
EDFA	Erbium Doped Fibre Amplifier
EIM	Effective Index Method
ESA	Excited State Absorption
FBGs	Fibre Bragg gratings
FPPR	Fluorescence Peak Power Ratio
FWHM	Full Width Half Maximum
GODC	Germanium-Oxygen Deficiency Centre
GSA	Ground State Absorption
LPGs	Long Period Gratings
MCVD	Modified Chemical Vapour Deposition
NA	Numerical Aperture
NICC	Normalised Integrated Coupling Coefficient
OFST	Optical Fibre Sensor Technology
RMS	Root Mean Square
SMF	Single Mode Fibre
SNR	Signal-to-Noise Ratio
TDM	Time Division Multiplexing
TMM	Transfer Matrix Method
UV	Ultra Violet
WDM	Wavelength Division Multiplexing
WDM/D	Wavelength Division Multiplexing/ Demultiplexing

ArF	Argon Fluoride
Al	Aluminium
B	Boron
Er	Erbium
Ge	Germanium
KrF	Krypton Fluoride
O	Oxygen
Sb	Antimony
Si	Silicon
Sn	Tin

T	Kelvin (temperature)
λ	Wavelength
λ_b	Bragg wavelength
$\lambda_{cut\text{-}off}$	Cut-off wavelength of an optical fibre
$\Delta\lambda_b$	Shift in Bragg wavelength
Δn_{mod}	Amplitude of the refractive index modulation
n_{eff}	Effective refractive index
$\mu\varepsilon$	Micro-strain
Λ	Pitch of a fibre Bragg grating
V	Normalised frequency number of an optical fibre

Chapter 1

Introduction

1.1. Abstract

This introduction to the thesis covers the background and context of the work, and particularly, the basis of the choice of fibre Bragg grating based measurement schemes for high temperature sensing applications. The aims and objectives of the work are put forward and the structure of the thesis is described in this chapter that provides an outline of the whole work carried out.

1.2. Background and context of the work

When the first experiments were conducted in the field of optical fibre sensing almost three decades ago, this area was very much in its infancy in comparison to the conventional sensing technologies available in the marketplace. However, the technology has begun to expand very rapidly over the last ten / twelve years, taking advantage of the important inherent characteristics of optical fibres, for example, their small size and light weight, immunity to electro-magnetic interference (although sensing of current is possible based on Faraday effect), their passive nature (i.e., non-electrical operation), easy access to remote hazardous areas, their ability to be multiplexed, their relatively low power consumption, and reasonably low cost. The initial view of the technology was that it had a broad range of applications across the needs of the sensor industries, but latterly the technology has been modified to emphasise the advantages seen in optical sensing for some niche areas like medical instrumentation, distributed sensing, aerospace and civil engineering [1] and in this way, optical fibre sensors have been of great interest with a wide range of applications in various process industries, in recent years [2].

Fibre optic based sensors may generally be sub-divided by transduction mechanisms and classified as intensity-based or interferometry-based systems. Intensity-sensors tend to be based on multi-mode fibres, whereas the interferometric sensors are usually constructed by using single-mode fibres. There is another type of sensor, called the 'hybrid sensor', which uses the electrical power (converted from the optical power transmitted by the optical fibres) to drive

some form of miniature conventional sensors. This is now a well-established technology and has been discussed in detail in several book series [1]-[3]. The optical fibre sensors have also been categorised according to the types of sensing devices (e.g., extrinsic or intrinsic), types of sensing techniques (e.g., intensity / phase / polarisation modulation, coherent / non-coherent detection, time / wavelength division multiplexing), types of applications (for the measurement of various physical and chemical parameters, distributed or quasi-distributed sensing) or the types of fibres used (e.g., single-mode fibre, multi-mode fibre, polarisation maintaining fibre, rare-earth doped fibres or any specially designed and fabricated fibres).

On the other hand, the area of fibre Bragg gratings (FBGs), a small sub-field of the optical fibre sensor technology (OFST), is almost contemporaneous with the first development of OFST, after the discovery of the FBG in 1978 by Hill and his co-researchers [4] in Canada. However, a very rapid progress in the work involving FBGs had started what is now a world-wide interest in this subject after the invention of a new technique of writing gratings into the photosensitive fibres, by Meltz *et al.* [5]. Today FBG-based fibre-optic sensing technology is so popular and promising that very few optical fibre sensing systems are designed without incorporating FBGs.

1.3. Choice of fibre Bragg grating (FBG)-based schemes for temperature and strain sensing

Presently, the FBG is one of the key elements in the established and emerging fields in optical fibre communications and optical fibre sensing. A considerable level of research has already been carried out in this field by various groups of researchers all over the world for different applications. Most of the significant work in this area has been accumulated in few recently published books [2],[6],[7] and few review articles [8],[9]. Review papers providing thorough overviews, particularly in FBG-based sensing, have also been published [10],[11]. However, applications of sensing technologies based on FBGs are still growing, rather than reaching saturation. This is mainly because of their relatively simple strain- or temperature-induced wavelength-shift properties for various multi-disciplinary activities for point or distributed sensing with or without time and / or wavelength division multiplexing. It is also important to study the grating characteristics very closely with applied strain and temperature and to incorporate the observed effects into the system design for achieving the best possible reliability for long-term use. Recently, extensive research work is on-going over the selection of the fibre material with various dopings incorporated. As a result, gratings written into a carefully designed and fabricated specialist photosensitive optical fibre can be used for high temperature measurement over a wide range, in addition to the simultaneous measurement of strain and temperature over wide ranges.

In addition, FBGs have a significant role in designing fibre laser-based systems, using either matched-pair gratings or a combination of a uniform grating and a chirped grating, with a suitable length of a rare-earth doped fibre as a gain medium, which can be used for very precise measurement of strain and temperature with a very high signal to noise ratio (SNR). FBGs also play an important role in distributed or quasi-distributed sensing of temperature and strain by fabricating gratings at the same or / and different wavelengths (using different phase-masks) depending upon the system design and the necessity of the measurement. Moreover, in addition to the various applications of uniform FBGs, there is significant scope for applications using special types of gratings like chirped gratings (as in-fibre broad-band reflectors for laser-based sensing systems), long length gratings (for distributed sensing and for very precise level of measurement by writing a grating of very narrow bandwidth), apodized FBGs (to avoid the side-lobes on either side of the main grating for some specific applications), super-imposed and super-structured multiple gratings (for discrimination of multiple physical parameters and for WDM applications), blazed gratings (for mode filtering) and long period gratings (for various sensing applications).

1.4. Aims and Objectives of this work

The work is aimed mainly at high temperature sensing applications, building upon research carried out in the Measurement and Instrumentation Centre of the City University on fluorescence of the optical fibres [12]. However, the basis of this work is fibre Bragg gratings, written in some specialised optical fibres. The major objectives of the work are -

- A thorough review of the literature on the work associated with FBGs, as a background to this research, and an evaluation of the possibilities for the future work in this area.
- Setting up and evaluating a facility for the fabrication of FBGs (as it is new in this Centre of the University) using a KrF excimer laser and fabrication of different types of gratings (type I and type IIA) into a range of photosensitive fibres using this fabrication system created.
- To carry out a series of experiments to observe the temperature stability of these different types of gratings written in commercial fibres and in several specially designed and fabricated fibres with selective dopings, for writing high temperature sustainable gratings and thereafter making a comparison over their ranges of temperature measurement.
- Analysis of thermal decay or stability of the FBGs written in some selective fibres (the most photosensitive fibre and the most useful fibre for high temperature applications), in terms of reflectivity (or the modulation of refractive index of the fibre core) and the irreversible blue-shift in the Bragg wavelength (or the effective refractive index of the fibre core) of the gratings, to model the process of the grating-decay at different temperatures over a certain period of predicted time.

- Verifying the non-linearity of the temperature dependence of the FBGs in terms of reversible changes in the Bragg wavelength in order to achieve the best possible calibration over a wide range of temperature measurements with the minimum acceptable errors.
- Based on a brief review of the recent work on the simultaneous measurement of strain and temperature, a new scheme is proposed to enhance the range of measurement by writing gratings in various specially fabricated Er^{3+}-doped [13],[14] optical fibres, using a combined fluorescence and grating based technique, with the best achieved calibration. In addition, the optimisation of the range of simultaneous measurement is made for both parameters using various specialised optical fibres.
- Developing a scheme for strain-independent temperature measurement and undertaking the cross-sensitivity analysis for independent and simultaneous measurement of strain and temperature.
- To extend the work on FBGs for fibre laser-based sensing applications by using a combination of a uniform grating and a chirped grating along with a length of a rare-earth doped fibre.
- Conclusion of the work and the discussion of the possibilities of extending the work towards the future direction.
- Reporting the results obtained at various stages of the research, in various International Conferences and the international Journals.

1.5. Structure and design of the thesis

The thesis is structured with a series of chapters describing the comprehensive work carried out to achieve the aims set out and meeting the objectives given.

The first chapter (Chapter 1) begins with review of the brief background to optical fibre sensing in the context of choosing the fibre Bragg grating-based schemes for high temperature sensing applications. The aims and objectives of the work, followed by the structure of the thesis designed to meet the objectives at various stages of the work are put forward, outlining of the whole work carried out.

Chapter 2 covers the mechanisms involved with the FBG fabrication followed by the relevant theory of FBGs required explaining the formation of FBGs and their properties. Different procedures for the inscription of gratings along with the properties and applications with the FBGs, carried out to date, by various researchers, are reviewed thoroughly and the scope of the future work in that field is evaluated.

Chapter 3 introduces the setting up and evaluation of a system for writing FBGs using UV light from a KrF excimer laser and the fabrication of different types (type I and type IIA) of gratings in

various commercially available (B-Ge doped, Ge doped) and specially fabricated (Er-Ge doped, Sn-Er-Ge doped, Sb-Er-Ge doped) photosensitive fibres. The temperature sustainability of the gratings written into all of these fibres is examined and compared with a chemical composition grating (CCG), supplied by a collaborator with the City University. The maximum ranges of temperature measurements with different types of gratings written in various photosensitive fibres are evaluated and discussed.

Chapter 4 describes the analysis of thermal stabilities of the FBGs written in a few selective fibres, in terms of the decay of the refractive index modulation (which is related to the reflectivity of the gratings) and the effective refractive index (related to the Bragg wavelength) of the core of the fibre. The selective photosensitive fibres are B-Ge codoped fibre (for the best available photosensitivity) and the specially fabricated Sn-Er-Ge codoped fibre (for high temperature sensing applications). The predicted decays of the gratings written into these fibres, at different temperatures, were simulated over a period of time, by conducting experiments on accelerated aging. Also, the thermal stabilities of the FBGs fabricated in various fibres were analysed and compared in this chapter by evaluating the activation energies.

Chapter 5 discusses the requirement of the process of annealing over the fabricated gratings to achieve the repeatable data for temperature measurements. A number of ascending and / or descending cycles through temperature-induced reversible changes in the Bragg wavelengths of the FBGs written into various photosensitive fibres have been carried out and evaluated. This chapter compares the linear and non-linear regressions over the experimental data for temperature measurement with different types of gratings written in various fibres and shows the necessity of considering the non-linear characteristics to optimise the calibration for a wide range of temperature measurement.

Following a brief review of recent work published in the area of simultaneous measurement of strain and temperature and the limitations of the schemes, Chapter 6 gives the description of a new approach for simultaneous measurement of both parameters over wider ranges, by writing gratings in the specially fabricated rare-earth doped fibres (tin-erbium doped and antimony-erbium doped photosensitive fibres), using a combined fluorescence and grating based technique. A scheme for a strain-independent temperature measurement is also demonstrated by writing type I and type IIA gratings in the same fibre. Cross-sensitivity of the parameters for independent and simultaneous measurements are discussed here.

Finally, Chapter 7 concludes the whole work carried out in this project with a future scope to continue and enhance the work towards a right direction. This chapter includes a sketch of possibilities of writing chirped gratings, long length gratings and long period gratings, using a

translation stage and the upgraded writing system, in addition to their various applications in the field of sensing.

1.6. Summary

This chapter has contained the background and context of the work, with a particular emphasis on the fibre Bragg grating based measurement schemes for high temperature sensing applications, including the simultaneous measurement of strain and temperature. The aims and objectives of the work are put forward and the structure of the thesis has been described in this chapter as an outline of the whole work carried out.

Chapter 2

Background and Review of optical fibre Bragg gratings

2.1. Abstract

A considerable amount of work in the field of optical fibre Bragg grating research has been carried out over the last ten to twelve years. This chapter reviews briefly the photosensitivity mechanism involved and underpinning the formation of FBGs, followed by the relevant theory required to explain the nature of the FBGs formed, their properties and applications. Different techniques for the inscription of various types of gratings are also discussed. The applications of the FBGs for measuring a range of physical and / or chemical parameters such as – temperature, strain, pressure, relative humidity, carried out to date, in various fields, ranging from their use in the process industries to medical instrumentation, by various researchers, are reviewed thoroughly and the scope for future work in this field is envisaged, in terms of high temperature sensing potential of the FBGs written in several specialised optical fibres.

2.2. Photosensitivity of the fibre

Fabrication of FBGs was of great interest since the discovery of photosensitivity in the optical fibres. In such fibres, the core refractive index of the optical fibre alters when it is exposed to strong ultra violet light. This photosensitivity allows the fabrication of phase structures in the fibre core, as a result of a periodic perturbation of the core refractive index along the length of the fibre and forms a fibre Bragg grating, after satisfying the Bragg condition. The magnitude of the modulation of the core refractive index along with the number of planes of modulation determines the reflectivity of the grating.

2.2.1. Discovery of photosensitivity

Fibre photosensitivity was first observed in germanosilicate fibres by Hill and co-researchers in 1978 [4] using 488 nm ultra violet (UV) light from an argon-ion laser launched into the fibre. Coherent light propagating in the fibre interferes with a small amount of back-reflected light from

the end of the fibre (~ 4% Fresnel reflection) to form a standing wave pattern, which through photosensitivity writes a grating in the fibre core. Unfortunately, this 'Hill grating' functioned only over the region around the writing wavelength light and due to this limitation, the phenomenon was not taken forward at that time. This limitation was overcome in 1989, when Meltz *et al.* [5] demonstrated the formation of FBGs in optical fibres by a transverse holographic method by using 244 nm UV light from a frequency-doubled argon-ion laser. In this experiment, the fibre was irradiated from the side with two intersecting coherent UV light beams. The two overlapping UV beams interfere producing a periodic interference pattern, which writes a corresponding periodic index grating in the fibre core. This transverse holographic technique is possible because the fibre cladding is transparent to the UV light whereas the fibre core is highly absorbing to that. Since then, the fabrication of FBGs is of great interest, mainly because of the ease of the technique of grating writing without removing the glass cladding of the optical fibre, and functioning of the FBGs at much longer wavelengths, which are of interest for a range of applications.

2.2.2. Physical process and the mechanisms of photosensitivity

The demonstration of the transverse holographic technique for the FBG writing showed that a 'strong' change in the core refractive index of a germanosilicate fibre occurred when it was exposed to 244 nm UV light, which is very close to the absorption peak of the germania-related defect over the wavelength range of 240-250 nm. At that time, the germanium-oxygen deficiency centre (GODC), Ge-Si wrong bonds or Ge-Ge wrong bonds (which occur during the fabrication process of the fibre perform by the MCVD method) were thought to be responsible for the photosensitivity of the fibre, where on UV illumination, the bond readily breaks, creating a GeE' centre with an extra liberated electron (associated with the Ge atom), free to move within the glass matrix via hopping or tunnelling, or by two-photon excitation into the conduction band that facilitates the formation of new defect centres like Ge(1) and Ge(2), through charge retrapping elsewhere in the matrix. Fig. 2.1 shows a schematic of the above phenomenon. However, photosensitivity has also been observed in a wide range of fibres, many of which do not contain germanium as a dopant. With the demonstration of photosensitivity in most of these fibres, it is now apparent that the photosensitivity is a function of various mechanisms (photo-chemical, photo-mechanical and thermo-chemical) and the relative contribution will be fibre-dependent, as well as dependent on the UV light intensity and the wavelength. The precise origins of the photosensitivity and the accompanying refractive index change in the fibre core are not yet fully understood. Various researchers have proposed several models to explain these photo-induced refractive index changes; however, no single model can explain all the experimental results obtained. The main models used to explain the mechanism are discussed here briefly.

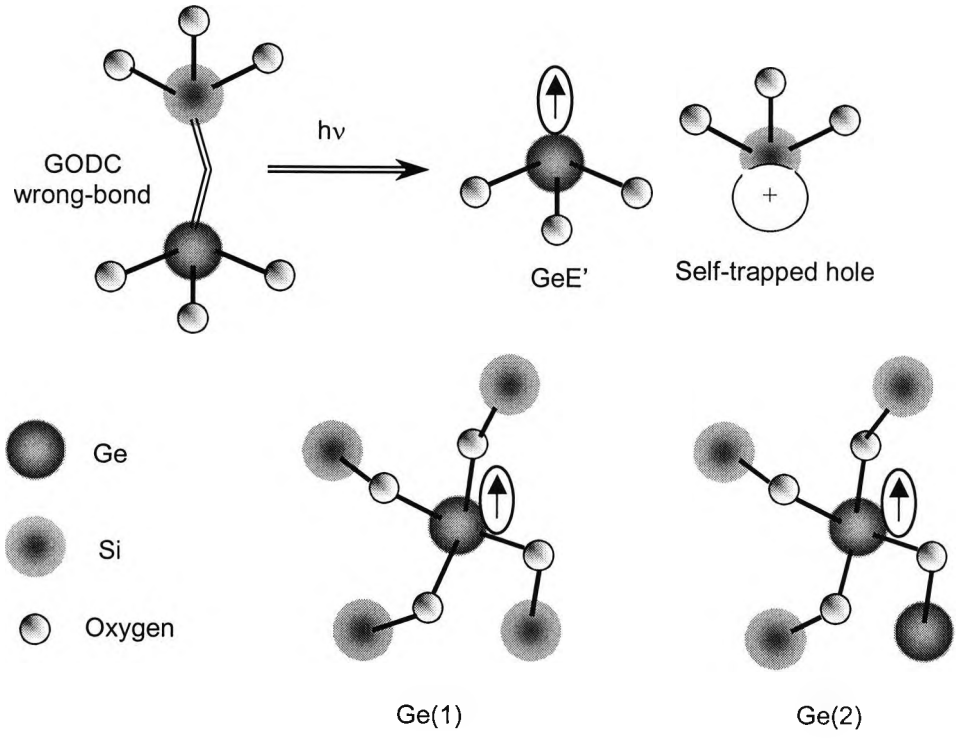

Fig. 2.1: Formation of GODC and possible GODC candidates.

Colour centre model: This model assumes that photo-induced changes in the absorption spectrum give rise to a change in the refractive index through the Kramers-Kronig relationship. In this model, a colour centre can be formed when a GODC absorbs a photon. Photo-excitation can break the Ge-Ge or Ge-Si bonds by producing a paramagnetic GeE' centre – a germanium/silicon hole with an extra released electron. These electrons from the colour centres are free to move within the glass network and eventually they are trapped at two types of germanium-dopant sites forming Ge(1) centre (with an electron trapped at a Ge atom coordinated to four O-Si next-nearest neighbour atoms, at longer wavelengths of the absorption spectrum) and Ge(2) centre (with an electron trapped at a Ge atom coordinated by one O-Ge and three O-Si next-nearest-neighbour atoms, at shorter wavelengths of the absorption spectrum). According to this model, the refractive index at a point is related only to the number density and the orientation of the defects (i.e., colour centres) in that region and this is determined by their electronic absorption spectra. To date, the colour centre model is the most widely accepted model to explain the mechanism of formation of FBGs with some experimental results in support of this [15]-[18]. Results on the thermal annealing of the FBGs, with very less amount of decay at lower temperatures and a substantial level of decay at higher temperatures, are also supportive of this model. However, this model cannot explain satisfactorily all the

experimental observations [19],[20] relating to the behaviour of all fibre types and their dopants like hydrogen-loaded, rare-earth doped and alluminosilicate fibres, where the Kramers-Kronig analysis performed over the wavelength range of 190-800 nm fails to account for the refractive index changes [6] (pp. 66).

Dipole model: The dipole model is based on the formation of built-in periodic space-charge electric fields by the photo-excitation of the defects. Photo-ionisation of GODCs, Ge-Si, or Ge-Ge wrong bonds create positively charged GeE' hole-centre along with a free electron. The free electron diffuses away and gets trapped by the nearest neighbouring sites of Ge(1) and Ge(2) to form negatively charged $Ge(1)^-$ and $Ge(2)^-$ centres respectively [21]. The GeE' hole-centres and $Ge(1)^-$ and $Ge(2)^-$ electron-centres result in electric dipoles with a separation of few hundred picometers. Each dipole produces a static d.c. polarization field that extends over many molecular spacings. These static electric fields induce local changes in refractive index, which is proportional to the square of the electric field, E^2, according to the Kerr effect. During the FBG fabrication process, when the fibre is exposed to the UV interference pattern, free electrons are created in the high intensity regions and diffuse in either side of the low intensity until they are trapped by the defects in those regions. This distribution of charges within the fibre creates periodic space-charge electric fields and thus modulates the refractive index of the fibre periodically. Although this model works well for photo-refractive crystals, it is quite difficult to justify in the case of all photosensitive fibres due to the requirement of large number density of dipoles, which is much higher compared to that estimated from experiments.

Compaction / Densification model: The compaction model is based on laser irradiation-induced density charges, which results in changes in the refractive index. UV-based laser irradiance, well below the breakdown threshold, has been shown to induce thermally reversible linear compaction of amorphous silica leading to a change in refractive index. Fiori *et al.* [22] conducted an experiment using 248 nm KrF excimer laser to irradiate a thin film of a-SiO_2 sample grown on a silicon wafer and based on the observations they proposed the compaction / densification model. They observed a reduction in the thickness of the film and the corresponding evolution of the refractive index changes during the laser exposure. After annealing of the sample, the compaction disappeared and the original thickness and the pre-irradiated refractive index were retrieved. An approximate linear relationship was found between the refractive index change and the density change. A continuous UV irradiation beyond this reversible compaction regime led to irreversible compaction, until the film was entirely etched. Several microscopic mechanisms can lead to the volume change such as a phase transformation, a change in the polymerisation of the glass, or a change of coordination. This hypothesis explains the physical mechanism with compaction of amorphous silica through internal structural rearrangements rather than through the process of defect-creation. A

comprehensive study of the UV-induced compaction / densification process in hydrogen-loaded and non-hydrogen-loaded germanosilicate fibres has been carried out to understand the critical formation dynamics of the FBGs [23],[24]. It is believed that this model is one of the major mechanisms to explain the photosensitivity. However, its exact contribution under various experimental conditions has to be investigated further.

Stress-relief model: The stress-relief model [25] is based on the hypothesis that the refractive index change arises from the alleviation of built-in thermo-elastic stress in the fibre core. The core of the optical fibre is under tension due to the difference in the thermal expansion of the core and the cladding, as the glass is cooled below certain temperature during the fibre drawing. It is known from the stress-optic effect that the tension reduces the refractive index and therefore, it is expected that stress-relief will increase the refractive index. During UV exposing, the wrong bonds break and promote relaxation in the tensioned glass matrix, and hence reducing the frozen-in thermal stresses in the fibre core. The index change produced by the relaxation of stress can be calculated by considering the stress-optic effect in terms of Kramers-Kronig relation, which attributes a shift in the electronic band-gap with stress. The work on a measurement of increased axial tension in the core of the fibre during the formation of FBGs [26] supports the model, however, the thermal reversibility of the grating writing cannot be explained by this model [16].

2.2.3. Enhancing photosensitivity in the optical fibres

Since the first demonstration of FBG formation in germanosilicate fibres, considerable effort has been undertaken to understand and increase the photosensitivity of the optical fibres for writing gratings with very high reflectivity and at the same time, to optimise the UV exposure time. There are a few techniques have been invented to enhance the photosensitivity in the optical fibres and they are discussed briefly.

Hydrogen loading (hydrogenation) is one of several effective approaches to enhance the photosensitivity in the fibres, which was first reported by Lemaire *et al.* [27]. Hydrogen loading is carried out by diffusing the hydrogen molecules into the fibre core at high pressure (typically 150 atmospheric pressure) and comparatively low temperature (20-75 °C) prior to the UV exposure. Hydrogen molecules react in the glass at normal Si-O-Ge sites, forming OH species and UV bleachable GODCs, which are responsible for the enhancement of photosensitivity. One advantage of hydrogen loading is the fabrication of very strong FBGs (very good amount of reflectivity) in any germanosilicate or germanium-free fibres. In addition, in unexposed fibre sections the hydrogen diffuses out, leaving negligible absorption losses at the important optical windows. It may be noted that hydrogenation does not give any permanent effect to the fibre, as the hydrogen diffuses out, and the photosensitivity decreases. Also, a certain amount of drift in

the Bragg wavelength of the grating fabricated in a hydrogenated fibre was observed [28], which cannot be reliably predicted, as it is related to the residual hydrogen concentration in the fibre at the time of UV exposure and the degree of hydrogen depletion into the fibre core. However, the post-exposure annealing can stabilise the gratings for long-term use at comparatively low temperatures.

Flame brushing [29] is another simple technique to enhance the photosensitivity in germanosilicate fibres. A flame fuelled with hydrogen and a small amount of oxygen brushes the selected region of the optical fibre to enhance the photosensitivity, repeatedly. The temperature of the flame reaches to approximately 1700 °C and the process needs around 20 minutes of time to complete. At this temperature, the hydrogen diffuses into the germanosilicate fibre core and creates GODCs, resulting in a strong absorption band around 240 nm wavelength regions in the core, which is responsible for this enhanced photosensitivity for creating a significant amount of UV-induced refractive index change in the fibre core. The techniques of hydrogen loading and the flame brushing follow the same concept to enhance the photosensitivity. In both cases, hydrogen is used in a chemical reaction with germanosilicate glass to form GODCs, to be responsible for photosensitivity. In spite of various advantages of this technique (as hydrogen loading technique), one major drawback of this technique is that the high temperature flame brush processing weakens the mechanical strength of the optical fibre.

Boron codoping [30] in a germanosilicate fibre enhances the UV photosensitivity of the optical fibre. A comparison shows that the fibre containing boron codoping is much more photosensitive than the fibre with higher germanium concentration and without boron. Moreover, the saturated index changes are higher and achieved faster for this fibre than any other fibres, which suggest that there is an additional mechanism operating to enhance the photosensitivity. It is known that the addition of boron oxide to silica can result in a compound glass of having lower refractive index compared to silica. This effect is assumed to be due to a build-up in thermo-elastic stresses in the fibre core resulting from the large difference in thermo-mechanical properties between the boron-contained core and the silica cladding. It is known from the stress-relief model that tension reduces refractive index through the stress-optic effect. The absorption measurements suggest that boron codoping does not enhance the fibre photosensitivity through productions of GODCs as in the case of hydrogen loading or flame-brushing. Instead, it increases the photosensitivity of the fibre by allowing the photo-induced stress relaxation through the breaking of the wrong bonds in the glass matrix under UV exposure.

Use of ***ArF excimer laser UV-irradiation*** is another approach [31] to achieve better absorption within the optical fibres. Albert et al. fabricated FBGs using a UV light from a 248 nm KrF, as well as, a 193 nm ArF excimer laser separately with a phase mask and demonstrated that the FBGs

written under 193 nm UV exposure appeared to be of much stronger reflectivities than those inscribed with 248 nm exposure in similar excitation conditions. The experimental results show that the 193 nm excimer laser light provides an efficient grating writing technique in the optical fibres. The use of this shorter wavelength light for grating writing gives a possibility of achieving higher spatial resolution.

2.3. Inscription of fibre Bragg gratings (FBGs)

Inscription of Bragg gratings may be classified as *internally* or *externally* written, depending on the fabrication technique. Even though the FBG was first written through the internal writing technique by Hill and co-researchers [4], this technique is not very useful, particularly for its limited operating region, where the grating is only visible around the excitation laser wavelength. Also, a useful reflectivity of the grating can be achieved with a long length of optical fibre, as the UV-induced refractive index change is very much less in this method. In comparison to the internal writing technique, the technique of externally grating writing is quite useful and popular. Some of these techniques are described below.

2.3.1. Interferometric fabrication technique

The interferometric fabrication technique, the first external writing technique for the inscription of FBGs in photosensitive optical fibres, was demonstrated by Meltz and co-researchers [5]. An interferometer is used in this technique to split the incoming UV light into two beams and then to recombine them to form an interference pattern of the UV light, which can be used to expose a photosensitive fibre to create the refractive index modulation within the fibre core. FBGs can be fabricated in the optical fibres by using both amplitude-splitting and wave-front-splitting interferometers.

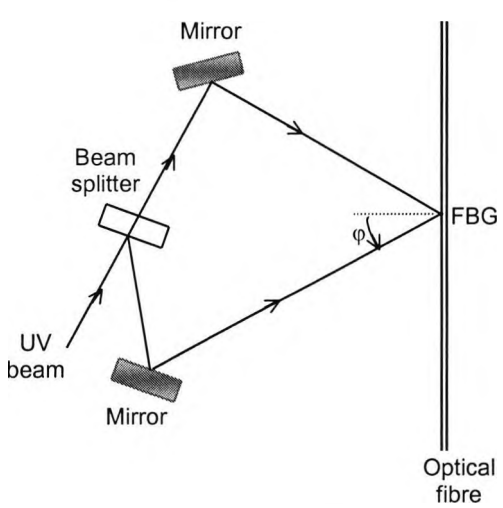

Fig. 2.2(a): A schematic of an amplitude-splitting interferometer used by Meltz *et al.*

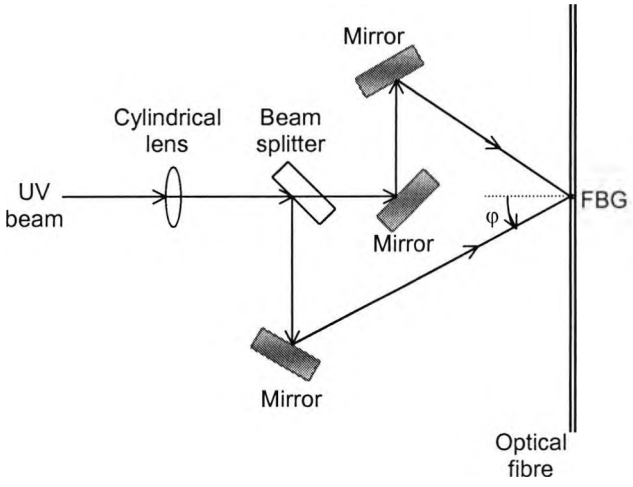

Fig. 2.2(b): An improved version of amplitude-splitting interferometer.

In an ***amplitude-splitting interferometer***, the UV light is split into two equal intensity beams and then recombined after traversing through different optical paths to produce an UV interference pattern, which illuminates the fibre to create the FBG within the fibre core. A pair of cylindrical lenses is used to focus the light along the length of the fibre. A broadband light source and a high-resolution monochromator are used to monitor the on-line growth of the grating by observing the reflection or transmission spectrum. Fig. 2.2(a) shows a schematic diagram of an amplitude-splitting interferometer used by Meltz *et al.*, which was improved further (schematic diagram is shown in Fig. 2.2(b)) to achieve better spatial coherence, thereby improving the efficiency of the grating inscription technique. The Bragg grating period, Λ, which is identical to the interference fringe pattern period and depends on both the exciting light wavelength, λ, and the half of the angle between the intersecting UV beams, φ, can be expressed by

$$\Lambda = \lambda/(2\sin\varphi) \tag{2.1}$$

Considering the Bragg condition with

$$\lambda_b = 2n_{eff}\Lambda \tag{2.2}$$

the Bragg resonance wavelength, λ_b, can be represented in terms of the UV light wavelength and the half-angle between the intersecting beams as

$$\lambda_b = (\lambda/\sin\varphi)n_{eff} \tag{2.3}$$

where n_{eff} is the effective refractive index of the fibre core. So, the Bragg wavelength of the FBG can be varied by changing either λ or φ, where the choice of λ is limited to the absorption region of the fibre and there is no restriction over φ. Thus, the FBG can be written at any desired wavelength in this technique. This method also offers the flexibility of producing FBGs of any arbitrary length and bandwidth. The main disadvantage of this method is its susceptibility to any mechanical vibrations, which degrade the formation of stable UV fringe patterns and requirements for a UV light source having very good temporal and spatial coherence along with the stability in the wavelength and the output power.

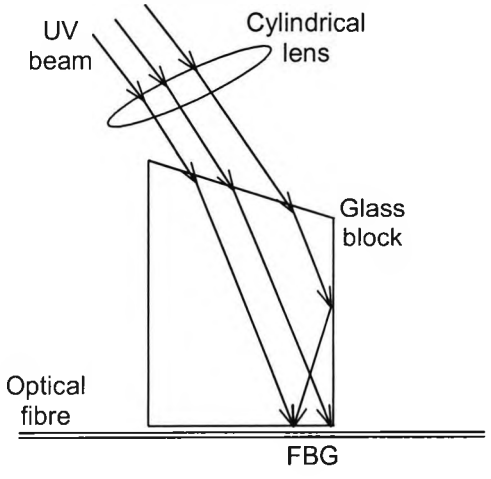

Fig. 2.3(a): A schematic of wavefront-spilitting block interferometer.

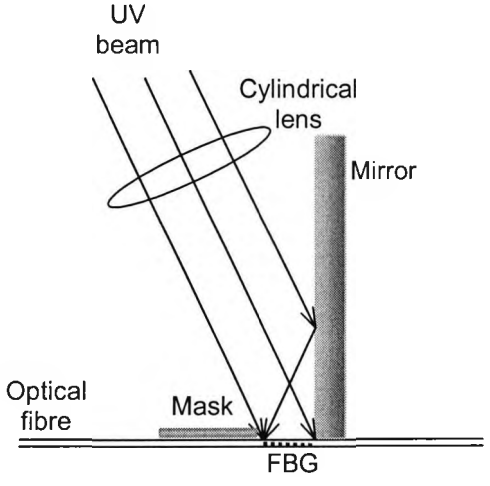

Fig. 2.3(b): A schematic of wavefront-spilitting Lloyd interferometer.

Wave-front-splitting interferometers are not so popular as the amplitude-splitting interferometers for the writing of FBGs; however, the approach offers a few advantages. Figs. 2.3(a) and 2.3(b) show the schematic diagram of two examples of the wave-front-splitting interferometers using a prism interferometer and a Lloyd's interferometer respectively. In the prism interferometer, the UV light is spatially bisected by the prism edge with half of the light spatially reversed by the total internal reflection from the prism face. The two beams are then recombined at the output face of the prism resulting in a fringe pattern parallel to the photosensitive optical fibre to write a grating. Lloyd's interferometer consists of a dielectric mirror, which directs half of the UV beam to the fibre that is placed perpendicular to the mirror. The writing beam is centred at the point of intersection between the fibre and the mirror. The recombination of the direct UV beam and the reflected UV beam from the mirror-face creates the interference fringe pattern to produce a grating. In both cases, cylindrical lenses are used to focus the beam along the length of the core of the fibre. One key advantage of the wave-front-splitting interferometer is mainly for use of only one optical component, which reduces the susceptibility to mechanical vibration. The disadvantages of the approach are the limitation on the grating length, which is restricted by the half of the beam size and the range of the Bragg wavelength tenability, which is caused by the physical arrangement of the system.

2.3.2. Phase mask technique

This is one of the most effective techniques for writing gratings into a photosensitive fibre [32],[33] which employs a diffractive optical element, called phase mask, for spatially modulating the UV beam to produce the grating. Phase masks may be created holographically or by electron-beam lithography [33]. Holographically produced phase masks do not have any stitch error, which is normally present in the phase masks formed through the electron-beam lithography due to the electron-beam size and affects the quality of the phase mask. However, any complicated structured phase masks can be fabricated by the electron-beam lithography technique.

A normal uniform phase mask has a one-dimensional periodic surface-relief structure, with a period of Λ_{PM}, etched into a high quality fused silica that is transparent to the UV light. The profile of the periodic surface-relief pattern is so chosen that that when an UV light is incident on the phase mask, the zero-order diffracted beam is suppressed to less than few percent (typically less than 3%) of the transmitted optical power and the diffracted plus and minus first orders are maximised (each typically containing more than 35% of the transmitted optical power). A near-field fringe pattern is developed by the interference of the diffracted plus and minus first order beams with a period, Λ, which is exactly one-half of the period of the phase mask ($\Lambda = \Lambda_{PM}/2$). This interference fringe pattern photoimprints a modulation in the refractive index of the core of the photosensitive optical fibre, which is placed just behind and in a close proximity to the phase

mask. A cylindrical lens is used generally to focus the UV-induced interference fringe pattern along the fibre core. The schematic diagram of the technique is described in Fig. 2.4.

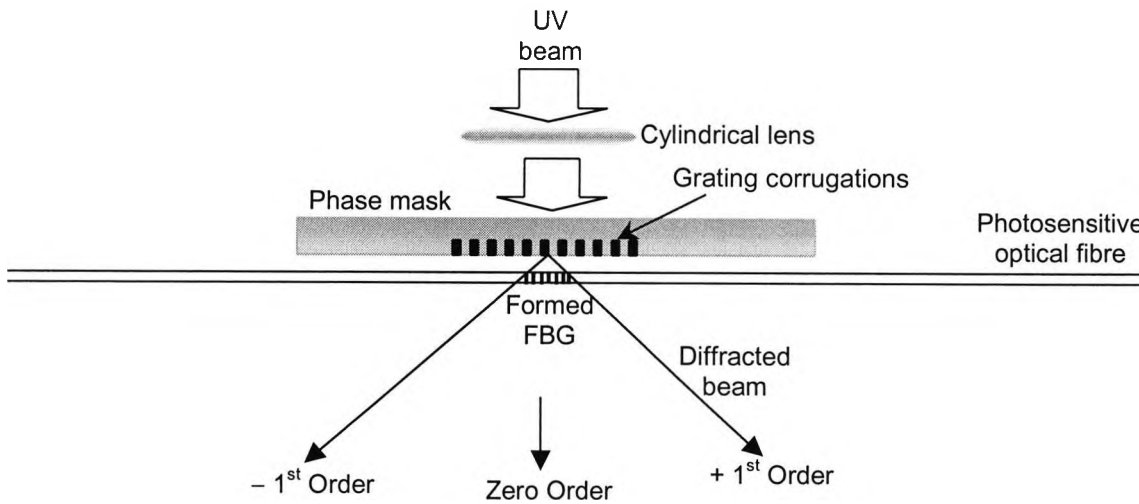

Fig. 2.4: A schematic of fabrication of FBGs using a phase mask.

The phase mask technique greatly reduces the complexity in the FBG fabrication process, which also provides a robust and much stable method to reproduce FBGs. Furthermore, low temporal coherence does not affect much on the grating writing capability. KrF and ArF excimer lasers are the common UV light sources used for the fabrication of FBGs using a phase mask. As the UV laser sources are of typically low spatial and temporal coherence, the fibre is required to be placed in a close proximity to the phase mask in order to minimise the spatial coherence effect. On the other hand, temporal coherence effect is not critical here, as long as the distance between the fibre and the phase mask remains the same along the fibre length. Othonos and Lee [34] have demonstrated the importance of the spatial coherence of the UV light sources at the time of writing gratings using phase mask by varying the distance between the phase mask and the photosensitive fibre. They have also demonstrated the advantage of the phase mask technique to write a blazed grating and to change the Bragg centre wavelength of the grating, by placing the fibre at an angle to the phase mask (fibre is not in parallel to the phase mask, i.e., one end of the fibre is very closed to the phase mask, whereas the other end of the fibre is away from that).

The close proximity between the phase mask and the photosensitive fibre during grating writing through phase mask technique is critical and touching of fibre may cause the possible damage in the phase mask for further use. This situation can be overcome by a non-contact phase mask technique using a silica block in between the phase mask and the fibre [35], as shown in Fig.

2.5(a). The plus and the minus first orders of the diffracted UV beams are internally reflected within the rectangular block to form an interference fringe pattern. The other useful non-contact technique is the Talbot interferometer arrangement [36], shown in Fig. 2.5(b), which consists of two separated plane parallel mirrors placed perpendicularly between the phase mask and the fibre. The positive and negative first order diffractive beams get reflected from the surfaces of the mirrors and recombine among themselves, to form the interference pattern of UV light to write the FBGs.

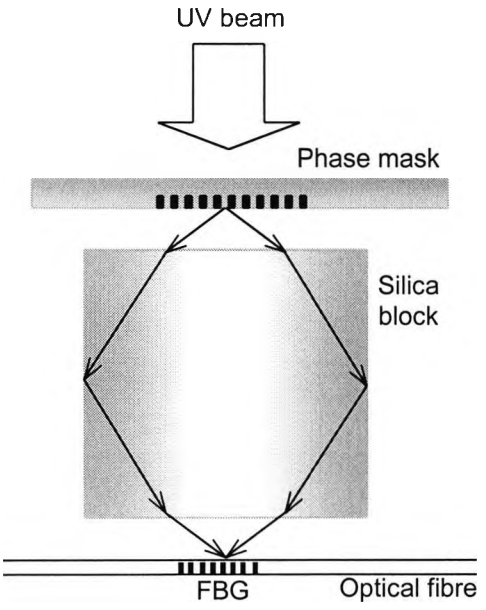

Fig. 2.5(a): Non-contact interferometric phase mask technique for grating writing using a silica block.

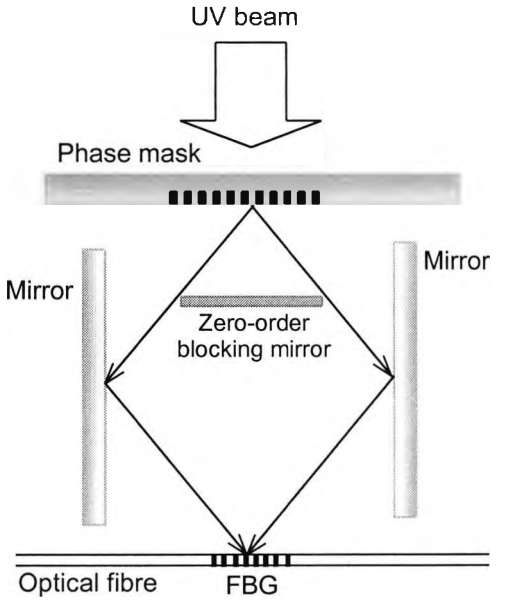

Fig. 2.5(b): Non-contact Talbot interferometric configuration for grating writing using a phase mask.

In general, the FBGs of different Bragg resonance wavelengths can be written using phase masks having different periods. However, using the same phase mask, this technique has the flexibility of writing tuneable gratings, whose Bragg wavelengths are close to its original Bragg resonance wavelength. Prohaska *et al.* [37] have demonstrated a shift in the Bragg wavelength (more than 1.5 nm) of the grating towards a shorter wavelength side by placing a converging lens before the phase mask. This shift of the wavelength depends on the demagnification factor of the system, which is limited by the separation between the phase mask and the fibre. Tenability of the Bragg wavelength of the FBGs can also be achieved by applying strain to the fibre during the process of fabrication [38]. In this case, the wavelength shift of more than 2.5 nm (towards the shorter wavelength side, by applying strain) is possible; however, this method is limited by the mechanical strength of the fibre.

2.3.3. Point-by-point writing of FBGs

The point-by-point writing method [39] for the fabrication of FBGs can be made possible by inducing a change in the refractive index of each grating plane, one step at a time, along the length of the fibre core. In a typical experimental arrangement, a single pulse of UV light from an excimer laser passes through a slit and converges onto the core of the fibre, after being focussed through a lens, to modulate the core refractive index locally. At the same time, the fibre has to be moved along the fibre-axis using a translation stage, with a velocity matching to the frequency of the excimer laser so that each pulse of the UV light produces a grating plane with a period of Λ. This method of writing gratings is also possible by using the UV light from a continuous wave (CW) laser; however, an optical chopper has to be used in this case, to block the continuous UV radiation periodically to match with the velocity of the translation stage. It should be noted that a very stable and precise sub-micron translation system is essentially needed in addition to a longer process time and precise focussing, for successfully writing FBGs through this technique. The main advantage of this writing technique lies in its flexibility to form gratings of any length and of any pitch. Furthermore, grating apodization can be possible via this method by varying the intensity of the UV light along the length of the core of the fibre.

2.3.4. Special techniques for FBG fabrication

Several techniques are used to inscribe the special grating structures. Fabrication of FBGs using a single excimer laser pulse, writing of gratings during fibre drawing, long length grating and complex structured grating formation using a translation system are the examples. Writing grating using a single pulse laser was first demonstrated by Askins *et al.* [40] and formation of gratings of high reflectivities are reported at the later stage [41],[42] by use of a highly photosensitive fibre.

One of the major drawbacks of writing gratings is to strip-off the polymer coating of the fibre to achieve better UV exposure within the fibre core. This process weakens the mechanical strength of the fibre, even if it is recoated after grating fabrication, due to the surface contamination. Mass production of FBGs is another difficulty. These problems can be overcome by writing gratings during the fibre drawing process, just before the fibre is coated [43]. However, a little fluctuation in pulling tension during fibre drawing may cause the changes in the Bragg centre wavelengths. An alternative approach is to use near-UV light around the wavelength of 334 nm [44]. All the standard polymer coatings are transparent to this region of wavelength and thus there is no need to remove the polymer jacket of the optical fibre before grating writing or the post-fabrication recoating, even though this near-UV light may not be that much efficient as the UV lights of wavelengths of 248 nm or 193 nm.

Many of the applications require the complex grating structure, which can be made possible by using a computer-controlled translation stage to synchronize the movement of the photosensitive fibre to write various complex grating structure involved. The fabrication of long length gratings with very narrow bandwidth [45], complex grating structure [46], chirped gratings [47], step-chirped, super-step-chirped and long super-step-chirped gratings [48]-[51] long period gratings [52] and super-structure gratings [53] has already been reported.

2.4. Properties of FBGs

A fibre Bragg grating, in a simplest form, consists of a periodic perturbation of the refractive index of the core of the optical fibre. This type of uniform FBGs is considered as the fundamental building block for most grating structures. The structure of a uniform FBG has been illustrated in Fig. 2.6. The guided light along the core of the optical fibre will be scattered by each grating plane (modulated refractive index region). If a certain phase matching condition, called the Bragg condition (discussed later), is not satisfied, the reflected light from each of the subsequent grating planes becomes out of phase among them and eventually cancels out. Moreover, in this condition (not satisfying the Bragg condition), a very weak reflection occurs at each grating plane due to the mismatch of the core refractive index in the fibre and virtually no effect can be observed in the transmitted optical output. When the Bragg condition is satisfied, the contributions of reflected light from each grating plane will be in-phase and will create a back-reflected peak light component with a centre wavelength defined by the grating parameters.

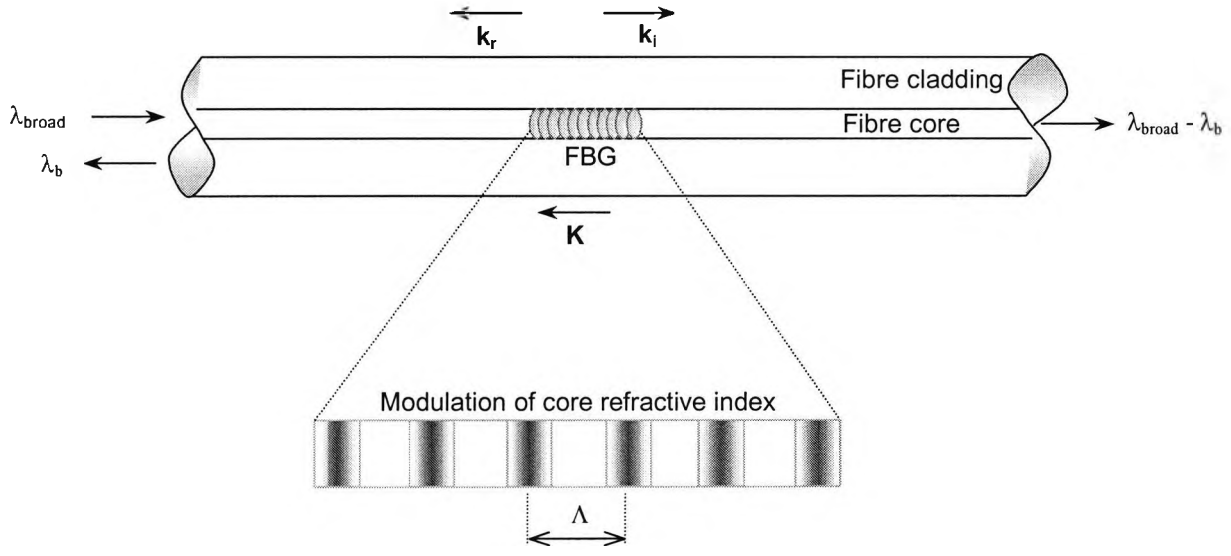

Fig. 2.6: A simple illustration of a uniform fibre Bragg grating.

2.4.1. Bragg condition and Bragg wavelength of the FBGs

Bragg condition is simply the desired condition that satisfies both energy and momentum conservation. The energy conservation states that the frequency of the incident radiation would be the same of that of the reflected radiation, i.e.,

$$h\nu_i = h\nu_r \tag{2.4}$$

where h is the Planck's constant and ν_i and ν_r are the frequency of the incident and the reflected radiation respectively. Momentum conservation shows that the grating wave vector, **K**, will be the vectorial difference between the wave vectors associated to the incident ($\mathbf{k}_i$) and the reflected ($\mathbf{k}_r$) radiation, i.e.,

$$\mathbf{K} = \mathbf{k}_i - \mathbf{k}_r \tag{2.5}$$

where the grating wave vector has a direction normal to the grating planes with a magnitude of $2\pi/\Lambda$ (Λ is the spacing between the grating planes). However, the reflected wave vector and the incident wave vector are equal in magnitude, but opposite in phase. Hence, Eq. (2.5) becomes

$$K = 2\pi/\Lambda = 2k_i = 2k_r = 2(2\pi n_{eff}/\lambda) \tag{2.6}$$

where n_{eff} is the effective refractive index of the fibre core at wavelength, λ, which is the free space centre wavelength of the input light that back-reflects from the Bragg grating, called as the Bragg wavelength, λ_b. Hence finally the Bragg condition appears as

$$\lambda_b = 2n_{eff}\Lambda \tag{2.7}$$

2.4.2. Reflectivity of the FBGs

Even though for a schematic of an FBG, the modulation of the core refractive index has been assumed to follow a rectangular profile, the most acceptable practical modulation of the refractive index can be considered as a sinusoidal profile along the length of the fibre and can be expressed as

$$n(z) = n_o + \Delta n \cos(2\pi z/\Lambda) \tag{2.8}$$

where n_o is the average refractive index of the core, Δn is the amplitude of the UV-induced refractive index modulation and z is the distance along the fibre longitudinal axis. Using the coupled mode theory [54]-[57] (discussed in the next section), the reflectivity of a grating with constant amplitude of modulation of the core refractive index and period, can be expressed as

$$R(l,\lambda) = \Omega^2\sinh^2(sl)/[(\Delta k)^2\sinh^2(sl) + s^2\cosh^2(sl)] \tag{2.9}$$

where R is the reflectivity of the grating, which is a function of the grating length, l, and the operating wavelength, λ. Ω is the coupling coefficient, $\Delta k = [k - (\pi/\lambda)]$ is the detuned wave vector, $k = 2\pi n_o/\lambda$ is the eigen wave vector and $s = (\Omega^2 - \Delta k^2)^{1/2}$. Again, the coupling coefficient, Ω, for sinusoidal variation of core refractive index along the fibre length, can be written as

$$\Omega = (\pi\Delta n/\lambda)(1-V^{-2}) \tag{2.10}$$

where the mode power confinement factor, $(1-V^{-2})$, can be represented in terms of the normalised frequency number of the fibre, V, which may be estimated by

$$V = (2\pi/\lambda)a(n_{co}^2 - n_{cl}^2)^{1/2} \quad (2.11)$$

with the core radius of the fibre, a, and the core and cladding refractive indices of n_{co} and n_{cl} respectively. At Bragg resonance wavelength of a uniform FBG, the value of the detuned wave vector becomes zero and hence the Eq. (2.9) simplifies to

$$R(l,\lambda) = \tanh^2(\Omega l)$$
$$= \tanh^2[(\pi \Delta n l/\lambda)(1 - V^{-2})] \quad (2.12)$$

During an experiment, the reflectivity of the FBG can be measured by observing the optical power at the Bragg resonance wavelength through an optical spectrum analyser and thus the amplitude of the modulation of the core refractive index for an FBG can be estimated as

$$\Delta n = [\lambda/\pi l(1 - V^{-2})] \tanh^{-1}(R^{1/2}) \quad (2.13)$$

The reflectivity of the grating increases with the increase of the amplitude of the UV-induced core refractive index modulation in the fibre. Also, as the length of the FBG increases keeping the same value of core refractive index modulation, the reflectivity of the grating enhances.

2.4.3. Effect of strain and temperature on the FBGs

The Bragg resonance wavelength is one of the vital parameters of FBGs, which depends on two main parameters, namely, the effective core refractive index of the fibre and the grating period, as shown in Eq. (2.7). Both of these parameters alter, when strain and / or temperature are applied on the grating, resulting in a change in its Bragg wavelength. From Eq. (2.7), the shift in the Bragg wavelength of the grating, due to the applied strain and temperature, can be expressed as

$$\Delta\lambda_b = 2[\Lambda(\partial n_{eff}/\partial l) + n_{eff}(\partial\Lambda/\partial l)]\Delta l + 2[\Lambda(\partial n_{eff}/\partial T) + n_{eff}(\partial\Lambda/\partial T)]\Delta T \quad (2.14)$$

where the first part of Eq. (2.14) represents the effect of strain on the grating, which corresponds to a change in the grating spacing and a change in the effective refractive index through dilation or compression of the fibre and assuming the strain is homogeneous and isotropic, it can be written in a simplified form as [8]

$$\Delta\lambda_b = \lambda_b(1 - p_e)\varepsilon \quad (2.15)$$

where the strain-induced photo-elastic coefficient, p_e, can be defined by

$$p_e = (n_{eff}^2/2)[p_{12} - \nu(p_{11} + p_{12})] \quad (2.16)$$

in terms of the strain-optic tensor components depending on the fibre Pockel's coefficients, p_{ij}, and the Poisson's ratio, ν. Using the above equations, a typical value of strain sensitivity can be obtained as around 0.64 pm/$\mu\varepsilon$ at the wavelength region of 820 nm, 1pm/$\mu\varepsilon$ at around 1300 nm and 1.2 pm/$\mu\varepsilon$ at 1500 nm wavelength region. The strain response has been found be to linear and no evidence of hysteresis was noticed [8].

The second part of the Eq. (2.14) represents the effect of temperature on the fibre grating, which depends on the thermal expansion coefficient and the thermo-optic coefficient of the fibre material and thus this component of the Bragg wavelength shift may be written as

$$\Delta\lambda_b = \lambda_b[\ (1/\Lambda)(\partial\Lambda/\partial T) + (1/n_{eff})(\partial n_{eff}/\partial T)]\Delta T \qquad (2.17)$$

where $(1/\Lambda)(\partial\Lambda/\partial T)$ is the thermal expansion coefficient and $(1/n_{eff})(\partial n_{eff}/\partial T)$ is the thermo-optic coefficient of the fibre. As the typical value of the thermal expansion coefficient (0.55×10^{-6} /°C for silica) is one order less compared to the value of the thermo-optic coefficient (8.6×10^{-6} /°C for germanosilicate fibre), the latter component is having the dominant effect for this thermal response of the FBGs. The thermal sensitivity of the FBGs fabricated in a germanosilicate fibre is typically around 12 pm/°C at the wavelength region of 1500 nm; however, this sensitivity is found to be slightly non-linear at higher temperatures, although no hysteresis has been observed.

2.4.4. Other properties of FBGs

Second harmonic of FBGs: It is observed during the formation of FBGs that once the growth of the grating saturates, the spectrum broadens under continuous UV exposure because the incident UV light is reflected entirely before reaching to the end the grating. Thus the core refractive index modulation of a strongly saturated grating is no longer sinusoidal, rather becomes almost square-wave fashion. It is interesting that the second harmonic of the grating appears about the wavelength of one-half of the fundamental Bragg wavelength with other higher order modes at shorter wavelengths [8].

Cladding and radiation-mode coupling: FBGs written in a highly photosensitive fibre, or the FBGs written under a high strength of UV exposure over a long time, have a pronounced transmission structure (a number of dips of less strength compared to the main grating) only on the shorter wavelength side of the fundamental Bragg wavelength [58]. This feature can only be found in the transmission spectrum and due to the component of the guided light radiated from the side of the core, which may be analysed by considering the radiation-mode coupling. This effect may be overcome by dipping the fibre-cladding into glycerine (as an index matching liquid), which eliminates the cladding-air interface effect. The other ways of minimising this situation are the use of high-NA fibre, which increases the gap between the fundamental grating and the cladding-modes, and use of a specially designed fibre with depressed cladding of proper index and thickness in between the photosensitive core and the normal cladding of the optical fibre, which suppresses the coupling of the guided mode to the cladding modes [59],[60].

Apodization of FBGs: In general, a series of side-lobes with less intensity appears with the main grating at adjacent wavelengths in either side. It is important to eliminate these side-lobes in some applications like to eliminate cross-talk in between information channels in the application of dense-WDM, for applications of add-drop filters, demultiplexers and for improvements in dispersion compensation characteristics of chirped gratings and therefore grating apodization is required. The apodization of gratings using a phase mask with variable

diffraction efficiencies [61],[62] and a cosine apodization technique by repetitive and symmetric longitudinal stretching of the fibre during grating formation [63] have been reported.

Chirped FBGs: A chirped FBG can be realised either by monotonically increasing or decreasing grating period, or modulation depth in core refractive index of the fibre or by both and it has some special applications in telecommunication and sensing. The structure of this grating may be considered as made of a series of very small length of uniform Bragg gratings with increasing period, so that the shorter wavelength light signal reflects from the portion having shorter grating period and longer wavelength signal reflects from that of longer grating period, satisfying the Bragg condition, which results in a broadband reflector. This grating can be used as a dispersion compensator in long-haul communication and as a broad-band reflector to form an all-in-fibre grating-based laser system in association with a uniform Bragg grating. The fabrication of chirped gratings of various types like simple chirped gratings [47], step-chirped, super-step-chirped and long super-step-chirped gratings [48]-[51] by concatenating several apodized gratings with increasing period have been demonstrated.

Blazed gratings: Blazed gratings are formed when the grating planes are parallel to each other but at some angle to the optical fibre longitudinal axis, which creates an alteration in the guided light through the fibre core, resulting in coupling of the fundamental guided mode into loosely bound guided cladding modes or into radiation modes outside the fibre core. For blazed gratings, not only different incident wavelengths emerges at different wavelengths, but different modes of the same wavelength also emerges at slightly different wavelength due to their different propagation constant, and thus can be used as a mode discriminator [64]. Another important application of blazed gratings is in mode conversion in the optical fibre [65],[66]. Mode converters can be fabricated by creating a periodic core refractive index modulation along the fibre length with a periodicity that creates the momentum mismatch between the modes to allow phase-matched coupling among them. Different grating periods are used for mode conversion at different wavelengths.

2.4.5. Various types of FBGs

There are three types of fibre gratings in general, namely, type I, type IIA and type II, and those may be classified according to the fibre properties and the writing condition of the gratings.

Type I FBGs: Type I Bragg gratings are formed in normal photosensitive optical fibres under the influence of moderate laser fluence. The fundamental characteristics of this type of grating is the complementary property between the reflection spectrum of the guided mode and the transmission spectrum, which implies that there is a very negligible loss due to the absorption into or reflection from the fibre cladding. Type I gratings are erased at comparatively low

temperatures depending on the material of the photosensitive fibre. For example, type I gratings written in B-Ge codoped fibre are erased at approximately 300°C, whereas the same type of gratings written in Ge doped fibre survive up to around 500°C. This type of grating is being widely used for various telecommunication applications and comparatively low temperature sensing applications.

Type IIA FBGs: Type IIA gratings are almost the same as the type I gratings regarding the complimentary nature of reflection and transmission spectral characteristics. This makes the type IIA grating almost indistinguishable from type I grating in a static situation with the only exception of relatively broad bandwidth of the grating. However, under dynamic condition, this type of gratings show a noticeable difference in feature during the fabrication or thermally erasure of the gratings, as the mechanism involved in forming the type IIA grating is different from that of a type I [20],[67] . Inscription of type IIA gratings require a long time UV-exposure following the formation and partially erasure of a type I grating. Also, type IIA gratings show an improved thermal stability performance compared to type I in a photosensitive fibre [68]. Typically, for a B-Ge codoped fibre, the time required to form a type IIA grating is around 12-15 minutes, whereas a type I grating can be written within a minute in that fibre under the same intensity of UV light. However, type IIA gratings are more thermally stable compared to type I FBGs written into this fibre, where almost no decay in reflectivity was observed up to 400°C for type IIA gratings.

Type II FBGs: Type II gratings are completely different in nature from type I and type IIA gratings and are formed under very high power single-pulse laser fluence [41],[42]. The reflection and transmission spectra of this type of gratings are not complementary to each other. These gratings pass wavelengths longer than the Bragg wavelength, whereas the shorter wavelengths are strongly coupled into the fibre cladding. It is apparent that when the laser pulse energy is beyond a threshold level (typically 650 mJ/cm^2), the UV-induced core refractive index modulation increases dramatically and becomes saturated by a highly non-linear mechanism involved in the formation of grating. Examine of a type II grating through an optical microscope shows a significant localised damage at the core-cladding interface on the UV-exposed side of the fibre, which is responsible for the strong localised change in the core refractive index of the fibre. This type of FBG is shown to be extremely thermally stable (can survive up to 800°C without any significant decay in reflectivity); however, the process of fabricating type II gratings in a stripped-off fibre weakens the fibre drastically due to the occurrence of localised damage and surface contamination.

2.4.6. Reliability of FBGs

Bragg gratings fabricated in optical fibres play an important role in the next generation in terms of the operational lifetime and the reliability of FBGs used in a telecommunication or a sensor system. Regardless of whether the optical fibre has undergone any kind of pre-treatment prior to writing an UV-induced grating, a thermal decay of the grating is occurred over a period of time, even when it is stored at room temperature. So, to operate the FBGs satisfactorily over a period of its lifetime, thermal stability of the device is much essential. The thermal stability and the decay of the Bragg gratings has been analysed using a power-law approach [69],[70] and the master aging-curve approach [69],[71]. Various models of the decay of gratings written in various types of fibres including hydrogen-loaded fibres [68]-[73] have been developed to explain the thermal stability of the FBGs in terms of the activation energy. It is shown that by conducting a process of accelerated aging [68]-[70],[74] a grating can be made stable (by wiping the unstable portions of the grating) to operate reliably at comparatively low temperatures for a long period of time.

FBGs are of considerable interest in various optical fibre sensing applications in civil structures for measuring temperature, strain and pressure. Therefore, the mechanical strength of the gratings is also another important factor, although it is mainly dependent on the host material of the optical fibre. However, the degradation of the mechanical strength of the optical fibres resulting from the UV exposure (during the process of grating writing), from the surface contamination caused by the stripping-off the fibre jacket and from the temperature cycle (to pass through the accelerated aging test) has been reported [75]-[77].

2.5. Theory of FBGs

A fibre Bragg grating (FBG) can be described in a simple way with a periodic modulation of the refractive index of the optical fibre core. The theory of FBGs may be developed by considering the propagation of the modes in the optical fibre. An FBG with constant refractive index modulation and period therefore has an analytic solution. A complex grating may be considered to be a concatenation of several small sections, with each of constant refractive index modulation and period. In this way, the modelling of the transfer characteristics of FBGs becomes comparatively easier. There are various techniques for solving the transfer function of FBGs, proposed by various researchers. Matrix methods like the effective index method (EIM) and the transfer matrix method (TMM) have also been developed for the analysis of the gratings. EIM [78] is especially suitable for the integrated optic gratings, where in the analysis, the grating is divided into sections, with the length of each one being much smaller compared to the grating period and the fields are computed inside each section assuming constant refractive index for that section. In TMM [79], the grating is divided into sections, with length of each one being larger than the period of grating and the variation of refractive index within the sections have

been considered according to the uniform gratings. This approach is suitable for periodic, aperiodic as well as long-length gratings. Several other researchers have also analysed the gratings by Rouard's method [80] and Bloch wave approach [81]. However, without going into the detailed analysis, the basic theories associated to a uniform FBG has been described here using the coupled-mode theory.

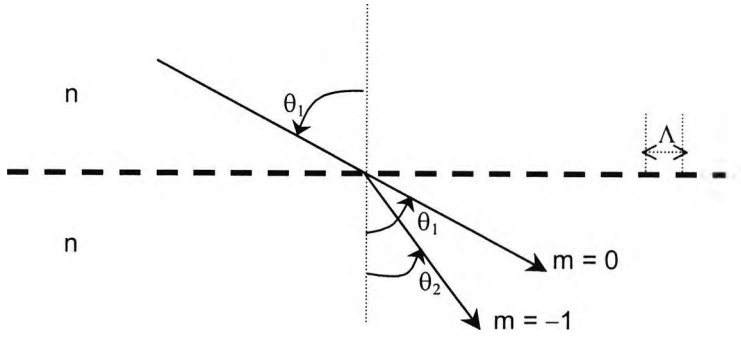

Fig 2.7: The diffraction of a light ray through a grating.

2.5.1. Resonance wavelength of fibre gratings

For simplicity of analysis, the coupling between two modes of a uniform grating and a qualitative picture of the basic interactions have been considered here. A simple schematic diagram of diffraction through a fibre grating is shown in Fig. 2.7. The effect upon a light wave incident on the grating at an angle θ_1 can be described as [56]

$$n \sin\theta_2 = n \sin\theta_1 + m(\lambda/\Lambda) \qquad (2.18)$$

where θ_2 is the diffracted angle and the integer, m, determines the order of the diffraction. The above equation predicts the angle of θ_2 into which the constructive interference occurs.

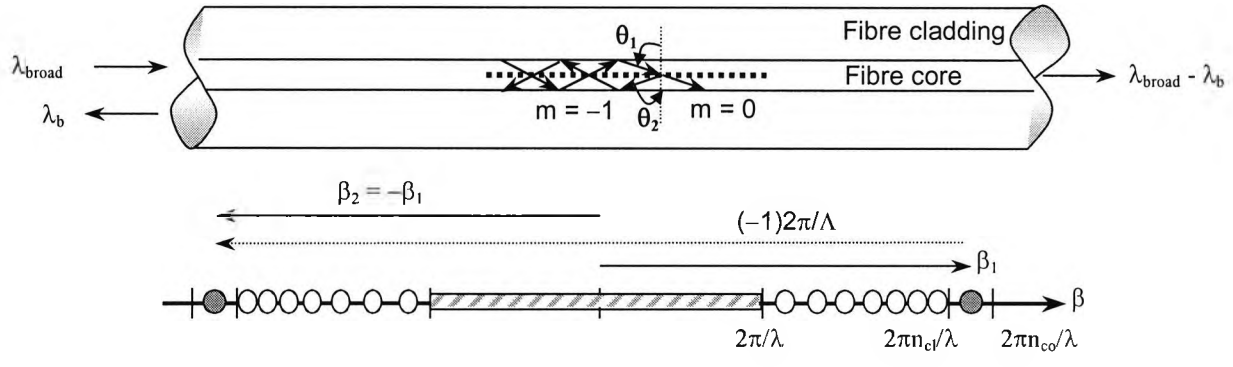

Fig. 2.8(a): A simple illustration of core-mode reflection of a fibre Bragg grating.

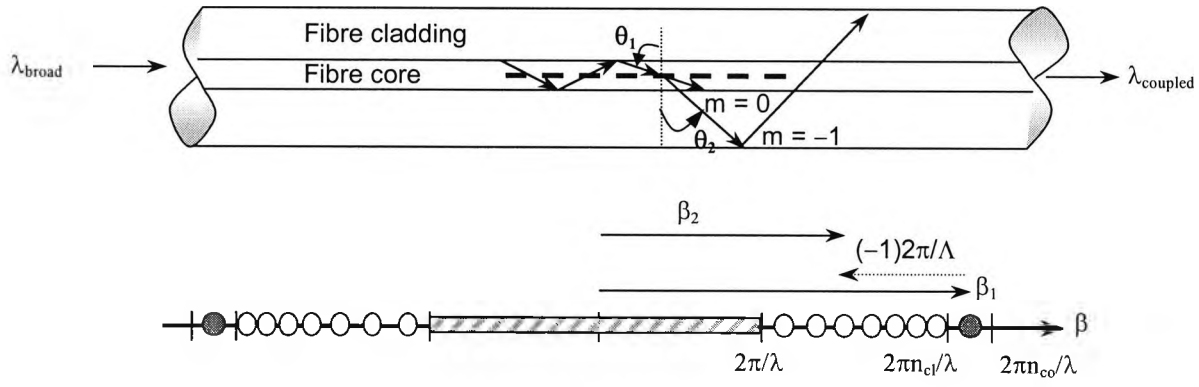

Fig. 2.8(b): A simple illustration of core-mode and cladding-mode coupling for an LPG.

Fibre gratings can be classified generally into two types; Bragg gratings (also called as short-period gratings), in which coupling occurs between modes travelling in the opposite directions, and the long period grating (LPG), in which the coupling occurs between the modes travelling in the same (forward) direction. Fig. 2.8(a) illustrates the reflection of a mode by a Bragg (short-period) grating with an angle θ_1 into the same mode travelling in the opposite direction with a bounce angle of $\theta_2 = -\theta_1$. As the propagation constant of the mode simply $\beta = (2\pi/\lambda)n_{eff}$ with $n_{eff} = n_{co}\sin\theta$, Eq. (2.18) can be rewritten for the guided modes as

$$\beta_2 = \beta_1 + m(2\pi/\Lambda) \qquad (2.19)$$

For first-order diffraction, m = −1. This condition has been illustrated on the β-axis in the figures, where the solid circles represent the core-modes ($n_{co} > n_{eff} > n_{cl}$), the open circles represent the cladding-modes ($n_{cl} > n_{eff} > 1$) and the hatched regions represent the continuous radiation-modes. As the negative β values represent the modes that propagate in the opposite direction, the resonant wavelength for a reflection grating of a mode of index, n_{eff1}, into a mode of index, n_{eff2}, can be written, using Eq. (2.19) as,

$$\lambda = (n_{eff1} + n_{eff2})\Lambda \qquad (2.20)$$

When two modes are identical ($n_{eff1} = n_{eff2} = n_{eff}$), the familiar result for the Bragg reflection condition appears as

$$\lambda = 2n_{eff}\Lambda \qquad (2.21)$$

In case of an LPG, diffraction of a core-mode with a bounce angle of θ_1 into a co-propagating cladding-mode with a bounce angle of θ_2 (as shown in Fig. 2.8(b)) occurs and the resonance wavelength of an LPG can be predicted as

$$\lambda = (n_{eff1} - n_{eff2})\Lambda \qquad (2.22)$$

For a co-propagating coupling of modes at a certain wavelength requires much longer grating period compared to that is required for a counter-propagating coupling of modes.

2.6. Applications of FBGs in Communications and Sensing

FBGs have emerged as an important component to be used in a variety of lightwave applications. Their unique properties, versatility as in-fibre devices and relatively simple signal processing techniques make them much popular through their various uses such as fibre lasers, fibre filters, wavelength division multiplexers and demultiplexers, add/drop multiplexers, wavelength converters, dispersion compensators. In addition, recently FBGs are significantly being used for sensing applications to measure various physical parameters like temperature, strain, relative humidity, pressure etc. including simultaneous measurement of dual or triple physical parameters. In this section, a range of applications using FBGs is reviewed briefly.

2.6.1. Fibre lasers

Fibre lasers are attractive because of their simplicity, compact size and fibre compatibility. By coupling an FBG to a semiconductor laser chip, a "hybrid" fibre Bragg grating-based diode laser [82] can be achieved, as shown in Fig. 2.9. A single-frequency laser operating at the Bragg resonance wavelength, with a very narrow line-width, can be obtained through this arrangement, where the temperature-induced wavelength drift of the semiconductor laser can be reduced significantly.

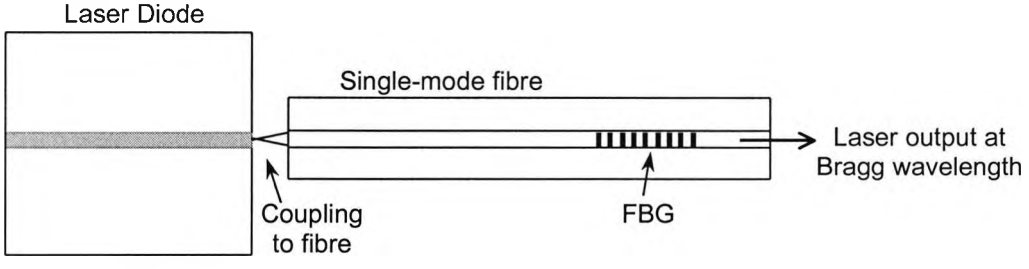

Fig. 2.9: A schematic of a "hybrid" FBG-based diode laser.

There is another approach to build an all-in-fibre Bragg grating-based laser by using a finite length of a rare-earth doped fibre as a gain medium with a pair of gratings of matched wavelength (to act as a mirror and a partial reflector) in either side of it [83]-[86]. A basic schematic diagram of the scheme has been shown in Fig. 2.10. A rare-earth doped fibre is used as a gain medium and by using a pump laser diode at a suitable wavelength (depending on the rare-earth doped fibre) to achieve the amplification. An FBG with reflectivity of more than 99% acts as a mirror and an FBG with lower reflectivity forms the partial reflector, which can couple the output of the fibre laser. With less pump power, a notch in the fluorescence, at a wavelength corresponding to the Bragg wavelength of the partial reflector grating is observed. With increasing the pump power, the loss in the fibre laser cavity is overcome and starts lasing. At

pump powers just above the threshold, the notch begins to grow in the positive direction resulting in a fibre laser with very high signal-to-noise ratio with a very narrow bandwidth on the top of the fluorescence.

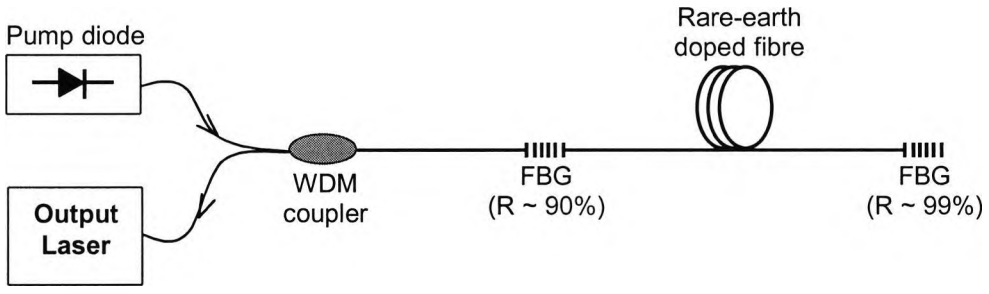

Fig. 2.10: A schematic of FBG-based rare-earth doped fibre laser.

Single-mode operation of the fibre laser can be achieved by using intracore Bragg gratings as cavity feedback at both ends of an appropriate length of the rare-earth doped fibre. However, the design parameters like length of the cavity, reflectivity and the bandwidth of the Bragg gratings are some of the important factors to be considered to achieve a proper and stable single-mode operation of the fibre laser [83]. In addition, the mode-locking for ultra-short pulse lasers can be achieved by modulating a cavity parameter at the fundamental or a harmonic of a cavity round-trip frequency and has been demonstrated by using both uniform [87] and chirped gratings [88].

2.6.2. Fibre filters and mode converters

A single FBG written into a single-mode fibre can be used as a wavelength selective reflector or a band rejection filter from the reflection at around Bragg resonance wavelength. Fig. 2.11 shows a schematic of a basic filter constructed by writing an FBG in a fibre and by introducing a 3-dB coupler. This is one of the simplest methods of accessing a narrow-band signal reflected from an FBG. The disadvantage in this system is around 6-dB loss for passing of the signal through coupler twice. However, this problem can be removed to some extent by using a 3-port circulator, instead of a coupler.

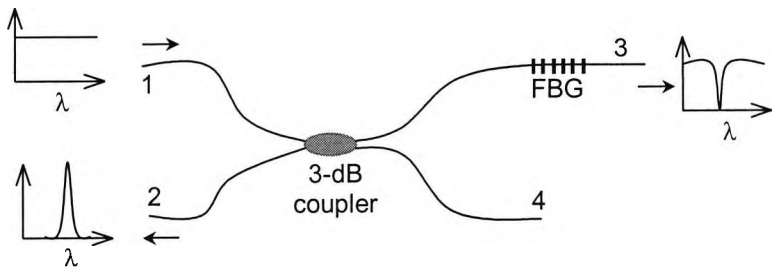

Fig. 2.11: A schematic of a basic Bragg grating filter.

Also, the band-pass filters can be designed by placing two identical FBGs in two arms of a fibre coupler, either as in a Michelson arrangement [89] or as in a Mach-Zehnder configuration [90]. Fabry-Perot etalon filters can also be designed by placing two identical gratings in series on a single-mode fibre, which has been demonstrated by Town *et al.* [91] by using two identical linear chirped gratings. A comb and superstructure filter is also very useful in wavelength division multiplexing and demultiplexing systems, which can also be realised by writing a series of gratings into a section of optical fibre at different wavelengths using various phase-masks [92].

By tilting or blazing the FBG at an angle to the fibre axis, light can be coupled out of the core of the fibre into loosely bound cladding modes or to radiation modes outside the fibre. This wavelength selective tap occurs over a relatively broad range of wavelengths, which can be controlled by the grating design parameters. These signals are not reflected back, as the core-mode couples with co-propagating cladding-modes, and thus forms an absorption type filters. Furthermore, a reflecting spatial mode coupler or a mode-converter can be made with a small tilt of the grating planes to the fibre axis, and has been demonstrated by Hill *et al.* [65].

2.6.3. WDM technique and Add/Drop Multiplexers

With the rapid growth of the telecommunication tariff, the capacity of the fibre has become very important. Wavelength division multiplexing/ demultiplexing (WDM/D) is a promising solution for this; however, it requires low loss, compact, stable and reliable components leading to be used as wavelength selective dropping or inserting channels.

A WDM demultiplexing system comprising FBGs was first presented by Mizrahi *et al.* [93]. The concept of this system has been illustrated in Fig. 2.12, which consists of a single 1×4-fibre splitter followed by an FBG transmission filter at each output port. The filters were designed to pass one signal wavelength at each port, while rejecting the other three adjacent wavelength channels. Using a pair of gratings that do not overlap in wavelength, a simple band-pass filter was designed, in which each of the two gratings rejected a broad range of wavelength with the unaffected transmission of the desired wavelength. Although the basic concept of the device is very simple, the implementation of the system needs careful grating design and fibre optimisation.

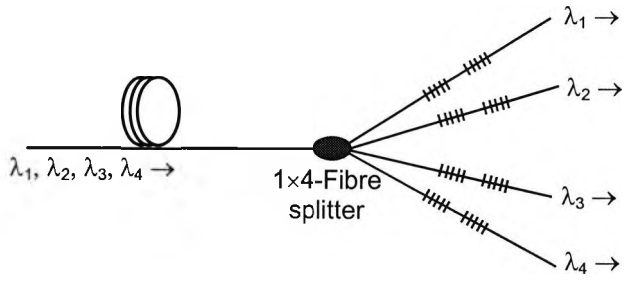

Fig. 2.12: A schematic of a 4-channel FBG demultiplexer.

A very simple scheme of an add/drop filter [94] can be designed by adding an extra 3-dB fibre coupler to the Michelson arrangement filter; a schematic diagram is shown in Fig. 2.13 to describe the operation of the add/drop multiplexer/demultiplexer. A multi-wavelength signal is launched into one input (e.g., port 1) of the device. Assuming the Bragg resonance wavelength of the pair of identical gratings as λ_b, the signal corresponding to the wavelength λ_b is emerged from the output port 2, whereas the remaining wavelengths are emerged from output port 3. Port 3 acts now a "drop"-filter by dropping the λ_b wavelength of a multiwavelength signal, which can be operated as a demultiplexer. Again if the output port 2, with the signal wavelength of λ_b, is connected to the port 4 (as input), then all the wavelengths of the multi-wavelength signal are returned through the output port 3. Port 3 acts as an "add"-filter in this configuration, which operates as multiplexer.

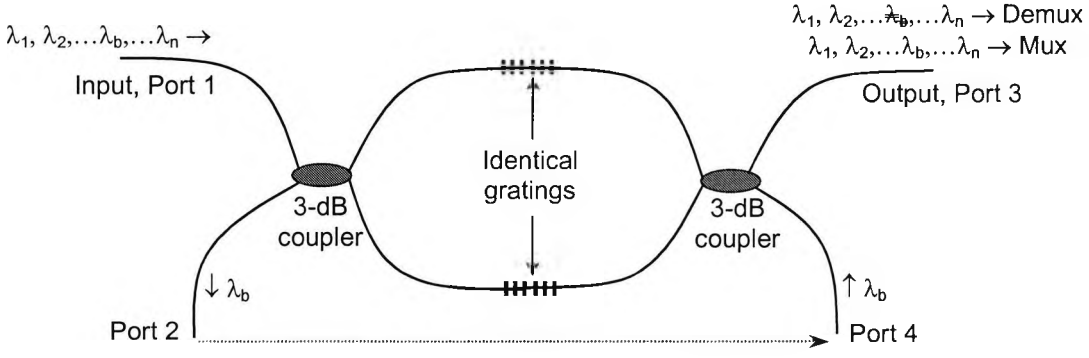

Fig. 2.13: A schematic of Add/Drop Multiplexer/Demultiplexer.

2.6.4. FBGs for dispersion compensation

Chromatic dispersion is one of the main problems in long-haul communication through the single-mode optical fibre, which is caused by travelling of different wavelength components of a data pulse with different group velocities. This causes the pulse broadening and increases the bit-error rates. This problem can be minimised by using a chirped fibre Bragg grating. The spacing of the grating planes is chirped, increasing along its length, so that the different wavelength components are reflected from the different points of the grating along its length. Thus, the grating can serve as a selective delay line, which delays the wavelengths that travel faster through the fibre until the other wavelengths catch up, resulting in the device as a dispersion compensation element. A schematic diagram of a chirped FBG is shown in Fig. 2.14.

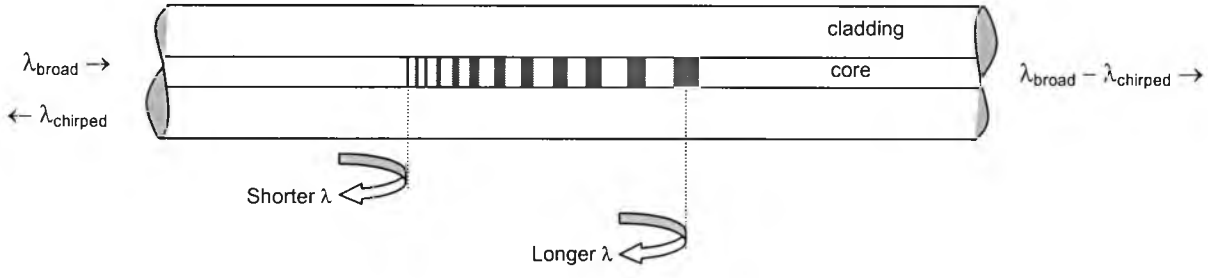

Fig. 2.14: A schematic diagram of a chirped grating with an aperiodic pitch.

Even though the picture is simplified, as a dispersed pulse includes a range of wavelengths rather than several separate wavelengths, the idea is the same- the distance of traverse of light along the grating length depends on its wavelength. However, the chirped FBGs are simple and compact and thus do not require much long fibre to compensate the dispersion. Dispersion compensation was first practically demonstrated by using short pulses travelling through single-mode fibre and a chirped fibre grating to compensate the pulse broadening arises from negative group delay dispersion and the non-linear self-phase modulation in the fibre [95],[96]. However, higher levels of compensation in dispersion may be achieved by using more complex grating structures or a combination of gratings [97]-[100].

2.6.5. FBGs for sensing strain and temperature

FBGs have been considered as excellent sensing devices since the early stage of their development, for measuring various physical parameters like temperature, strain, pressure, vibration and so on, in static and dynamic conditions [1]-[3],[6],[7],[10],[11]. The key advantage lies in the wavelength-encoded measurand information, thereby making the sensor self-referencing and independent of fluctuation of the signal level. In addition, the system is immune

to source power and connector losses, which are the common problems in many of the optical fibre sensing systems.

Fibre Bragg gratings were demonstrated as a temperature sensor for measuring temperatures up to 500°C [5] starting from room temperature and then extended up to 800°C [8] depending on the fibre material. However, a slight non-linearity in the thermal response of the gratings [101],[102] was observed, for which the non-linear behaviour of the thermo-optic coefficient of the fibre material [103] is believed to be responsible. FBGs were also used for cryogenic temperature measurements to the liquid nitrogen temperature (77 K) [104],[105] and to the liquid helium temperature (4 K) [106]. The similar non-linearity in thermal response of the gratings was found at lower temperatures as well. The thermal sensitivity of the fibre gratings was enhanced by proper bonding of the grating to other substrate that is having greater thermal expansion compared to the fibre [104]-[106]. The thermal expansion and the thermo-optic effect causes the changes in the periodicity and the refractive index of the fibre core when temperature is applied resulting in the changes in the Bragg wavelength of the grating, which is the basis of the use of grating as a temperature sensor. A typical value of temperature sensitivity of FBGs was found to be ~ 10 pm/°C (on average) at the wavelength region of 1500 nm, with a slight variation depending on the material of the fibre.

Fibre Bragg gratings are also well capable of measuring strain. The effective refractive index, as well as the periodic spacing between grating planes are affected by the applied strain resulting in a change in the Bragg resonance wavelength of the grating. At room temperature the strain sensitivity has been found to be ~ 1pm/με at the wavelength region of 1300 nm [10] and ~1.2 pm/με at the region of 1500 nm wavelength, [6],[11] where the range of the strain measurement was reported up to around 2000 με. The strain response of the FBGs at cryogenic temperatures were measured and reported [107].

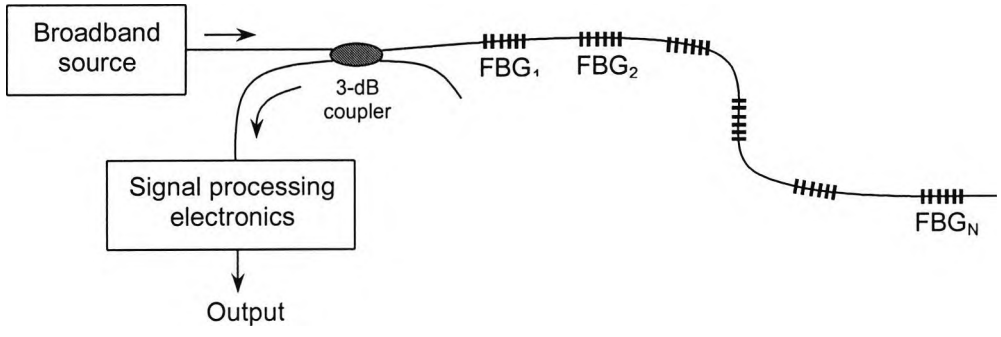

Fig. 2.15: A schematic of quasi-distributed sensing system using FBG elements.

The narrow bandwidth wavelength encoded nature of output also enables an FBG-based quasi-distributed sensing system for measuring strain, temperature and other physical parameters at different strategic spatial locations. A basic schematic of a quasi-distributed system has been shown in Fig. 2.15, where a number of reflected wavelengths from various FBGs are demodulated and processed through the signal processing electronics unit. Several techniques have been demonstrated for performing this wavelength analysis. Among those, the most common technique is to assess the FBG-reflected wavelengths through a suitable band-pass filter [108], which can be further improved by using a wavelength dependent transfer function [109] and a tuneable band-pass filter [110] for scanning the desired signal.

2.6.6. Simultaneous measurement of strain and temperature

Although FBGs are well suited for measuring strain and temperature, one of the most significant limitations of FBG-based sensors is the actual separation of the parameters as the Bragg wavelength of a grating is sensitive to both strain and temperature. It is impossible to differentiate the effects of strain and temperature through a single measurement. Various researchers have proposed several schemes to discriminate these parameters; however, the basic principle of operation is the same for all the schemes. If $\Delta\varphi_1$ and $\Delta\varphi_2$ are two observables that represent the strain and temperature induced changes in an experimental scheme, then these two variables can be expressed in a simple matrix form as [6]

$$\begin{bmatrix} \Delta\varphi_1 \\ \Delta\varphi_2 \end{bmatrix} = \begin{bmatrix} k_{1T} & k_{1\varepsilon} \\ k_{2T} & k_{2\varepsilon} \end{bmatrix} \begin{bmatrix} \Delta T \\ \Delta\varepsilon \end{bmatrix} \tag{2.23}$$

assuming the strain and temperature-induced perturbations are linear. In this equation, k_{iT} and $k_{i\varepsilon}$ (i = 1, 2) are the temperature and strain coefficients respectively for the above-mentioned variables. And thus, the induced temperature and strain can be determined by the matrix inversion technique as

$$\begin{bmatrix} \Delta T \\ \Delta\varepsilon \end{bmatrix} = \frac{1}{(k_{1T}k_{2\varepsilon} - k_{2T}k_{1\varepsilon})} \begin{bmatrix} k_{2\varepsilon} & -k_{1\varepsilon} \\ -k_{2T} & k_{1T} \end{bmatrix} \begin{bmatrix} \Delta\varphi_1 \\ \Delta\varphi_2 \end{bmatrix} \tag{2.24}$$

The validity of this approach lies in different values of the temperature and strain coefficients and the non-zero determinant of the matrix coefficients, i.e., $(k_{1T}k_{2\varepsilon}-k_{2T}k_{1\varepsilon}) \neq 0$.

Discrimination of strain and temperature has been practically demonstrated by various researchers in several approaches like using two superimposed FBGs of different wavelengths [111], by splicing two gratings written in fibres having dissimilar diameters [112], or written in different photosensitive fibres [113], using a combination of FBG and LPG [114] and a single LPG [115], using a single FBG written in a rare-earth doped fibre [116],[117], by writing a grating in a splice-joint between two different photosensitive fibres [118], using a fibre grating Fabry-Perot cavity structure [119], by use of a superstructure fibre Bragg grating structure [120], by an

experimental characterisation of the first- and the second-order diffraction wavelengths of the FBGs [121],[122], based on a combination of a Bragg grating element and a Brillouin scattering interrogation system [123], relying on a combination of a sampled FBG and an LPG [124] and by using different types of gratings written in close separation in a fibre with and without hydrogen-loading [125]. However, all the approaches have used the matrix inversion technique to discriminate the parameters, where the maximum measurement range of temperature is up to around 150°C.

For the simultaneous measurement of strain and temperature, it is also useful to obtain a measurement of the errors in temperature and strain, which results in a limited resolution in the wavelength measurement. The effect of cross-sensitivity in this measurement has also been considered and reported [126]. The systematic errors in temperature and strain associated with the measurement can be expressed as [3],[6]

$$|\delta T| = |\delta\varphi_1/k_{1T}| \quad \text{and} \quad |\delta\varepsilon| = |\delta\varphi_2/k_{2\varepsilon}| \tag{2.25}$$

for an independent measurement. In case of a practical simultaneous measurement of both parameters, the corresponding errors can be presented as [127]

$$|\delta T| = (|k_{2\varepsilon}||\delta\varphi_1| + |k_{1\varepsilon}||\delta\varphi_2|)/|k_{1T}k_{2\varepsilon} - k_{2T}k_{1\varepsilon}| \quad \text{and}$$
$$|\delta\varepsilon| = (|k_{2T}||\delta\varphi_1| + |k_{1T}||\delta\varphi_2|)/|k_{1T}k_{2\varepsilon} - k_{2T}k_{1\varepsilon}| \tag{2.26}$$

2.6.7. Multiplexing techniques for sensing

'Multiplexing' plays a very important role in the area of optical fibre sensing, where a major impact of distributed sensing is anticipated. By sharing the optical source and the signal-processing unit, the cost of the sensor is reduced with the improvement in the performance of the optical-based sensors compared to the conventional sensors. Due to the narrow-band wavelength reflection spectra of the FBGs, they are being used significantly with a multiplexed configuration in the fibre optic network regardless whether the area is communication or sensing. There are several techniques of multiplexing such as time-division-multiplexing [128], wavelength-division-multiplexing [109],[110] and spatial [129],[130] have been reported. However, the multiplexing capacity of any of these techniques is limited to approximately 10 sensors [6] due to various factors including speed, cross-talk, signal-to-noise ratio and the wavelength bandwidth. The most popular approaches for increasing the sensor numbers are to combine the techniques [10],[11],[131],[132] of multiplexing, for example, time and wavelength division multiplexing.

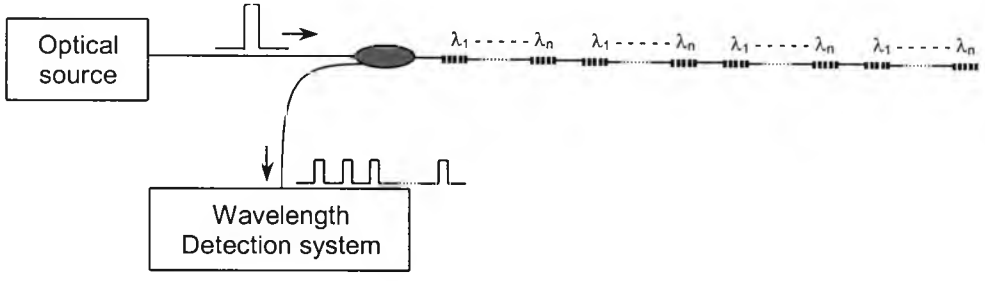

Fig. 2.16(a): WDM/TDM combination of FBG arrays: serial system.

One of the primary advantages of using FBG-based distributed sensing is that large numbers of sensors may be interrogated along a length of a single fibre. WDM provides tens of sensors per fibre, and TDM can multiply this number by several times by sharing the optical source with a pre-defined delay at each time. By combining WDM/TDM in a serial configuration, as shown in Fig. 2.16(a), several wavelength-stepped arrays are concatenated, each at a greater distance along the fibre length. By launching a short light-pulse from a source, the reflection spectra from FBGs can be received by the detector at successively later times according to the successive distant positions of the gratings along the fibre. The detection instrumentation system can be configured to respond to the reflected signals only during a selected window of time after the pulse is launched to detect a single WDM set of sensors at a time.

Low reflectivity gratings with high sensitivity detection system would be crucial for interrogating a large number of FBGs in a single fibre as a serial configuration because of two deleterious effects that can arise from gratings with high reflectivity. Reflected signals from FBGs that are separated in time with overlap in the wavelength can experience cross-talk through '*multiple-reflection*' and '*spectral-shadowing*'. The TDM/WDM parallel and branching optical fibre network topologies, as shown in Figs. 2.16(b) and 2.16(c), are useful to eliminate these deleterious effects. However, the overall optical efficiency is reduced and gratings with high reflectivities with a number of additional couplers are required in these configurations.

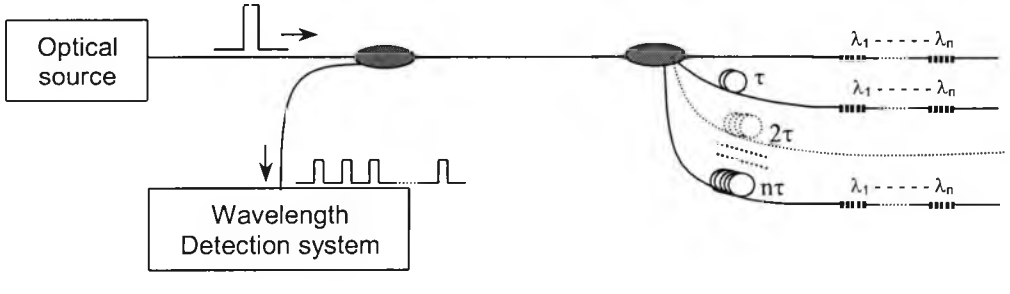

Fig. 2.16(b): WDM/TDM combination of FBG arrays: parallel network.

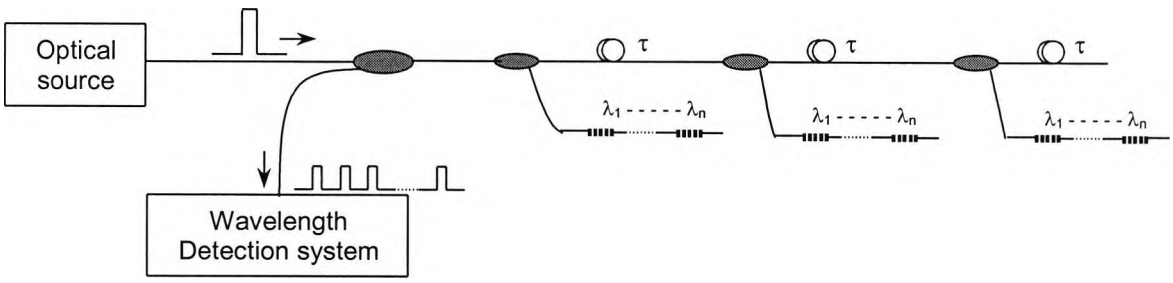

Fig. 2.16(c): WDM/TDM combination of FBG arrays: branching network.

2.6.8. Fibre Bragg grating laser-based sensors

FBGs are also very much useful for creating in-fibre cavities for fibre lasers because of their narrow-band reflection spectra. This field has grown interest in the area of communication for tuneable single frequency devices for WDM networks [133]-[135], as discussed in the earlier sections. At the same time, this field is emerging in the sensing area for very high-resolution measurement of temperatures and static and dynamic strains, as reported for past few years [10],[135]-[137].

A basic FBG-based laser sensor can be formed by either two gratings of matched Bragg wavelength, or a combination of a uniform grating and a chirped grating to create all-in-fibre cavity, or one grating combined with a broadband reflector. A certain length of a rare-earth-doped fibre, placed between the gratings or the grating and the reflector, allows the system to provide the cavity gain leading to the lasing action. A basic structure of this system has been shown in Fig. 2.10 and is described in 'fibre-lasers' section. The device can be implemented through various configurations and operated either in single frequency or multi-mode fashion [133],[134],[136],[138]. When this device is configured as a sensor element, the changes in the environmental conditions or the physical parameters subjected to the laser cavity and the gratings can be detected by monitoring the change in some characteristics of the laser output. For the variations in strain and temperatures on the gratings themselves, the shift in the wavelength of the laser output is identical to that obtained through the passive configuration of FBGs. The advantage of the laser configuration is that the bandwidth of the output light from the laser sensor can be much narrower than that from the passive FBG configuration, resulting in better resolution in sensing system. In addition, high SNR can be achieved either by applying higher pump power or by high amplification (through long length or rare-earth doping concentration), which is very useful in some critical applications. However, detection of the beating effects between different longitudinal cavity modes within the system is also possible [139] with the FBG-based laser sensor configuration. The inherent wavelength division capabilities of the gratings also allow the implementation of the distributed laser-sensor configuration [140],[141].

Another interesting application of FBG-based laser sensor can be implemented by exploiting the compactness and the high sensitivity features of it. Compact laser sensor can be formed by using a short cavity length, which allows the single frequency operation. The narrow linewidth of the laser output from such lasers permits the detection of very weak dynamic strain perturbations through a low-level frequency-modulation of the laser output resulting in a very small shift in the wavelength of the laser output [142].

2.6.9. FBG-based sensing for various applications

Bragg gratings have been shown to have great importance in recent few years for their wide range of sensing application in several multi-disciplinary areas and industries. In previous sections, the properties, simple writing techniques and the working principle of the gratings in various configuration have been discussed, which are the basis of the popular and wide spread applications of this device in various areas. In this section, a brief survey of such work has been made.

FBG-based sensors have tremendous potential in *aerospace engineering applications* as temperature, pressure and strain sensors. These devices can also be used as embedded sensors that can monitor the performance and fabrication of reinforced carbon fibre composites and advanced testing of gas turbine engines, for which there is no acceptable competing technology. These materials offer a greater strength-to-weight ratio than steel and can be moulded into more complex shapes. An embedded sensor system can provide the real-time information, enabling an intelligent manufacturing process monitoring, such as *in-situ* temperature profiling and strain release monitoring of the composite directly in the autoclave, thereby improving the real-time manufacturing and product quality. Furthermore, the sensor can improve the design of the smart structures and skins for the structural monitoring by distributed strain and temperature measurements. Distributed strain sensing in various composites through embedded FBG-based sensors [143],[144] and the real-time strain development during composite curing [145] have been demonstrated and studied. FBGs can also be used in space vehicles to measure the dynamic loads on a lightweight antenna reflector [146].

There is a great potential of down-hole instrumentation using FBGs in *marine applications* for exploration of natural oil resources, where conventional electronic sensors may not tolerate extremely harsh environments. Attempts have been made using FBGs for the characterisation of scaled marine vehicle models [147] and composite hull embedded sensor system is being developed for instrumenting an in-service fibreglass mine countermeasure vessel by exploiting the static and dynamic strain measuring capabilities of the FBGs [148].

There is a growing interest of FBG-based sensors in civil engineering structural monitoring, for example, to measure the mechanical loading for maintaining bridges, dams, tunnels, buildings, stadiums etc. One of the most important applications of Bragg gratings is as sensors for smart structures, where the grating is embedded directly into the structure to monitor its strain distribution; however, for the error-free quasi-static strain measurement, temperature compensation is required. Gebremichael *et al.* [149],[150] have demonstrated the grating-based system for the long-term monitoring of the bridge structure using a system having 64 gratings multiplexed through 8 channels.

The field of medical applications [151] is also one of the most interesting application areas of FBG-based sensors mainly because they are electrically passive in nature. With the advancement of optical fibre-based sensors, there has been interest to employ it for the physiological parameter measurements, for which extrinsic fibre optic sensors are most commonly used. For medical applications where a resolution of 0.1°C over a range of around 35-50°C is required, with a special need for sensor multiplexing for the measurement of temperature profiling, FBGs appear to be particularly very useful. A grating-based scheme has also been presented for the remote temperature measurements in an NMR machine and for the use of cardiac monitoring [151]-[153].

2.6.10. Sensing based on the fibre fluorescence

Fluorescence in the optical fibres has been observed with a range of different fibre hosts, particularly in various rare-earth doped silica fibres. The variety of such available fibres has increased dramatically over the years, from the early use of the most successful of the laser solid-state media, neodymium-doped glass, to sensors containing erbium, ytterbium, thulium and holium, for example [12]. However, there is a wide range of other fluorescent materials that have been doped into plastic optical fibres, particularly for sensing applications, where the loss mechanisms in plastic hosts, usually responsible for the laser quenching action, are not important and when the only fluorescent output is used. A major difference between the silica and plastic host fibres is the flexibility in the latter allowing to bend it often, to a greater context. On the other side, silica-based fibres have the advantage of both lower attenuation and higher durability over plastic fibres (particularly for high temperature sensing applications).

Rare-earth doped materials in low-loss silica-based fibres are of significant interest for temperature-sensing applications because of their temperature-dependent emission and absorption properties. This behaviour is due to the broadening of the homogeneous linewidth and to the changing population of the energy sub-levels or levels with temperature [13], [14]. When a rare-earth doped fibre is pumped, the carriers of the doped ions in the ground-state energy level are excited and quasi-instantaneously a meta-stable energy level is populated

through a non-radiative transition, depending upon energy and the wavelength of the pump power. As a result of this type of population-inversion, an amplified spontaneous emission (ASE)-based fluorescence occurs in various regions of wavelength, depending on the presence of different rare-earth ions in the host material. A fluorescence in an erbium-doped fibre in a region of wavelength of 1540 nm with two distinct peaks has been observed by Imai *et al.* [187] and the variation of the fluorescence peak power ratio was exploited for temperature-sensing over a limited range of temperature (-50°C to +90°C). The technique of fluorescence intensity ratio has been used by Maurice *et al.* [217] for different rare-earth doped fibres for measuring temperature up to ~ 600°C. The effects of high temperature on the sensors based on erbium-doped fibres have been discussed comprehensively by Zhang *et al.* [219]. Temperature measurement based on the fluorescence lifetime has also been explored extensively and the merits and demerits of this scheme have been discussed [12].

2.7. Scope of new work of this thesis

A brief and comprehensive review on various aspects of fibre Bragg gratings has been made in previous sections. A significant amount of work on FBGs has already been done in recent few years. However, very little work has been reported in the field of high temperature sensing applications in association with the FBGs. This is mainly because of the material of the fibre into which the gratings are written. The gratings inscribed into the conventional photosensitive fibres are commercially available, but they can survive hardly higher temperatures and may only be used up to the temperature of 250°C (for B-Ge codoped fibre) and 500°C (for Ge doped fibre) for a reliable sensing applications.

In this project, thus, the attention has been focused on the high temperature sensing potential of FBGs written in some specially fabricated photosensitive fibres. Doping of Sn (tin)-ions introduced into the core of the fibre can make the gratings written into these fibres more thermally stable [154]-[157]. Based on these reports, some special optical fibres have been fabricated at the University de Nice, France. Er^{3+}-ion doping has also been introduced in addition to the tin-ions into the fibre core, to make the fibre more useful for other various high temperature applications associated to the fibre fluorescence, caused by the rare-earth ion doping specifically for simultaneous measurement of strain and temperature. The thermal stability of the gratings written into these specially fabricated fibres have been studied and analysed. The analysis of the thermal decay of the FBGs written into one of these (highest temperature sustainable) fibres has been compared to those written into one of the commercially available and the most photosensitive fibre (B-Ge codoped) in terms of both the refractive index modulation and the effective refractive index of the core of the fibre.

Furthermore, the thermal response of the gratings has been studied over the whole range of temperature measurement. The observation of non-linear thermal response of the gratings should lead to work in a new direction to modify the sensing and measurement schemes for individual temperature measurement, for simultaneous measurement of temperature and the other parameter like strain and for temperature compensation approach associated to the measurement of other physical parameters. The simultaneous measurement of strain and temperature over the wide ranges, for both the parameters, by writing gratings into the specially fabricated rare-earth doped fibre is another pathway to continue the work. The temperature-dependent ASE-based fluorescence intensity of the rare-earth doped photosensitive fibre and the dual response of the grating to temperature and strain are the basis of this simultaneous measurement scheme. Consideration of non-linear thermal response of the grating is taken into account in this scheme to overcome the limitations of the matrix inversion technique that is conventionally used for the simultaneous measurement scheme. The work done to investigate this has been described in detail sequentially in the following chapters.

2.8. Summary

FBGs are fast becoming one of the most essential elements both in the area of communications and sensing. A reasonably significant amount of work in the field of optical fibre Bragg gratings has already been done in last ten / twelve years. This chapter has reviewed briefly the photosensitivity mechanism involved behind the formation of FBGs, followed by the relevant theory required to explain the FBGs, its properties and applications. Different techniques for the inscription of gratings along with various types of gratings are described. The applications of the FBGs for measuring any physical and / or chemical parameters like – temperature, strain, pressure, relative humidity, carried out to date, in various fields, starting from the process industries to medical instrumentation, by various researchers, are reviewed extensively in this work and then, the scope of the new work in this field is evaluated, in terms of high temperature sensing potential of the FBGs written in some specialised optical fibres.

Chapter 3

Fabrication of FBGs: Photosensitivity and thermal sustainability

3.1. Abstract

This chapter introduces the setting up of a system for writing FBGs using UV light of wavelength of 248 nm from a KrF excimer laser. The fabrication of different types (type I and type IIA) of gratings in various commercially available (B-Ge doped, Ge doped) and specially fabricated (Er-Ge doped, Sn-Er-Ge doped, Sb-Er-Ge doped) photosensitive fibres has been described. During grating writing, the on-line growth in grating reflectivity and the shift of the Bragg wavelength have been observed and studied. The temperature sustainability and the performance characteristics of the gratings written into all of these fibres were examined and compared with those of a chemical composition grating (CCG), supplied by ACREO, Sweden, a collaborator in the work at City University. Long-term testing (more than 600 hours) involving a series of step-wise incremental temperature changes shows the potential of FBGs for high temperature measurement applications (up to and beyond 1100°C), this depending on the type of FBG involved and the material and composition of the substrate fibre. The maximum ranges of temperature measurements with different types of gratings written in various photosensitive fibres were evaluated.

3.2. System set-up for grating fabrication

There are several approaches to fabricate FBGs through the use of various techniques. Among these, the phase-mask technique is the most popular approach because of the requirement of relatively simple system set-up for fabricating gratings. UV light plays a major role for the inscription of gratings into the photosensitive optical fibres. Various researchers have used UV light of different wavelengths from various types of lasers like 248 nm KrF excimer laser [32], 193 nm ArF excimer laser [68],[159]-[161], 157 nm F_2 laser [162], a hybrid 157 nm and 248 nm laser exposure [163], 244 nm frequency-doubled argon-ion CW laser [70],[72], 242 nm frequency-doubled dye laser pumped by a XeF excimer laser [69], a frequency-doubled copper

vapour laser operating at the wavelength of 255 nm [164] and a 264 nm femto-second pulses from a frequency-quadrupled Nd:glass laser [165]. Even a near infrared pulsed radiation at 800 nm from a Ti:sapphire laser amplifier [166] and a far infrared direct exposure at 10.6 μm from a CO_2 laser [167] have been used to write gratings with different levels of writing efficiencies.

In this project, all gratings have been fabricated by using a 248 nm UV-light from a KrF excimer laser. The specifications of the laser system used are given in Appendix II. The other important equipment required for the system set-up are the plano-convex cylindrical lens, the phase-mask, a piece of photosensitive fibre spliced with normal single-mode fibres and connectors at both sides, a broad-band light source and an optical spectrum analyser (OSA). A photographic picture of the present system set-up for writing gratings is shown in Fig. 3.1.

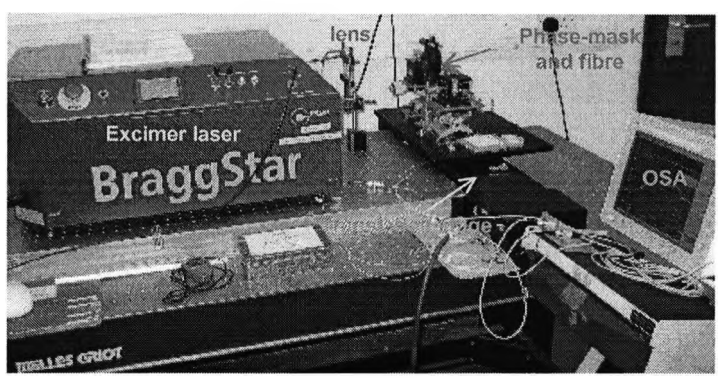

Fig. 3.1: Present system set-up for writing gratings.

A translation stage (Model: M-IMSCC HA, resolution: 0.1 μm, from Newport, France) and its associated Motion Controller/Driver (Model: MM4006, from Newport, France) are interfaced to a PC through a RS-232 serial port for a proper positioning of the phase-mask and the photosensitive fibre for a proper exposure to the UV light. A program has been developed using LabVIEW-6i to operate the translation stage in a user-friendly manner.

The strain in the photosensitive fibre during the growth of an UV-induced grating plays an important role in determining the Bragg resonance wavelength of the grating. In order to fabricate a series of almost identical gratings with the same Bragg wavelength, exactly the same strain on the photosensitive fibre is required. On the other hand, for the same photosensitive fibre and using the same phase-mask, gratings with different Bragg wavelengths (within a limited range of wavelength) can be fabricated by applying different levels of strain on the photosensitive fibre. Hence, a strain-gauge amplifier unit was designed and attached to the system to monitor the strain in the fibre, which was also interfaced to the PC using LabVIEW-6i.

3.2.1. Phase-mask technique

As mentioned above, the phase-mask technique has been adopted in this project for writing gratings; this is being the most simple and effective approach to inscribe the gratings into the optical fibre efficiently. Fig. 3.2 has been drawn to explain the process of grating fabrication more elaborately.

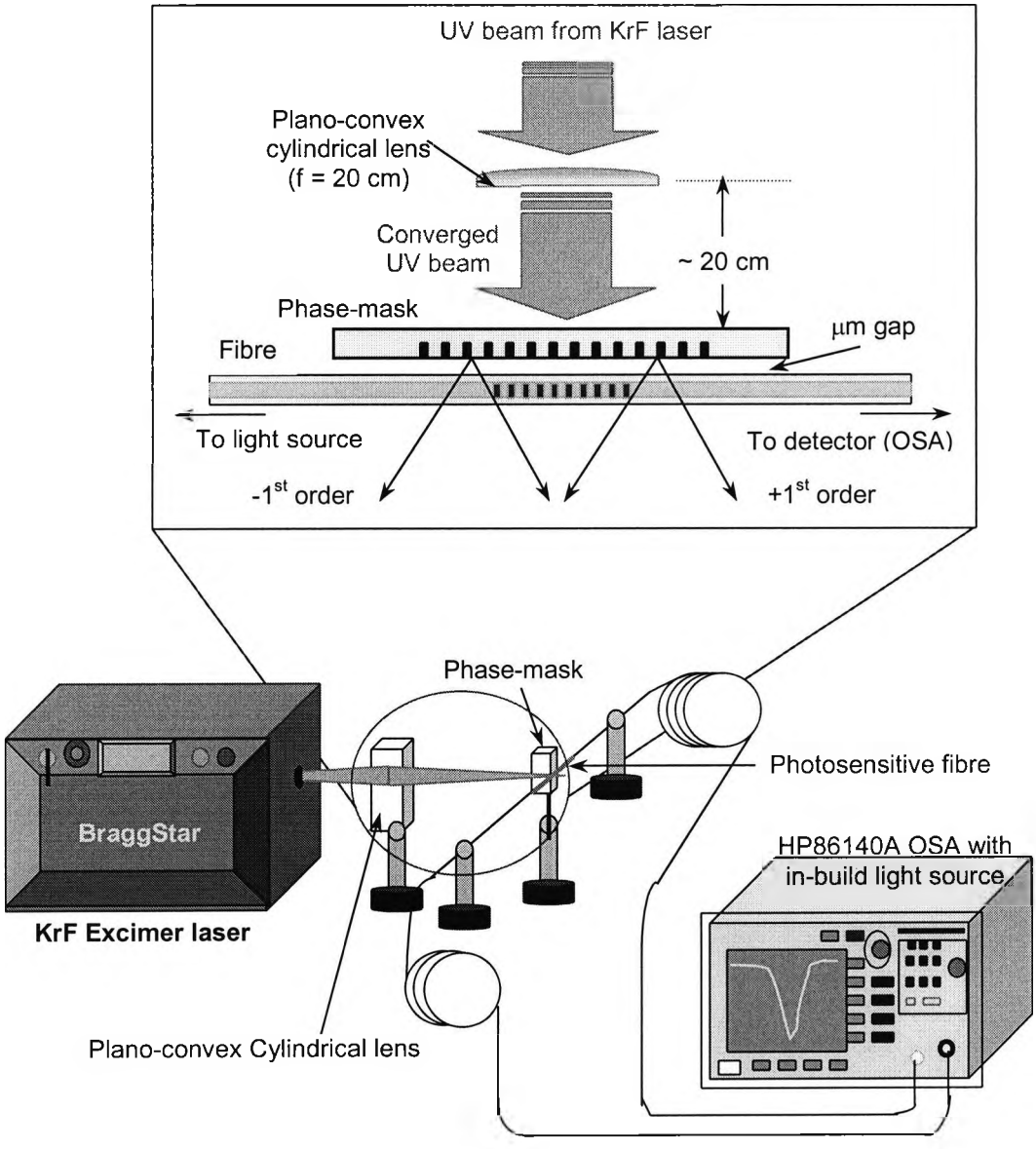

Fig. 3.2: A schematic of the system set-up to explain the process of grating writing.

A number of gratings were fabricated through this phase-mask technique using 248 nm UV light from a KrF excimer laser (Model: Braggstar 500, from Tuilaser AG, pulse duration of 10 ns). By

selecting from the display panel of the laser, it can be operated at various laser pulse energies with different pulse frequencies, thereby producing the UV exposure of various levels of laser-fluence. In this work, gratings were fabricated by using the following phase masks, specified in Table-3.1. In addition, other phase masks with various different uniform period and chirped phase masks, from O/E Land Inc., Canada, were also used for the fabrication of a range of gratings at various wavelengths. A phase-mask was placed perpendicularly to the UV exposure to create the interference pattern of the UV beam depending on the period of the phase-mask and a photosensitive fibre was placed immediately behind the phase-mask. The fibre should be placed in a very close proximity of the phase-mask without touching it to achieve the best performance of the set-up without any damage of the phase-mask. In this set-up, zeroth order of the diffraction pattern caused by the phase-mask cannot be blocked, which results in one advantage of partial annealing during the growth of the grating (caused by the heat generated within the fibre through the zeroth order diffracted light) by the cost of more d.c. offset in the effective refractive index (creates more shift in the Bragg wavelength during the growth of the grating) of the core of the optical fibre. It also causes less contrast between the dark and bright fringes in the interference pattern. In the portion of the photosensitive fibre, where the grating has to be written, the optical fibre jacket needs to be stripped off to reach the maximum possible UV-induction into the photosensitive fibre. A plano-cylindrical convex lens (focal length: 20 cm) was used in between the laser and the phase mask to converge the UV beam along the length of the optical fibre. The on-line growth of the gratings was monitored by using a HP86140A (Agilent) optical spectrum analyser (OSA). As the OSA was integrated with an in-built broad-band light source at the region of wavelength of 1500 nm, there was no need of any extra broad-band light source. For the measurements, where light source of strong intensity is required, an amplified spontaneous emission (ASE)-based broad-band light source may be used.

Table-3.1: Specification of the phase-masks used for inscription of the gratings.

Phase-mask	Period	Dimension	Zero-order	+/- 1st orders	Suppliers
Phase-mask_1	1060 nm	25mm × 3mm	0.94 %	+: 39 % -: 39 %	O/E Land Inc., Canada.
Phase-mask_2	1061 nm	10mm × 5 mm	2.21 %	+: 37.3 % -: 37.8 %	Bragg Photonics Inc., Canada.
Phase-mask_3	1061 nm	10mm × 5 mm	1.74 %	+: 38.7 % -: 37.5 %	Bragg Photonics Inc., Canada.

3.2.2. System performance

After the preliminary setting up work, the performance of the system was tested by writing a number of gratings into the commercially available B-Ge doped photosensitive fibres. The placement of the lens, phase mask and the photosensitive fibre were optimised to achieve the maximum possible reflectivity of the grating to be written into the fibre with optimum laser fluence. Fig. 3.3 shows a typical transmitted spectrum of a grating written into a B-Ge doped fibre, where 99.9% of reflectivity could be achieved within a minute of time by operating the laser at a pulse-frequency of 200 Hz with laser energy of 12 mJ.

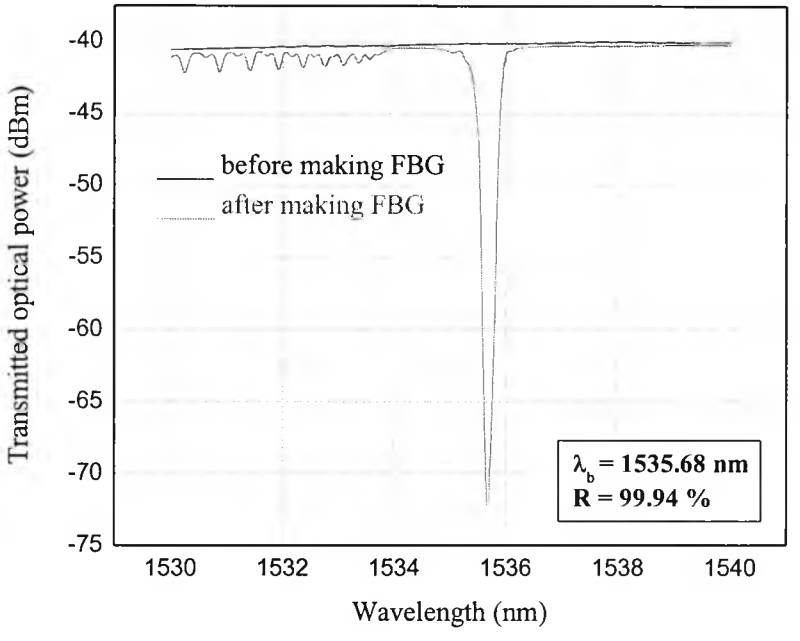

Fig. 3.3: A typical transmitted spectrum of a grating written into a B-Ge doped fibre.

In the next stage, the performance of the system was tested by writing gratings at various laser energies and pulse-frequencies. The time required to reach the level of saturation in the grating evolution was different depending upon the energy and the pulse frequency of the operating excimer laser. The higher the energy and pulse-frequency of the laser, the time required to reach the saturation of the grating reflectivity was less. However, a slightly higher level of saturation of the grating reflectivity was achieved by using the laser at higher energy and at higher frequency [168]. A 3-dimensional plot has been shown in Fig. 3.4 to realise graphically the change of the time required to reach the saturation level of the grating reflectivity in a B-Ge doped fibre with the variations in energy and the pulse-frequency of the laser.

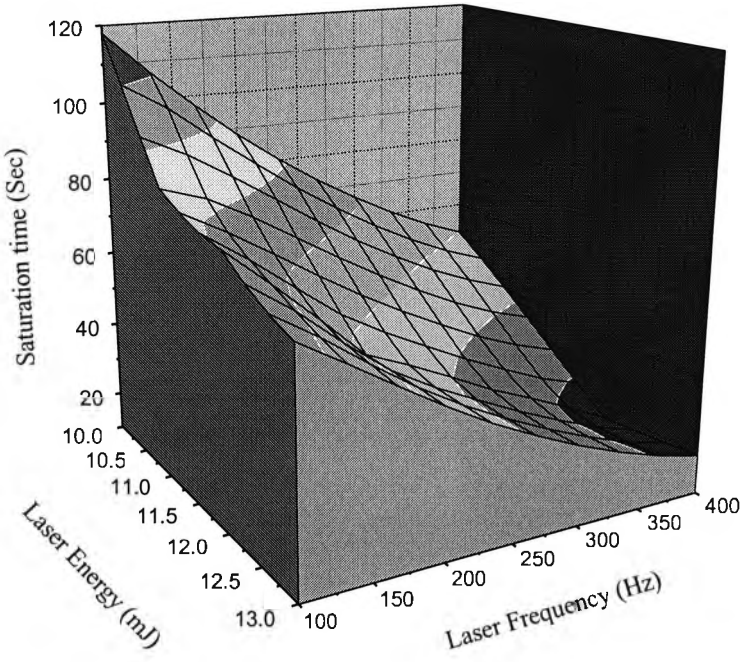

Fig. 3.4: A typical 3-dimensional representation of time to reach saturation of grating reflectivity in a B-Ge doped fibre with the variations in energy and pulse-frequency of the excimer laser used.

3.3. Writing gratings in various photosensitive fibres

After the optimisation of the system set-up, gratings were written into a range of photosensitive fibres including commercially available B-Ge doped, Ge-doped single-mode photosensitive optical fibres and specially fabricated Er-High Ge doped, Sn(tin)-Er-Ge doped and Sb(antimony)-Er-Ge doped fibres. The detailed specifications of the used fibres are listed in Table-3.2.

Table-3.2: Fibres used for the fabrication of FBGs and their specifications.

Fibre type	Specifications
1. B-Ge doped fibre (Fibercore Ltd., UK)	Fibre type: PS 1250/1500, fibre diameter: 125 μm, NA: 0.14 Mode Field Diameter @1550 nm: 9.6 μm, $\lambda_{cut\text{-}off}$: 1247 nm (Core diameter: 6.2 μm)
2. Ge doped fibre (Nufern, CT) and (Redfern, Australia)	Fibre type: GF1, fibre diameter: 125 μm, Mode Field Diameter @1550 nm: 10.5 μm, $\lambda_{cut\text{-}off}$: 1260 nm (Core diameter: 6.8 μm)
3. Er-High Ge doped fibre (Université de Nice, France)	Fibre type: A021, fibre core/cladding diameter: 4.0/125 μm, n_{core}: 1.488, n_{clad}: 1.458, $\lambda_{cut\text{-}off}$: 1.54 μm (GeO_2: ~20 mole%, Er^{3+}: ~2700 ppm, Al^{3+}: 0.083 mol/l)
4. Sn-Er-Ge codoped fibre (Université de Nice, France)	Fibre type: A022, fibre core/cladding diameter: 5.0/125 μm, NA: 0.2, $\lambda_{cut\text{-}off}$: 1.4 μm (Sn: ~1.1 mol/l, Er^{3+}: 0.025 mol/l, Al^{3+}: 0.083 mol/l in solution)
5. Sb-Er-Ge codoped fibre (China Building Materials Academy, China)	Fibre core/cladding diameter: 4/125 μm, NA: 0.23 Mode Field Diameter @1500 nm: 9.6 μm, $\lambda_{cut\text{-}off}$: 1200 nm (Core diameter: 6.2 μm, GeO_2: ~15 wt%, Sb^{3+}: ~5000 ppm, Er^{3+}: 500 ppm)

3.3.1. Evolution of gratings

UV-induced gratings were inscribed into the above-mentioned photosensitive fibres and the evolution of the gratings was studied and compared. The time required to reach the saturation level of grating reflectivity is different for various photosensitive fibres studied depending on their photosensitivity. For a comparison, gratings were written into all the fibres under a same condition using the same set-up. Fig. 3.5 shows the evolution and the growth of the gratings in various fibres with the same UV-exposure. In the studies carried out, the B-Ge doped fibre was found to be the most photosensitive, which required the exposure time of 50 seconds with a pulsed laser energy of 12 mJ at a pulse-frequency of 200 Hz, with a pulse fluence of ~ 180 mJ/cm^2 to reach the saturation of grating reflectivity (~99.9%). Er-High Ge doped fibre was also found to be a similar efficient to write gratings; however, a slightly less saturated value of grating reflectivity (~ 98.7%) was observed in this fibre. With all the other photosensitive fibres studied, the maximum reflectivities (> 95% for Ge doped fibre and ~ 99% for both Sn-Er-Ge and Sb-Er-Ge doped fibres) of the gratings were achieved within 8-10 minutes of time under the same UV exposure condition.

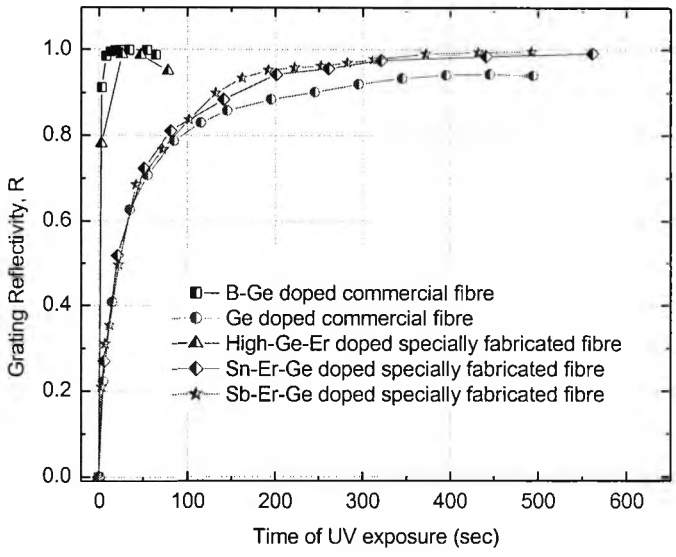

Fig. 3.5: Growth of gratings in various photosensitive fibres with the UV exposure.

Depending on the fibre material and the dopings introduced into the core of the fibres, different Bragg resonance wavelengths were observed for the gratings written into different fibres. However, shifts in the Bragg wavelengths were also observed during the fabrication of the gratings. The on-line red-shift of the Bragg resonance wavelengths during the growth of all the gratings [125],[169],[170] has been studied and plotted in Fig. 3.6. The shift-rates of the Bragg wavelengths were found to be greater in the most photosensitive fibres compared to the less photosensitive fibres. The consistency of these results was observed after fabricating a number of gratings under the same condition of UV exposure.

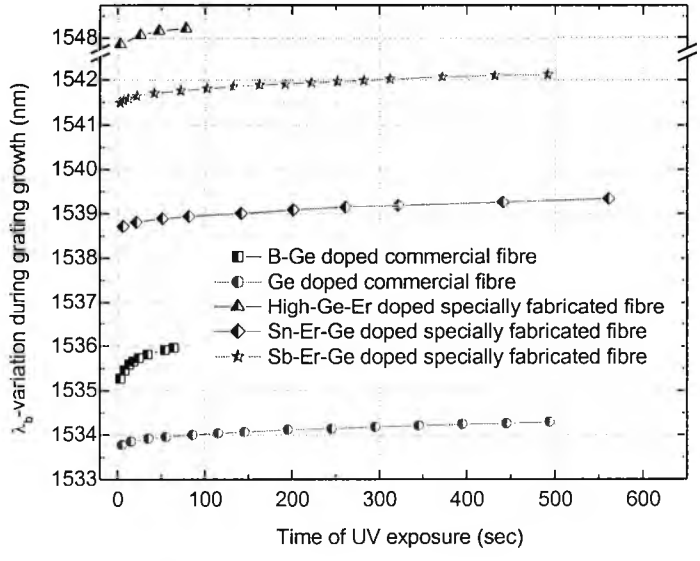

Fig. 3.6: The variation of the Bragg resonance wavelengths during grating writing in various photosensitive optical fibres.

3.3.2. Estimation of refractive-index modulation (Δn_{mod}) and the effective refractive-index (n_{eff})

A periodically modulation of the refractive index of the core of the optical fibre is essentially responsible for the existence of the reflectivity of the grating. The amplitude of the refractive index modulation in the core of the fibre can be determined [6],[7] from the following equation as

$$\Delta n_{mod} = \{\lambda/\pi L\eta(V)\}\tanh^{-1}(1-T_{min})^{1/2} \quad (3.1)$$

where λ is the operating wavelength (the Bragg wavelength, λ_b, in this case) for a grating of length, L, with an overlap function, η. T_{min} is the minimum transmission at the Bragg wavelength, i.e., the grating peak reflectance R = 1-T_{min}. The overlap function, η, is a function of the normalised frequency (V-number) of the fibre, and this can be described as

$$\eta = \{1 - 1/V^2\} \quad (3.2)$$

where the V-number can be determined from the cut-off wavelength of the fibre, $\lambda_{cut\text{-}off}$, through the equation

$$V = 2.405\ (\lambda_{cut\text{-}off}/\lambda) \quad (3.3)$$

This results from combining the following equations

$$V = (2\pi/\lambda)\cdot a\cdot(NA) \quad \text{and} \quad (3.4a)$$

$$2.405 = (2\pi/\lambda_{cut\text{-}off})\cdot a\cdot(NA) \quad (3.4b)$$

with the fibre core radius, a, and the numerical aperture of the fibre, NA.

The on-line growth in the reflectivity of the gratings was then expressed in terms of the refractive index modulation of the fibre core during the time of grating writing into the fibres and the results were plotted in Fig. 3.7. The discrepancy between Figs. 3.5 and 3.7 occurs due to the presence of a highly non-linear relationship between the values of the reflectivity and the amplitude of the refractive index modulation. Thus, although the reflectivity values for all the gratings fabricated in various fibres were within the range of (95-99.9)% (as shown in Fig. 3.5), a significant variation in the values of the amplitude of the refractive index modulation in the cores of the fibres (1.7×10^{-4} to 3.7×10^{-4}) was observed, as shown in Fig. 3.7.

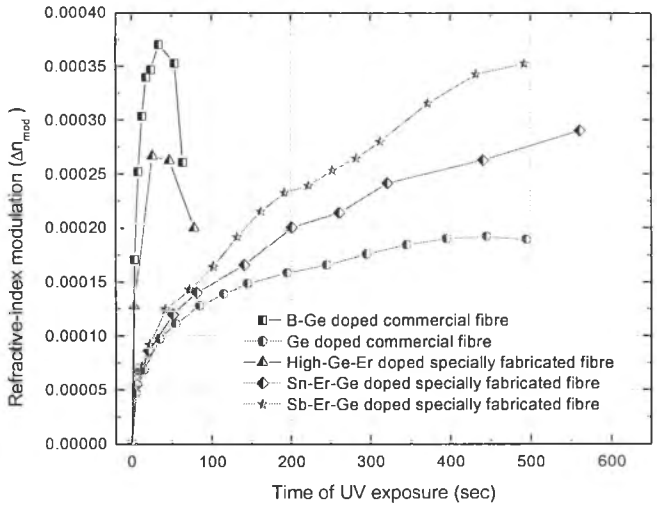

Fig. 3.7: Variation of the amplitude of the refractive index modulation of the fibre cores during the grating writing time.

In a similar fashion, the shift in the Bragg resonance wavelength, λ_b, during the fabrication of the gratings may be expressed in terms of the change in the effective refractive index of the fibre core, n_{eff}, as they are related with a simple equation

$$n_{eff} = \lambda_b/2\Lambda \qquad (3.5)$$

where Λ is the grating period, i.e., half of the phase mask period. For the simplicity of plotting, the estimated shift in the effective refractive indices (Δn_{eff}) of the gratings, without mentioning the absolute values of the effective refractive indices, has been plotted in Fig. 3.8.

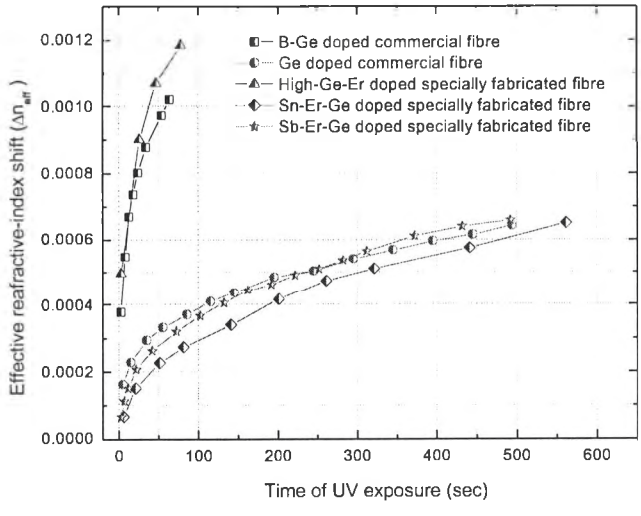

Fig. 3.8: Variation of the effective refractive index of the fibre cores during grating writing.

3.3.3. Photosensitivity involved during the growth of the gratings

Photosensitivity is the property of the optical fibre, depending on the material and dopants introduced into the core of the fibre during the fibre fabrication or through some externally imposed techniques like hydrogen loading, for which the gratings can be written into the fibre through an UV-induced optical phenomenon. Qualitative analysis of the enhanced photosensitivity of boron codoped germanosilicate fibres [29] and of hydrogen-loaded fibres [27] has been reported earlier. One and two photon process of photosensitivity of GODCs has also been explained through a photo-decomposition model [171]. Recently, a new technique based on the Bragg grating Fabry-Perot interferometers, for a precise measurement and study of the fibre-photosensitivity using the Fourier spectra, has been reported [172]. However, the process of photosensitivity of the fibres has been investigated quantitatively in this section.

To investigate the process of photosensitivity in the experiment (whether it is based on a single-photon or multi-photon process) [155],[156],[173], gratings were fabricated with different levels of laser fluence and a measurement of the growth of the gratings was carried out. If the initial growth of the refractive index modulation (Δn_{mod}) is assumed to be proportional to the UV exposure time, t, with a laser-fluence of I_p, then this can be expressed as

$$\Delta n_{mod} = (I_p)^{\gamma} \cdot t \qquad (3.6)$$

and the growth-rate can be represented as

$$G = d/dt\ (\Delta n_{mod}) = (I_p)^{\gamma} \qquad (3.7)$$

where the numerical coefficient, γ, through which the process of photosensitivity is estimated, can be determined from the slope of the growth-rate versus laser-fluence graph as a logarithmic plot.

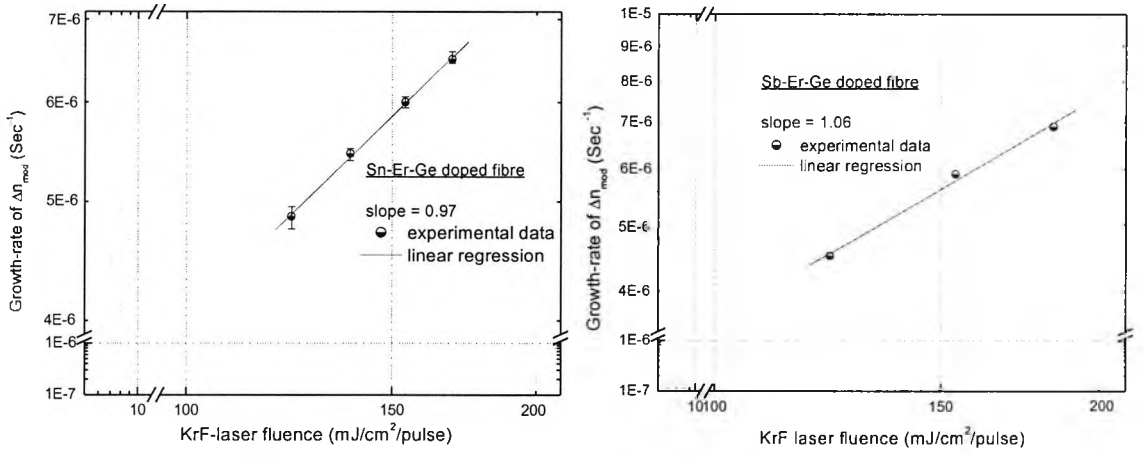

Fig. 3.9: Logarithmic plot of growth-rate of Δn_{mod} versus laser pulse fluence to evaluate the photosensitivity process involved for the initial growth of gratings in Sn-Er-Ge and Sb-Er-Ge doped fibres.

The laser pulse-fluence was estimated form the value of laser pulse-energy used and the area of the UV-exposed region in the plane of the fibre position, which is normal to the laser radiation. The slopes of the graphs were evaluated to be 0.97 (± 0.05) for the gratings written into the tin(Sn)-Er-Ge doped fibre and 1.06 (± 0.06) in case of the growth of the gratings into antimony(Sb)-Er-Ge doped fibre, which are plotted in Fig. 3.9. This above phenomenon gives the evidence that the photosensitivity involved in both of the fibres for the initial growth of the gratings at the laser-fluence used (at a wavelength of 248 nm) is dominated by a single-photon process, although there are some reports in the literature that the total growth of the photorefractivity may arise from not only a single-photon but also from a multi-photon process [156],[173].

3.3.4. Effect of UV-radiation on the gratings during writing

The dynamic changes that occur during the process of writing gratings under UV exposure are complex. Fig. 3.10 shows one of these complex changes, where the shifts in the dip/peak resonance wavelengths of the transmission and the reflection spectra of the gratings in two different photosensitive fibres were measured, with the UV radiation from a 248 nm excimer laser switched ON and OFF. A specially fabricated Sb-Ge doped fibre and a commercial photosensitive fibre supplied from O/E Land Inc., Canada were considered for this experiment and the measurements were taken after sufficient growth of the gratings. For both measurements, a significant blue-shift of the Bragg wavelengths was observed, in addition to a slight change in the reflectivity values when the operating laser was switched OFF. Blue-shifts of around 0.13-0.16 nm were observed; the variation of these values depend on the fibre material and the stage of the grating growth. This wavelength shift is equivalent to a change in temperature of approximately 20-25 °C at room temperature. Different amounts of wavelength shift at different stages of the growth of a grating in the same fibre have also been observed and reported [7] (pp. 31).

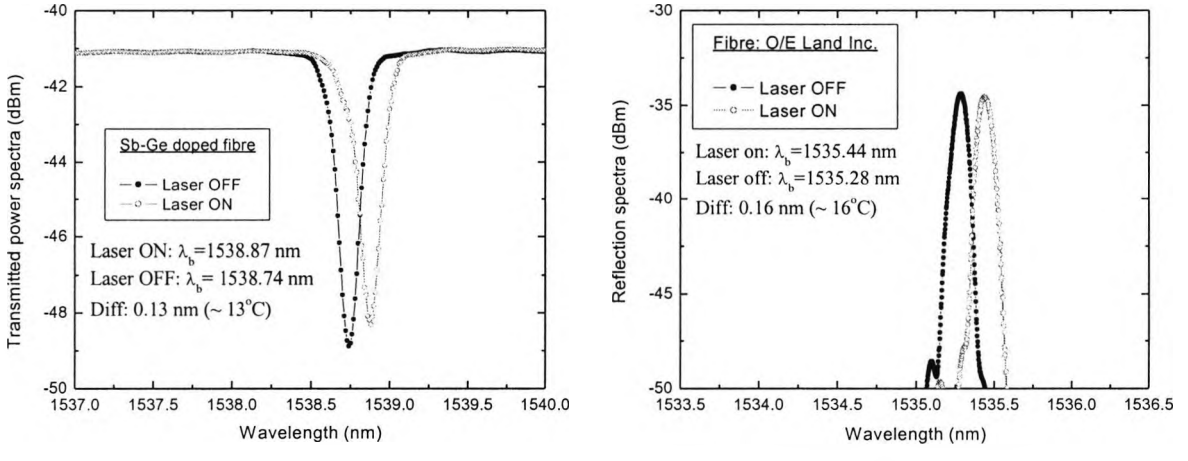

Fig. 3.10: Shift of the Bragg wavelength as the UV radiation is switched ON and OFF for the gratings written into two different fibres: measured in transmission mode and in reflection mode.

During the process of grating fabrication using a phase-mask, the zeroth-order diffracted light can also be passed through (although it is very weak and less than 3% of the total incident light power) the phase-mask in addition to the plus and minus first and other higher order diffracted beam. However, for an UV exposure with higher laser energy and higher pulse-frequency over a long period of time, the cumulative effect of the zeroth-order diffracted light may develop a significant temperature that is well above the operating temperature, which is believed to be responsible for the increase of the grating wavelength during the process of on-line fabrication. Thus, when the operating laser is switched OFF, it may result in the shift of the Bragg resonance wavelength towards the shorter wavelength side according to the fall in temperature.

3.4. Types of gratings written: type I and type IIA

The description of type I and type IIA gratings has already been given in the previous chapter. In this section, the fabrication of these two types of gratings in different photosensitive fibres by using a 248 nm excimer laser and a phase-mask (Period of 1060 nm) has been studied. An HP86140A OSA has been used for the on-line monitoring of the variation of the grating reflectivities and the Bragg wavelength shifts under the influence of the UV exposure. Two types of photosensitive fibres were used in this experiment: (i) Ge-doped silica fibre (Redfern GF1) and (ii) B-Ge codoped silica fibre (Fibercore Ltd). Fig. 3.11 shows the Bragg wavelength and the refractive index modulation of the FBGs varying as a function of UV exposure time. It should be noted that the time scale of the graph has been plotted in the logarithmic scale for the better viewing of the graph over a long period of time. The growth of the refractive index modulation stops when the Type I grating is being saturated, and drops to a very low level before increasing once again to form a Type IIA grating.

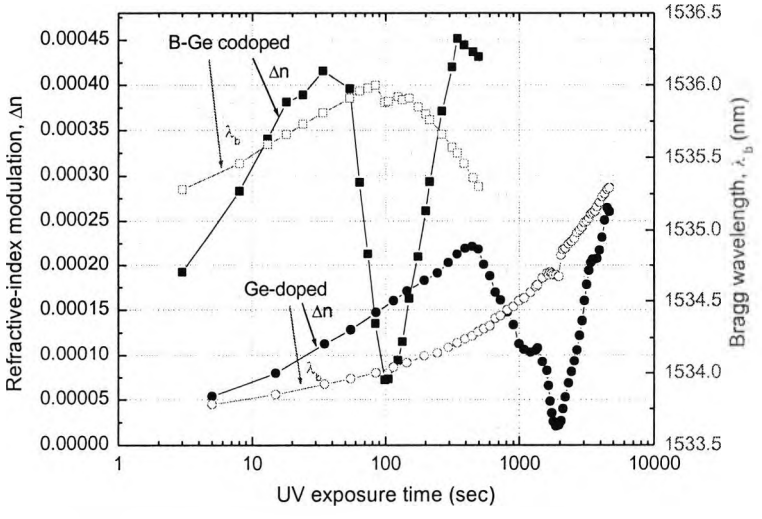

Fig. 3.11: Variation of refractive-index modulation and the Bragg wavelength shift of a B-Ge and a Ge-doped fibre as a function of the UV-exposure time.

In the studies carried out, the B-Ge codoped fibre was found to be more photosensitive to the fabrication of type I as well as type IIA gratings (using exposure times of 50 seconds for type I and less than 10 minutes for type IIA with a pulsed laser energy of 12 mJ at a frequency of 200 Hz, with a pulse fluence of ~ 180 mJ/cm^2) when compared to the Ge doped fibre, which required ~ 8 minutes and ~ 75 minutes to form the type I and IIA gratings respectively under the same UV exposure conditions. The values of the refractive-index modulation were estimated from the on-line values of the grating reflectivity. The refractive-index modulation values for both type I and type IIA gratings written in B-Ge doped fibre were found to be almost two times higher than those written in the Ge-doped fibre. Also, the refractive-index values of type IIA gratings were observed to be slightly higher compared to those of the type I for both photosensitive fibres.

In addition, when the photosensitive fibres were exposed to the UV beam from the excimer laser, the shift in the Bragg wavelength (λ_b) of the gratings was observed during the fabrication of type I and type IIA gratings. The Bragg resonance wavelength of the grating written into a B-Ge doped fibre was seen to shift to the longer wavelength side even though it remained a Type I grating. However, when it was over-exposed, its center wavelength changed, moving to the shorter wavelength side, indicating the formation of a Type IIA grating. In case of gratings written in a Ge-doped fibre, the nature of the Bragg wavelength shift was found to be different from the above observation. The shift of the Bragg wavelength (λ_b) of the Ge-doped fibre was found to be always towards the longer wavelength side throughout the whole process of fabrication of type I and type IIA gratings. Both of these effects have been shown in Fig. 3.11. The opposing effect of the Boron and Germanium on the refractive index change may be one of the major factors causing the bi-directional shift of the Bragg wavelength (λ_b) of the gratings written into B-Ge doped fibres.

Fig. 3.12 shows a comparison between a typical transmitted spectrum of a type I grating with that of a type IIA grating, when they were written in the same fibre (B-Ge doped fibre) with the same phase-mask (period of 1060 nm) by extending the time of the UV exposure under the same writing condition. A shift in the Bragg wavelength of the grating towards the lower wavelength side was observed with the transformation of a type I to a type IIA grating by using a continuous UV exposure from the excimer laser. The reflectivity of the type IIA grating was observed to be around 2 dB higher than that of the type I grating. However, the full width half maximum (FWHM) band-width of the type IIA grating was found to be larger (almost double of the band-width of the type I grating) than that of the type I grating, which may affect the precision of the measurement for any sensing application. Moreover, the spectrum of the type IIA grating

was observed to be slightly non-uniform; this is being caused by the formation of a non-sinusoidal refractive-index modulation into the photosensitive fibre arising from a long-term UV exposure. However, it is interesting to be noted that the type IIA gratings were found to be more thermally stable compared to the type I gratings, which has been elaborately discussed in the next section.

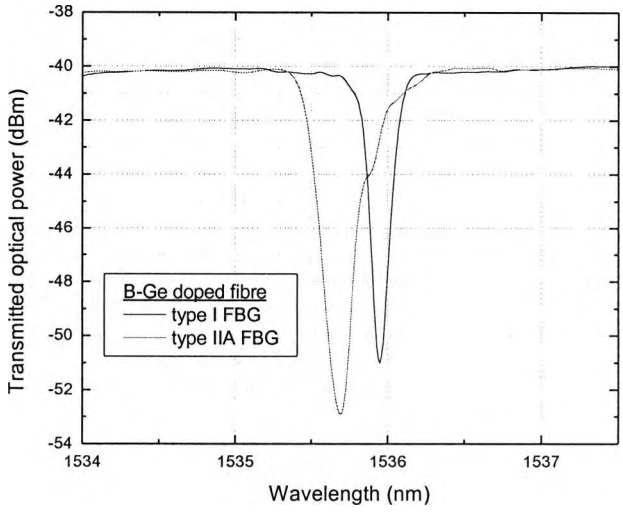

Fig. 3.12: A comparison between a type I and a type IIA grating spectrum, which were written into the same fibre, using the same phase-mask.

3.5. Thermal sustainability of the gratings

Following grating fabrication, the next step in the study was to evaluate the temperature performance of these gratings, as it has been considered to be important to test how well these devices would perform at elevated temperatures, this being highly relevant to the higher temperature sensing in some remote areas, combustion studies etc. for example.

3.5.1. Experimental arrangements used in this work

To observe their thermal decay characteristics, all the gratings (type I and IIA gratings for each of the Ge, B-Ge and Er-High Ge doped fibres, type I gratings written in Sn-Er-Ge and Sb-Er-Ge doped fibres) as well as a "chemical composition grating (CCG)" [The formation of the CCG and its properties have been discussed in detail in section 3.5.3.] were placed inside a well-characterised and calibrated CARBOLITE tube oven (Model: MTF 12/38/400). The experimental set-up for this test has been shown in Fig. 3.13, where the on-line transmitted spectra of the gratings were observed through an OSA. As the OSA provided an in-built broadband source, an extra ASE source was not required here. The gratings were spliced with normal single mode

fibres and connected with FC/PC connectors at both ends for the connection to the in-built source and the detector of the OSA. The gratings were placed in the middle of the tube oven (the most thermally stable region) carefully in order to avoid any axial strain on them.

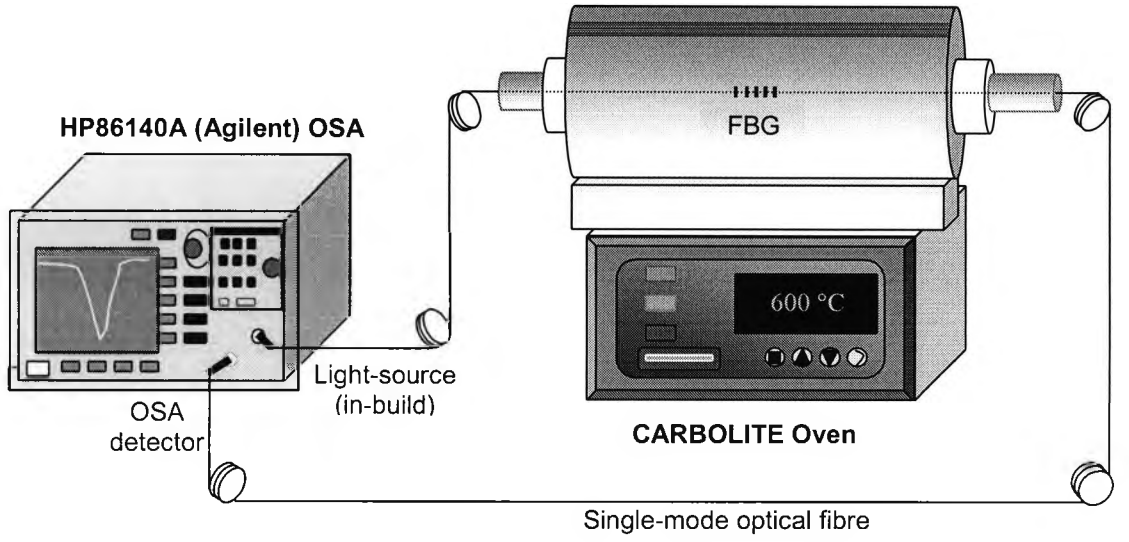

Fig. 3.13: Experimental set-up for testing the thermal stability of the gratings.

The studied gratings were tested for a long term under two different thermal regimes. The specifications of all the gratings studied in this experiment have been listed in Tables 3.3(a) and 3.3(b).

Table-3.3(a): Parameters of the fibres and gratings studied in this work.

Parameters	FBG written in B-Ge codoped fibre (Fibercore, UK)		FBG written in Ge-doped fibre (Redfern GF1, Australia)		CCG (Acreo, Sweden)
	Type I FBG	Type IIA FBG	Type I FBG	Type IIA FBG	
Bragg wavelength, λ_b (nm) at 23°C	1535.73 nm	1535.03 nm	1535.13 nm 1534.82 nm	1534.99 nm	1549.81 nm
Grating length, L (mm)	6.5 mm	6.5 mm	6.5 mm	6.5 mm	10 mm
V-value of the fibre	1.95 at 1535 nm	1.95 at 1535 nm	1.88 at 1535 nm	1.88 at 1535 nm	1.90 at 1550 nm
Initial Reflectivity at 23°C, %R	99.9%	99.8%	95.5% 99.9%	96.7%	40.0%
Initial amplitude of refractive index modulation at 23°C, Δn_{mod}	4.78×10^{-4}	4.07×10^{-4}	2.34×10^{-4} 4.82×10^{-4}	2.51×10^{-4}	5.11×10^{-5}

Table-3.3(b): Parameters of the fibres and gratings studied in this work (continued).

Parameters	FBG written in Er-High Ge doped fibre (AO21)		FBG written in Sn-Er-Ge doped fibre (AO22)	FBG written in Sb-Er-Ge doped fibre
	Type I FBG	Type IIA FBG	Type I FBG	Type I FBG
Bragg wavelength, λ_b (nm) at 23°C	1549.58 nm	1549.96 nm	1540.64 nm	1542.39 nm
Grating length, L (mm)	6.5 mm	6.5 mm	6.5 mm	6.5 mm
V-value of the fibre	2.40 at 1549 nm	2.40 at 1549 nm	2.18 at 1540 nm	1.87 at 1542 nm
Initial Reflectivity at 23°C, %R	98.5%	99.7%	95.3%	99.5%
Initial amplitude of refractive index modulation at 23°C, Δn_{mod}	2.56×10^{-4}	3.30×10^{-4}	2.11×10^{-4}	3.53×10^{-4}

3.5.2. Thermal decay characteristics of the gratings

The results of the long-term thermal characteristics of the gratings have been shown separately in Figs. 3.14(a)-(d), as the gratings were tested separately in different regimes. Fig. 3.14(a) shows the decay of the reflectivity of type I and type IIA gratings written in Ge and B-Ge doped fibres with step-wise increase of temperature keeping the gratings a long time (24-48 hours) at each temperature. Fig. 3.14(b) shows a comparison of the decay in the grating (type I) reflectivities written in Ge, Sn-Er-Ge doped fibres and the CCG, whereas the decay of the grating in Sb-Er-Ge doped fibre, tested under different regime, has been shown in Fig. 3.14(c). Fig. 3.14(d) shows the overall comparison of all gratings with the operating temperature considering their reflecitivities after keeping the gratings for ~24 hours at each temperature.

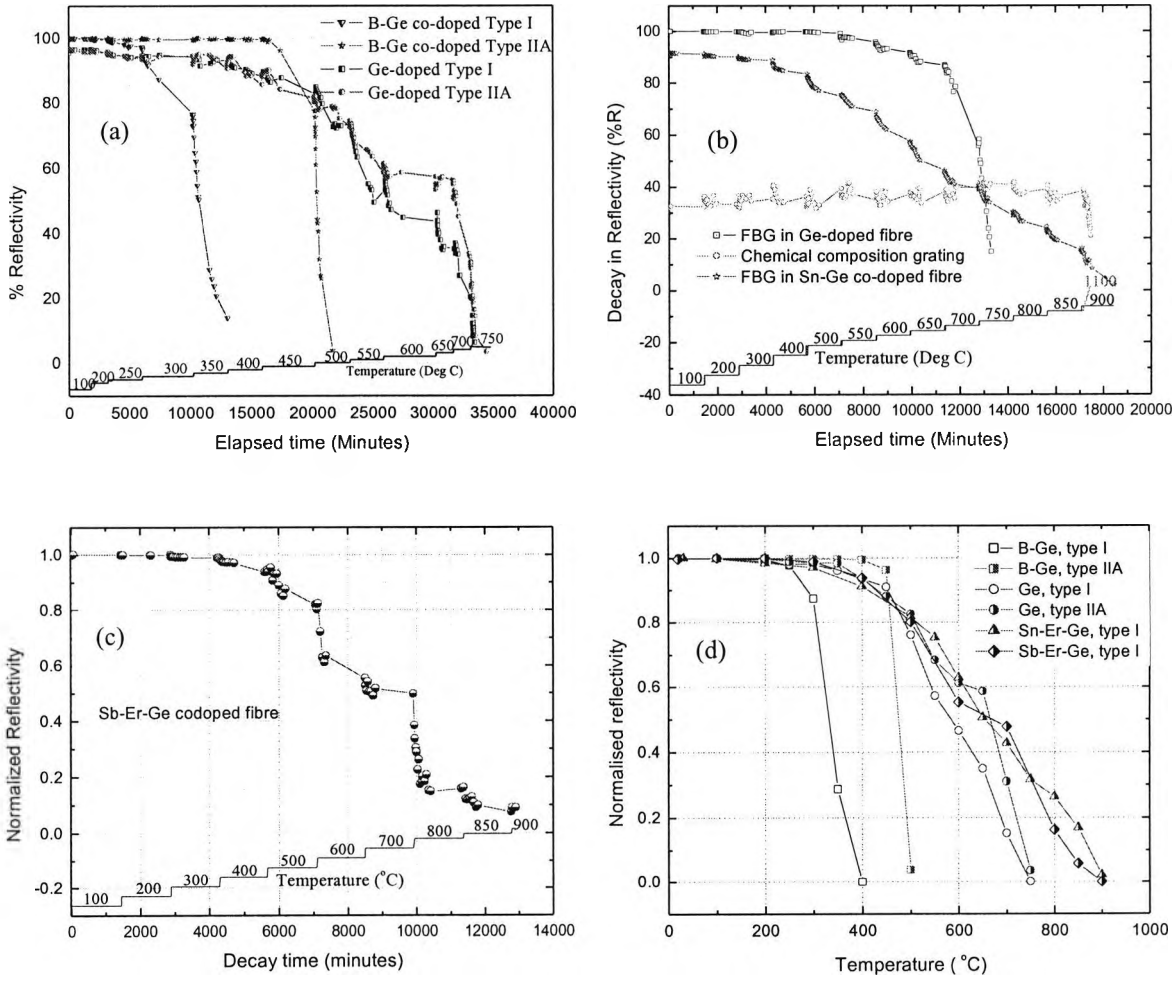

Fig. 3.14: Decay in the grating reflectivities: (a) type I and type IIA gratings written in Ge and B-Ge doped fibre, (b) type I gratings written in Ge, Sn-Er-Ge doped fibre and the CCG, (c) type I grating written in a Sb-Er-Ge doped fibre. Comparison of the normalised reflectivity for all gratings after 24 hours of time at each temperature with step-wise increment has been shown in (d).

The decay in the grating reflectivities can be represented more scientifically in terms of the decay in the refractive index modulation of the gratings written into these fibres [175]. Fig. 3.15(a) shows the variation of the refractive index modulation (Δn_{mod}) when the type I and type IIA gratings fabricated in Ge and B-Ge doped fibres were subjected to a series of long-term thermal exposures (24-48 hours at each temperature) at 100°C, 200°C and then progressively to 750°C with a temperature increment of 50°C. It was observed that the type IIA gratings were more thermally stable, compared to the type I, both for Ge and B-Ge co-doped samples. The decay of the index modulation, Δn_{mod}, of the B-Ge codoped type I grating is negligible up to 200°C with a value of 3.6×10^{-4}, after which a substantial decay was observed and it was found that it did not survive over a long period of time at 350°C – its reflectivity fell to zero effectively. The type IIA grating in the B-Ge codoped fibre was almost unaffected by the thermal exposure up to 400°C with a value of Δn_{mod} of 3.7×10^{-4}, following which the rapid decay "washed out" the grating within a few minutes at 500°C. By comparison to the above samples, the gratings fabricated in Ge doped fibre were observed to be more stable (type I can withstand a temperature of 600°C, with ~45% of its initial Δn_{mod} [9.6×10^{-5}] showing an almost negligible decay rate and the similar demarcation point for type IIA is 650°C, with more than 55% of its initial Δn_{mod} [1.0×10^{-4}] remaining after exposure).

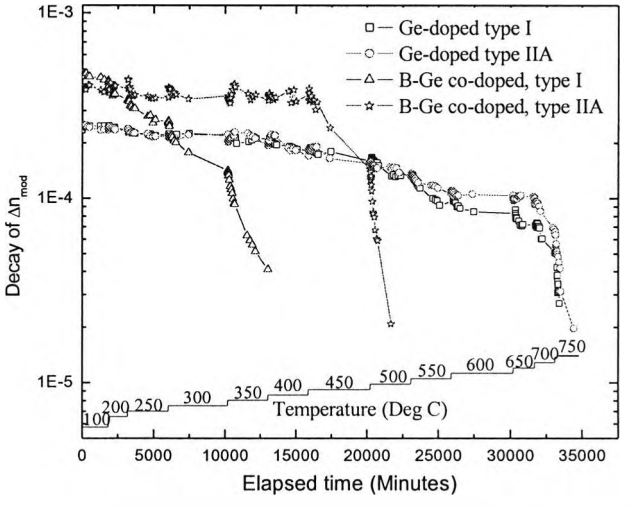

Fig. 3.15(a): Variation of the refractive-index modulation (Δn_{mod}) of the type I and type IIA gratings written in Ge and B-Ge doped fibres. Δn_{mod} values were estimated from the on-line grating reflectivity values.

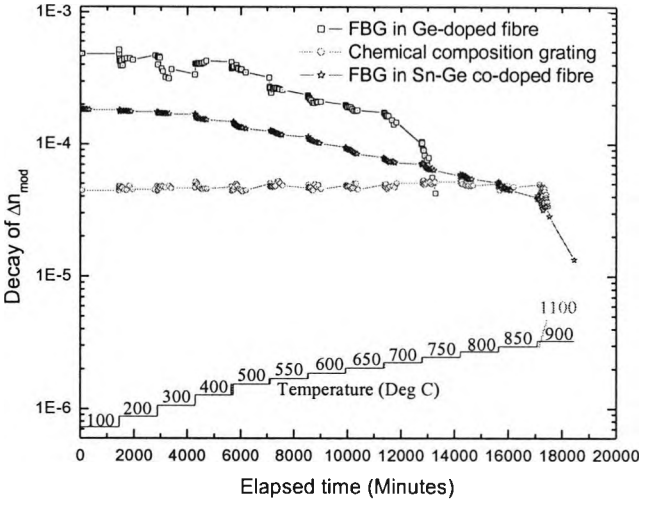

Fig. 3.15(b): Comparison of the variation of Δn_{mod} of type I gratings written in Ge, Sn-Er-Ge doped fibre and the CCG with elapsed time over various temperature ranges.

Fig. 3.15(b) demonstrates the difference between the "chemical composition grating (CCG)", the second most stable grating (a Ge doped type I grating) shown in Fig. 3.14(a) and a type I grating written in a Sn-Er-Ge doped fibre, when all were exposed to a series of 24 hour exposures at temperatures rising from 100°C to 500°C in incremental steps of 100°C, and then with 50°C increments from 500°C to 850°C, followed by a series of 1 hour treatments with a further temperature increment of 50°C, up to 1100°C. The thermal sustainability of the gratings written in Sn-Er-Ge and Sb-Er-Ge doped fibres were found to be almost similar (shown in the reflectivity decay graph, but not shown in the refractive index modulation graph). The CCG was observed to be the "strongest" among all the samples, as it could survive up to 1100°C, with more than half of its initial value of Δn_{mod} preserved even after such a high temperature exposure. Unlike conventional fibre Bragg gratings, the CCG can survive these higher temperatures because the refractive index modulation of CCG is the result of a periodic change in the chemical composition within the core of the fibre. However, the reflectivity of CCG is relatively low and its thermal stability is limited by the diffusion properties of the modulated dopant, which is quadratically dependent on the grating period [176].

3.5.3. High temperature sustainable chemical composition grating (CCG)

The chemical composition grating (CCG) tested in the above experiment, was manufactured by ACREO, Sweden, one of the collaborators with City University, London, on this work. The CCG was formed, in this case, following the high temperature thermal processing of an UV exposed hydrogen-loaded germanosilicate fibre with fluorine dopant. After the inscription of the grating into this special fibre, it was heated in a tube furnace to promote the chemical reactions and the diffusion required for CCG formation. The grating was placed carefully inside the tube furnace

without any strain effect on it and the temperature of the furnace was increased from room temperature at a rate of 20°C/minute. This grating, however, started to be erased, as expected, during the high-temperature heat-treatment process. The grating reflectivity was found to be decaying with ramping up the temperature from room temperature to 1000°C. At a temperature of 950°C, the initial grating was completely erased. This erasure was followed by the growth of a second grating, the CCG, which is highly thermally stable. The wavelength of the CCG matched with the wavelength of the initial grating. The reflectivity of the CCG was saturated after few minutes of time of formation of CCG. The ratio of the refractive-index modulation of the initial grating to the developed CCG was estimated to be around 7.3:1 [177],[178]. This was the reason of the less value of the reflectivity (refractive-index modulation) of the CCG tested in this experiment.

The final refractive-index modulation of the CCG can be ascribed to the variations in the chemical composition (fluorine concentration) attained by periodically increased diffusion of fluorine. Hence the decay characteristics of this CCG was found to be different from typical decay behaviour of the conventional gratings [69] and the thermal stability of this grating is limited by the fringe-to-fringe diffusion of the modulated concentration of the dopants. Because of the quadratic dependence on distance in the diffusion process, the grating period of the modulation will have an effect on the thermal stability [176],[178]. Thus, the grating of lower resonance wavelength was found to show a faster decay compared to that for a grating of higher resonance wavelength. For long period CCG gratings, it was found to be extremely high thermally stable. One method for creating a variation in chemical composition is to change the diffusion properties of dopants locally by utilising periodically induced chemical reactions to modify the bond structure in the glass matrix. By subsequent homogeneous thermal treatment, the spatial difference in diffusion properties will result in selective diffusion and a periodic redistribution of the dopant. Once the modulation is created and the diffusion process has been saturated, the limited thermal stability of the system is governed by the diffusing properties of the remaining modulated dopant and possibly by further chemical reactions. The periodic change in the glass composition along the fibre will then likely result in a periodic change in the refractive index [178].

3.5.4. Blue-shift in the Bragg wavelength of the gratings during thermal decay

The Bragg wavelength (λ_b) shifts towards a longer wavelength with any increase of temperature. However, at each temperature, a small but discernible shift of the Bragg wavelength towards a shorter wavelength was observed with time taking about 8-10 hours to reach the asymptotic point of the stable value for λ_b at each temperature. This shift of λ_b at each temperature for the gratings fabricated in Ge and B-Ge doped fibre is shown in Figure 3.16(a). The phenomenon of

the shift of the Bragg wavelength was observed and discussed by the authors recently [170]. A similar nature of blue-shift in the Bragg resonance wavelengths of all gratings written in various photosensitive fibres was observed. However, it is interesting to note that there was no similar effect of the shift of the Bragg wavelength observed at each temperature in the case of the CCG (as shown in Fig. 3.16(b)) up to the same maximum temperature of ~ 800°C. This is because the grating has already passed the first stage of the annealing process during the high-temperature heat-treatment at the time of the formation of the CCG [178]. For the thermal stability analysis of other gratings (fabricated in Ge, B-Ge, Sn-Er-Ge and Sb-Er-Ge doped fibres), at any particular higher temperature, during the first stage of the annealing the decay in the reflectivity of the grating was caused by the decrease of the amplitude of the core refractive index modulation of the fibre. This indirectly caused a lowering of the value of effective refractive index of the fibre. Thus the Bragg wavelength reduced with time at each of the temperature increments, as it is directly related to the effective refractive index of the fibre.

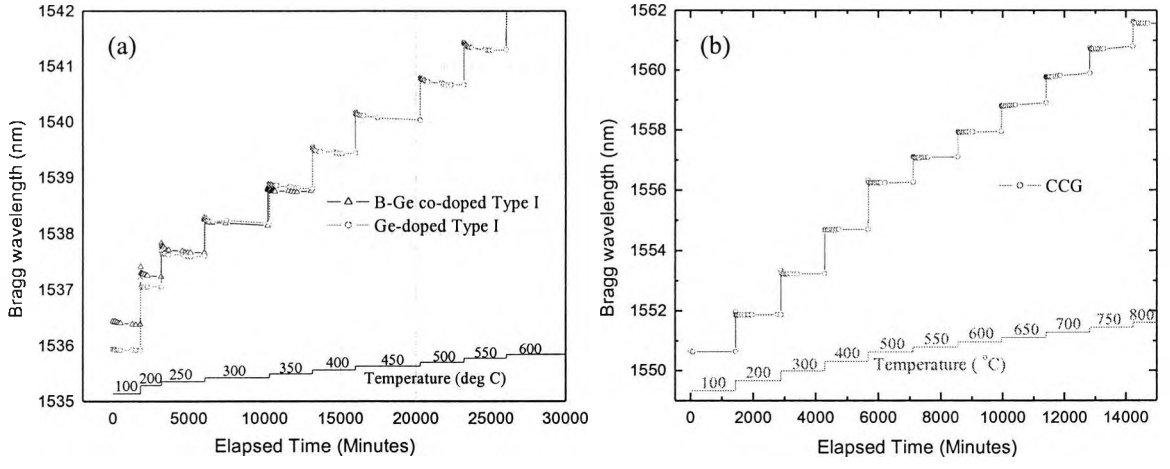

Fig. 3.16: The blue-shift of the Bragg wavelengths (λ_b) of the gratings written in Ge and B-Ge doped fibres at each temperature. It takes ~ 8-10 hours for the λ_b to the asymptotic point of the stabilised value as shown in (a). No blue-shift in λ_b was observed in case of the CCG in (b).

3.5.5. Temperature performance of the FBGs for sensing applications

The shift of the Bragg wavelength with temperature has been widely used as an effect for temperature sensing or temperature compensation in other sensors. The temperature sensitivities of the gratings were determined by observing the change of the Bragg wavelength with temperature (after it became stable: data were recorded ~ 24 hours after increasing the temperature in each case). The Bragg wavelength versus temperature curves were almost linear over a wide range of testing temperatures for each grating, but with each showing a slightly different slope. Fig. 3.17(a) shows the temperature–sensitivity graphs for type I and IIA gratings

written in B-Ge codoped fibre. The sensitivity for the B-Ge codoped type I grating was 9.12 pm/°C but for the type IIA the dynamic range increased by 100°C at the cost of a slightly lower value of sensitivity of 8.37 pm/°C. The corresponding sensitivity values for the Ge doped types I and IIA were 12.80 pm/°C and 12.35 pm/°C respectively and the graphs relating these are shown in Fig. 3.17(b). The dynamic range of the CCG was observed to be the greatest among the entire range of samples tested, with a sensitivity of 15.96 pm/°C. Fig. 3.17(c) describes the temperature-sensitivity graph of the CCG along with that of a type I grating written in Ge-doped fibre. Fig. 3.17(d) shows the thermal response of the type I gratings written in Sn-Er-Ge and Sb-Er-Ge doped fibres, after completing the process of annealing, which gives the estimated linear temperature-sensitivity values of 14.76 pm/°C and 15.28 pm/°C respectively. The details of the linear fittings used to evaluate the thermal sensitivity for all the gratings are described in Table-3.4.

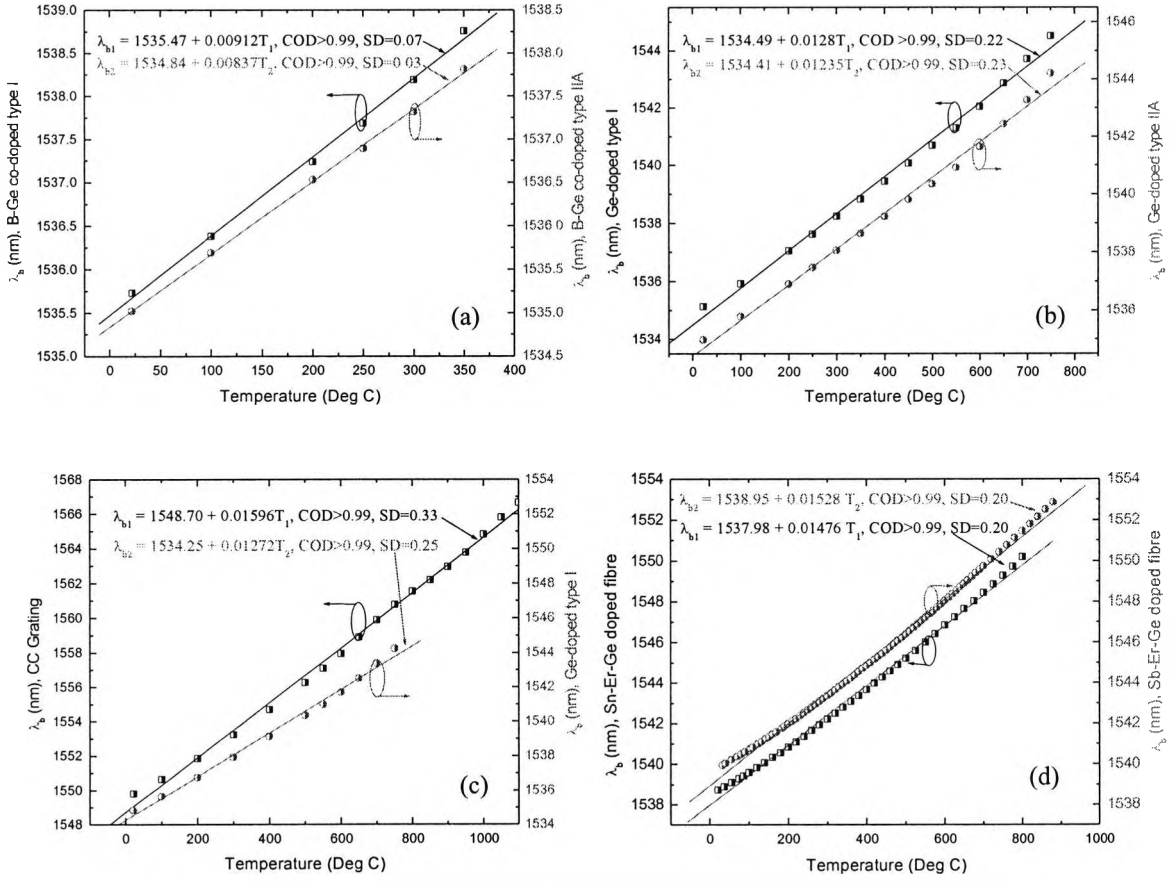

Fig. 3.17: Stabilised Bragg wavelengths versus temperature response of various gratings. Linear fits to data were used to estimate the temperature-sensitivity values. (a) type I and type IIA gratings written in a B-Ge doped fibre, (b) type I and type IIA gratings written in a Ge doped fibre, (c) type I grating in a Ge doped fibre and a CCG, (d) type I gratings written in Sn-Er-Ge and Sb-Er-Ge doped fibres.

Table-3.4: Details of the data used to evaluate the temperature sensitivity of the gratings studied.

FBG type	Range of operation (°C)	Temperature Sensitivity (pm/°C)	Coefficient of determination (COD)	Standard deviation (SD) (nm)
B-Ge codoped, Type I	(0 – 250) °C	9.12	> 0.99	0.01
B-Ge codoped, Type IIA	(0 – 350) °C	8.37	> 0.99	0.03
Ge-doped, Type I	(0 – 600) °C	12.80 12.72	> 0.99 > 0.99	0.13 0.25
Ge-doped, Type IIA	(0 – 650) °C	12.35	> 0.99	0.23
Sn-Er-Ge doped, Type I	(0 – 850) °C	14.76	> 0.99	0.20
Sb-Er-Ge doped, Type I	(0 – 850) °C	15.28	> 0.99	0.20
CCG	(0 – 1100) °C	15.96	> 0.99	0.33

3.6. Summary

A system set-up was prepared and optimised for writing FBGs using UV light of wavelength of 248 nm from a KrF excimer laser. Different types (type I and type IIA) of gratings in various commercially available (B-Ge doped, Ge doped) and specially fabricated (Er-Ge doped, Sn-Er-Ge doped, Sb-Er-Ge doped) photosensitive fibres have been fabricated. The on-line process of writing gratings in various photosensitive fibres was studied thoroughly. During grating writing, the on-line growth in grating reflectivity and the shift of the Bragg wavelength have been observed and studied. The temperature sustainability and the performance characteristics of the gratings written into all of these fibres were examined and compared with those with a chemical composition grating (CCG), supplied by ACREO, Sweden. Long-term testing (more than 600 hours) involving a series of step-wise incremental temperature changes shows the potential of FBGs for high temperature measurement applications (up to and beyond 1100°C), this depending on the type of FBG involved and the material and composition of the substrate fibre. The maximum ranges of temperature measurements with different types of gratings written in various photosensitive fibres along with their average temperature-sensitivities were evaluated.

Chapter 4

Analysis of thermal stability of the FBGs

4.1. Abstract

The thermal stability of type I fibre Bragg gratings, written into two selected photosensitive fibres (B-Ge doped and Sn-Er-Ge doped fibre) using a 248 nm KrF excimer laser, has been examined and analysed in this chapter, in terms of their reflectivity and Bragg wavelength change. A B-Ge doped fibre has been selected for its very highly photosensitivity nature, whereas the type I gratings written into a tin(Sn)-Er-Ge doped specially fabricated fibre have been considered for their high temperature sustainability, in association with many other utilities for high temperature sensing applications. In the studies, in addition to the decay in reflectivity of the gratings, which was observed, a shift in Bragg wavelength over the temperature range considered was seen. A mechanism for the decay in the reflectivity was developed and modelled according to a power-law and the results were compared with those from the aging curve approach. The wavelength-shift was simulated by modifying the power-law, which also was found to fit well to the experimental data. Temperature-induced reversible and irreversible changes in the grating characteristics were observed and considered as a means to predict the working lifetime of the grating at comparatively low temperatures. Accelerated-aging was reviewed and compared in terms of reflectivity and Bragg wavelength-shift. It was shown that the temperature-induced irreversible shift in the Bragg wavelengths could not be predicted by using the isothermal decay of the refractive index modulation. These results were discussed within the framework of the current theoretical approaches for predicting the stability of gratings of this type. Finally, the stability of the type I FBGs written into various photosensitive fibres have been compared by evaluating their activation energies.

4.2. Analysis of thermal stability of the FBGs: Previous work and the selection of fibres

4.2.1. Previous work

UV-induced fibre Bragg gratings (FBGs) have shown themselves of great importance in recent years and they have been used in a wide range of applications in fibre-optic sensing and

telecommunications [1]-[3],[6],[7]. However, the thermal stability of the gratings plays a prime role if these devices are to function effectively over a long period of time. To explain the thermal decay characteristics of fibre Bragg gratings, Erdogan *et al.* [69] proposed a model based on a power-law with an alternative approach using the master aging curve, which explained well the observed rapid thermal decay of the gratings, followed by a substantial slow decay rate, for any particular temperature considered in their work.

Several groups have analysed the thermal stability of the fibre Bragg gratings written in different fibres, under different conditions [68]-[71],[157] and the results have been fitted well to a power-law function, with different decay factors and coefficients observed for different types of fibres. Comparisons of isochronal and isothermal decays [179] have also been made and it was observed that isochronal step decays could be used to predict isothermal decays, with some corrections. However, the decay of the FBGs written into hydrogen-loaded fibres [73] has shown to be different and this can be explained by using the log-time model [70]. Fokine has reported the formation of a highly thermal-stable chemical composition grating (CCG) [178] in fluorine-doped germanosilicate fibre and has discussed its thermal stability [176], when the grating was subjected to the first stage of an annealing process during the high-temperature treatment that occurred at the time of its formation. For uses in different applications, gratings have often been pre-annealed to wipe out the unstable portion of the refractive index change within a very short period of time. The annealing time and temperature may be determined by studying the accelerated aging [68]-[70],[74] process. In the investigation of the thermal decay of the gratings, a shift of the Bragg wavelength [160],[170],[180] has also been observed. At temperatures higher than ambient, the UV-induced refractive index modulation decay degrades the reflectivity of the grating and at the same time affects the effective refractive index of the fibre, which is responsible for the drift of the Bragg wavelength.

4.2.2. Selection of the fibres

As discussed earlier, two major factors - the photosensitivity of the fibre in which the grating is written and the thermal stability of the grating are of prime importance in terms of choosing the most appropriate fibre to use and the long term functionality of the grating over a wide range of temperatures. B-Ge doped fibre has been reported to give much higher level of photosensitivity [29] when compared to other fibres and the technique of hydrogen loading [27] can further enhance this property of the fibre, but the gratings written in these fibres, with or without pre- or post-treatment, are reported to have a much poorer high temperature stability [68],[70],[74],[181]. Alternatively, work on an enhanced photosensitivity in tin (Sn)-doped germanosilicate fibre [154] and tin-silicate fibre [155]-[157], showing improved thermal stability of the gratings, has been published. Unlike boron doping, tin doping does not introduce significant loss at the telecommunication window of 1.55 μm [154]-[157]. In addition, Sn-codoping increases

the mechanical strength of the fibre [77], which is very useful both in telecommunications and sensing applications, with the added advantage of enhancing the dynamic range of measurement for both strain and pressure.

In the previous chapter the photosensitivity and the thermal sustainability of the gratings written into various photosensitive fibres have also been studied. Among those, B-Ge doped fibre was found to be the most UV-photosensitive for writing gratings, whereas the gratings written into the specially fabricated (Tin)Sn-Er-Ge and (Antimony)Sb-Er-Ge doped fibres were observed to be the most thermally stable. It is worthwhile to note that both Sn^{4+} (or Sb^{3+}) and Er^{3+} doping have been introduced in the specially fabricated fibre to achieve a high-temperature stability along with a ASE-based fluorescence property, which arises from the rare-earth doping in the fibre. At the same time, the high temperature sustainability of the FBGs written into the fibre can be used for several high temperature sensing applications [182],[183]. Based on the above discussion, the most photosensitive optical fibre (B-Ge doped fibre) and one of the most useful fibres for the high temperature sensing applications (Sn-Er-Ge doped fibre) have been selected for the analysis of the thermal stability of the gratings written into these fibres. The specifications of the fibres used for this analysis have already been listed in Table-3.2.

4.3. Analysis of thermal stability of gratings written in B-Ge doped fibre

In this section, the thermal decay of the gratings fabricated in boron germanium doped silica fibre was studied in terms of its reflectivity, which was found proportional to the integrated coupling coefficient (ICC) using the power-law dependence [69] and the result was compared with the use of the aging curve approach. The shift in the Bragg wavelength has also been modelled by modifying the power-law, which was found to fit well with the experimental data. A prediction of the operational lifetime and of the accelerated-aging of the grating have been described and are compared in terms of the ICC and the shift in the wavelength. For pre-annealed gratings, a reversible change in the spectral characteristics with temperature [184] was observed. This temperature-induced effect was considered to modify the predicted degradation of the gratings and has been discussed in the 'Discussion' section. The effect of the step-stress experiment [185] was discussed by LuValle *et al.* to achieve more accurate results in the accelerated testing. Different decay-rates of the refractive index modulation (Δn_{mod}) and the effective refractive index (Δn_{eff}) were observed in terms of reflectivity-decay and the Bragg wavelength shift at various temperatures. These are related to the consideration of the complex phenomenon of the thermal decay of the UV-induced gratings, with the possibility of differences in the activation energy distribution in terms of the decay in Δn_{mod} and Δn_{eff}.

4.3.1. Experimental details of the writing of FBGs in B-Ge doped fibre and their thermal testing

Initially, a type I FBG was fabricated in a B-Ge codoped photosensitive fibre (fibre specification has been mentioned in Table-3.2) using light from a KrF excimer laser (Braggstar-500 supplied by Tuilaser AG) at 248 nm with a pulse duration of about 10 ns and employing the FBG-writing technique of UV-exposure through a phase-mask (phase-mask_1: specification is given in Table-3.1). It took ~ 50 seconds to form a type I grating with a peak reflectivity of 99.9% with a laser energy of 12 mJ at 200 Hz and a pulse fluence of ~ 180 mJ/cm^2. The detailed process of grating-fabrication using phase-mask has already been discussed in Chapter 3. Fig.4.1 shows the typical transmission spectrum of the grating, measured using an HP-86140A (Agilent) optical spectrum analyser (OSA).

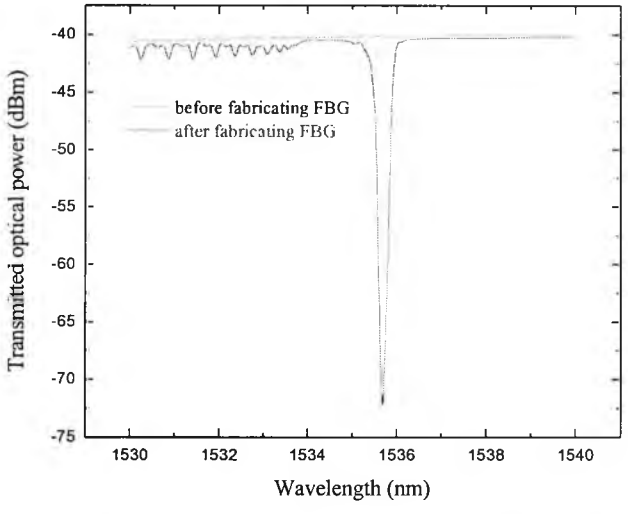

Fig. 4.1: Typical transmission characteristics of an FBG written at 248 nm in a B-Ge doped silica fibre.

For the study of thermal analysis of the FBGs, a series of nearly identical gratings of length ~ 6.5 mm and of reflectivity ~ 90% was fabricated in the same fibre. Grating reflectivities were controlled by stabilising the energy, pulse frequency and the exposure time of the excimer laser. With the reasonable assumption that the gratings were all uniform (sample tests confirmed this), the amplitude of the refractive index modulation (Δn_{mod}) was estimated using the following equation [6],[7]:

$$\Delta n_{mod} = \{ \lambda/\pi L n(V)\} \tanh^{-1}(R)^{1/2} \qquad (4.1)$$

where λ is the operating wavelength for a grating length, L, of reflectivity, R, with an overlap function of the fibre, $n(V) = \{1 - [1/2.405(\lambda_{cut\text{-}off}/\lambda)]^2\}$. The corresponding value of Δn_{mod} was ~ 1.9 $\times$ 10 $^{-4}$. It may be noted that the fibre photosensitivities were still not saturated in this situation. This is deliberate because the reflectivities were measured in this study by considering only the minimum of the transmission spectrum at the Bragg wavelength, not the spectral width, which is

directly related to the Δn_{mod} for strong gratings [71]. Following the UV-exposure during the grating fabrication, the Bragg wavelength shift was observed to be ~ 0.51 nm towards the longer wavelength side, which corresponds to an increase in the effective refractive index of the fibre-core (Δn_{eff}) of ~ 4.7×10^{-4}, determined using the equation:

$$\Delta n_{eff} = (\Delta\lambda_b)/2\Lambda \qquad (4.2)$$

where $\Delta\lambda_b$ is the Bragg wavelength shift during the grating-fabrication and Λ is the grating period, i.e., half of the phase-mask period.

The thermal degradation of the fibre Bragg gratings with time was then monitored at several temperatures of 100, 200, 300 and 400°C by placing the individual gratings very carefully (so that there was no excess strain effect on the gratings) inside a well-characterised and calibrated CARBOLITE tube oven (Model Type: MTF 12/38/400). The real-time reflectivities of the gratings were measured from the transmission spectra observed on the OSA. At each temperature, a fast decay of the grating followed by a substantial slow decay was observed. The thermal decay was modelled in terms of the normalised integrated coupling coefficient (NICC, η), as the integrated coupling coefficient (ICC) is directly proportional to the peak-reflectivity. The peak-reflectivity of the grating at any time can be calculated by using Eq. (4.3) where

$$R = (1 - T_{min}) \qquad (4.3)$$

and T_{min} is the transmission-minimum of the grating at Bragg wavelength (λ_b). The value of ICC can be calculated as

$$ICC = \tanh^{-1}[(R^{1/2})] \qquad (4.4)$$

which can be used subsequently for the evaluation of NICC, η, as

$$\eta = \{\tanh^{-1}[(R_{t,T}{}^{1/2})]/ \tanh^{-1}[(R_{0,RT}{}^{1/2})]\} \qquad (4.5)$$

where $R_{t,T}$ and $R_{0,RT}$ are the reflectivities after an annealing time t at a temperature T and the initial reflectivity at room temperature (~ 23°C) respectively.

4.3.2. Analysis of the decay in Reflectivity based on the '*Power-Law*'

Using the experimental data obtained, the thermal decay characteristics were modelled according to the "power-law" function proposed by Erdogan *et al.* [69] and this can be expressed as

$$\eta = 1/[1+ A(t/t_1)^{\alpha}] \qquad (4.6)$$

where t, A and α are the decay time in minutes, the power-law factor and the power-law decay coefficient respectively. To keep the dimensions consistent, a time t_1 = 1 minute was introduced. Both A and α are dimensionless in this form but they are temperature dependent. It was found that the model fits reasonably well to the experimental data. Fig. 4.2 shows the thermal decay characteristics along with the model-fitted graph (solid-line).

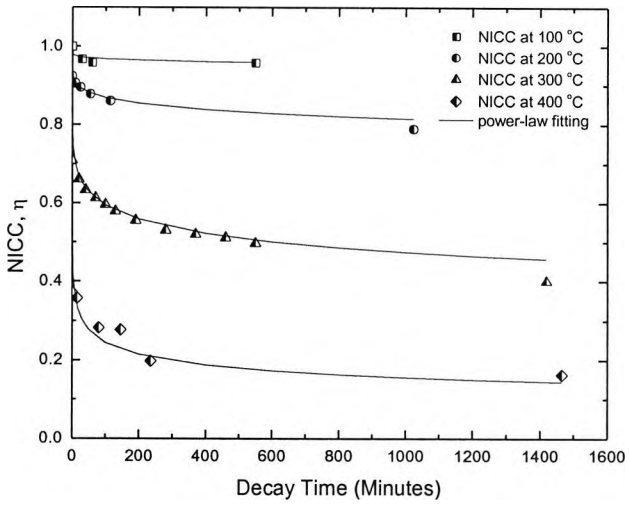

Fig. 4.2: Thermal degradation of the FBGs written in B-Ge doped fibre, with time, in terms of the NICC at various temperatures.

The set of values of A and α used were calculated from the experimental points for each temperature, according to Eq. (4.6). Following that, A and α were plotted against temperature to evaluate the temperature dependence of these parameters, this being shown in Figs. 4.3(a) and 4.3(b). The variation of α with temperature was assumed to be linear, passing through zero on the temperature axis (K) and the temperature dependence of this parameter can be expressed as

$$\alpha = T/T_R \qquad (4.7)$$

where T is the temperature in Kelvin and from the slope of the linear fit, the value of T_R = 2754 K can be estimated. Fig. 4.3(a) shows the dependence of the exponent, α, on temperature displayed as a linear relationship only above 450 K, with a large statistical variation below that. These large errors arose primarily because of the large uncertainty in the value of ICC due to the measurement errors of T_{min} along with the substantially smaller grating decay at low temperatures, on which α is very much dependent. Fig. 4.3(b) shows a plot of A, with temperature, on a linear scale, where the value of A was evaluated by exponential growth fitting, the nature of which can be written as

$$A = A_o \exp(aT) \qquad (4.8)$$

with $A_o = 1.20 \times 10^{-4}$ and $a = 13.42 \times 10^{-3}$ K^{-1}.

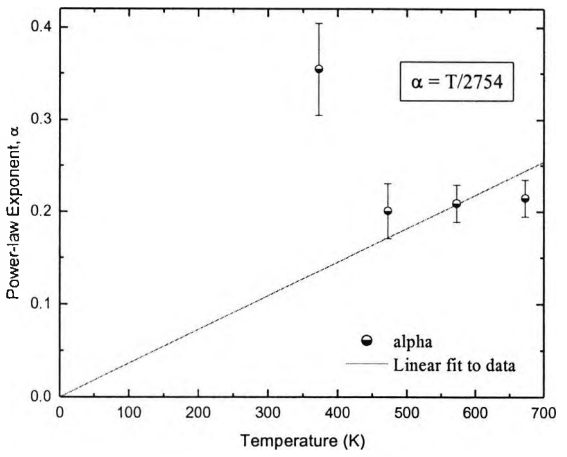

Fig. 4.3(a): Linear fit for the Power-Law decay coefficient, α.

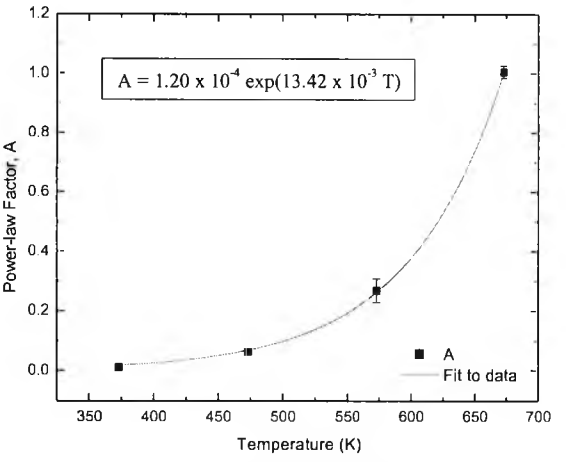

Fig. 4.3(b): Exponential fit for the Power-Law factor, A, on a linear scale.

Table-4.1: Comparisons of the reflectivity decay factor and decay coefficient of this work with other related work for gratings fabricated in similar fibres under different conditions.

Reference	Fibre and technique used	Value of α	Value of A
Baker *et al.* [70]	B-Ge codoped (NORTEL) Fibre with 244 nm CW laser.	T/2941	1.92×10^{-4} exp(0.0131T)
Williams *et al.* [74]	B-codoped germanosilicate Fibre with frequency quadrupled Nd:YLF laser at 262 nm.	T/1667	5.98×10^{-6} exp(0.00764T)
Dong *et al.* [68]	B-doped germanosilicate fibre with 193 nm excimer laser.	T/2200	1.73×10^{-3} exp(0.00824T)
Pal *et al.* [181] (this work)	B-Ge co-doped silica fibre (Fibercore) with 248 nm excimer laser.	T/2754	1.20×10^{-4} exp(0.0134T)

Table-4.1 shows the comparison of the decay parameters evaluated for FBGs written under different conditions in boron germanium (B-Ge) codoped silica fibre from reports published by several research groups. The values of T_R, A and a in this work are closely comparable to those reported by Baker *et al.* [70] but are slightly different from results given in the two other references, published by William *et al.* [74] and Dong *et al.* [68]. The variation of the

concentrations of boron and germanium within the photosensitive fibres used and the wavelengths and types of the different UV-exposures during the fabrication of the gratings are most likely to have caused these reported differences in the parameter values. It is noticeable that the closest comparison (with the work of Baker *et al.*) occurs for a fibre with the same dopants, with a grating written at approximately the same wavelength. It has not, however, been possible to compare the effect of dopant concentrations as in neither case were these data available.

4.3.3. Analysis of the decay in reflectivity based on the '*Master Aging Curve*'

It should be noted that the successful application of the power-law depends on the α versus T and A versus T relationships being expressed by the two earlier equations. This may, however, not always be correct (as discussed above), as a deviation of the regression was observed from the experimental data for α, particularly at lower temperatures. Thus in this work, attempts were made to fit the data from the accelerated aging experiments at 100, 200, 300 and 400°C to obtain a "master curve" using the aging curve approach [69],[71], in order to predict the operational lifetime of the grating. In this approach, it is assumed that the grating inscription causes a broad distribution of the activation energy of thermodynamically unstable traps and the aging of any grating at any time, t, and temperature, T, can be described by an aging parameter [69],[71],[186], E_d, (namely the demarcation energy) as:

$$E_d = k_B T \ln(\nu t) \qquad (4.9)$$

where k_B is the Boltzmann's constant and ν is a frequency term, which can be obtained from the sets of data at various temperatures (say, 100, 200, 300 and 400°C) fitted together through an iterative process. The correct shape of the master curve can also be deduced from the power-law expression [69],[179] and is described using the following equation:

$$\eta(E_d) = 1/\{1+\exp[(E_d - \Delta E)/k_B T_R]\} \qquad (4.10)$$

where the total number of the trapped carriers at time t was assumed to be proportional to the experimentally determined values of η. Fig. 4.4 illustrates the master aging curve for the grating using the same earlier experimental data. For this plot, the optimum value of ν used was 2.6×10^{14} Hz for the best fitting to a single master curve. After the establishment of the master aging curve, the degradation of the grating for any combination of time and temperature can be projected, as discussed in the later part of the work.

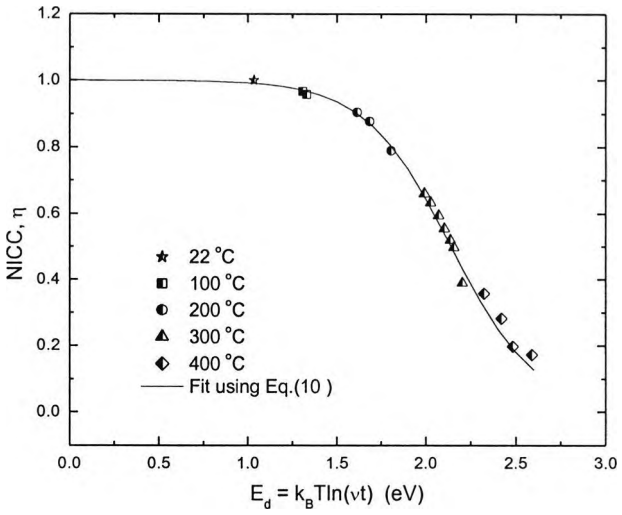

Fig.4.4: Plot of the NICC as a function of the demarcation energy, Ed, for the gratings. The frequency term (ν) used for this plot is 2.6×10^{14} Hz.

The activation energy distribution for the fibres can be derived from the above coefficients, as described by Erdogan *et al.* [69] with the peak of the bell-shaped activation energy distribution, $\Delta E \approx - k_B T_R \ln(A_o)$ with its FWHM $\approx 3k_B T_R$. Fig. 4.5 represents the energy distribution of the trapped carriers for boron-germanium codoped fibre, as calculated from the slope of Fig. 4.4. The solid portion of the graph represents the range of the demarcation energies actually sampled during the experiment with the dotted portions the prediction of the model.

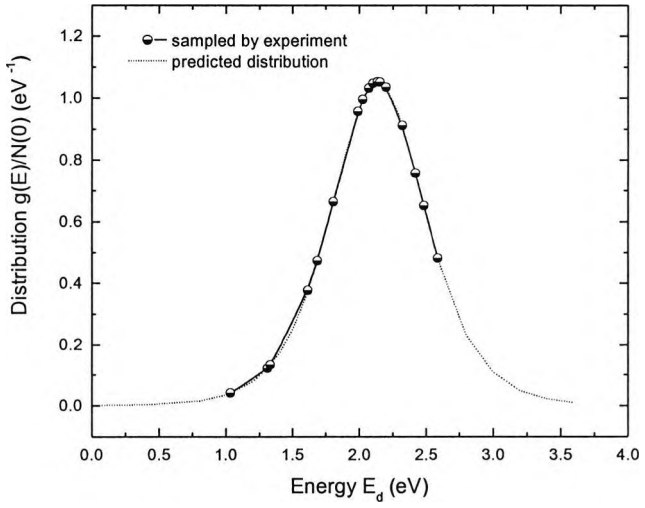

Fig.4.5: Distribution of the activation energy, plotted from the slope of the Fig.4.4. The symbols represent the demarcation energies actually sampled by the experiment.

The fibre used by Baker *et al.* [70] had an activation energy distribution peak at 2.2 eV with a FWHM of 0.9 eV, which are closely comparable with values derived in this work where the activation energy distribution peak was at 2.14 eV with a FWHM of 0.85 eV. Compared to the gratings fabricated in the Ge-doped fibre used by Erdogan *et al.* [69] (distribution peak at 2.8 eV with FWHM of 1.6 eV), the lower value of the activation energy in this work suggests that lower energy is needed to "wash out" the grating and the grating is less sustainable at higher temperatures, although it appears to have better photosensitivity.

4.3.4. Analysis of the shift in the Bragg wavelength

The shift of the Bragg wavelength with temperature has been widely employed as the measurand in temperature sensing or in temperature compensation e.g. for strain monitoring. In such systems, at each temperature studied, the Bragg wavelength shift [160],[170],[180],[181] is observed. So, in this work, it was seen as equally important to model the shift of the Bragg wavelength with time at each temperature, in the same way as the reflectivity was measured, before a grating could be used reliably in any particular application for a long time. This shift at each temperature was then modelled, in a similar way, with a slight modification of the power-law. The change of the Bragg wavelength was shown to be related to the effective refractive index of the fibre. The refractive index modulation of the fibre decreases with temperature, as does its effective refractive index. Thus the trend of this decay with temperature is almost identical to that of the earlier case, with the difference only of having a lower decay rate. With this assumption, the power-law can be modified and expressed as

$$\lambda_b(t) = \lambda_b(0)/[1+B(t/t_1)^{\beta}] \qquad (4.11)$$

where $\lambda_b(t)$ is the Bragg wavelength, monitored after t minutes of annealing at the temperature studied and $\lambda_b(0)$ is the initial Bragg wavelength at each defined and stabilised starting temperature. In the same fashion as was used in the power-law expression, a value of $t_1 = 1$ minute was introduced to keep the dimensions consistent. B and β may be expressed as the modified power-law factor and the modified power-law decay coefficient, used to evaluate the shift in the wavelength. These two parameters are also dimensionless and temperature-dependent, and may be calculated in the same way as is described above. Fig. 4.6 shows the shift of the Bragg wavelength with time at each temperature.

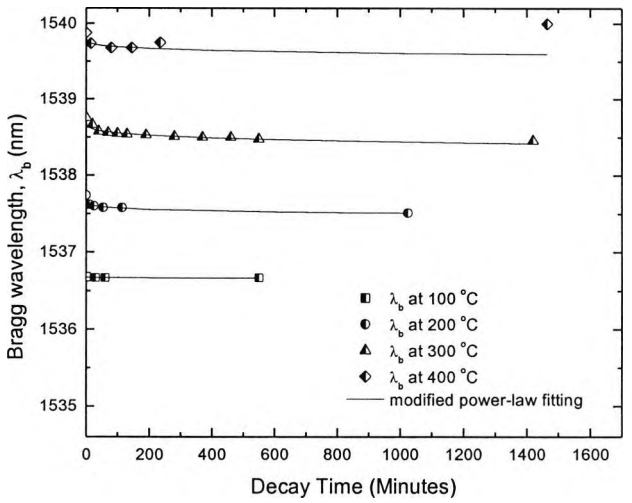

Fig. 4.6: Thermal degradation of the FBGs written in a B-Ge doped fibre with time in terms of the Bragg wavelength shift at various temperatures.

The expressions for β and B, through which the above equation can be fitted well with the experimental data, which have been shown in Figs. 4.7(a) and 4.7(b) and can be expressed as

$$\beta = T/T_\lambda \text{ with } T_\lambda = 3434 \text{ K} \quad (4.12)$$

and

$$B = B_o \exp(bT) \text{ with } B_o = 8.35 \times 10^{-6} \text{ and } b = 3.06 \times 10^{-3} \text{ K}^{-1} \quad (4.13)$$

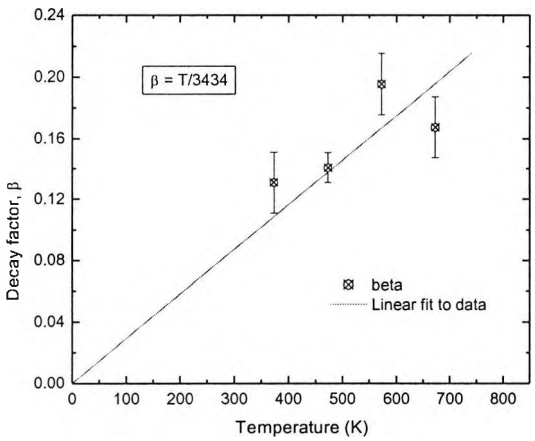

Fig. 4.7(a): Linear fit to data for the modified power-law decay coefficient, β.

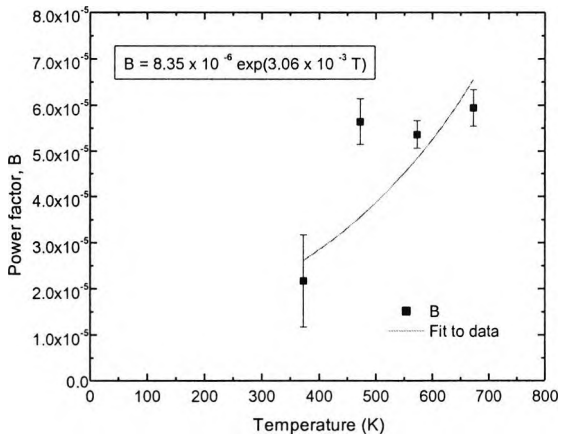

Fig. 4.7(b): Exponential fit to data for the modified power-law factor, B.

In Fig. 4.6, the modified power-law model is seen to fit well to the experimental points showing the shift in the Bragg wavelength, except for a few points at higher temperatures measured after a much longer time, where the experimental value of the Bragg wavelength is seen to lie above the fitted graph. This deviation of the experimental data from the fitted regression is supported by the results of work done by Chisholm *et al.* [180], where the effect of the boron composition of

the fibre on the thermal annealing has been studied and discussed in detail. The positive shift of the Bragg wavelength (i.e., towards the longer wavelength) was observed in the gratings fabricated in boron-germanium codoped fibre at comparatively higher temperatures. It may be noteworthy that the shift due to the boron composition was observed to be negligible up to ~ 300°C, after which the effect became dominant. To achieve a better precision in the prediction of the Bragg wavelength shift, the effect due to boron composition may be included, although the grating studied here could hardly survive at this high temperature (~ 400°C) for more than a few hours.

4.3.5. Prediction of operational lifetime of the FBGs through an '*Accelerated-Aging*' test

From the decay parameters evaluated, and using both the power-law and the modified power-law functions, the lifetime of the gratings in terms of the decay of the reflectivity and the shift in Bragg wavelength was estimated. Fig. 4.8 shows the variation of reflectivity over a simulated aging experiment, representing an estimated time period of 100 years, with initial reflectivity values of 99% and 90% at 100°C, 200°C and 300°C. Time has been plotted in this figure in logarithmic scale to take into account the decay in the grating reflectivities over a long period of simulated time. The results show that one grating with an initial reflectivity of 99% decays to 97% if it is kept at 100°C, and decays to 70% at 200°C over the equivalent period of 100 years. However at 300°C, only 11% and 8% of the reflectivity would remain after equivalent periods of 25 and 100 years respectively. The prediction of the grating reflectivity using the aging curve approach and the temperature-induced reversible effect on reflectivity is discussed in 'Discussion' section.

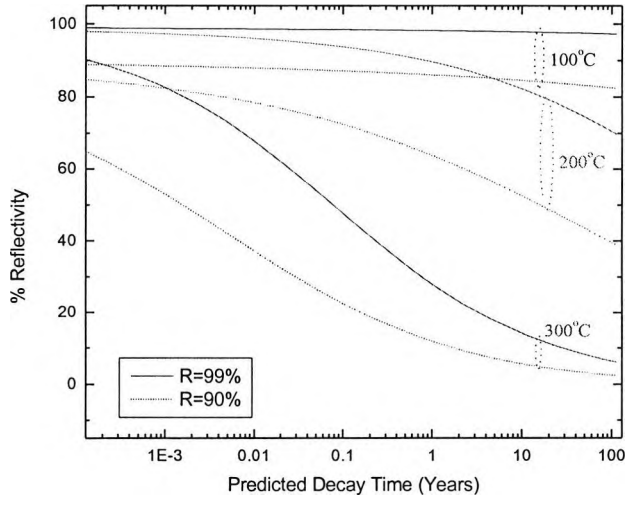

Fig. 4.8: Prediction of thermal decay of FBGs in terms of reflectivity, with initial reflectivity values of 99% and 90% at 100°C, 200°C and 300°C over a simulated period of 100 years.

Similarly, the shift of the Bragg wavelength of the grating was estimated over a long period of time. Using the predictions of this work, Fig. 4.9 shows that there would be only a 0.22 nm shift of the centre Bragg wavelength over a period of 100 years if it were kept at 100°C, but for gratings at 200°C and 300°C, the corresponding shifts would be ~ 0.6 nm and ~ 1.5 nm respectively for the same time period.

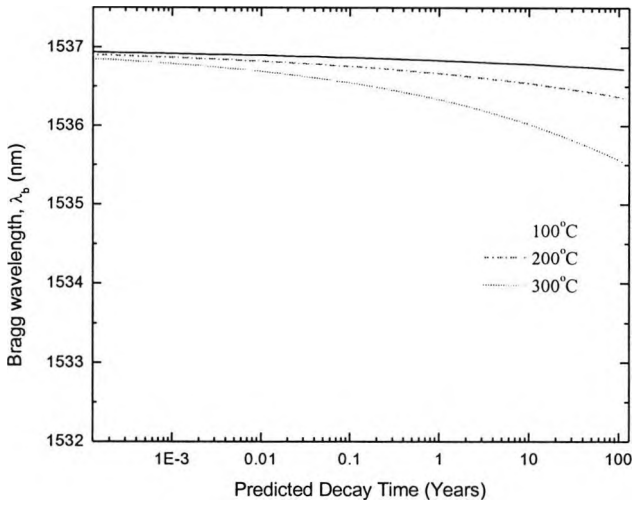

Fig. 4.9: Prediction of thermal decay of the FBGs in terms of the shift in the Bragg wavelength at various temperatures over an estimated period of 100 years.

These results are important in practical applications, as they have demonstrated that exposure to higher temperatures is likely to degrade the system performance with the use of dense WDM or wavelength-selective switching, for example, in sensor or communication systems. However, the natural thermal decay of the gratings can be predicted by considering an accelerated-aging process. A comparison of the accelerated-aging of the gratings in terms of reflectivity and Bragg wavelength shift has been shown in Fig. 4.10. The empirical equations for the calculation of the accelerated-aging in terms of reflectivity and the shift in Bragg wavelength were evaluated from Eqs. (4.6) and (4.11) respectively, using the values of A, α, B and β, and these are given as follows:

$$t_2 = \{\exp [aT_R(T_1/T_2 - 1)]\ t_1^{(T1/T2)}\} \quad \text{(in terms of reflectivity)} \tag{4.14}$$

$$t_2 = \{\exp [bT_\lambda(T_1/T_2 - 1)]\ t_1^{(T1/T2)}\} \quad \text{(in terms of shift in Bragg wavelength)} \tag{4.15}$$

where T_1 is the accelerated-aging temperature (K) for the grating after t_1 minutes, which is equivalent to another decay temperature T_2 for the grating at t_2 minutes. T_R and T_λ are the values derived from the decay coefficients from Eqs. (4.7) and (4.12).

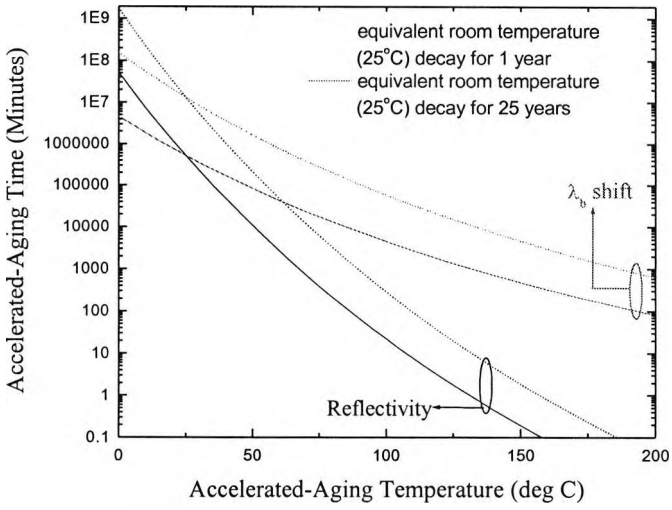

Fig. 4.10: Comparison of the accelerated aging in terms of the reflectivity and the shift in the Bragg wavelength of the FBGs written in a B-Ge doped fibre.

It is very clear from the two sets of graphs in Fig. 4.10 (equivalent to a room temperature decay for periods of 1 year and 25 years) that the accelerated-aging slope for the wavelength-shift is much lower compared to that for the reflectivity, due to the fact that the decay of refractive index modulation is much faster when compared to the decay of the effective refractive index.

4.4. Analysis of thermal stability of gratings written in Sn-Er-Ge doped fibre

In this section, prior to study of the thermal decay of the gratings fabricated in tin-erbium-germanium doped silica fibre, the fabrication of the special fibre has been described very briefly. Thermal stability of the FBGs was studied in terms of its reflectivity, using the power-law dependence [69] and the result was compared with the use of the aging curve approach, in a similar way as described in the earlier section. The shift in the Bragg wavelength has also been modelled by modifying the power-law, which was found to fit well with the experimental data. A prediction of the operational lifetime, and of the accelerated-aging of the grating have been described and these are compared in terms of the ICC and the shift in the wavelength. In this study as well, different decay-rates of the refractive index modulation (Δn_{mod}) and the effective refractive index (Δn_{eff}) were observed in terms of reflectivity-decay and the Bragg wavelength shift at various temperatures, as observed in case of gratings written in a B-Ge doped fibre. These are related to the consideration of the complex phenomenon of the thermal decay of the UV-induced gratings, with the possibility of differences in the activation energy distribution in terms of the decay in Δn_{mod} and Δn_{eff}. The possibility of arising multiple peaks in the distribution of the activation energies has been described in 'Discussion' section.

4.4.1. Fabrication of FBGs in the specially fabricated Sn-Er-Ge doped fibre

The special erbium-doped tin-germanosilicate fibre (core/cladding diameter: 5/125 μm, numerical aperture (NA): 0.2, cut-off wavelength of 1400 nm) was designed and fabricated at the University of Nice, France, by using the modified chemical vapour deposition (MCVD) technique. Tin, erbium and aluminium (1.1 mol/l, 0.025 mol/l and 0.083 mol/l in the solution, respectively) were introduced to achieve both high temperature sustainability [154]-[157],[182] and a suitable fluorescence spectrum from the fibre, covering the sensing range of the Bragg wavelength of the FBG written into that. Aluminium was introduced to confine the Er^{3+}-ions within the fibre core, to improve the pumping efficiency of the fibre (to generate ASE) as well as to avoid any clustering effects that may occur [13],[14].

Initially, a type-I grating was written in the specially fabricated Sn-Er-Ge codoped photosensitive fibre using ultraviolet light from a KrF excimer laser at 248 nm with a pulse duration of 10 ns and employing the phase-mask technique (using phase-mask_2: specification is written in Table-3.1), as described earlier. The grating reflectivity reached ~ 99% within 6 minutes of exposure time with a laser energy of 12 mJ at 200 Hz and a pulse fluence of ~ 180 mJ/cm^2, but it took further 5 minutes to reach the highest achievable peak reflectivity of 99.6% with a comparatively slow growth rate. The red shift of the Bragg wavelength has also been observed with the UV-exposure during the growth of the grating, where the on-line measurement of the grating spectrum has been made by using an HP-86140A (Agilent) optical spectrum analyser (OSA). The consistency of this result was observed by fabricating a number of gratings under the same conditions.

With a reasonable assumption that the gratings were all uniform (sample tests confirmed this), the amplitude of the refractive index modulation (Δn_{mod}) was estimated using the Eq. (4.1). The corresponding estimated value of Δn_{mod} was ~ 3.3×10^{-4} for a grating length of ~ 6.5 mm. Following the UV-exposure during the grating fabrication, the Bragg wavelength shift was observed to be ~ 0.82 nm towards the longer wavelength side, which corresponds to an increase in the effective refractive index of the fibre-core (Δn_{eff}) of ~ 7.7×10^{-4}, this having been determined using the Eq. (4.2). Fig. 4.11 shows the variation of the amplitude of the refractive index modulation (Δn_{mod}) and the effective refractive index (n_{eff}) with the UV-exposure time during the growth of the grating. The evolution of the grating reflectivity and the corresponding Bragg wavelength as a function of UV-exposure time has been reflected by the diagram shown as an inset in Fig. 4.11.

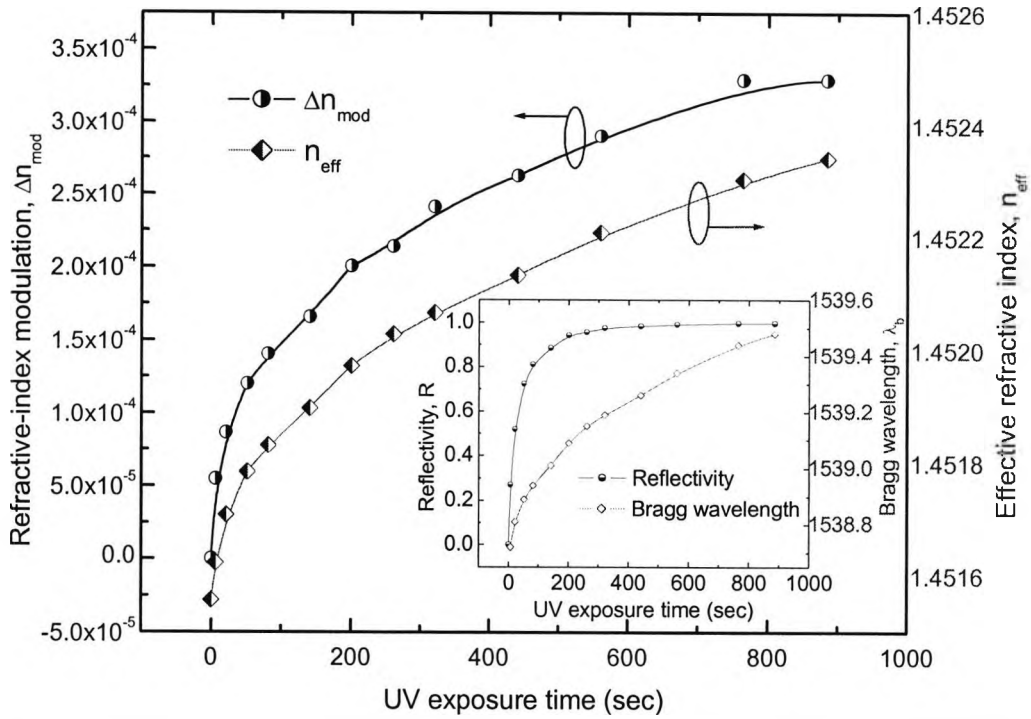

Fig. 4.11: Variation of the refractive-index modulation and the effective refractive index with the UV exposure time for laser fluence of ~ 180 mJ/cm^2/pulse by using a 248 nm excimer laser. The inset shows the evolution of the grating reflectivity and the Bragg wavelength shift during the growth of the FBG.

4.4.2. Decay of refractive-index modulation (Δn_{mod}) based on the '*Power-Law*'

For this study, a series of nearly identical gratings of reflectivity ~ 90% was fabricated in the same Sn-Er-Ge codoped fibre. Grating reflectivities were controlled by fixing the energy, pulse frequency and the exposure time of the excimer laser. The estimated values of Δn_{mod} and Δn_{eff} [using Eqs. (4.1) and (4.2)] were ~ 1.8×10^{-4} and ~ 4.5×10^{-4} respectively. No saturation was required in this work because the reflectivities were measured in this study by considering only the minimum of the transmission spectrum at the Bragg wavelength, not the spectral width, which is directly related to Δn_{mod} for strong gratings [71].

The thermal degradation of the fibre Bragg gratings, with time, was then monitored separately at several temperatures of 100°C, 300°C, 500°C, 700°C, 800°C and 900°C by placing the individual gratings very carefully (so that there was no excess strain on the grating) inside a well-calibrated CARBOLITE tube oven (type MTF 12/38/400). Temperatures were kept constant for each measurement over a period of about 8 hours after which the gratings were returned slowly to room temperature (~ 23°C) to measure their decay in reflectivity and the irreversible blue shift of Bragg wavelength. The real-time reflectivities of the gratings were measured from the

transmission spectra observed on the OSA. At each temperature, a fast decay of the grating, followed by a substantial slow decay was observed. The thermal decay was modelled in terms of the normalised integrated coupling coefficient (NICC, η), as the integrated coupling coefficient (ICC) is directly proportional to the peak-reflectivity. The peak-reflectivity of the grating and the NICC were estimated in a similar way, as described through Eqs. (4.3) – (4.5), in the earlier section.

Using the experimental data obtained, the thermal decay characteristics were modelled according to the power-law function proposed by Erdogan *et al.* [69], which has already been described in Eq. (4.6). For the type I FBGs written into the specially fabricated Sn-Er-Ge doped fibre also, it was found that the model fits reasonably well to the experimental data except for a few data points at 900 °C, which likely arises from the uncertainties in the measurement for very low values of reflectivities with oscillatory pattern of reference power spectrum. This oscillatory pattern of the reference power spectrum may likely to be arisen from the mismatch of the refractive index between the Sn-Er-Ge doped photosensitive fibre used (for writing FBGs) and the fibres in the connector used to connect to the light source and the detectors. Fig. 4.12 shows the isothermal decay characteristics of the FBGs written into this specially fabricated fibre at various temperatures along with a graph fitted to the model (solid-line).

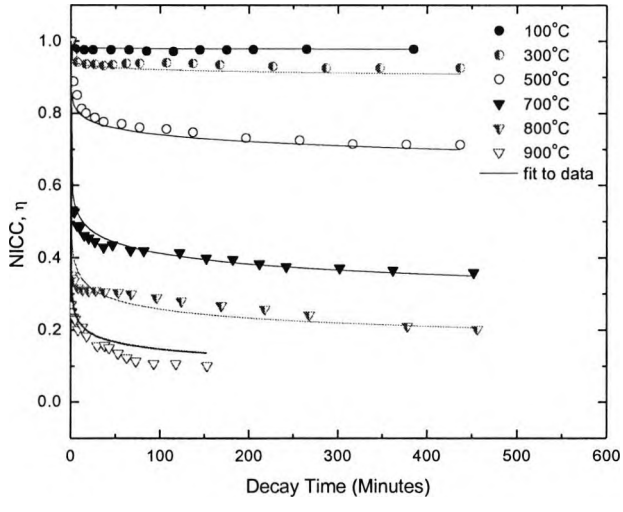

Fig. 4.12: Isothermal decays of the type I FBGs written in an Sn-Er-Ge doped fibre, with time, in terms of NICC at various temperatures.

The set of values of A and α used were calculated from the experimental points for each temperature, according to Eq. (4.6). Following that, A and α were plotted against temperature to evaluate the temperature dependence of these parameters, this being shown in Figs. 4.13(a) and 4.13(b). The variation of α with temperature was assumed to be linear, passing through zero on the temperature axis (K) and the temperature dependence of this parameter can be expressed in a similar way as described in Eq. (4.7). In this plot, from the slope of the linear fit,

the value of T_R = 5563 K can be estimated. Fig. 4.13(b) shows a plot of A, with temperature, on a linear scale, where the value of A was evaluated by exponential growth fitting, the nature of which can be written according to the Eq. (4.8). The values of the coefficients, A_o = 1.54 x 10^{-3} and a = 6.19 x 10^{-3} K^{-1} were evaluated from the regression.

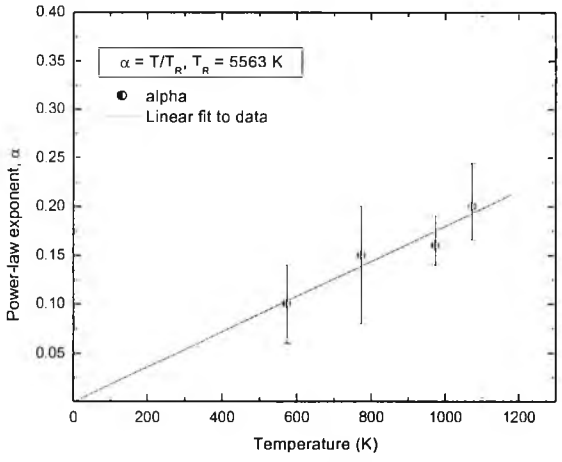

Fig. 4.13(a): Linear fit for the Power-Law decay coefficient, α.

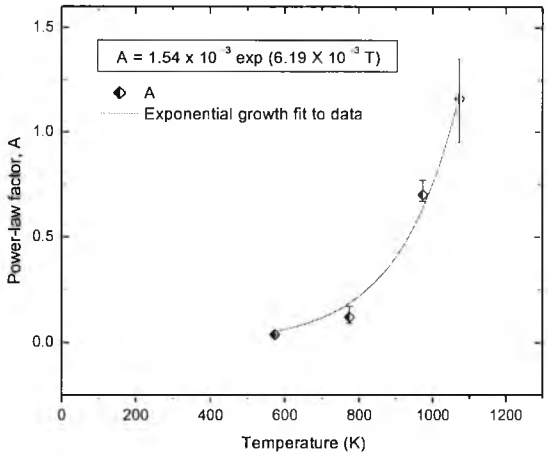

Fig. 4.13(b): Exponential fit for the Power-Law factor, A, in a linear scale.

The values of T_R, A and α in this work are slightly different from the brief results, reported by Brambilla *et al.* [157] for tin-silicate fibre. The variation of the composition and the dopants (specially selecting Er and Ge, in addition to Sn) and the concentrations of the dopants within the core of the photosensitive fibres used are most likely to have caused these differences in the values determined for these parameters.

4.4.3. Decay of refractive-index modulation (Δn_{mod}) based on the '*Master Aging Curve*'

The success in the use of the power-law to represent the decay of the gratings depends on the α versus T and A versus T relationships, as discussed in earlier sections, being expressed by the Eqs. (4.7) and (4.8). This may, however, not always be correct, as a deviation of the regression may be observed from the experimental data for α, particularly at lower temperatures. This is mainly due to the large uncertainty in the value of ICC due to the measurement errors in T_{min} for the substantially small grating decay at lower temperatures. Thus in this work, attempts were made to fit the data from the accelerated aging experiments at 100, 300, 500, 700, 800 and 900°C to obtain a "master curve", using the aging curve approach [69],[71],[157],[179],[181], in order to predict the operational lifetime of the grating. In this approach, it is assumed that the grating inscription causes a broad distribution of the activation energy of thermodynamically unstable traps and the aging of any grating at any time, t, and temperature, T, can be described

by an aging parameter [69],[71],[157],[179],[181], E_d, (namely the demarcation energy), as explained in the Eq. (4.9), where the frequency term, ν, can be obtained from the sets of data obtained at various temperatures (i.e., 100°C, 300°C, 500°C, 700°C, 800°C and 900°C) fitted together through an iterative process. The correct shape of the master curve can also be deduced from the power-law expression [69],[179],[181] and is described using the same equation, as described by Eq. (4.10), where the total number of the trapped carriers at time t was assumed to be proportional to the experimentally determined values of η. Fig. 4.14 illustrates the master aging curve for the grating, using the same earlier experimental data. For this plot, the optimum value of ν used was 1.54×10^{13} Hz, for the best fit to a single master curve. After the establishment of the master aging curve, the degradation of the grating for any combination of time and temperature can be projected, as discussed in the later part of the work.

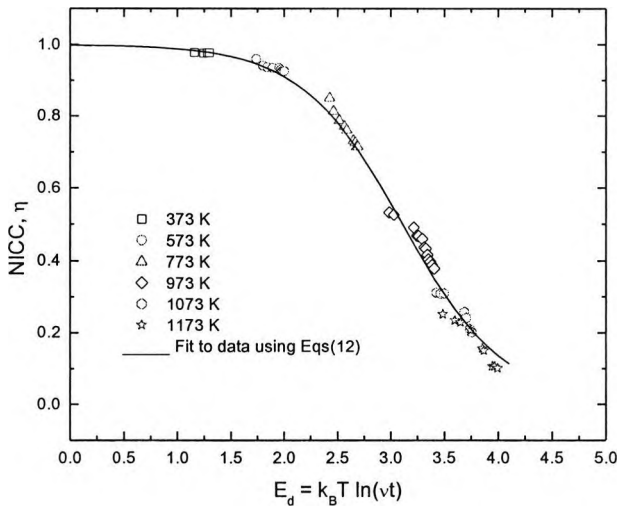

Fig. 4.14: NICC as a function of the demarcation energy, Ed, for the gratings written in a Sn-Er-Ge doped fibre. The frequency term (ν) used for this plot is 1.54×10^{13} Hz.

The activation energy distribution for the fibres can be derived from the above coefficients, as described by Erdogan *et al.* [69] with the peak of the bell-shaped activation energy distribution, $\Delta E \approx - k_B T_R \ln(A_o)$ with its FWHM $\approx 3k_B T_R$. Fig. 4.15 represents the energy distribution of the trapped carriers for the Sn-Er-Ge codoped fibre used, as calculated from the slope of Fig. 4.14. The solid portion of the graph represents the range of the demarcation energies actually sampled during the experiment with the dotted portions the prediction arising from the model. The activation energy distribution peak was estimated at 3.1 eV with a FWHM of 1.4 eV in this work.

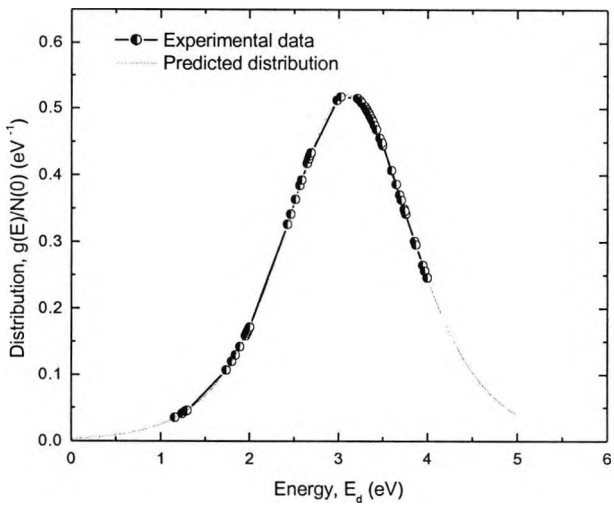

Fig. 4.15: Activation energy distribution for Sn-Er-Ge doped fibre, plotted from the slope of the Fig. 4.14. The symbols represent the demarcation energies actually sampled from the experiment.

4.4.4. Decay in the effective refractive index (n_{eff}) and the simulation of the predicted grating-decay

The shift of the Bragg wavelength with temperature has been widely employed as the measurand in temperature sensing over a wider range or in strain monitoring. In such systems, for any unstabilised (not annealed) grating, at each temperature studied, the Bragg wavelength shift [160],[170],[180],[181] is observed. So, in this work, it was seen as equally important to model the decay in the effective refractive index (which is directly related to the shift of the Bragg wavelength) with time at each temperature (in the same way as the reflectivity was measured), before a grating could be used reliably in any particular application for a long time. This decay at each temperature was then modelled, in a similar way, with a slight modification to the power-law. The refractive index modulation of the fibre decreases with temperature, and this affects its effective refractive index. Thus the trend of this decay with temperature is almost identical to that of the earlier case, with the difference only in their being a lower decay rate. With this assumption [181], the power-law can be modified and expressed as [which is correlated to the Eq. (4.11)]

$$n_{eff}(t) = n_{eff}(0)/[1+B(t/t_1)^{\beta}] \qquad (4.16)$$

where $n_{eff}(t)$ is the effective refractive index (estimated by monitoring the Bragg wavelength) after t minutes of annealing at the temperature studied and $n_{eff}(0)$ is the initial effective refractive index at each defined and stabilised starting temperature. In the same fashion as was used in the power-law expression, a value of t_1 = 1 minute was introduced to keep the dimensions consistent. B and β may be expressed as the modified power-law factor and the modified power-

law decay coefficient respectively, used to evaluate the shift in the Bragg wavelength as well as the decay in the effective refractive index. These two parameters are also dimensionless and temperature-dependent, and may be calculated in the same way as was described above. Fig. 4.16 shows the decay in effective refractive index with time at each temperature, whereas the inset in the figure describes shift of the Bragg wavelength with time at those temperatures. The expressions for β and B, through which the above equation can be fitted well to the experimental data, can be expressed as

$$\beta = T/T_\lambda \text{ with } T_\lambda = 5943 \text{ K} \quad (4.17)$$

and

$$B = B_o \exp(bT) \text{ with } B_o = 5.20 \times 10^{-6} \text{ and } b = 2.66 \times 10^{-3} \text{ K}^{-1} \quad (4.18)$$

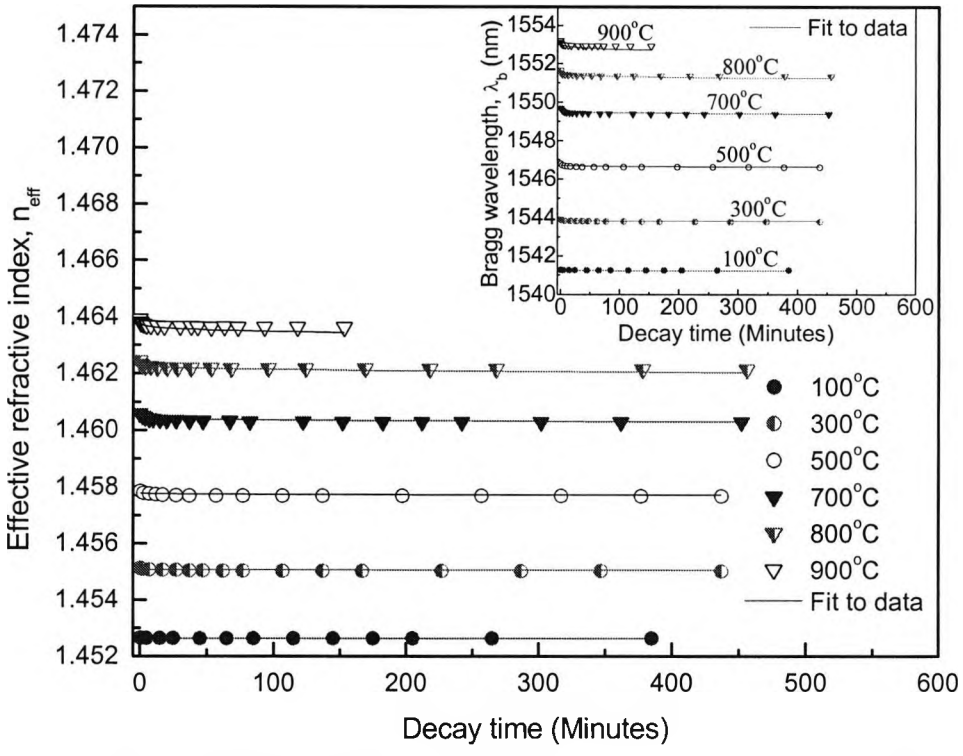

Fig. 4.16: Thermal degradation of the FBGs with time in terms of the effective refractive index at various temperatures. The inset shows the corresponding blue-shifts in the Bragg wavelengths.

In Fig. 4.16, the modified power-law model is seen to fit well to the experimental points showing the decay in the effective refractive index, which results in the shift in the Bragg wavelength. Thus the predicted shift in the Bragg wavelength of the grating after any time, at some lower temperature, may be simulated using the above values of the parameters evaluated.

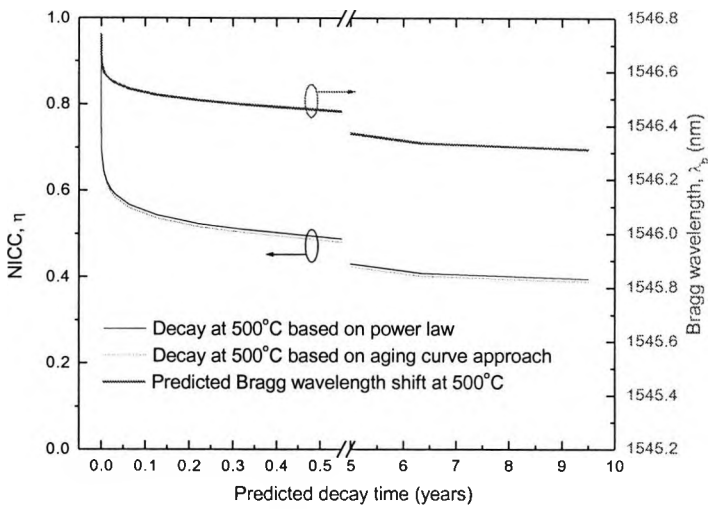

Fig. 4.17: Prediction of thermal decays at 500°C for the gratings written into an Sn-Er-Ge doped fibre according to the power-law and the master aging curve along with the blue-shift of the Bragg wavelengths of the gratings.

From the parameters evaluated, and using the power-law, the modified power-law and the master aging curve approach, the lifetime of the grating can be estimated in terms of the decay in the reflectivity and the shift in the Bragg wavelength. Fig. 4.17 describes the predicted decay in reflectivity and the shift in the Bragg wavelength for a pristine (not annealed) grating written in a Sn-Er-Ge codoped fibre at 500 °C for the period of time of ~ 10 years. The results show the value of NICC reaches a value of 0.66 with a shift of the Bragg wavelength of 0.18 nm after only one day, when the grating remains at a temperature of 500 °C, which is almost half of the total decay that would occur at that temperature, over a predicted period of 10 years. A negligible difference in the decay paths has been observed from the figure, when the power-law and the master aging curve are compared. This is mainly due to the consideration of the pristine (not annealed) grating in this case, so that there is no truncation of the initial distribution of the activation energy [71].

4.4.5. High-temperature sensing potential of the Sn-Er-Ge doped fibre and the FBGs written into this fibre

One of the most important physical parameters for many individual applications, temperature, can be measured from a calibration of the shift of the Bragg wavelength of the grating. Sn-doping in the fibre enhances the thermal stability [154]-[157] of the grating, resulting in a wider range of measurement of temperature, establishing the prime reason for choosing a fibre with this element as one of the dopants of the core, during fabrication. Temperature-induced reversible and irreversible changes in the Bragg wavelengths [181],[184] of the gratings were observed when the thermal decay of the gratings was analysed. For sensing purposes, to enable a reproducible sensor probe to be developed, the irreversible changes of the Bragg

wavelength should be removed to achieve repeatable measurement data by a well-defined process of annealing, which stabilises the gratings and allows only reversible changes in the Bragg wavelengths, thus resulting in a high level of repeatability over useful ranges of measurement for sensor applications.

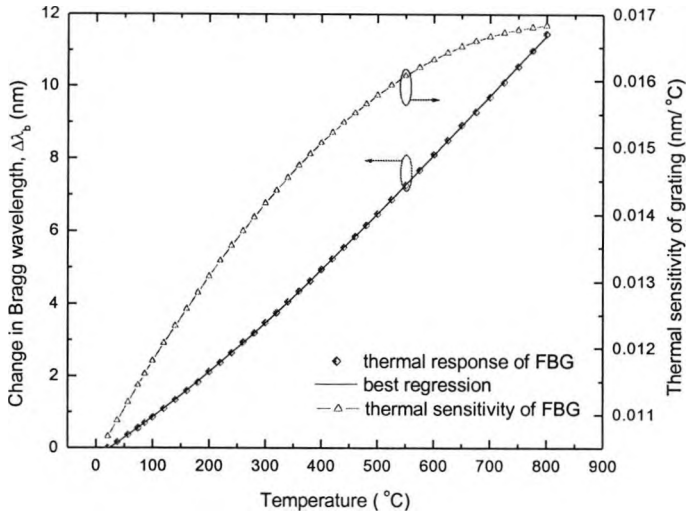

Fig. 4.18: Thermal response and the thermal sensitivity of a grating written into an Sn-Er-Ge doped fibre after proper annealing of the sample.

In this work, a grating was annealed properly (until the blue-shift of the Bragg wavelength settles at that temperature; discussed in detail in Chapter 5 in section 5.3.3) at 850 °C for ~ 10 hours before being used for temperature measurement up to 800 °C (from room temperature, in increments of 20 °C) by monitoring the reflection spectrum of the grating, by use of only the temperature-induced reversible changes in the Bragg wavelength. A settling time of 15 minutes was allowed at each temperature to ensure a thermal equilibrium between the grating and the oven had been achieved, before recording data for several cycles of both ascending and the descending temperatures. The measured data for the ascending and the descending temperature cycles, in terms of the Bragg wavelength change with temperature were observed to be quite consistent over a number of repeated measurements, with a wavelength uncertainty of $\pm$ 0.01 nm (the peak/dip resolution of the OSA used). The variation of the Bragg wavelength with temperature was found to be slightly non-linear and the temperature-dependent temperature sensitivity values of the grating were estimated to be 10.6 pm/°C and 16.8 pm/°C at room temperature (~23 °C) and 800 °C respectively. The thermal response of the grating, along with its temperature sensitivity, is plotted in Fig. 4.18.

This specially fabricated fibre has the added advantage of yielding fluorescence generated by the amplified spontaneous emission (ASE) caused by the rare earth (Er^{3+}) doping that was introduced, and this has been shown to be very useful in the design of special fibre amplifier and

fluorescence-based temperature sensing devices [187],[188]. Moreover, this adding of erbium ion does not affect the photosensitivity, which is almost comparable to that of only tin-doped silica fibre [189]. Simultaneous measurement of strain and temperature over a wide range of temperature can also be achieved, based on the temperature dependence of the fluorescence peak power ratio (FPPR) of the ASE in rare earth-doped fibre and the dual functionality of the FBG [182],[188]. Fig. 4.19 shows the ASE spectra obtained from this fibre, of length of 10 cm, with a grating written in one end of the fibre, where the FPPR approach may be applied for wavelengths of 1535 nm and 1552 nm.

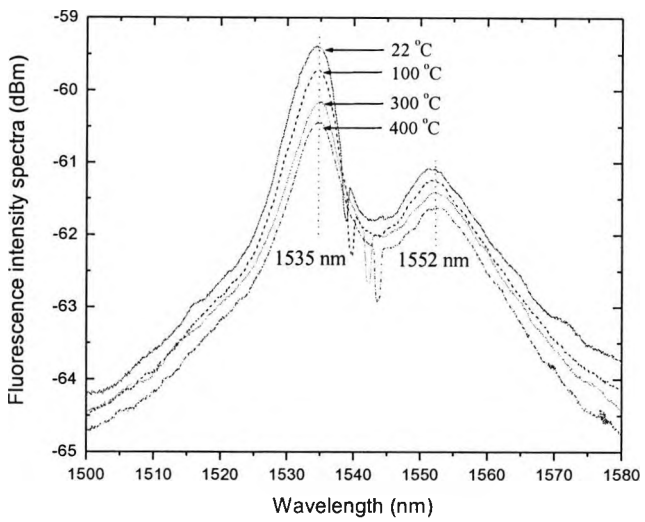

Fig. 4.19: Fluorescence spectra obtained at various temperatures from ~ 10 cm long Sn-Er-Ge doped fibre. The 'dip's in the spectra indicate the grating written into this fibre.

4.5. Comparison of thermal stability of type I gratings written in different fibres

Thermal stability is one of the important parameters of the fibre Bragg gratings, based on which it can be used in the systems, to be installed for various practical applications in sensing and telecommunication, for a long period of time. The thermal decays of the type I gratings fabricated in B-Ge and Sn-Er-Ge doped fibres have already been analysed in the previous sections. In this section, the thermal stability of type I gratings fabricated in various photosensitive fibres has been compared qualitatively and quantitatively.

The type I gratings written in B-Ge and Ge doped fibres can survive for any long-term sensing applications up to the temperatures of around 300°C and 650°C respectively, whereas the type I gratings written in a Sn-Er-Ge doped fibre can reliably be used up to the temperature higher than 850°C. In the analysis of the thermal stability of the gratings written in Sn-Er-Ge doped fibre, the peak of the activation energy distribution was estimated at 3.1 eV with a FWHM of 1.4 eV.

Compared to the gratings fabricated in the Ge-doped fibre used by Erdogan *et al.* [69] (distribution peak of the activation energy at 2.8 eV with FWHM of 1.6 eV), and gratings in B-Ge codoped fibre [70],[181] (distribution peak at ~ 2.2 eV with FWHM of ~ 0.9 eV), the higher value of the activation energy in this work suggests that a higher energy is needed to "wash out" the grating and thus the grating has a higher level of sustainability at higher temperatures, although the gratings written in tin-silicate [157] fibre has been reported more resistant to temperature with a distribution peak at 3.7 eV with a FWHM of 1.1 eV. Fig. 4.20 describes a comparison of the activation energy distributions of the density of states for gratings written in B-Ge codoped [181], Ge doped [69] and Sn-Er-Ge doped fibres [190]. The inset in the figure shows the variation of the normalised reflectivity of those gratings with temperature, taking results as a series of isothermal steps starting from 100 °C, with increments in temperature, with an annealing time of ~ 24 hours at each step. A visual comparison shows the considerable difference in the energy distributions, which implies a significant improvement of high temperature stability of the gratings written in Sn-Er-Ge codoped fibre over those written in B-Ge or Ge doped fibres.

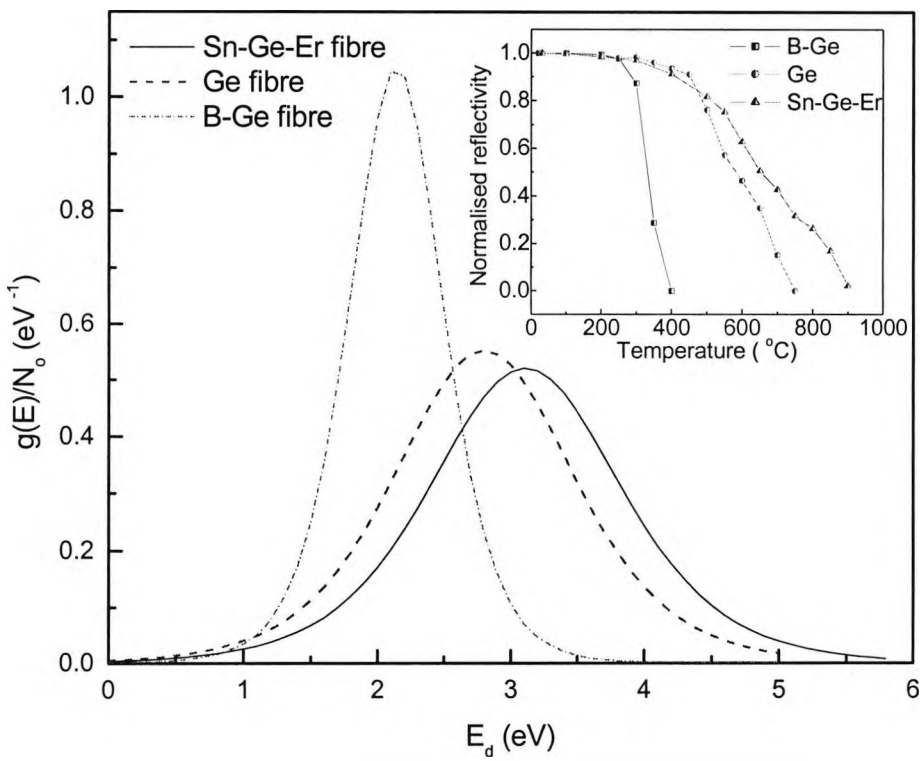

Fig. 4.20: Comparison of the activation energy distribution of the density of states for B-Ge [70],[181] Ge [69] and Sn-Er-Ge [190] doped fibres. The inset shows the normalised reflectivities of the gratings written in the respective fibres after ~ 24 hours of annealing at each temperature.

Table-4.2: Comparison of the reflectivity decay factor and decay coefficient for various type I gratings fabricated in different photosensitive fibres

Parameters	B-Ge doped Silica fibre [181] Pal *et al.*	Ge-Er doped silica fibre [69] Erdogan *et al.*	Sn-Er-Ge doped silica fibre [190] Pal *et al.*	Sn-silicate fibre [157] Brambilla *et al.*
T_R (K)	2754	5250	5563	3792
A_O (min^{-1})	1.20×10^{-4}	1.86×10^{-3}	1.54×10^{-3}	8.13×10^{-6}
a (K^{-1})	13.4×10^{-3}	7.64×10^{-3}	6.19×10^{-3}	1.12×10^{-2}
ν (Hz)	2.6×10^{14}	1.9×10^{15}	1.54×10^{13}	4.64×10^{16}
E_{Peak} (eV)	2.14	2.8	3.1	3.7
$FWHM_E$ (eV)	0.85	1.6	1.4	1.13
T_λ (K)	3434	-	5943	-
B_O (min^{-1})	8.35×10^{-6}	-	5.20×10^{-6}	-
b (K^{-1})	3.06×10^{-3}	-	2.66×10^{-3}	-

Table-4.2 summaries the thermal stability analysis of the gratings written into various photosensitive fibres. The table includes the estimated values of the different decay coefficients and factors for different fibres, which were found to be responsible for the stability of the gratings written into these fibres, in terms of reflectivity (or the refractive-index modulation) and the Bragg wavelength (or the effective refractive index). In addition, an overall predicted decay and the shift in the Bragg wavelength of the gratings, at comparatively lower temperatures, over a certain period of time, can be simulated from these estimated values of the coefficients listed in the table.

4.6. Discussion

Although the thermal stability of Bragg gratings written in boron-germanium doped silica fibre and in tin-erbium-germanium doped silica fibre has been analysed in this paper both in terms of the normalised integrated coupling coefficient and the shift in the Bragg wavelength, both of which are directly related to the refractive index modulation and the effective refractive index of the fibre, the accurate prediction of the grating stability is very difficult because of the highly complex phenomena associated with the grating decay. The reasons for this are discussed below.

4.6.1. Temperature-induced reversible and irreversible changes in the grating reflectivity

Recently studies of the temperature-induced reversible and irreversible changes in grating reflectivity have been reported by Razafimahatratra et *al.* [179] and Hidayat *et al.* [184], these being dependent on the type of the gratings and the processing of the fibres. A reversible temperature-induced increase in the reflectivity for pre-annealed type I grating was observed, which has a vital importance in predicting the grating decay, as the isothermal decay of the grating would be compensated to some extent by this effect. The dependence of the refractive index modulation (Δn_{mod}) on the temperature, based on the defect-related absorption bands has been considered as the cause of the above phenomenon rather than through the dependence of overlap integral, n(V), on temperature. The temperature-induced refractive index modulation (Δn_{mod}) at any temperature, T, can be expressed [184] as:

$$\Delta n_{mod}(T)/\ \Delta n_{mod}(296\ K) = [1 + \gamma(T - 296)] \qquad (4.19)$$

In this study, γ was evaluated as 4.9×10^{-4} for $296\ K \leq T \leq 473\ K$ with a pre-annealed grating in the above-mentioned fibre of $\Delta n_{mod} \approx 9.1 \times 10^{-5}$, which is comparable to the value reported by Hidayat *et al.* [$\gamma = (5.5 \pm 0.3) \times 10^{-4}$, with $\Delta n_{mod} \leq 1.6 \times 10^{-4}$). The spectrum of an annealed grating (written in a B-Ge doped fibre), at two distinct temperatures (i.e., 22°C and 250°C), has been shown in Fig. 4.21, which clearly showed the spectral changes with temperature.

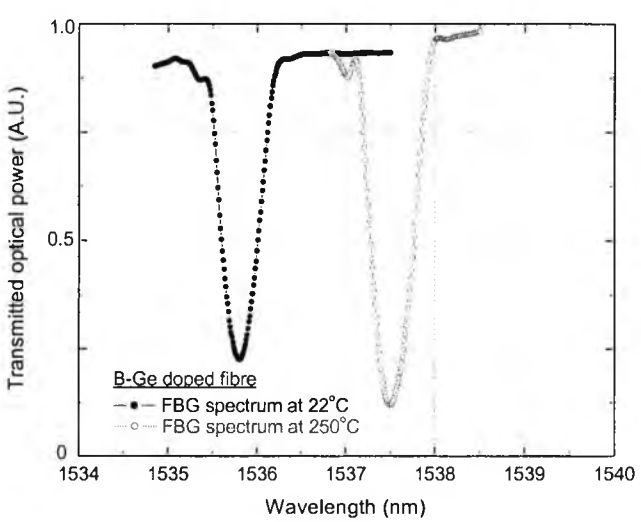

Fig. 4.21: Temperature-induced changes in the spectral characteristics of an annealed FBG written into a B-Ge doped fibre.

When consideration of the temperature-induced reversible effect on the reflectivity is included, the grating decay can be predicted more precisely. Fig. 4.22 illustrates the predicted decay of an unstabilised (not pre-annealed) grating written in a B-Ge doped fibre over a period of 25 years (according to the power-law and the aging curve approach) and including the temperature-

induced reversible effect in the aging curve with the broad assumption that this temperature-induced reversible effect is not time-dependent for any fixed temperature. A considerable difference in the decay paths was observed from the figure when the temperature-induced reversible effect was taken into account, compared to the difference between the decay paths extrapolated from the power-law and the master aging curve. The difference was very little in this latter case, as the unstabilised gratings were considered in this study so that there is no truncation of the initial distribution of activation energies after the grating inscription. If it were a stabilised grating, a considerable degree of difference in the decay paths would be displayed [71]. The frequency term calculated from the coefficients of the power-law ($\nu = 1/\tau \approx 1/[\exp(-aT_R)$ $\min^{-1}] = 1.86 \times 10^{14}$ Hz) showed the little difference from the value fitted to the master curve and thus a very small difference in the predicted decay graphs was estimated.

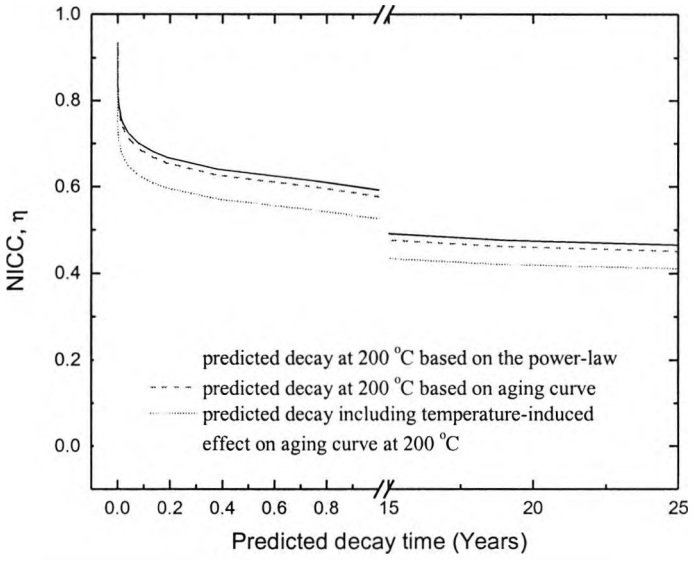

Fig.4.22: Prediction of thermal decay of an FBG written in a B-Ge doped fibre, at 200°C, according to the power-law and the master aging curve, including the reversible temperature-induced effect in the aging curve approach, over a period of 25 years.

The temperature-induced reversible change in the grating reflectivity [181],[184], where very accurate measurement is required, has not been considered for the analysis of the gratings written in the Sn-Er-Ge doped fibre. This is because of the limited uncertainty in the measurement of the reference power level during reflectivity monitoring of the grating. The oscillatory pattern of the reference power level was possibly caused by the mismatch of the refractive index between the Sn-Er-Ge codoped fibre used and the fibres in the connectors, connected to the light source and the detector, and the interference between the core and cladding modes occurs in the fibre section within the splice intersections [191], for the measurement of the reflectivity. Consideration of the above effect (i.e., the temperature-induced reversible changes in the grating reflectivity) will cause little further degradation of the gratings.

4.6.2. Consideration of Step-Stress Aging

Using the aging curve approach, the demarcation energy can be estimated by assuming a single value of the attempted frequency ν, for the best fitting to achieve a master curve from which the grating decay may be extrapolated. A strategy for the extrapolation of the accelerated aging was developed and reported by LuValle *et al.* [185] where demarcation mapping has been used to understand the process, with the assumption of multiple values of the attempted frequency and a step-stress experiment has been designed to minimise the effect of any larger values of ν than that estimated. In this study also, a step-stress experiment was carried out, in which two nearly identical gratings written in B-Ge codoped fibre were used, keeping one grating at 200°C to examine the isothermal decay and the other was raised to 200°C in stages after holding it at 100°C for 405 minutes. Fig. 4.23 shows the comparison between the isothermal and the step-stress decay curves. It can be seen that the isothermal decay that occurred after 400 minutes at 200°C for the first grating can be achieved within ~ 70 minutes for the step-stress decay for the other grating, when it was kept initially at 100°C for 405 minutes before applying a temperature of 200°C. The values of ν derived from these two decay graphs were slightly different and this indicated the hidden parallel degradation, which may be ruled out by using the demarcation mapping, although an assurance of the reliability of the accelerated testing cannot be given because of the highly complex nature of the grating decay mechanism.

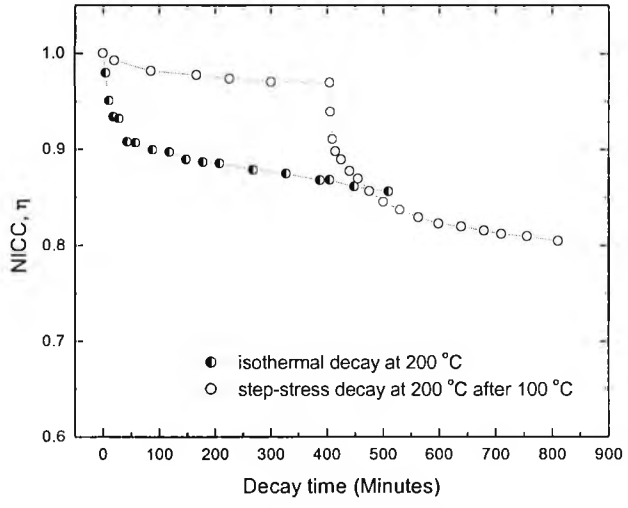

Fig. 4.23: Comparison of the isothermal decay and the step-stress decay when one grating written in a B-Ge doped fibre was kept at 200°C for isothermal decay and the other was raised to 200°C after being kept at 100°C for 405 minutes.

4.6.3. Temperature-induced reversible and irreversible changes in the Bragg wavelength shift of the gratings

Although temperature-induced reversible and irreversible changes in the Bragg wavelength shift were observed, only the irreversible changes have been considered in this study of the decay of effective refractive index with temperature, taking the Bragg wavelength at the beginning of the experiment (time t = 0+) as the reference. To separate the irreversible from the reversible shift of the Bragg wavelength, the Bragg wavelength at room temperature (i.e., 23°C) was measured initially as λ_{RT} before annealing. If the Bragg wavelengths after annealing at any temperature and at the room temperature to which grating returned were λ_{Final} and λ_{Return} respectively, then $(\lambda_{Final} - \lambda_{Return})$ can be considered as the reversible shift whereas $(\lambda_{RT} - \lambda_{Return})$ is the irreversible shift of the Bragg wavelength. In fact, this type of measurement has also been considered to calculate the decay in the effective refractive index (Δn_{eff}) of the fibre to evaluate the fringe contrast or the "visibility factor" ($\Delta n_{mod}/\Delta n_{eff}$) of the grating after each temperature cycle in this work. This is very important for the analysis of the grating decay in terms of both the reflectivity and the Bragg wavelength shift.

4.6.4. Possibility of multi-peaks in the activation energy distribution

The simulation of the exact distribution of the activation energy of the fibre material consisting of various dopants with different concentrations is not very simple. The development of the multi-peaks instead of a simple bell-shaped activation energy distribution is possible depending upon various dopants in the fibre core. Although the possibility of multiple peaks developing in the energy distribution has been suggested by observing a slight non-smooth thermal decay in the grating-reflectivity (for the gratings written in Sn-Er-Ge doped fibre: see the inset of Fig. 4.20), only one peak has been considered in this work. This is just to simplify the analysis of the complexity in the energy distribution, arising from the presence of various dopants in the fibre (e.g., Ge, Sn and Er), at different concentrations. An energy distribution with multiple peaks has also been reported by Rathje *et al.* [191] for gratings written in a hydrogen-loaded fiber. In fact, an energy distribution showing multiple peaks may be realised for this work by considering lower-temperature (below 700 °C) and higher-temperature (above 700 °C) isothermal tests separately, to evaluate the decay coefficients in two different thermal states and combining the respective energy distributions.

4.6.5. Consideration of the 'Visibility Factor' of the gratings

As mentioned earlier, the visibility factor ($\Delta n_{mod}/\Delta n_{eff}$) plays a vital role to correlate the decay of the grating in terms of the reflectivity and the Bragg wavelength shift. Wang *et al.* [160] have discussed the possible effects that may arise, taking into account the assumptions suggested by Kannan *et al.* [71] or the variable reaction pathway approach by Poumellec [186]. Two

possibilities have been predicted. The first is the case when the visibility factor remains constant. Even when the grating decay occurs after heat-treatment, the same master aging curve can be used to predict the grating decay, in terms of both the reflectivity and the Bragg wavelength shift. In the second case, the contrast or the visibility factor changes with the decay of the grating involving microscopic local mechanisms in such behaviour. To investigate this behaviour, a set of experiments was carried out in this work, where a grating of reflectivity ~ 90 % was written in B-Ge codoped fibre and both the refractive index modulation [$\Delta n_{mod}(296K)$] and the change in the effective refractive index [$\Delta n_{eff}(296K)$] were estimated at room temperature, just after the grating inscription and in each case of completing a heat-treatment at one of several temperatures. Table-4.3 shows the detailed results of the experiment, from which it can be seen that the visibility factor increases with the decay of the grating (except for the data at 400°C, where the effect of the boron composition may be assumed to dominate). This means that the thermal stabilities of the refractive index at the bright and dark fringes are different, i.e., the decay of Δn_{mod} andΔn_{eff} are different for any combination of time and temperature and the shift of the Bragg wavelength cannot be predicted simply from the decay in grating reflectivity. Different master curves may be used to predict the Bragg wavelength shift. The result obtained from the modified power-law also supports the argument.

Table-4.3: Comparisons of the temperature-induced irreversible Bragg wavelength shift, refractive-index modulation, change in effective refractive index and the visibility factor of the grating after annealing at various temperatures.

Experimental Measurements	Δn_{mod} ($\times 10^{-4}$)	$\Delta\lambda^*$ (nm)	Δn_{eff} ($\times 10^{-4}$)	V.F. ($\Delta n_{mod}/\Delta n_{eff}$)
Initial value at 23°C after inscription and before annealing	2.34	+ 0.55	5.19	0.45
At 23°C, after 405 mins of annealing at 100°C	2.17	+ 0.49	4.62	0.47
At 23°C, after 405 mins of annealing at 200°C	1.69	+0.34	3.21	0.53
At 23°C, after 405 mins of annealing at 300°C	0.94	+ 0.15	1.41	0.66
At 23°C, after 405 mins of annealing at 400°C	0.16	+0.03	0.28	0.57

* $\Delta\lambda$: Bragg wavelength shift, measured with the Bragg wavelength at the start of inscription as the reference.

A similar set of experiments has been carried out for the gratings written in Sn-Er-Ge doped fibre also, where the values of 'visibility factor' have been estimated not only for the thermal treatment process, but also during the time of growth of the UV-induced grating. Fig. 4.24 shows the detailed plot of the 'visibility factor's of the gratings written in Sn-Er-Ge doped fibre during the growth and various isothermal treatments. The figure gives the details of the experiment, from which it can be seen that the visibility factor increases with the decay of the grating (though the margin of the values are different for the gratings before and after the annealing being carried out at various temperatures) and decreases with the time of exposure during the growth of the grating. This means that the visibility factor for a grating is not constant with time during its growth or during the decay. Thus, the thermal stabilities of the refractive index at the bright and dark fringes are different, i.e., the decay of Δn_{mod} and Δn_{eff} are different for any combination of time and temperature and so the shift of the Bragg wavelength cannot be predicted simply from the decay in grating reflectivity. Different master curves may be used to predict the Bragg wavelength shift. The result obtained from the modified power-law also supports the argument.

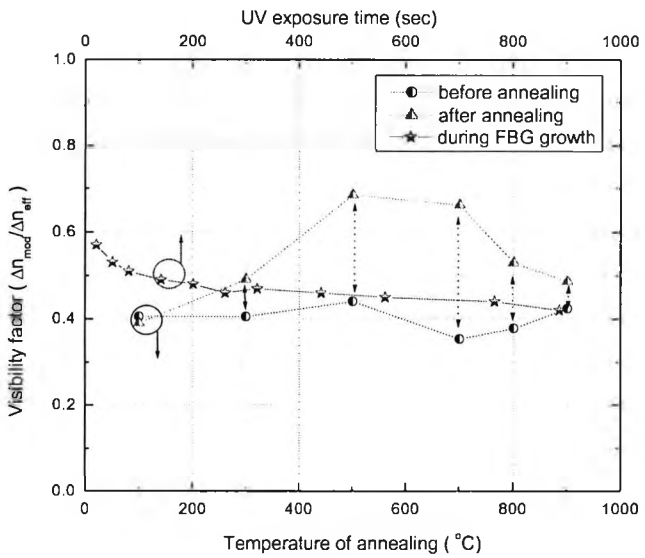

Fig. 4.24: Variation of the 'visibility factor' ($\Delta n_{mod}/\Delta n_{eff}$) of the gratings written in Sn-Er-Ge doped fibre, before and after annealing at various temperatures and that with the time during the growth of the grating.

Considering all of the above factors discussed earlier, the analysis of the grating decay can be thought of as comprising both local and non-local complexities. In the absence of a better analysis and for simplicity keeping within the range of current theoretical approaches, the empirical power-law or the master aging curve can be used for the approximate prediction of the grating lifetime. This involves considering the values of Δn_{mod} and Δn_{eff} of the fabricated grating used in the experiment (as mentioned earlier in this work), as the decay rate in the refractive

index of the bright and dark fringe patterns of the grating, which may change according to their initial values [186].

4.7. Summary

The thermal decay of fibre Bragg gratings, written into non-hydrogen loaded fibres, has been examined and analysed in this chapter, in terms of their reflectivity and Bragg wavelength change. Prior to this analysis, two photosensitive fibres (B-Ge doped fibre and Sn-Er-Ge doped fibre) have been selected and gratings were fabricated into these fibres using a UV light from a 248 nm krypton fluoride (KrF) excimer laser. A B-Ge doped fibre has been selected for its very high photosensitivity nature, whereas a tin(Sn)-Er-Ge doped specially fabricated fibre has been considered for its high temperature sustainability, in association with many other utilities for high temperature applications. In the studies, in addition to the decay in reflectivity of the gratings, a shift in Bragg wavelength over the temperature range considered was observed. A mechanism for the decay in the reflectivity was developed and modelled according to a '*power-law*' and the results were compared with those from the '*master aging curve*' approach. The wavelength-shift was simulated by modifying the power-law, which also was found to fit well to the experimental data. Accelerated-aging was reviewed and compared in terms of reflectivity and Bragg wavelength-shift to predict the operational lifetime of the gratings at comparatively low temperatures. Temperature-induced reversible and irreversible changes in the spectral characteristics of the gratings were observed for the gratings written in B-Ge doped fibre and considered in the analysis to predict the operational lifetime of the gratings more accurately. Finally, the stability of the type I FBGs written into various photosensitive fibres has been analysed by evaluating their activation energies. It has been shown through this analysis that the temperature-induced irreversible shift in the Bragg wavelengths could not be predicted by using the isothermal decay of the refractive index modulation. The results were discussed within the framework of the current theoretical approaches for predicting the stability of gratings of this type.

Chapter 5

Non-linear temperature dependence of FBGs

5.1. Abstract

Temperature measurements have been made by using fibre Bragg gratings (FBGs) written in a range of fibres and detailed data on their characteristics are presented. The data are fitted to polynomials that may be used in the calibration of temperature measurements with these types of gratings in automated systems. Issues of precision in such measurement of temperatures have been considered for several gratings of type I and IIA written in various photosensitive fibres, taking into account the non-linear temperature response of the fibre Bragg gratings. Measurements of temperatures were demonstrated from room temperature to 250°C (for gratings written in B-Ge doped fibre), to 500°C (for gratings written in Ge-Er doped fibre), and to ~ 850°C (for gratings written in Sn-Er-Ge, Sb-Er-Ge doped fibres and for the CCG). Comparison between the linear and the higher order polynomial regression showed a better performance in calibrated temperature measurement applications by using the non-linear temperature coefficients. This yields an acceptable RMS error of less than or comparable to 2.5 °C, compared to linear regression with the RMS error range of 3.3 – 19.5°C for the various gratings studied, over the whole measurement range.

5.2. Background of the work

In this section, the background of the thermal response of the FBGs, specifically for sensing applications, has been described briefly. In addition, a theoretical explanation of the grating thermal response is introduced.

5.2.1. Introduction

In recent years, fibre Bragg gratings (FBGs) have been extensively used in various sensing schemes because of their significant potential for temperature and strain measurements over a wide range of applications [1]-[3]. The relative ease of fabrication of FBGs in optical fibre is also one of the major factors underpinning their popularity, in addition to exploiting the other well-known advantages of fibre optic sensors. Temperature measurement, especially of high

temperatures, is one of the major interests in industry today, with FBG sensors being utilised in various applications. To achieve a higher level of repeatability in the measurement, the gratings should be annealed carefully prior to use. At the same time, to make accurate measurements of temperature, the temperature-dependence of the Bragg wavelength of the grating should be known and data on this incorporated accordingly into the system design. Similarly, in various other applications where temperature is not the primary measurand, e.g. strain monitoring, the additional shift of the Bragg wavelength (λ_b) due to the temperature must be considered and measured accurately to compensate for any temperature effect in the measurement.

The performance of the temperature-dependence of various FBGs has been observed to be non-linear in the region from room temperature to cryogenic temperatures (to 77 K [104],[105] and to 4.2 K [106]) because of the non-linearity of both the thermal expansion and the thermo-optic effect[104]-[106] of the silica fibres. However, the temperature response of the Bragg wavelength of a FBG is assumed to be linear around room temperature (within a limited range of measurement in most of the cases), particularly when used for the discrimination of parameters in the simultaneous measurement of strain and temperature using a range of different techniques [111]-[125],[192]. This has created a problem of limited range measurement in the above applications, even when high-resolution systems have been used. However, Hill and Meltz [8] have briefly reported a slightly non-linear temperature response of the gratings they made at higher temperatures, in studies carried out up to ~ 850 °C and Flockhart *et al.* [101],[102] have reported the non-linearity in the temperature coefficients of Bragg gratings over a more limited range, this being between –30 °C and +80 °C. The non-linear temperature sensitivity of FBGs has also been considered in the recent work by some of the authors [182] for the simultaneous measurement of a wide range of temperatures and strains. In recent research, Shu *et al.* [125] have observed the dependence of the grating temperature coefficient on the type of the gratings. In this work, however, the non-linear temperature response of the Bragg wavelength-shifts has been observed and studied in detail over a wide range of temperatures, which is particularly valuable for sensing applications, addressing the range from room-temperature to ~ 850 °C, using various FBGs (of type I and IIA) fabricated in different photosensitive fibres and incorporated in systems designed to achieve the best possible level of precision [193].

5.2.2. Theoretical explanation

The Bragg wavelength, λ_b, of an optical fibre grating with a period, Λ, can be represented as $\lambda_b = 2n\Lambda$ (as mentioned in Eq. (2.7) in Chapter 2), where n is the effective refractive index of the core of the fibre. Due to temperature changes, the grating-period varies as a result of the thermal expansion coefficient of the material and the thermo-optic effect creates a change in the

effective refractive index of the fibre-core. Thus, the shift of the Bragg wavelength, $\Delta\lambda_b$, can be expressed as

$$\Delta\lambda_b/\lambda_b = (1 - p_e)(\Delta L/L) + \Delta n/n \quad (5.1)$$

where p_e is the photo-elastic coefficient of the fibre (≈ 0.22 for fused silica glass[2], [104], [105]), $(\Delta L/L)$ is the strain induced in the fibre arising from the thermal expansion and $(\Delta n/n)$ is the fractional refractive index change due to the thermo-optic effect. If the thermal-strain and the fractional effective refractive index changes are assumed to be proportional to the applied temperature, Eq. (5.1) may be rewritten as

$$\Delta\lambda_b/\lambda_b = [(1 - p_e)\alpha + \xi]\,\Delta T \quad (5.2)$$

where $\alpha = (1/L)(dL/dT)$ is the thermal expansion coefficient and $\xi = (1/n)(dn/dT)$ is the thermo-optic co-efficient of the material. Eq. (5.2) is only valid for a limited range of temperatures, when the linear behaviour of the parameters with temperature is considered. Otherwise, for a wide range of measurement of temperature, Eq. (5.1) must be used. Combining Eqs. (5.1) and (5.2), the thermo-optic coefficient of the fibre can also be determined, which can be expressed as a function of the Bragg wavelength as

$$\xi = (1/n)(dn/dT) = (1/\lambda_b)(d\lambda_b/dT) - (1 - p_e)\alpha \quad (5.3)$$

5.3. Experimental arrangement

Prior to the measurement of temperature by using different types of FBGs in various optical fibres, following steps were considered.

5.3.1. Fabrication of gratings

In order to carry out a series of the experiments on the temperature response of fibre Bragg gratings of this type, initially gratings of type I and IIA were fabricated in four different types of photosensitive fibres (B-Ge, Er-High Ge, Sn-Er-Ge and Sb-Er-Ge doped fibres). The specifications for the fibres have already been listed in Table-3.2. Gratings were fabricated through the phase-mask technique (using phase-mask_1 and phase-mask_3: specifications were given in Table-3.1) using a 248 nm KrF excimer laser, which has been described in detail in Chapter 3. For all the gratings considered, the length was ~ 6.5 mm, the reflectivities were more than 95 %. The Bragg wavelengths of the fabricated gratings were at around 1540 nm with slight variations in the actual wavelength produced, this depending upon the variation of the effective refractive indices of the fibres used. The FWHM of the type I gratings was measured to be ~ 0.3 nm and that of the type IIA gratings was ~ 0.6 nm, before annealing.

5.3.2. Choice of the fibres, types of gratings and their operational range

Four different types of photosensitive fibres, mentioned above, were chosen to conduct this experiment. Both types I and IIA gratings were written in B-Ge and Er-High Ge doped fibres and

only type I gratings were written in other two photosensitive fibres. No hydrogen-loaded fibre was considered in this experiment. B-Ge codoped silica fibre was chosen for its highest photosensitivity among the materials considered, but the gratings fabricated in that fibre can only survive lower temperatures (~ 300 °C, for type I and ~ 400 °C, for type IIA gratings [175]). Er-High Ge, Sn-Er-Ge and Sb-Er-Ge doped silica fibres were fabricated specially for the purpose of exploiting their fluorescence properties caused by the amplified spontaneous emission due to the Er^{3+}-doping, added to enable the fibre to be used for sensing applications, at higher temperatures [182]. Type I and type IIA gratings fabricated in Er-High Ge doped fibre were studied and it was observed that they could be operated at more than 500 °C with significant values of reflectivity remaining. Sn-doping [157] or Sb-doping [168] enhances further the thermal stability of the gratings compared to other dopants studied. A chemical composition grating (CCG) written in a fluorine-doped fibre (supplied by ACERO, Sweden) has also shown its high temperature sustainability and thus it was also tested in this experiment. So, in this series of tests, the gratings written in B-Ge doped fibre were tested at temperatures up to 250°C, whereas the gratings written in Er-High Ge doped fibre were tested up to 500 °C. However, the gratings written in Sn-Er-Ge and Sb-Er-Ge doped fibres along with the CCG were operated up to ~ 850°C.

5.3.3. Annealing of the gratings

Temperature-induced reversible and irreversible changes in the Bragg wavelengths[181],[184] of the gratings were observed when the thermal decay of the gratings was analysed. For sensing purposes, to enable a reproducible sensor probe to be developed, the irreversible changes of the Bragg wavelength should be removed to achieve repeatable measurement data. These changes can be avoided by a well-defined process of annealing of the gratings, which stabilises them and allows only reversible changes in the Bragg wavelengths, resulting in a high level of repeatability over useful ranges of measurement for sensor applications. The gratings fabricated in B-Ge codoped fibre were annealed at 275 °C for 8 hours (to fit them for temperature measurement up to 250 °C; however, the maximum operational temperature, $T_{max} \leq 275°C$), whereas the gratings written in Ge-Er and Ge-Sn-Er codoped fibres were annealed for 8 hours at 525 °C (to fit them for a temperature range up to 500 °C; however, $T_{max} \leq 525°C$ in this case). Fig. 5.1 shows a typical type I grating transmission-spectrum measured before and after the annealing process, fabricated in a B-Ge codoped fibre. The blue-shift of the Bragg wavelength, λ_b, of 0.17 nm was observed after the full annealing process had been carried out on the grating. This corresponds to temperature measurement errors of ~ 15 °C and 19 °C at room temperature, using the linear and best polynomial regression respectively for the characteristics of this grating (this is discussed thoroughly in the next section). Even after annealing, the

reflectivities of all the gratings were high (more than 70 %) and thus well suited to most of the measurement needs envisaged.

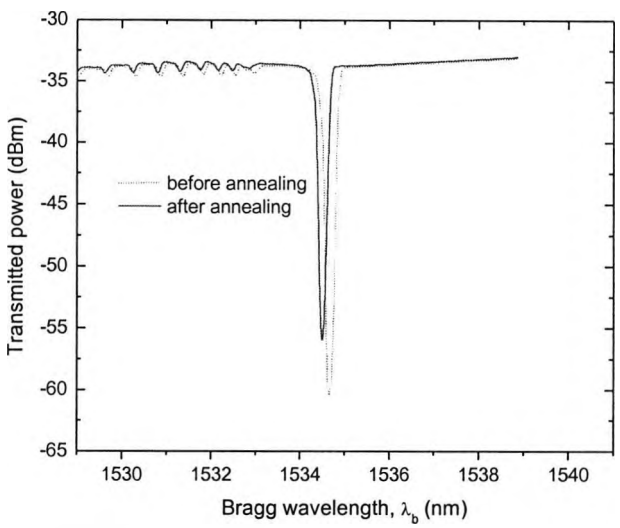

Fig. 5.1: A typical stabilised grating spectrum in transmission mode after the complete annealing process has been carried out (dotted line represents the grating spectrum before annealing).

5.4. Temperature measurement

Following the fabrication and full annealing of the gratings, the next stage in the study was to evaluate the temperature response of the gratings at elevated temperatures. To observe the thermal characteristics of the Bragg wavelengths of the gratings, the sample gratings were placed inside a well-characterised and calibrated CARBOLITE tube oven. The temperature of the oven was verified during the tests by placing a thermocouple in intimate contact with the FBG. All the gratings were tested separately so that the 'grating under test' could be carefully placed in the middle of the tube oven (the most stable region), avoiding any strain on the fibre. A broadband amplified spontaneous emission (ASE) source was used to provide light at an appropriate wavelength to the grating characteristic and the transmitted spectra of the gratings were measured by using the OSA, with a resolution bandwidth of 0.1 nm. For gratings fabricated in B-Ge doped fibre, the temperature was measured up to 250 °C, using 10 °C increments, and the other gratings written in Er-High Ge and Sn-Er-Ge doped fibres were tested up to 500 °C and 850°C, respectively, using increments of 20 °C. In other separate tests, the grating written in Sb-Er-Ge doped fibre and the CCG were operated up to ~ 850 °C, using incremental steps of 10°C and 50°C, respectively. A settling time of 15 minutes was allowed at each temperature to achieve a thermal equilibrium between the grating and the oven, before recording data for several cycles of both ascending and the descending temperatures.

5.4.1. Consideration of non-linear regression

The measured data for the ascending and the descending temperature cycles, in terms of the Bragg wavelength change with temperature for all the gratings tested, were observed to be quite consistent over a number of repeated measurements, with a wavelength uncertainty of ± 0.01 nm (the peak/dip resolution of the OSA used). The results, measured for all the gratings used, are plotted in Figs. 5.2(a)–5.8(a). The dotted lines on all the graphs represent the linear fit to the experimental data, whereas the solid lines represent the best higher order polynomial fit in each case. Taking into account the linear fit to experimentally measured data, the thermal sensitivity was observed to vary from 10.69 to 15.29 pm/°C for the seven different gratings (type I and IIA gratings in B-Ge and Er-High Ge doped fibres, type I gratings in Sn-Er-Ge and Sb-Er-Ge doped fibre and the CCG). The deviations of the linear regression from the actual experimental results can be observed in Figs. 5.2(b)-5.8(b) for each of these gratings, where the residual wavelengths from the linear and the polynomial fits are plotted separately over the temperature range considered. It can be observed for all the gratings that the deviation of the regression from the data is dependent on the measurement range and may be quite large (in both directions - positive and negative) in a parabolic fashion over the whole measurement range. The RMS deviation varies between 0.04 nm and 0.10 nm, on average, over temperatures of 250 °C and 500 °C respectively, which would lead to a significant error in the temperature calculation.

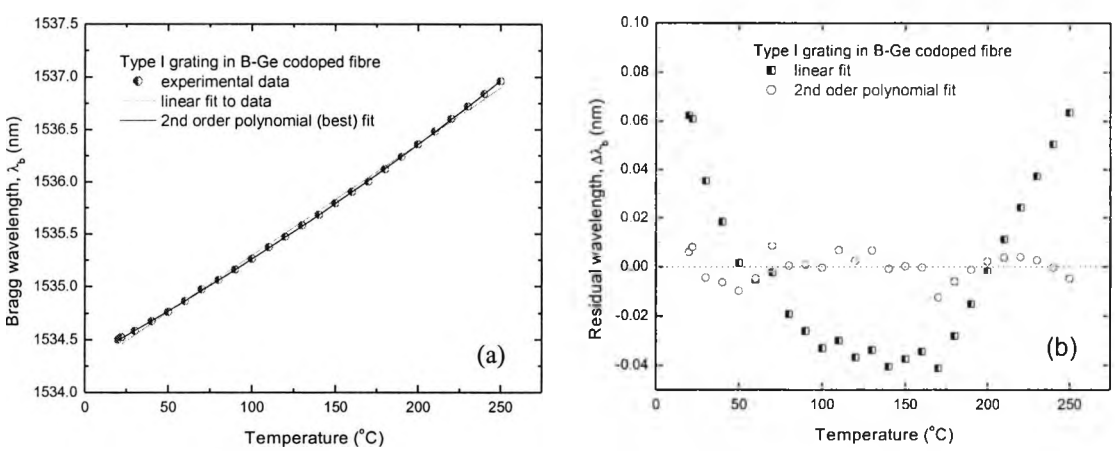

Figs. 5.2: Thermal response of a type I FBG written in B-Ge doped fibre and comparison between the linear and the best non-linear fittings (a), along with a plot of residual wavelengths (b).

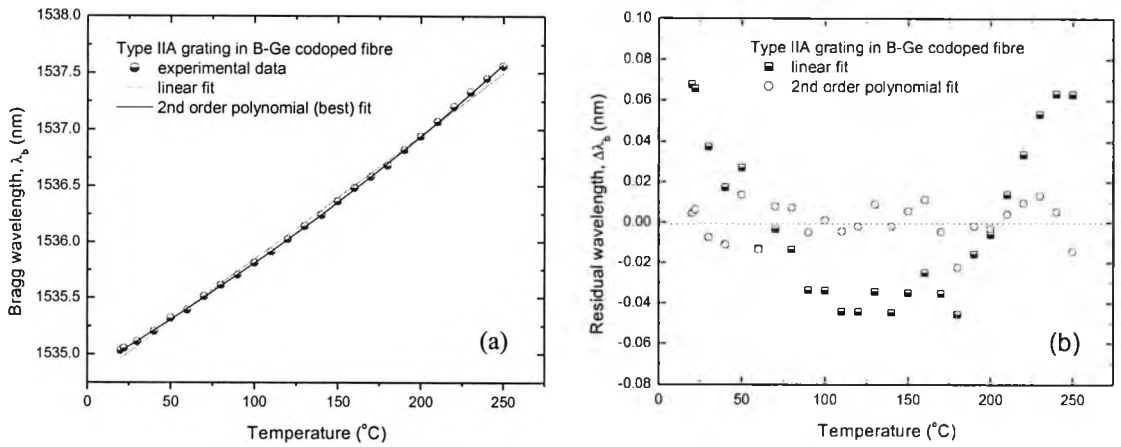

Figs. 5.3: Thermal response of a type IIA FBG written in B-Ge doped fibre and comparison between the linear and the best non-linear fittings (a), along with a plot of residual wavelengths (b).

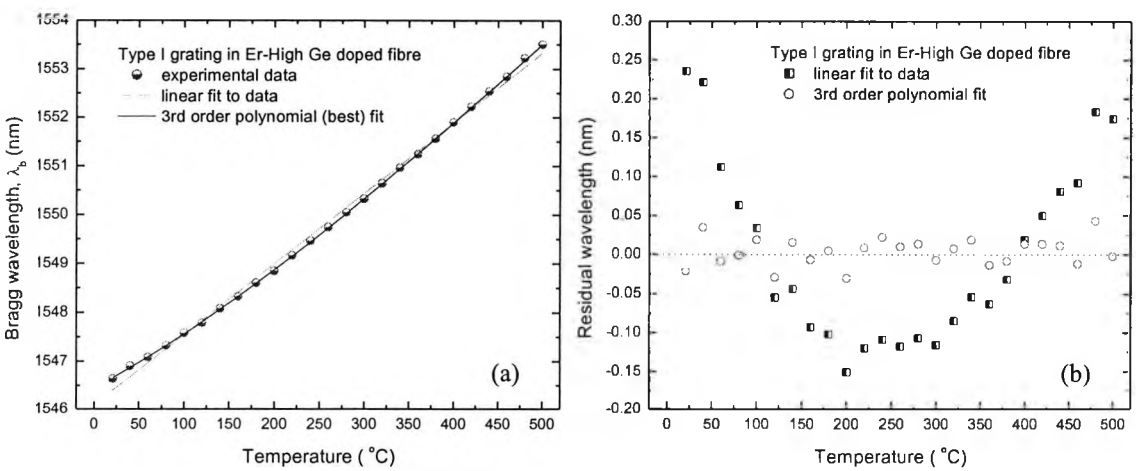

Figs. 5.4: Thermal response of a type I FBG written in Er-High Ge doped fibre and comparison between the linear and the best non-linear fittings (a), along with a plot of residual wavelengths (b).

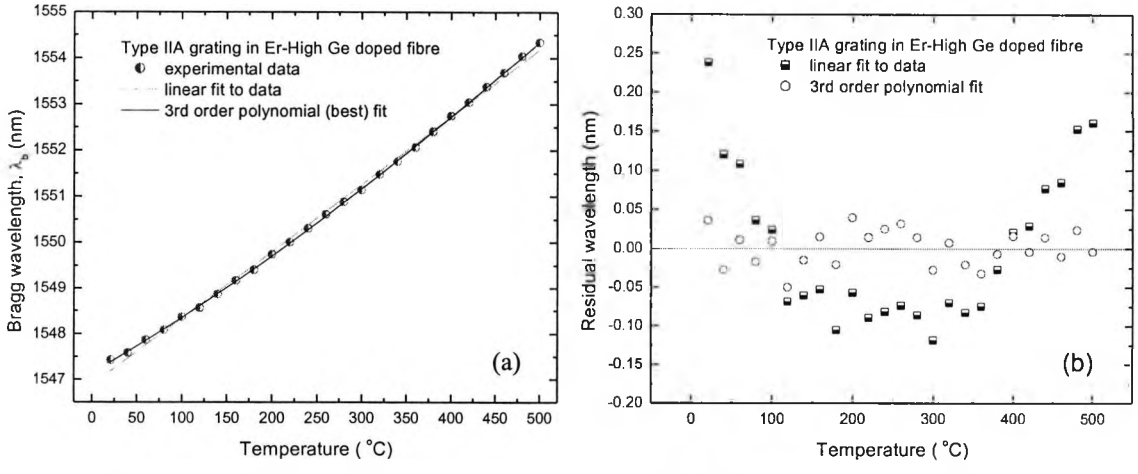

Figs. 5.5: Thermal response of a type IIA FBG written in Er-High Ge doped fibre and comparison between the linear and the best non-linear fittings (a), along with a plot of residual wavelengths (b).

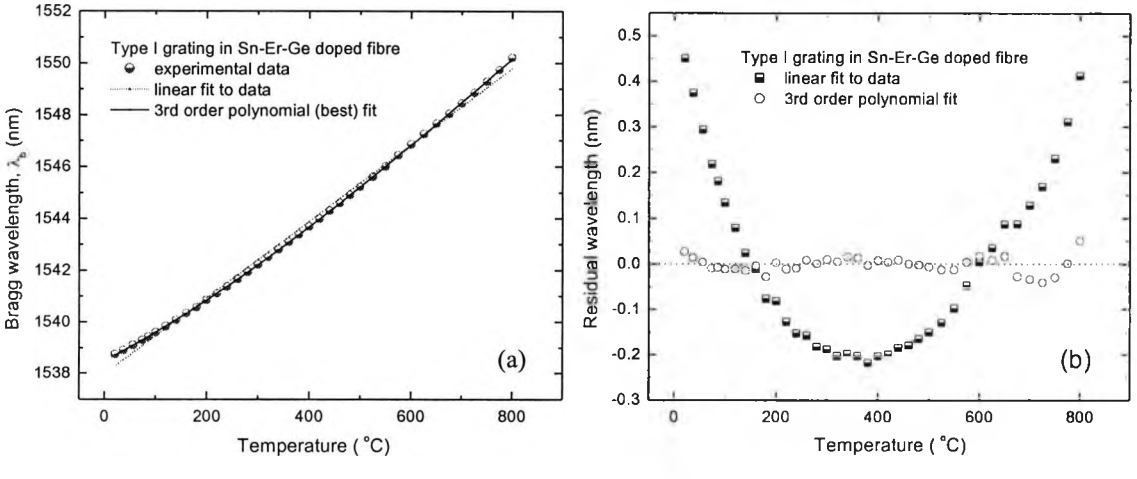

Figs. 5.6: Thermal response of a type I FBG written in Sn-Er-Ge doped fibre and comparison between the linear and the best non-linear fittings (a), along with a plot of residual wavelengths (b).

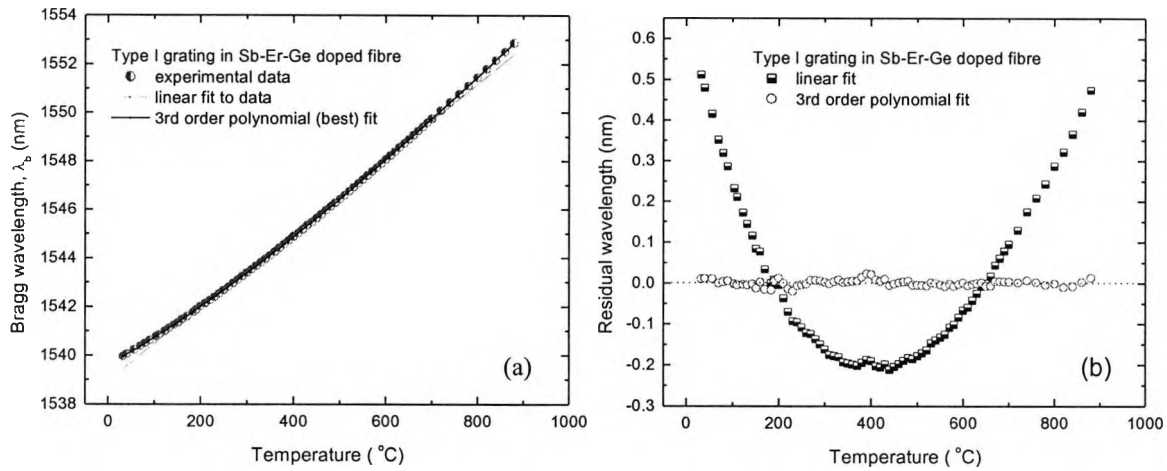

Figs. 5.7: Thermal response of a type I FBG written in Sb-Er-Ge doped fibre and comparison between the linear and the best non-linear fittings (a), along with a plot of residual wavelengths (b).

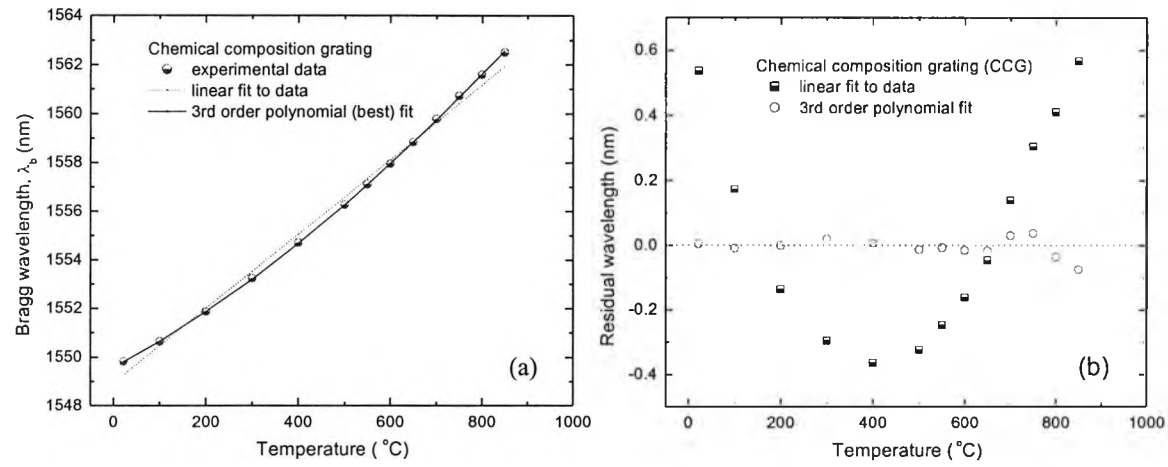

Figs. 5.8: Thermal response of a chemical composition grating (CCG) written in a fluorine doped fibre and comparison between the linear and the best non-linear fittings (a), along with a plot of residual wavelengths (b).

The thermal response of the Bragg wavelengths of the gratings can be described, using the linear regression, as

$$\begin{aligned}
\lambda_b &= 1534.22 + 0.01069\,T && \text{(type I FBG, B-Ge fibre)} \\
&= 1534.74 + 0.01102\,T && \text{(type IIA FBG, B-Ge fibre)} \\
&= 1546.10 + 0.01445\,T && \text{(type I FBG, Ge-Er fibre)} \\
&= 1546.88 + 0.01461\,T && \text{(type IIA FBG, Ge-Er fibre)} \\
&= 1537.98 + 0.01476\,T && \text{(type I FBG, Sn-Er-Ge fibre)} \\
&= 1538.95 + 0.01528\,T && \text{(type I FBG, Sb-Er-Ge fibre)} \\
&= 1548.94 + 0.01529\,T && \text{(CCG)}
\end{aligned} \quad \Big\} \; (5.5)$$

where λ_b is the corresponding Bragg wavelength for each grating at temperature, T °C. In all plots, the linear regression of the experimental data has been shown by the dotted lines.

The temperature response of the Bragg wavelengths for all the gratings studied, using the best polynomial regression, can be expressed as

$$\begin{aligned}
\lambda_b &= 1534.32 + 0.00865\,T + 7.7\times10^{-6}\,T^2 && \text{(type I FBG, B-Ge fibre)} \\
&= 1534.85 + 0.00876\,T + 8.6\times10^{-6}\,T^2 && \text{(type IIA FBG, B-Ge fibre)} \\
&= 1546.45 + 0.01005\,T + 1.2\times10^{-6}\,T^2 - 7.5\times10^{-9}\,T^3 && \text{(type I FBG, Ge-Er fibre)} \\
&= 1547.14 + 0.01126\,T + 8.5\times10^{-6}\,T^2 - 4.5\times10^{-9}\,T^3 && \text{(type IIA FBG, Ge-Er fibre)} \\
&= 1538.49 + 0.01035\,T + 7.7\times10^{-6}\,T^2 - 3.1\times10^{-9}\,T^3 && \text{(type I FBG, Sn-Er-Ge fibre)} \\
&= 1539.59 + 0.01059\,T + 7.4\times10^{-6}\,T^2 - 2.7\times10^{-9}\,T^3 && \text{(type I FBG, Sb-Er-Ge fibre)} \\
&= 1549.59 + 0.00987\,T + 7.9\times10^{-6}\,T^2 - 1.9\times10^{-9}\,T^3 && \text{(CCG)}
\end{aligned} \quad \Big\} \; (5.6)$$

where λ_b is the corresponding Bragg wavelength for each grating at temperature, T °C. The best polynomial regression corresponding to each set of the experimental data has been displayed by solid lines in the plots. When compared to the linear regression, the best polynomial fit (2^{nd} order polynomial fit for gratings written in B-Ge codoped fibre and the 3^{rd} order polynomial for other gratings written in Ge-Er and Sn-Er-Ge doped fibre, including the CCG) was considered in each case and showed very good results with a much smaller deviations from the measured experimental data throughout the whole range of the measurement.

In light of the above set of equations (5.6), the RMS deviations from the data were always observed to be less than 0.02 nm for all the gratings studied, resulting in a RMS temperature error of less than 2 °C over the whole measurement range, for temperatures from room temperature to ~ 850 °C. Such a figure would be acceptable for many temperature calculations. Table-5.1 shows the details of the results of a comparison between the linear and the best polynomial fits to the data, for all the gratings studied.

Table-5.1: The detailed results of the thermal response of the FBGs studied in this experiment.

Parameters	FBGs written in fibres						
	B-Ge doped		Ge-Er doped		Sn-Er-Ge	Sb-Er-Ge	CCG
	type I	type IIA	type I	type IIA	type I	type I	
λ_b (nm) of the annealed grating at room temperature (~ 22 °C)	1534.51	1535.04	1546.64	1547.42	1538.74	1539.85	1549.81
Reflectivity at room Temperature (22 °C)	0.80	0.85	0.81	0.82	0.80	0.80	0.40
Range of temperature Measurement (°C)	20–250	20–250	21–500	21–500	21–850	30–850	21–850
Best polynomial fit for regression	2^{nd}	2^{nd}	3^{rd}	3^{rd}	3^{rd}	3^{rd}	3^{rd}
Temperature sensitivity considering linear fit (pm/°C)	10.69	11.02	14.45	14.61	14.76	15.28	15.29
Temperature sensitivity considering the best polynomial fit (pm/°C)	8.99 12.53 - -	9.14 13.06 - -	10.56 14.59 16.30 -	11.63 14.67 16.41 -	10.67 13.70 15.79 16.84	10.90 13.81 16.03 17.38	10.22 (22°C) 13.50 (250°C) 16.42 (500°C) 19.02 (800°C)
RMS error in the measurement with linear fit (nm)	0.035	0.039	0.109	0.096	0.194	0.201	0.298
RMS error in the measurement with the best fit (nm)	0.005	0.008	0.018	0.022	0.018	0.008	0.025
RMS error in the temperature with linear fit (°C)	3.27	3.54	7.54	6.57	13.14	13.15	19.49
RMS error in the temperature with the best fit (°C)*	0.55	0.87	1.70	1.89	1.69	0.76	2.53
Thermo-optic coefficient, ξ, $\times 10^{-6}$ (/°C)	5.47 7.76 - -	5.56 8.10 - -	6.44 9.03 10.10 -	7.13 9.07 10.17 -	6.54 8.46 9.83 10.47	6.75 8.56 9.98 10.81	6.20 (22°C) 8.29 (250°C) 10.16 (500°C) 11.79 (800°C)

* Calculation has been done by considering the thermal sensitivities of the gratings at room temperature.

5.4.2. Thermal sensitivity of the gratings

Considering the best polynomial fit and from the derivatives of Eq. (5.6), the thermal sensitivities of the gratings were observed to be temperature dependent and found lie over the range from 8.99 to 11.63 pm/°C at room temperature (22 °C), for seven different gratings studied. The corresponding temperature sensitivities at a temperature of 250 °C lay in the range from 12.53 to 14.67 pm/°C for the above gratings, resulting in an increase from the room temperature values of between 26 and 43 %. With further increase of temperature, the gratings those survived have shown further higher values of thermal sensitivity; however, the percentage increments of the values of their thermal sensitivity were found to be comparatively less at higher temperatures. The temperature-dependent thermal sensitivity for type I and type IIA gratings written in B-Ge and Er-Ge doped fibres studied with temperature has been illustrated in Fig. 5.9, whereas the thermal sensitivity of type I gratings written in Sn-Er-Ge and Sb-Er-Ge doped fibre along with the CCG has been shown in Fig. 5.10.

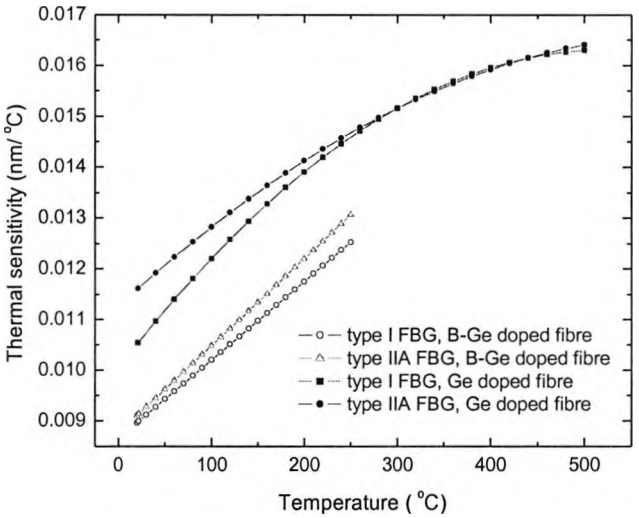

Fig. 5.9: Variation of the thermal sensitivity values of type I and type IIA gratings written in B-Ge and Er-High Ge doped fibres.

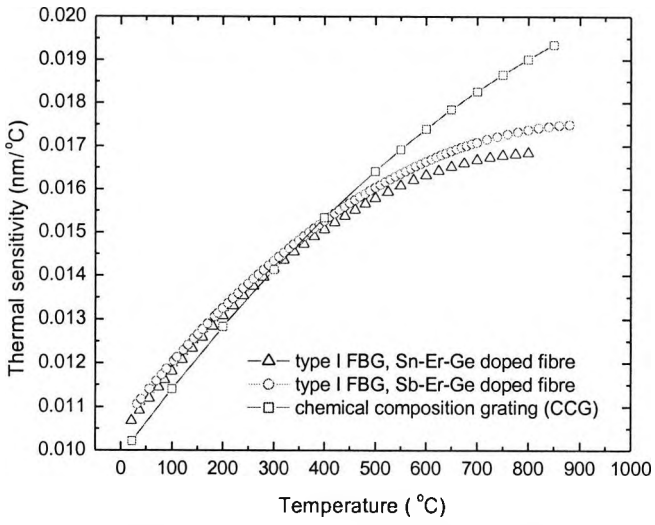

Fig. 5.10: Variation of the values of the thermal sensitivity of various gratings (type I FBG written in Sn-Er-Ge and Sb-Er-Ge doped fibre along with a CCG) over a wide range of studied temperatures.

It can be clearly seen from the Fig. 5.9 that not only are the thermal sensitivities different, but also the slope of the thermal sensitivities changes for type I and IIA gratings written in the same fibre. This effect could potentially be exploited in its application to the simultaneous and precise measurement of strain and temperature or a strain-independent temperature measurement, using various types of gratings written in the same fibre. Fig. 5.10 illustrates that the ranges of variation of the thermal sensitivity values of these three gratings are different within the same range of temperatures studied. This plot shows that variation-range of this sensitivity value is the largest in case of the CCG, whereas that of the grating written in Sn-Er-Ge doped fibre shows the smallest variation over the same range of measurement. The thermo-optic coefficient, ξ, can also be estimated from the derivatives of Eq. (5.6), assuming the thermal expansion coefficient for silica fibres, α (= 0.5×10^{-6}/°C), is constant, it being one order smaller than that of ξ.

5.5. Discussion

On the basis of the detailed results shown above with a comparative study between the linear and non-linear fittings of the experimentally measured data, the non-linear thermal response of the fibre Bragg gratings may be established.

5.5.1. Non-linear thermal response of thermo-optic coefficient: theoretical support

The non-linear temperature response of the thermo-optic coefficients obtained for several standard optical glasses [103] and silicate glasses [194] has been observed and studied by Ghosh. The basis of the model for standard optical glasses lies in the measurements of the thermo-optic coefficient and the thermal expansion coefficient of the material, for which silica is one of the main host materials. The model developed by Ghosh is based on the temperature

dependence of the excitonic band gap, an isentropic band gap and the thermal expansion coefficient of the material. Considering the thermo-optic coefficient of the material to be dependent on both the electronic transitions and the phononic transitions, the parameter can be described as

$$2n(dn/dT) = (n_0^2-1)[-3\alpha R-(1/E_{eg})(dE_{eg}/dT)R^2] \quad (5.7)$$

where n_0 is the value of the low-frequency refractive index (corresponding to the infra-red wavelength region), α is the thermal expansion coefficient, E_{eg} is the excitonic band gap and R is the normalised dispersive wavelength, which can be defined by

$$R = \lambda^2/(\lambda^2-\lambda_{ig}^2) \quad (5.8)$$

with λ_{ig} is the wavelength corresponding to the isentropic band gap, E_{ig}. The isentropic band gap has been found to be unaffected with the changes in temperature [195], whereas the excitonic band gap decreases with temperature. It is clear from Eq. (5.7) that the thermo-optic coefficient is controlled by two terms. The first parameter describes the contribution from the thermal expansion coefficient, α, and the second parameter can be described by the contribution from the temperature dependence of the excitonic band gap, $(1/E_{eg})(dE_{eg}/dT)$. The contribution from the first term, $[-3\alpha R(n_0^2-1)]$, is negative because α is positive for silica-based optical materials and the contribution is small as the value of α is of the order of 10^{-6}/°C. However, the temperature variation of E_{eg} is of the order of 10^{-4}/°C and is normally negative for the glasses [195]. Thus, the contribution from the second term, $[-(1/E_{eg})(dE_{eg}/dT)(n_0^2-1)R^2]$, is positive and this dominant term results in a positive value of the thermo-optic coefficient. Analysing the experimental data of the refractive indices of some standard glass materials, Ghosh has calculated the temperature dependence of the excitonic band gap, E_{eg}. He observed a non-linear response, with linearly decreasing values of dE_{eg}/dT with the increase of temperature, over a temperature range of 25–115°C. This model supports the quadratic behaviour of the FBGs for their thermal response. Based on the above model, Flockhart *et al.* [101] verified the quadratic behaviour of the fibre Bragg grating temperature coefficients over the range of temperatures from –30 °C to +80 °C. However, the above analysis within a limited range of temperature is based on a limited number of experimental data, which may not be adequate to explain the thermal response of the gratings over a wide range of temperatures. In that case, the values of dE_{eg}/dT may be fitted accurately with a second order function of temperature, instead of linear. This may be a possible explanation of the 3rd order (best) polynomial regression of the grating thermal responses studied over a wider temperature range (up to ~ 850°C, from room temperature), in this work.

5.5.2. Measurement precision

Measurement precision plays a very important role in the analysis of experimentally measured data, which has been described in detail in the previous sections. The precision of the

temperature measurement in this work seems to be determined by the central Bragg wavelengths of the gratings, as measured by the OSA. Although the measurements have been made with the 0.1 nm resolution bandwidth available from the OSA, the resolution available in the determination of peak/dip wavelength is 0.01 nm. Considering the typical FWHM bandwidth of the grating spectra to be around 0.3 nm, the centre wavelength of the Bragg wavelength can be determined with a resolution that is slightly lower. For both the type IIA gratings, the residual values, when considering the best polynomial regression, were higher comparatively than those of other type I gratings, as shown in Figs. 5.2(b) – 5.5(b), this being caused by the uncertainty in the measurement produced from the larger FWHM bandwidth (~ 0.6 nm) of the type IIA gratings. In this work, the RMS deviation of the best polynomial regression from the data has also been observed with a value which is less than or comparable to 0.02 nm, this being of the same order as the value of the resolution, and showing an acceptable level of precision. More precise measurements can be made possible by using an OSA having a better resolution or by including a high-resolution signal processing unit [10],[196]. Also, in this work, for the study of thermal response of pre-annealed gratings, the bending effect (due to the thermal expansion of the fibre) has not been considered. With the increase of temperature, no spectral deformation of the FBG was observed and thus the strain developed due to the fibre-bending has been neglected.

5.6. Summary

Temperature measurements have been made by using a series of FBGs written in a range of fibres and detailed data on their characteristics are presented. The data are fitted to polynomials that may be used in the calculation of temperature measurements with these types of gratings where the temperature is determined from the polynomial algorithms presented. Issues of precision in such measurements up to ~ 850 °C have been considered using a set of gratings, taking into account the non-linear temperature response of the fibre Bragg gratings, which were studied. Results were verified with several gratings of type I and IIA written in five different photosensitive fibres. Comparison between the linear and the higher order polynomial regressions showed a better performance was achieved for temperature measurement applications when the non-linear temperature coefficients are considered, yielding an acceptable RMS error of less than or comparable to 0.02 nm in terms of wavelength, over the whole measurement range. This corresponds to a RMS error in temperature typically of the range of 0.5 – 2.5 °C (considering the thermal sensitivity of the gratings at room temperature, which leads to the maximum error), which is more acceptable compared to the linear fittings with the RMS error of the range of 3.3 – 19.5 °C for various gratings studied, over the largest temperature excursion studied.

Chapter 6

Simultaneous measurement of wide range temperature and strain using FBGs

6.1. Abstract

An optical fibre based sensing scheme for the simultaneous measurement of a wide range of both strain (to 2000 με) and temperatures (to 600°C) has been investigated by combining the properties of the fibre Bragg grating (FBG) and the fluorescence from a rare-earth-doped photosensitive fibre. The temperature-dependent fluorescence peak power ratio (FPPR) of the two peaks occurring around 1535 nm and 1552 nm from the amplified spontaneous emission due to the $^4I_{13/2} \leftrightarrow {}^4I_{15/2}$ transitions in Er^{3+}-doped fibres, with 980 nm pumping and the dual functionality of the FBG written into the fibre were exploited in this scheme. Sn-Er-Ge and Sb-Er-Ge doped specially fabricated fibres were used in this scheme for two separate sets of experiments. The sensor is based on a single FBG written in a small length (~10 cm) of the above fibres. Simultaneous measurement of strain and temperature over ranges of 0–1150 με and 22–500 °C, with rms errors of 36 με and 6 °C respectively, can be measured for Sn-Er-Ge doped fibre. The operational range may be enhanced by using Sb-Er-Ge doped fibre, over ranges of 0–2000 με strain and 20–600 °C temperature, with rms errors of 36 με and 2.8 °C. A simple and effective scheme for strain-independent temperature measurement has also been demonstrated using the peak wavelengths of both type I and type IIA FBGs written in the same fibre (Er-High Ge doped fibre), which is also capable of monitoring strain and temperature simultaneously.

6.2. Previous work on this subject

6.2.1. Introduction and background of the work

Fibre Bragg gratings (FBGs) have generated considerable interest in recent years because of their potential for use in sensor applications [1]-[3],[6],[10],[11] such as structural integrity, oil-well monitoring and aerospace engineering, in addition to conventional and well known communications applications. Reliable, accurate, and simultaneous measurement of strain and temperature, and both strain-independent temperature measurements and temperature-independent strain measurements, by using FBGs are of significant interest for various

applications for the above-mentioned industries. Improved measurements of these parameters are very important for such industrial uses to achieve enhanced safety and reliability, and lower cost. However, for the measurement of parameters such as strain or temperature, both measurands produce a convoluted shift of the Bragg wavelength due to the inherent property of the FBGs, thus creating a possible error or ambiguity in any measurement of each of these parameters individually. This results in an unwanted cross-sensitivity, which creates several complications in grating-based sensing schemes for the measurement of both parameters simultaneously. In order to separate these two quantities and obtain a simultaneous measurement, an additional source of information is required to enable the individual effects on the FBG used to be identified.

To overcome the problem of cross sensitivity and the ambiguity in the measurement, researchers have proposed and investigated several techniques. These approaches include the dual-wavelength superimposed FBGs [111], spliced FBGs in different fibres [112], a single FBG inscribed in the spliced region of two different fibres [118], a hybrid FBG-long period grating [114], an FBG written in a rare earth doped fibre [116],[117],[197],[198] in combination with the fluorescence intensity ratio technique [197],[199], FBGs superimposed with polarisation-rocking filters [200], a fibre Bragg grating Fabry-Perot cavity structure [201], a sampled fibre Bragg grating based on a long period structure [124], a combination of a fibre Bragg grating and a Brillouin scattering interrogation system [202] and different types of gratings written in separate sections of a fibre, with and without hydrogenation [125]. However, in most cases, the limit of the temperature measurement is up to ~150 °C.

6.2.2. Simultaneous measurement of strain and temperature by writing a single FBG at the splicing joint of different fibres

Prior to discuss about a new scheme for the simultaneous measurement of strain and temperature, in this section, a similar measurement has been carried out by writing a single grating at the splicing joint of two different photosensitive fibres using the conventional matrix inversion technique. A boron-germanium doped and an erbium-high germanium doped fibres were used for this experiment and an UV-induced single grating was fabricated through the phase-mask technique at the spliced region of these two different photosensitive fibres. The length of the fabricated grating was ~ 6.5 mm, resulting in virtually two grating dips/peaks corresponding to the different values of the effective refractive index of the two fibres used. Fig 6.1 shows the structure of the grating-sensor used for this experiment, whereas the transmission spectrum of the sensor is shown in Fig. 6.2. In order to achieve a stable performance, the grating-sensor was annealed at 150°C for around 10 hours before being used for the measurement up to that temperature.

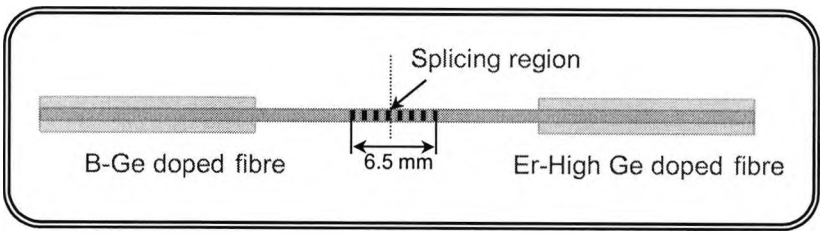

Fig. 6.1: Structure of the grating-sensor written in the splicing joint of two different fibres

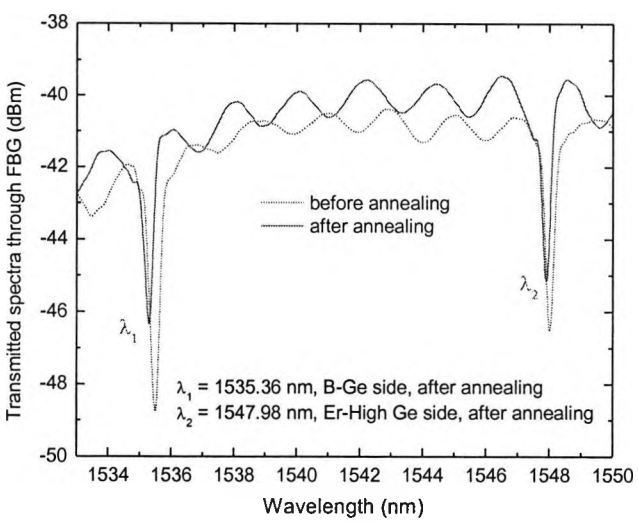

Fig. 6.2: Transmission spectrum of the grating-sensor, before and after annealing at 150°C for ~ 10 hours.

Assuming the strain and temperature response of the grating is essentially independent (i.e., the corresponding strain-temperature cross-term remains negligibly small), a single measurement of the Bragg wavelength shift from a perturbed grating can be written as

$$\Delta\lambda(\varepsilon,T) = k_T\Delta T + k_\varepsilon\Delta\varepsilon \qquad (6.1)$$

where the temperature coefficient, $k_T = \partial\lambda/\partial T$, can be determined by the thermal expansion and the thermo-optic coefficient of the fibre and the strain coefficient, $k_\varepsilon = \partial\lambda/\partial\varepsilon$, is related to the Poisson's ratio of the fibre, the photo-elastic coefficient, and the effective refractive index of the fibre-core. Thus, the shifts in two Bragg wavelengths of the grating-sensor perturbed by the changes in temperature and strain can be expressed in the form of a matrix structure as it is expressed in Eq. (2.23) (replacing the variable $\Delta\varphi_i$ by $\Delta\lambda_i$). The induced temperature and strain can be determined by the matrix inversion technique, in a similar fashion as described in Eq. (2.24).

As the two fibres used in this experiment are of same diameter, the strain-response of the Bragg wavelengths are expected to be almost same. However, the Bragg wavelengths of the grating-sensor would exhibit different temperature-response, as the compositions of the core of the two fibre materials are different. Once the matrix elements can be determined from Eq. (2.23) by independent measurements of the Bragg wavelengths of the grating-sensor corresponding to the known values of the applied strain and temperatures, the unknown values of these parameters can be determined by the matrix-inversion technique, as expressed in Eq. (2.24). The validity of this approach lies in different coefficient values for temperature and strain and in the non-zero determinant of the matrix coefficients, i.e., $(k_{1T}k_{2\varepsilon}-k_{2T}k_{1\varepsilon}) \neq 0$.

In this work, the centre Bragg wavelengths of the two gratings were observed to be at 1535.36 nm (boron-germanium doped fibre side of the splicing) and at 1547.98 nm (erbium-high germanium doped fibre side) after the appropriate annealing (as discussed in Chapter 5 in section 5.3.3) of the sample, as shown in Fig 6.2. The reflectivity values were found to be more than 60% for both of the gratings after the annealing. Temperature and strain response of the grating-sensor was measured separately in order to determine the matrix elements (i.e., strain and temperature coefficients of the grating-portions of the sensor corresponding to different fibres). The temperature response was measured by placing the sensor inside a well-calibrated tube oven without any axial strain and controlling the temperature up to 150°C starting from room temperature. Fig. 6.3 shows the temperature response of the grating-sensor at zero axial strain applied on it. The strain response of the sensor was measured up to 1600με at room temperature (22°C) by using a micrometer-driven stage and this response has been shown in Fig. 6.4. The temperature was kept constant throughout the whole range of strain measurement in order to avoid errors arising from the variation of temperatures. A broadband ASE-based light source was used to illuminate the grating-sensor and the shift of the Bragg wavelengths was measured by using a HP86140A (Agilent) OSA.

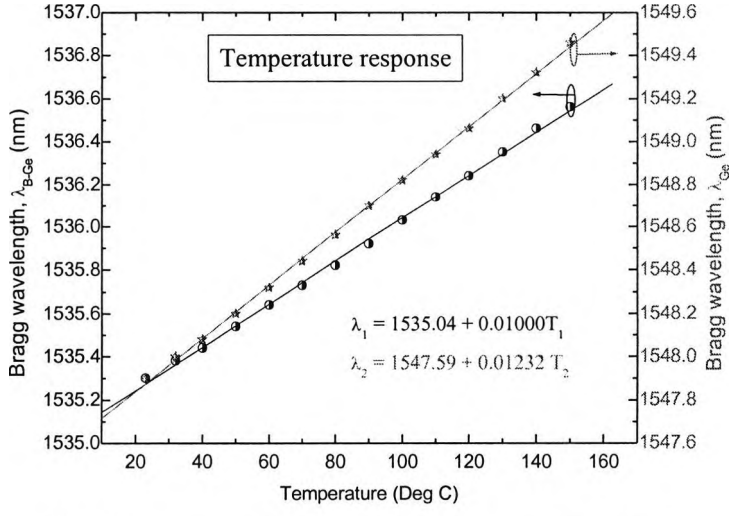

Fig. 6.3: Temperature response of the grating-sensor.

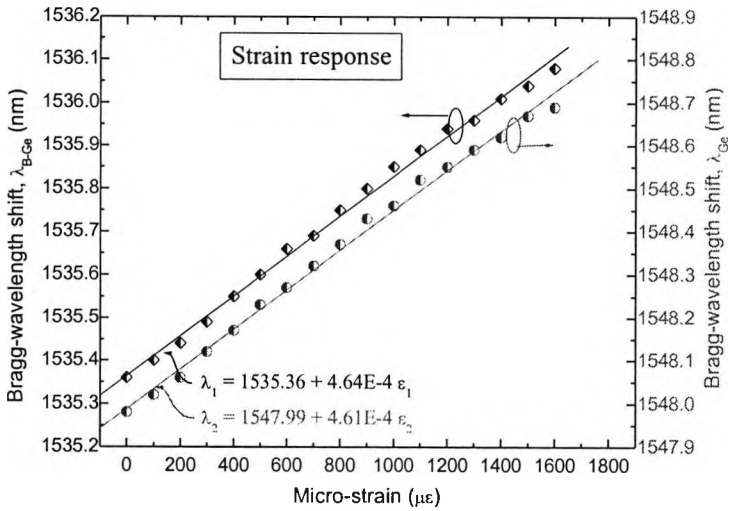

Fig. 6.4: Strain response of the grating-sensor.

Temperature and strain coefficients of the matrix elements can be determined from the linear regressions of the experimental data measured individually for these parameters, as shown in Figs. 6.3 and 6.4. The values of these coefficients, in this work, were found to be

$$\left.\begin{aligned} k_{1T} &= 10.00\ \text{pm/°C} \\ k_{2T} &= 12.32\ \text{pm/°C} \\ k_{1\varepsilon} &= 0.464\ \text{pm/με} \\ k_{2\varepsilon} &= 0.461\ \text{pm/με} \end{aligned}\right\} \quad (6.2)$$

Using the above values of temperature and strain coefficients in Eq. (2.24), the unknown values of temperature and strain can be estimated from the Bragg wavelength shift of the grating-sensor. In this work, the individual errors for temperature and strain measurement can be estimated by [3],[6]

$$\left.\begin{aligned} |\delta T| &= |\delta\lambda_1/k_{1T}|,\ |\delta\lambda_2/k_{2T}| \Rightarrow (0.8 - 1.0)\ °C \\ |\delta\varepsilon| &= |\delta\lambda_1/k_{1\varepsilon}|,\ |\delta\lambda_2/k_{2\varepsilon}| \Rightarrow (21.5 - 21.7)\ \mu\varepsilon \end{aligned}\right\} \quad (6.3)$$

These errors were estimated mainly from the limited resolution of the OSA used in this experiment. However, the combined errors for the simultaneous measurement of these parameters would be estimated by [6],[127]

$$\left.\begin{aligned} |\delta T| &\le (|k_{2\varepsilon}||\delta\lambda_1| + |k_{1\varepsilon}||\delta\lambda_2|)/(|k_{1T}k_{2\varepsilon} - k_{2T}k_{1\varepsilon}|) \Rightarrow 8.34°C \\ |\delta\varepsilon| &\le (|k_{2T}||\delta\lambda_1| + |k_{1T}||\delta\lambda_2|)/(|k_{1T}k_{2\varepsilon} - k_{2T}k_{1\varepsilon}|) \Rightarrow 201\ \mu\varepsilon \end{aligned}\right\} \quad (6.4)$$

6.2.3. Importance and limitations of the conventional technique

The conventional matrix inversion technique for simultaneous measurement of strain and temperature is much more convenient to use, as the matrix elements (i.e., strain and temperature coefficients) can easily be determined through separate and independent strain and temperature measurements. Once the values of the matrix elements are known, the absolute values of the unknown parameters can easily be determined for the simultaneous measurement scheme. In addition, relative ease of grating fabrication process makes the scheme more popular for several inter-disciplinary applications.

However, in most of the work reported, the range of temperature measurement is limited to around 150°C, which may not be sufficient for some high-temperature sensing applications. Also, the matrix inversion technique has been adopted in most cases in the system calibration to determine the strain and temperature coefficients, thereby assuming a linear thermal response of the gratings, which may not be appropriate when used over the wider range of temperatures recently reported [203]. The thermal response of the gratings may be considered as a linear fitting approximation [175] because of the simplicity in the calibration, which results in a reasonable level of deviation from the measured data. However, in a practical instrument, this could lead to a larger than acceptable deviation in the measured parameters, particularly for the simultaneous measurement of strain and temperature, as the thermal response of the Bragg wavelength of the gratings has been found to be non-linear [101],[102],[193], in research recently carried out by ourselves and others. This deviation in the temperature value will result in an approximately ten times greater impact on the strain parameter than the temperature measurement, leading to a lower precision in the strain determination in instrumentation designed using this approach.

6.2.4. New approach proposed: principle of operation

In this section, a novel sensing scheme is proposed, which is capable of measuring strain and temperature simultaneously over a wide range of temperatures, and based on the temperature-dependence of the fluorescence peak power ratio (FPPR) of the amplified spontaneous emission (ASE) in rare-earth-doped fibre and the dual functionality of the FBG. A single FBG fabricated at one end of a length of erbium-doped tin-germanosilicate fibre [190] and erbium-antimony-germanium doped silica fibre [204] are used as they offer a very wide range of measurement due to the high temperature sustainability of the FBG in these specialist erbium-doped fibres. Previous research by some of the authors [197],[205],[206] has indicated that the fluorescence intensity ratio [187],[197],[205]-[207] scheme is essentially strain-insensitive. However, in this work, a measurement of strain was important and so the desired strain measurement was obtained by monitoring the Bragg wavelength shift of the FBG, from which the temperature effect was removed in the data processing.

Er^{3+}-doped fibre has been used for laser and amplifier studies in the wavelength region around 1.5 μm, due to the occurrence of the $^4I_{13/2} \leftrightarrow {}^4I_{15/2}$ (ground state) transition. In this work, attention is focused on the transitions from two Stark levels [13],[14], having peaks around wavelengths of 1535 nm and 1552 nm, which were observed when a 980 nm pumping was used. Imai *et al.* [187] have also reported these two peaks with 1480 nm pumping and the FPPR approach was used for temperature measurement over a limited range between –50 °C and 90 °C. In this work, the temperature-dependence of the ratio of the intensities at these two wavelengths (i.e. the FPPR) was investigated over a much wider range of temperatures, and used for the measurement of strain and temperature simultaneously.

As both the $^4I_{13/2}$ and $^4I_{15/2}$ levels are really a comb of Stark sub-levels [208] and populated to various extent depending on the Boltzmann thermal distribution, the spectral shape of the ASE consists of two peaks, in general, at wavelengths around 1535 nm and 1552 nm, the exact wavelengths depending on the various glass hosts [13],[14]. The fluorescence intensities at these wavelengths are found to be temperature-dependent. The above phenomenon was exploited for temperature measurement in this scheme.

For the simultaneous measurement of strain and temperature, using the FPPR characteristics of the ASE in Er-doped fibre and the wavelength shift of the FBG fabricated in that fibre, the parameters required can be determined by the following equations:

$$R = f_1(T) \tag{6.5}$$

$$\Delta\lambda_b = f_2(\varepsilon) + f_3(T) \tag{6.6}$$

where R is the FPPR of the ASE power (obtained by dividing the intensities of the two peak wavelengths i.e., $R = I_{1535nm}/I_{1552nm}$) at temperature, T, and $\Delta\lambda_b$ is the shift in the Bragg wavelength arising from the effect of the combined applied strain and temperature change. In the curve-fitting analyses carried out, the temperature-dependent functions in the above equations, f_1 and f_3 were considered to be non-linear to achieve better measurement precision, whereas the strain-dependent function, f_2, was found to be linear over the whole range of measurement.

6.3. Wide range temperature and strain measurement using grating written in an Sn-Er-Ge doped fibre

Based on the above operational principle, a new scheme for simultaneous measurement of wide range temperature (to 500°C) and strain (to 1150 με) has been demonstrated in this section by writing a single grating at one end of a length of erbium-doped tin-germanosilicate fibre.

6.3.1. Fluorescence of the specially fabricated Sn-Er-Ge doped fibre

Prior to the work undertaken here, this Sn-Er-Ge doped fibre (specification is given in Table-3.2) was designed and fabricated by MCVD method at the University of Nice, France (details are given in Section 4.4.1 in Chapter 4). Small amount of aluminium was introduced to confine the erbium doping within the fibre-core to improve the pumping efficiency [13].[14] of the fibre without any clustering effect that may happen.

Amplified spontaneous emission (ASE) in the wavelength region around 1540 nm has been observed in Er^{3+}-doped fibre due to the $^4I_{13/2} \rightarrow {}^4I_{15/2}$ transitions. Fig. 6.5(a) shows the corresponding schematic diagram of the absorption and emission transitions among the relevant energy levels of the ions, when pumped at 980 nm. The $^4I_{15/2} \rightarrow {}^4I_{11/2}$ transitions occur for the absorption band in Er^{3+}-doped by using a pump-source at a wavelength of 980 nm. The populated $^4I_{11/2}$ level results in an immediate non-radiative phonon transition through the $^4I_{11/2} \rightarrow {}^4I_{13/2}$ transition to reach the metastable state, which subsequently creates the $^4I_{13/2} \rightarrow {}^4I_{15/2}$ transition, resulting in the generation of ASE in the region of the 1540 nm wavelength. The fluorescence intensities at these wavelengths are found to be temperature-dependent and this is exploited for temperature measurement in this scheme. A typical ASE spectrum from Er^{3+}-doped tin-germanosilicate fibre of length of ~ 10 cm, measured at room temperature (~ 22°C), is represented in Fig. 6.5(b).

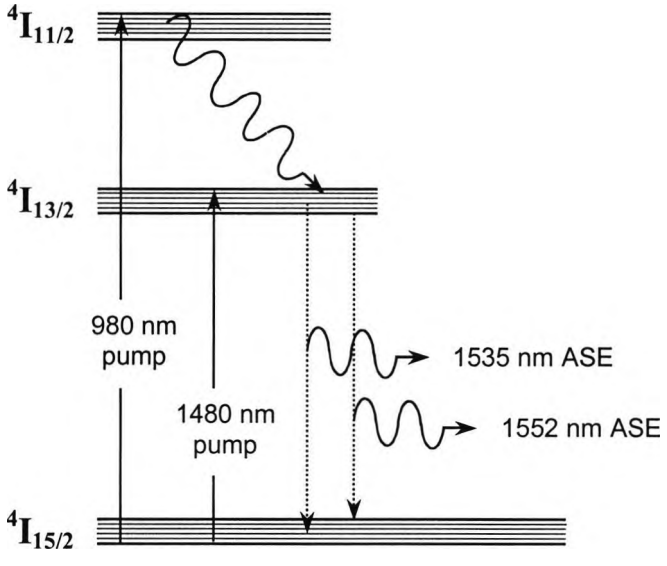

Fig. 6.5(a): Energy diagram of the relevant energy levels of Er^{3+}-doped silica fibre showing the absorption and emission transitions under pumping at the wavelengths of 980 nm and 1480 nm.

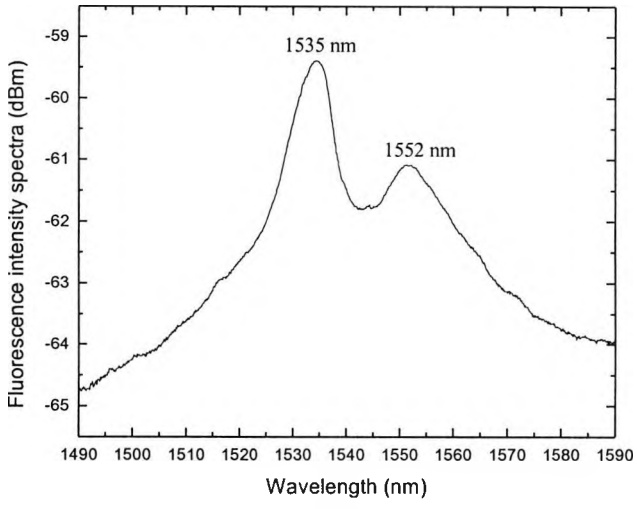

Fig. 6.5(b): Fluorescence spectrum of a 10 cm long Er^{3+}-doped tin-germanosilicate fibre observed using an OSA at room temperature (~22°C) with 980 nm pumping. Clearly observable fluorescence peaks were seen at the wavelengths of 1535 nm and 1552 nm, associated with the $^4I_{13/2} \rightarrow {}^4I_{15/2}$ transitions.

6.3.2. Experimental arrangements

A schematic diagram of the experimental set-up used for the simultaneous measurement of strain and temperature is shown in Fig. 6.6. A single FBG of length of ~ 6.5 mm was fabricated (using the phase-mask technique with a 248 nm KrF excimer laser) at one end of a 10 cm long Er^{3+}-doped tin-germanosilicate fibre with a reflectivity of ~ 90%. The estimated value of the refractive index modulation (Δn_{mod}) of the fibre-core was approximately 1.74×10^{-5} for this grating. The sample was annealed at 550 °C for 24 hours to wipe out the unstable portion of the FBG so that the sample could be used for sensing with better repeatability. The Bragg wavelength of the FBG was observed to be 1538.74 nm (at room temperature, ~22 °C) measured by the OSA (the best possible peak/dip wavelength resolution of 0.01 nm could be achieved with resolution bandwidth of 0.1 nm) after the annealing was completed. The Bragg resonance wavelength of the FBG is being within the fluorescence region of the sample. For simultaneous measurement of the strain and temperature, the sample was placed carefully in a tube-oven and at either side of the sample it was fixed with adhesive (Quick set epoxy, by mixing equal amount of resin and hardener for one minute and then curing for 24 hours) to two micrometer-driven translation stages. Before fixing the fibre, acrylic-coated jacket of the fibre was stripped off carefully covering the whole length within these two fixed glued points (40 cm, in our experiment). Care was taken to place the active portion of the fibre (an Sn-Er-Ge doped fibre of length of 10 cm including the written FBG) in the most thermally stable zone in the oven. The ASE power of the sample was generated by pumping at 980 nm (the pump power of 18 mW was held constant during the measurement) and the spectra obtained were monitored by using a HP86140A optical spectrum analyser (OSA).

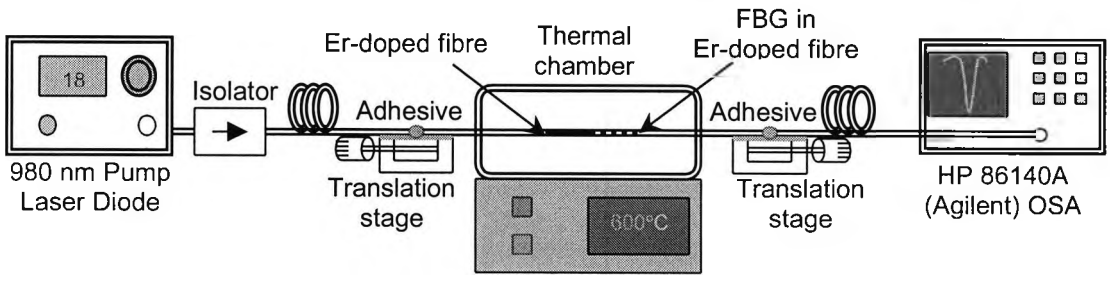

Fig. 6.6: Experimental set-up for simultaneous measurement of strain and temperature.

6.3.3. Simultaneous measurement of strain and temperature

With the experimental set-up discussed in the previous section, strain and temperature were measured independently and simultaneously. Firstly, the sensor was placed carefully inside the tube oven without imposing any strain on it and the thermal response of the sample was recorded in terms of the fibre-fluorescence characteristics and the Bragg wavelength shift. A series of ASE power spectra was observed with the variation of temperatures from 22 °C to 500 °C, using excitation from a 980 nm laser diode. Fig. 6.7 illustrates the ASE power spectra of the sensor-prototype for several distinct temperatures of 22 °C, 100 °C, 300 °C and 400 °C under zero axial strain, measured by the OSA with resolution bandwidth of 1 nm. A clear shift of the "dip" in the spectra indicates the shift in the Bragg wavelength of the FBG due to the temperature variation. From the ASE power spectra at various temperatures, two distinct peaks corresponding to wavelengths of 1535 nm and 1552 nm were observed. The intensities of these two peaks (both peak wavelengths were unchanged throughout the whole range of temperature measurement) were used to estimate the FPPR for use in the temperature determination.

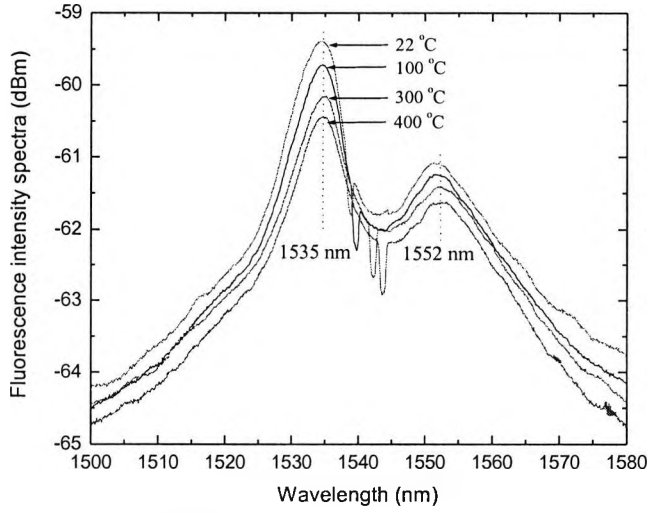

Fig. 6.7: ASE spectra obtained at various specific temperatures. The shift of the 'dip' in the spectra indicates the shift in the Bragg wavelength of the grating with the increase of temperature.

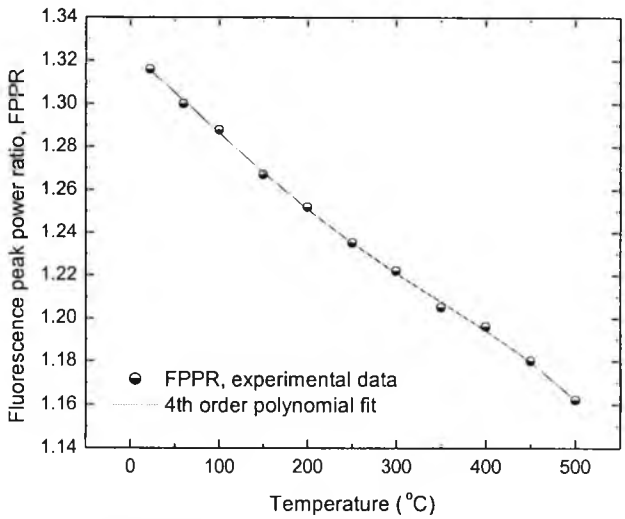

Fig. 6.8: Variation of FPPR with temperature (22-500)°C. The solid line is the best fitted 4th order polynomial regression to the experimental data. The error-bars are smaller than the data points.

Fig. 6.8 shows the variation of the temperature-dependent FPPR (I_{1535nm}/I_{1552nm}) under zero axial strain along with the best fitted 4th order polynomial regression (coefficient of determination, R^2 = 0.9993 and standard deviation, σ = 0.0017) to the experimental data obtained. In this work, Eq. (6.5) can be expressed as:

$$R = 1.323 - 3.362\times10^{-4}\,T - 5.093\times10^{-7}\,T^2 + 2.515\times10^{-9}\,T^3 - 2.877\times10^{-12}\,T^4. \qquad (6.7)$$

At the same stage of experiment, the thermal response of the FBG under zero strain was recorded by measuring the Bragg wavelength shift of the grating at various applied temperatures. The shift of the Bragg wavelength with temperature under zero strain is shown in Fig. 6.9 together with a 3rd order polynomial that produced the best fit (R^2 = 0.9998, σ = 0.0347), given by:

$$\lambda_b = 1538.473 + 0.01044\,T + 7.33\times10^{-6}\,T^2 - 2.30\times10^{-9}\,T^3. \qquad (6.8)$$

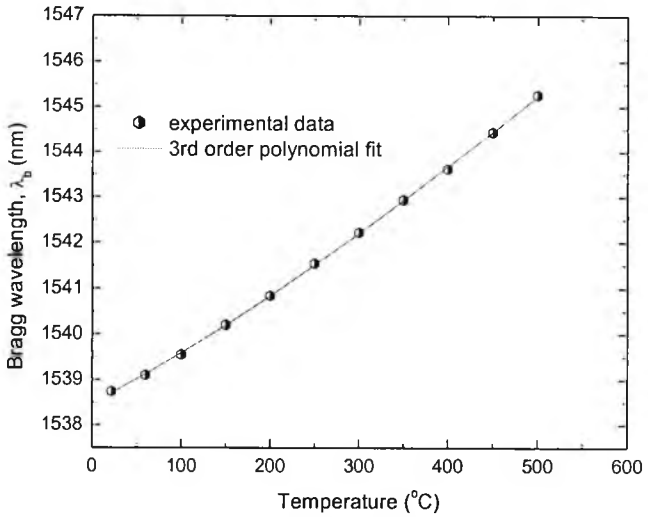

Fig. 6.9: Bragg wavelength shift of the FBG with temperature (22-500)°C. The solid line is the best fitted 3rd order polynomial regression to the experimental data. The error-bars are smaller than the data points.

In this case, consideration of the non-linearity of the thermal sensitivity [101],[102],[193] of the Bragg wavelength (λ_b) in the FBG over a wide range of temperature (22 °C to 500 °C) showed a better correlation to the data when compared to the linear-fitting, where the temperature-sensitivity of the FBG at 500 °C (16.04 pm/°C) was found to be 49% higher than that at 22 °C (10.76 pm/°C).

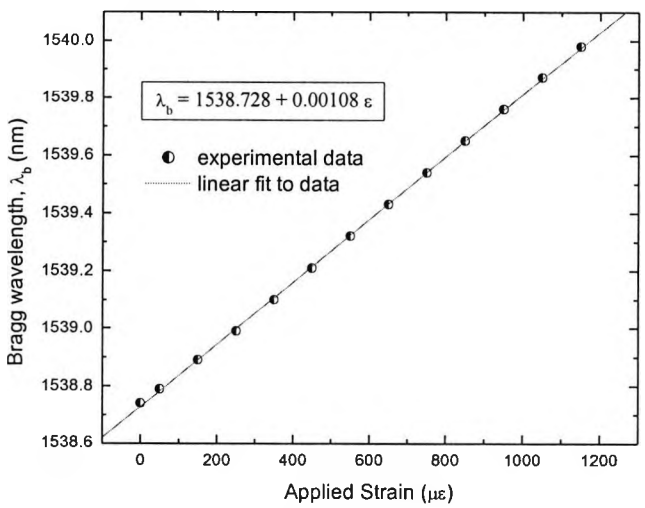

Fig. 6.10: Strain response of the FBG in terms of λ_b-shift, measured at 22°C. The solid line is linear fit to data. Error bars are smaller than the data points.

At the next stage, the strain-response of the grating was measured and the temperature of the oven was kept constant (22°C) to avoid error arising from the Bragg wavelength shift due to the variation of temperatures. Fig. 6.10 shows the Bragg wavelength shift with applied strain at room temperature (22°C) over a range from 0-1150 με. The temperature-independent strain-sensitivity determined from the above graph (1.08 pm/με) can be evaluated from Eq. (6.9) (giving a linear fit to the experimental data with $R^2 = 0.9998$ and $\sigma = 0.0063$) as:

$$\lambda_b = 1538.728 + 0.00108\,\varepsilon \quad \text{(at 22 °C)} \tag{6.9}$$

6.3.4. Effect of strain and temperature upon the grating cross-sensitivities

Further tests were carried out to observe the effect of strain on the FPPR at various temperatures and to measure the temperature effect on the strain-sensitivity of the FBG. For this purpose, the temperature of the oven was changed during the measurement process and at the same time various levels of strain were applied at each particular temperature. Figs. 6.11 and 6.12 show the graphs of the FPPR with the variation of the strain in the fibre, for several sets of temperatures and the strain-sensitivity at various temperatures, respectively. From the two plots below, it was confirmed that the FPPR was strain-insensitive and the FBG strain sensitivity was independent of any significant temperature variation.

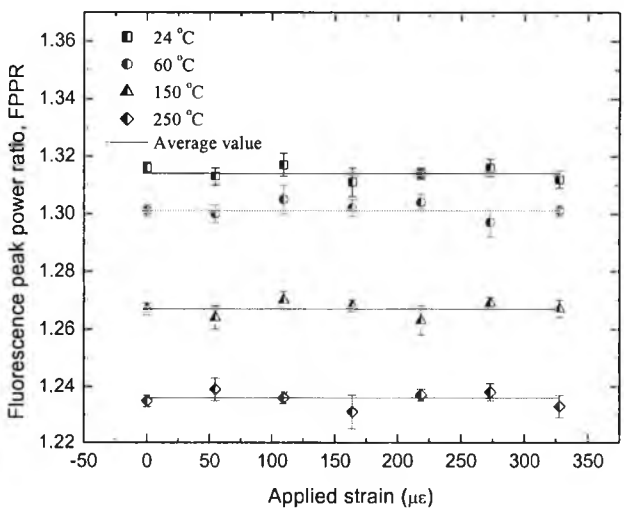

Fig. 6.11: The values of the fluorescence peak power ratio (FPPR) at various sets of temperatures (24°C, 60°C, 150°C and 250°C) under the applied strain, to measure the strain-effect on FPPR.

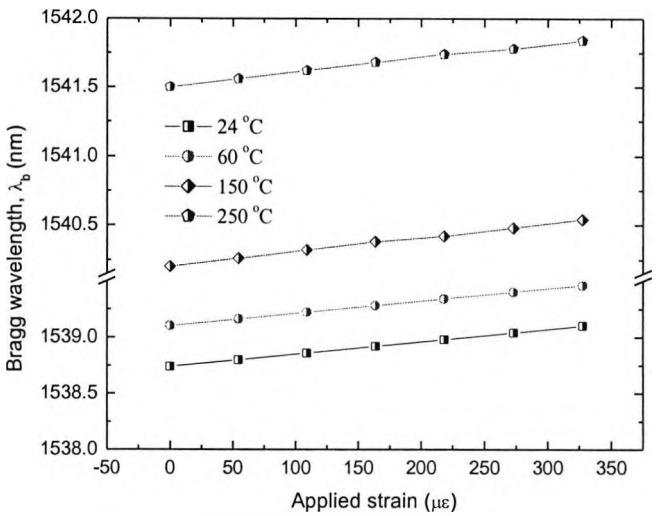

Fig. 6.12: Bragg wavelength shift versus the applied strain at various sets of temperature (24 °C, 60 °C, 150 °C and 250 °C) to observe the temperature-effect on strain-sensitivity. The error bars are smaller than the data points.

6.3.5. Cross-verification of result

A comparison between the measured values of the strain and temperature using the above model and the applied values, using a thermocouple and micrometers, has been made and shown in Fig. 6.13. The test was carried out when the strain and temperature were simultaneously and randomly applied over the whole measurement range of temperature and strain. The rms errors of strain and temperature in this initial work were 36 με and 6 °C over ranges of 0-1150 με and 22-500 °C, respectively. The measurement precision of the system depends on the FPPR dynamic range for both parameters of temperature and strain, and that for the strain measurement is limited mainly by the resolution of the OSA. A higher precision would be expected through improvements to the detection system or by using different special fibre with broader FPPR dynamic-range over the whole range of measurement.

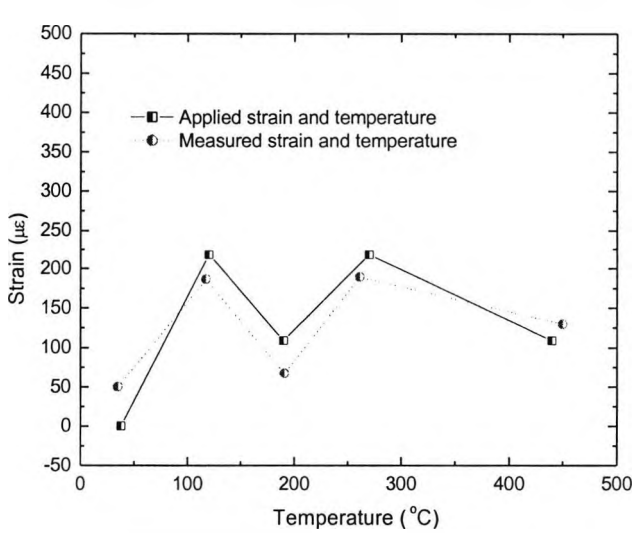

Fig. 6.13: Comparison between applied and measured strain and temperature, when both were varied simultaneously.

The above analysis has been used to measure strain and temperature simultaneously using a simple ASE-based fluorescence and Bragg grating-based approach over a wide temperature range, up to 500 °C. The overall precision of the system is determined by the temperature measurement and thus the parameter, which can be deduced using Eq. (6.7). The sensitivity of this parameter (I_{1535nm}/I_{1552nm}) was observed to be approximately 3.35×10^{-4} /°C (on average over the measured temperature range). The Bragg wavelength corresponding to that temperature was then calculated using Eq. (6.8), and subtracted from the overall Bragg wavelength shift to give the strain-induced Bragg wavelength shift. Finally the actual strain applied was obtained by using Eq. (6.9).

6.4. Enhanced range of measurement by writing grating in an Sb-Er-Ge doped fibre

In the previous section, an approach to the simultaneous measurement of strain (up to 1150 με) and a wide range of temperature (up to 500°C) using a grating written in an Sn-Er doped germanosilicate fibre, has been demonstrated. The approach was based on the temperature-dependence of the fluorescence peak power ratio (FPPR) of the amplified spontaneous emission (ASE) in the fibre and the dual functionality of the FBG to respond to both strain and temperature. This section demonstrates a further extension of the previous research using the same technique. A uniform grating with high reflectivity, written at one end of a 10 cm long erbium-doped antimony-germanosilicate (Sb-Er-Ge doped silica) fibre has been shown capable of being used for the simultaneous measurement of much wider ranges of temperature (up to 600°C) and strain (up to 2000 με). It is very interesting to note that the sensor enables the measurement of strain of more than 2000 με *without any breakage* to the fibre, even when heated to the maximum temperature in this study of 600°C, thus giving a wide range simultaneous measurement of both parameters.

6.4.1. Better fluorescence of the specially fabricated Sb-Er-Ge doped fibre

For the work discussed here, a special antimony-erbium-germanium (Sb-Er-Ge) doped silica fibre (specification is given in Table-3.2) was fabricated in China using the modified chemical vapour deposition (MCVD) technique. The choice of the element 'Sb' for inclusion in the fibre doping is based on the electronic charge effect of the outer shell electrons in the atom, arising from the large Sb^{3+} ion size of 76 pm (with the view that larger sizes of doping ions may effectively stabilise the performance of the material concerned) [204]. In addition, Er^{3+}-doping has been chosen in the fibre for lasing and optical amplification in the wavelength region around 1.5 μm, due to the occurrence of the $^4I_{13/2} \leftrightarrow {}^4I_{15/2}$ (ground state) transition with appropriate excitation source. In a similar way, attention has been focused on two peak wavelengths around 1535 nm and 1552 nm, as discussed in the previous section. Imai *et al.* [187] have also reported

an analysis using these two peaks with a 1480 nm pumping and a similar approach for temperature measurement over a limited range between –50 °C and 90 °C, using a 9 m long erbium-doped (968 ppm) fibre, to achieve a reasonable device-sensitivity. In this work, the temperature-dependence of the ratio of the intensities at these two wavelengths (i.e. the FPPR) was investigated over a much wider range of temperatures, and used in the sensor scheme for the simultaneous measurement of strain and temperature.

As this specially fabricated fibre was introduced with higher level of erbium-ion doping compared to that of the Sn-Er-Ge doped fibre, it is expected that this fibre would create a better fluorescence. Prior to undertaking a series of tests, an experiment was carried out with Sb-Er-Ge doped and Sn-Er-Ge doped fibres of identical length, to compare the fluorescence spectra using pumping sources at both 980 nm and 1480 nm. The transitions occurred by 980 nm and 1480 nm pumping sources are almost similar, only with an extra non-radiative transition for the excitation at the wavelength of 980 nm, which has been illustrated in Fig. 6.5(a). In case of using a pump-source at 1480 nm wavelength, the absorption and the generation of ASE are based upon $^4I_{13/2} \leftrightarrow {}^4I_{15/2}$ transitions without any other phononic transitions between the energy levels. A typical ASE spectrum from the specially fabricated Sb-Er-Ge doped silica fibre of length ~ 10 cm, in comparison to that from an Sn-Er-doped germanosilicate fibre of the same length, by using a fixed power of the pump-source of 980 nm, measured at room temperature (~ 20°C), is shown in Fig. 6.14(a). Fig. 6.14(b) displays the fluorescence spectra of the above-mentioned two fibres of the same length of ~15 cm, using a fixed power from the 1480 nm pump-source at room temperature [204]. As a result of the comparison of the performance of the different fibres in combination with the different exciting sources, the most suitable fibre with Sb-Er-Ge doping using the pumping source of 980 nm has been chosen for the further tests.

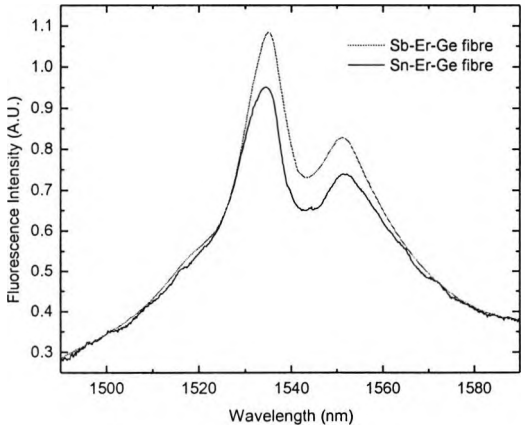

Fig. 6.14(a): Fluorescence spectra of ~10 cm long Sb-Er-Ge and Sn-Er-Ge doped fibre at room temperature, pumped by a 980 nm laser diode with optical power of 18 mW.

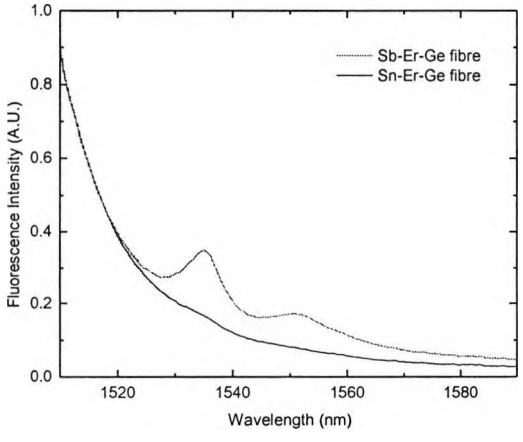

Fig. 6.14(b): Fluorescence spectra of ~15 cm long Sb-Er-Ge and Sn-Er-Ge doped fibre at room temperature, pumped by a 1480 nm laser diode with a fixed optical power of 50 mW.

6.4.2. Simultaneous strain and temperature measurement over an enhanced dynamic range

Prior to the actual measurement of the parameters, the range of the measurements has been optimised. For this, a series of gratings of length of ~ 6.5 mm, in Sb-Er-Ge doped fibre with the maximum achievable reflectivity (> 99%) was fabricated, using the phase-mask technique, with light from a 248 nm KrF excimer laser. The fabricated gratings were annealed inside a tube-oven separately at different fixed temperatures from 100 °C to 700 °C. Fig. 6.15(a) describes the isothermal decay of the normalised reflectivities of the gratings with time, which showed that the gratings were almost completely stabilised after an annealing time of 6-7 hours. It may be noted that the grating annealed at 700 °C was found to have stabilised with ~ 50 % of its initial reflectivity. However, that grating could not be used in this experiment because of the difficulty in distinguishing the grating 'dip' in the fluorescence spectrum of the ASE of the fibre and the possibility of deterioration of the mechanical strength of the grating in the fibre after it was annealed at such a high temperature. So, for this work, a grating was fabricated (using above-mentioned method) at one end of a 10 cm long Sb-Er-Ge doped fibre with the maximum achievable reflectivity of ~ 99.7% for which the estimated value of the refractive index modulation (Δn_{mod}) of the fibre-core was approximately 3.9×10^{-4}. The sample was annealed at 600°C for ~ 8 hours to remove the unstable portion of the FBG to achieve better repeatability in the sensing experiments with the detectable grating-dip in the ASE of the fluorescence. Fig. 6.15(b) represents the grating spectra at different times and temperatures during the process of annealing. This plot clearly explains the decay of the grating reflectivity, when the oven-temperature was increased to 600°C from room temperature (grating was moved in after the oven-temperature was settled) and the blue-shift of the Bragg wavelength along with the decay of reflectivity, when the grating was kept at that fixed temperature for 8 hours. Finally, the temperature of the oven was decreased slowly down to room temperature (20°C) and the reflectivity and the Bragg wavelength of the stabled grating was measured. The Bragg wavelength of the annealed FBG was observed to be 1541.55 nm (at room temperature, ~20 °C) with a reflectivity value of around 67%, measured by using the optical spectrum analyser (the best possible peak/dip wavelength resolution of 0.01 nm could be achieved with resolution bandwidth of 0.1 nm) after the annealing was completed, this being within the fluorescence region of the sample.

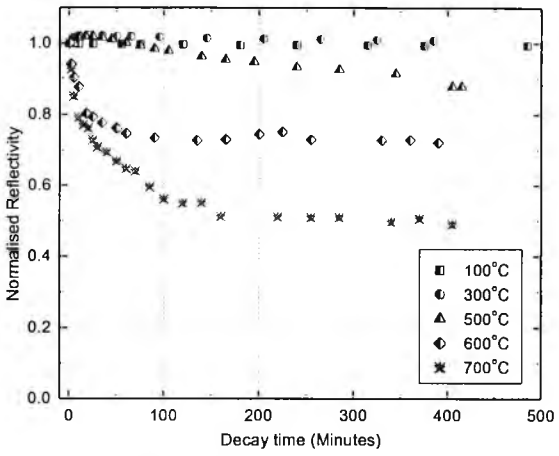

Fig. 6.15(a): Isothermal decay of the gratings written in Sb-Er-Ge doped fibre with time, at various temperatures.

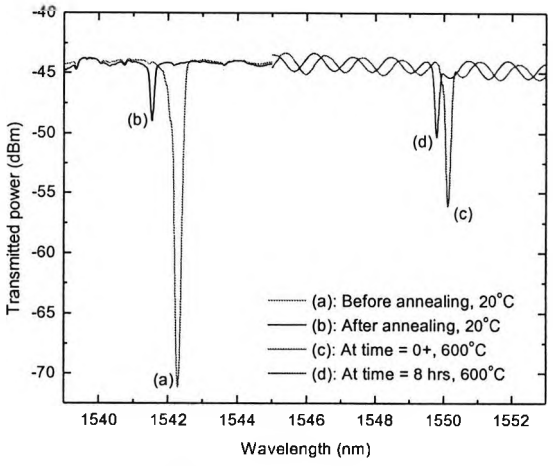

Fig. 6.15(b): Grating spectra at different times and temperatures during the process of annealing.

For the simultaneous measurement of the strain and temperature, the sample was placed carefully in a tube-oven and it was fixed on either side with adhesive, to two micrometer-driven translation stages, as illustrated by Fig. 6.6, demonstrated earlier. The ASE power of the sample was generated by pumping at 980 nm (the pump power of 18 mW was held constant during the measurement) and the spectra obtained were monitored by using a HP86142A optical spectrum analyser (OSA). A series of ASE power spectra was observed with the variation of temperatures from 20 °C to 600 °C, using excitation from the 980 nm laser diode. Fig. 6.16 illustrates the ASE power spectra of the sensor-prototype for several distinct temperatures of 20 °C, 100°C, 300°C, 400°C and 600 °C under zero axial strain, measured by using the OSA with a resolution bandwidth of 1 nm. A clear shift of the 'dip' in the spectra indicates the shift in the Bragg wavelength of the FBG due to the temperature variation. It is worthwhile to mention that although the reflectivity of the pre-annealed grating used in this scheme was ~ 67%, the "depth" of the grating dip was not observed to be very significant in the fluorescence spectra, as shown in Fig. 6.16. The ASE-based fibre-fluorescence is believed to be responsible to some extent to compensate the grating-depth (transmission dip in the spectra). From the ASE power spectra at various temperatures, two distinct peaks corresponding to wavelengths of 1535 nm and 1552 nm were observed. The intensities of these two peaks (both peak wavelengths were unchanged throughout the whole range of temperature measurement) were used to estimate the FPPR, in a similar way as previously demonstrated, for use in the temperature determination. From tests carried out earlier (for Sn-Er-Ge doped fibre) [182], it was confirmed that the FPPR was strain-insensitive and the FBG strain sensitivity was independent of temperature, which simplifies the signal processing technique required.

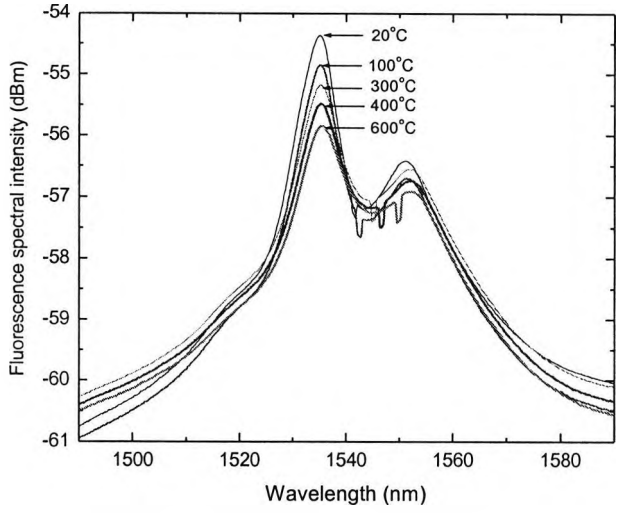

Fig. 6.16: ASE-based fluorescence spectra of the sensor at various temperatures starting from room temperature to 600°C. The 'dip' indicates the Bragg wavelength of the grating written into the fibre.

Fig. 6.17 shows the variation of the temperature-dependent FPPR under zero axial strain along with a fit to a 3rd order polynomial regression (with a coefficient of determination, R^2 = 0.9991 and a standard deviation, σ = 0.0062) to the experimental data obtained. In this work, Eq. (6.5) can be expressed as:

$$R = 1.705 - 1.92\times10^{-3}\,T + 3.57\times10^{-6}\,T^2 - 2.64\times10^{-9}\,T^3. \qquad (6.10)$$

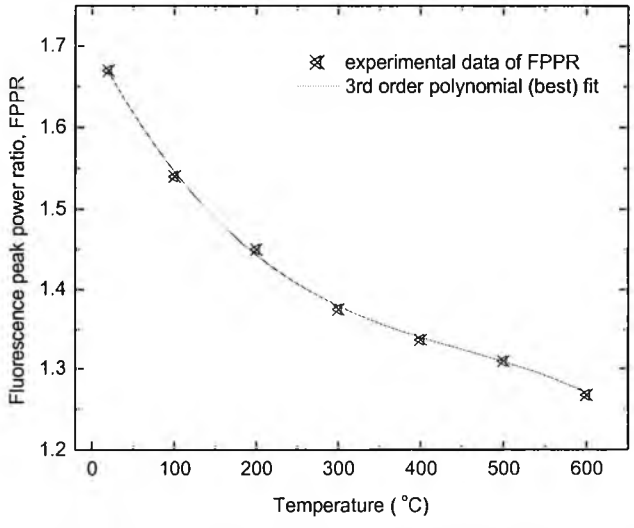

Fig. 6.17: Variation of FPPR with temperature over the range of 20-600°C. The solid line is the third order polynomial fit to the experimental data. The error-bars are smaller than the data points.

The shift of the Bragg wavelength with temperature under zero strain is shown in Fig. 6.18 together with a 3rd order polynomial that produced the best fit (R^2 = 0.9999, σ = 0.0107), and this is given by:

$$\lambda_b = 1541.33 + 0.01027\ T + 9.06\times10^{-6}\ T^2 - 4.43\times10^{-9}\ T^3. \quad (6.11)$$

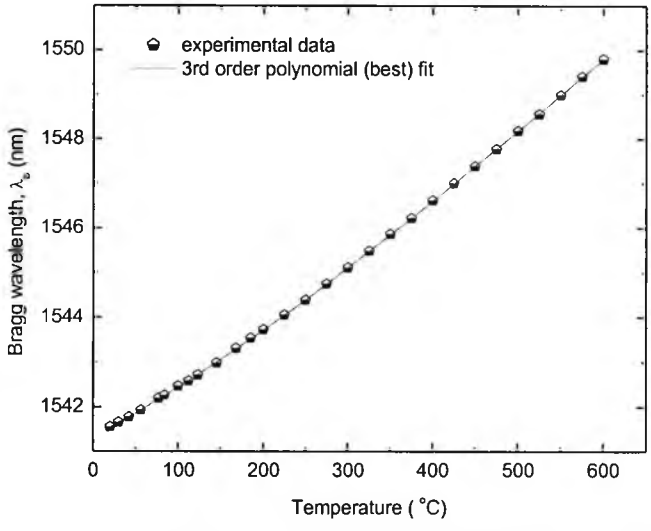

Fig. 6.18: Bragg wavelength shift of the grating with the applied temperature over a wide range of 20-600°C under zero axial strain. The solid curve represents the 3rd order polynomial (best) fit to the experimental data. The error-bars are smaller than the data points.

In this case, consideration of the non-linearity of the thermal sensitivity [101],[102],[193] of the Bragg wavelength (λ_b) in the FBG over a wide range of temperature (20°C to 600°C) revealed a better correlation to the data when compared to that achieved with a linear-fitting.

Fig. 6.19 shows the Bragg wavelength shift with applied strain at room temperature (20°C) over a range from 0 to 2000 $\mu\varepsilon$. The temperature was kept constant throughout the whole range of strain measurement in order to avoid any error arising from the variation of temperatures. The temperature-independent strain-sensitivity (1.15 pm/$\mu\varepsilon$) can be evaluated from Eq. (6.12) (giving a linear fit to the experimental data with R^2 = 0.9996 and σ = 0.0142) as:

$$\lambda_b = 1541.51 + 0.00115\ \varepsilon \ \text{(at 20°C)} \quad (6.12)$$

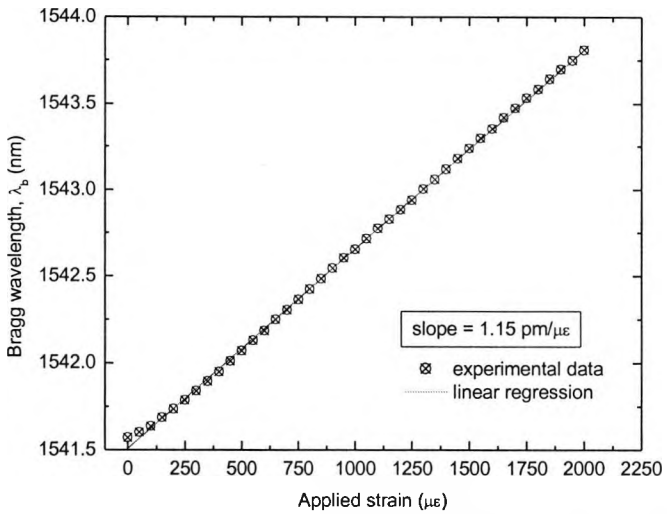

Fig. 6.19: Bragg wavelength shift of the grating sensor with the applied strain over a wide range of 0-2000με at room temperature (20°C). The solid line is the linear fit to data. The error-bars are smaller than the data points.

To reveal the values of the parameters required, firstly, the temperature was determined by using Eq. (6.10). The overall precision of the system is related to the sensitivity of the temperature measurement, which was observed to be approximately 6.95 $\times 10^{-4}$ /°C (on average over the measured temperature range) and found to be almost doubled that achieved from the Sn-Er doped germanosilicate fibre. The Bragg wavelength corresponding to that temperature was then calculated using Eq. (6.11), and the result was subtracted from the overall Bragg wavelength shift to give the strain-induced Bragg wavelength shift. Finally the value of the strain applied was obtained by using Eq. (6.12). This scheme has been used to determine the strain and temperature simultaneously over a wide range, both for temperature (up to 600°C from room temperature) and strain (up to 2000 με). To evaluate the performance of the scheme, a test in which strain and temperature were measured, was carried out over randomly and simultaneously applied measurands (reflected in Table 6.1) showing the RMS errors of 2.8°C and 36 με of temperature and strain, respectively over the whole range. Building upon this initial work with this special fibre, a higher precision could be expected through improvements to the detection system.

Table 6.1: Performance evaluation of the Sb-Er-Ge doped fibre based system by comparing the applied and measured strain and temperature, when both were varied simultaneously.

Applied measurands		Estimated measurands	
Temperature (°C)	Strain (με)	Temperature (°C)	Strain (με)
20	0	19.0	+ 33
200	0	197.4	+ 35
500	0	499.0	+ 14
25	950	24.1	+ 969
25	1500	24.0	+ 1521
100	1000	102.5	+ 946
400	500	402.1	+ 471

6.4.3. Comparison of the measurement scheme using these two different fibres: Sn-Er-Ge and Sb-Er-Ge doped fibre

Depending upon the composition and the concentration of the core of the specially fabricated fibres used in this work, the results achieved were slightly different, although the same approach was used for the measurements for both types of fibres. Introduction of tin or antimony into the fibre-core results in the gratings written into these fibres almost similar temperature-sustainable; this has been discussed in detail in Chapter 3. However, with the FBG-fabrication system set-up used in the *Measurement and Instrumentation Centre*, fabrication of more strong gratings (i.e., with higher reflectivities) was achieved with antimony-doped fibre in comparison to the tin-doped fibre. This caused the higher values of remaining stabilised reflectivities of the annealed gratings at a certain temperature, resulting in a comparative broader dynamic range for temperature sensing using the grating written in antimony-doped fibre than that in tin-doped fibre.

For strain measurement, 0-1150με was measured using Sn-Er-Ge doped fibre after annealing the grating-sensor at 550°C for 24 hours, whereas the measured range was 0-2000με in the case of Sb-Er-Ge doped fibre, where the grating-sensor was annealed at 600°C for 8 hours. However, the same annealed grating-sample written in Sn-Er-Ge doped fibre was used for a further test to carry out an extended range of strain measurement, where it was also successful to measure an axial strain of 0-2000με, without breaking the sample. Hence, regarding the strain measurement, the performance of both samples was almost similar in terms of the mechanical strength of the samples, as far as the samples were tested up to 2000με.

The most important and vital point of the comparison of these two fibres in terms of the fibre-fluorescence depending on the concentration of the Er^{3+}-doping introduced into the core of the fibres. To compare the fluorescence spectra from identical length of these two fibres (antimony-doped and tin-doped), tests have been carried out by using pumping sources at the wavelengths of 980 nm and 1480 nm and the plots were shown in the earlier section, in Figs. 6.14(a) and 6.14(b). Depending on the fibre-fluorescence, the dynamic ranges of the temperature-dependent-FPPR of these two fibres are different, which results in different sensitivity for measuring temperatures. Figs. 6.20 illustrates the variation of the FPPR with temperature for these two fibres.

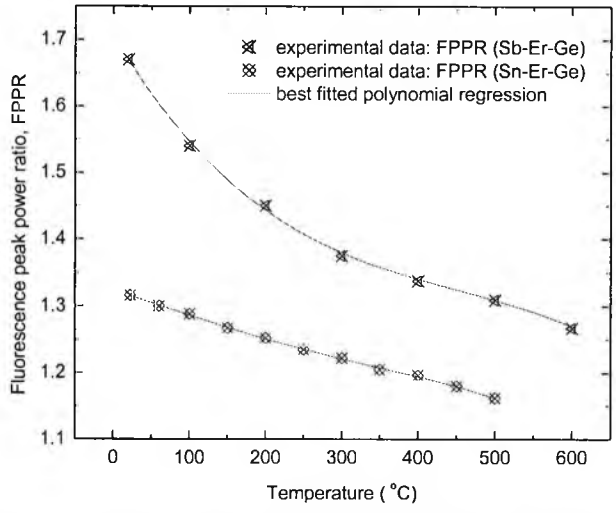

Fig. 6.20: Variation of FPPR with temperature for Sb-Er-Ge doped and Sn-Er-Ge doped fibres of identical length of 10 cm.

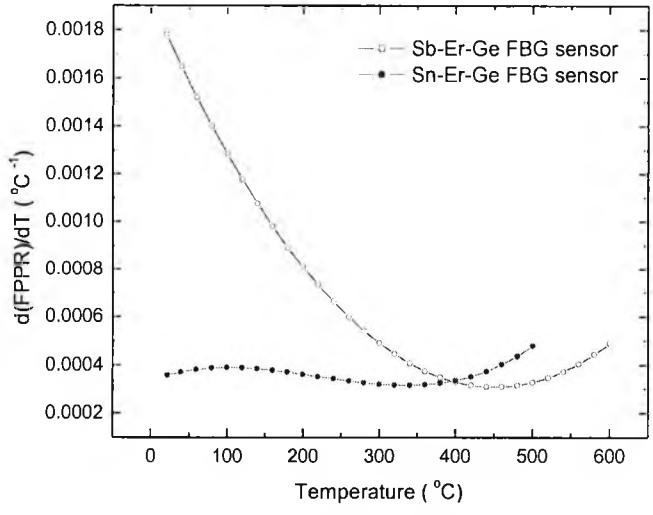

Fig. 6.21: Variation of temperature-dependent FPPR-sensitivities of Sb-Er-Ge and Sn-Er-Ge doped fibres of identical length of 10 cm.

From Fig. 6.20, it is very clear that the dynamic range of FPPR with the variation of temperature for Sb-Er-Ge doped fibre is much wider than that for Sn-Er-Ge doped fibre. The overall sensitivity for the temperature measurement was found to be approximately 6.95 $\times 10^{-4}$ /°C (on average over the whole range of temperature measurement) for the used Sb-Er-Ge doped fibre, which is more than doubled that achieved (3.35 $\times 10^{-4}$ /°C) from the same length of Sn-Er-Ge doped fibre. However, the variation of FPPR with temperature is not linear. Hence, the sensitivity of FPPR is not constant, rather temperature-dependent. Fig. 6.21 shows the temperature dependence of the FPPR-sensitivities for the studied two fibres of identical length of 10 cm. The FPPR-sensitivity for Sn-Er-Ge doped fibre is shown to be quite low and varies within the range of 0.00035-0.0005 /°C. This value is 0.0018 /°C for Sb-Er-Ge doped fibre at room temperature (20°C), which is almost five times of the value of Sn-Er-Ge doped fibre; however, for Sb-Er-Ge doped fibre the FPPR-sensitivity decreases with increasing temperature. These values are almost comparable for these two fibres studied above 350°C. As the thermal sensitivities of the gratings written into these two fibres are almost comparable (shown in Fig. 6.22), the overall precision of the systems using these two fibres can mainly be compared by the FPPR-sensitivity values.

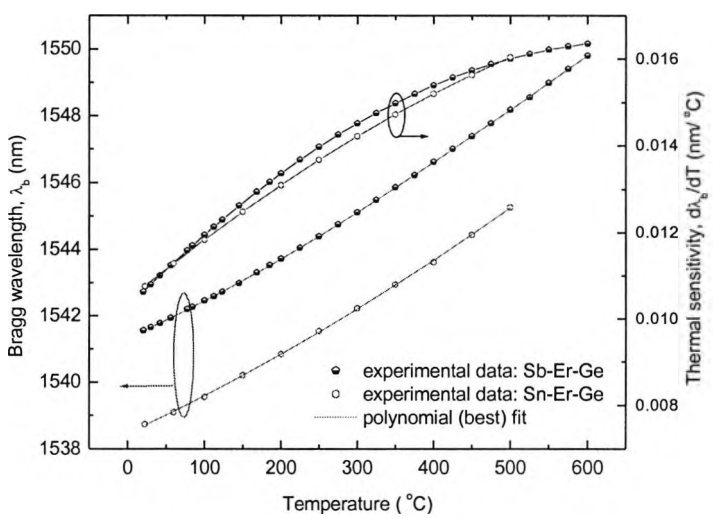

Fig. 6.22: Thermal response of the gratings written in Sb-Er-Ge and Sn-Er-Ge doped fibres along with their thermal sensitivity values.

6.4.4. Choice of the approach and the pumping source

The reasons of choosing the approach and the pumping source are discussed here. In the choice of this approach, the use of the FPPR approach is advantageous, as this avoids the problem of pump power fluctuations. Moreover, a highly Er^{3+}-doped fibre can be used to make the sensor prototype within a very short length. Sn-Er-doped and Sb-Er-doped germanosilicate fibres were chosen in this scheme to take advantage of the ASE generated from the fibre due to the Er^{3+}-ion doping, with the high temperature-sustainable behaviour due to the presence of tin or antimony and the photosensitive property of the fibre arising from the presence of germanium, to allow the FBG to be written into it. The Bragg wavelength of the grating written into these special fibres at around 1540 nm (for room temperature) with a slight variation depending on the effective refractive index of the core of the fibre and the phase-mask used for the grating-writing, has the advantage that the Bragg wavelength of the grating can be created in the same wavelength region where the ASE may be generated, caused by the erbium-ion doping. In addition, the strain-independence of the FPPR scheme makes the signal processing relatively easy for practical use.

For the pump source, a 980 nm laser diode has been used, which creates the $^4I_{15/2} \rightarrow {}^4I_{11/2}$ transition arising from the absorption band due to the Er^{3+} ion in the fibre. The ground state absorption (GSA) at this wavelength is almost free from the excited state absorption (ESA) from the $^4I_{13/2}$ level, which results in the best performance with respect to quantum-limited noise-figures, though ESA corresponding to the $^4I_{11/2} \rightarrow {}^4F_{7/2}$ transition has also been reported at 970-980 nm for silica [209]. The 980 nm pumping is also advantageous [13] compared to the region alternatives of 800 nm or 1480 nm pumping due to the lower pump power required to achieve a specified small-signal gain.

6.5. Combination of type I and type IIA gratings for strain-independent temperature measurement

A simple and effective technique for strain-independent temperature measurement has been demonstrated in this section using the peak wavelengths of both type I and type IIA fibre Bragg gratings written without hydrogen loading in the same fibre. The fibre was specially fabricated with a high concentration of germanium in the core composition to create a good amount of photosensitivity. The device is also found to be capable of monitoring strain and temperature simultaneously. The sensor can be used to measure temperature over the range of 25 – 300°C with a strain range of 0 – 500 $\mu\varepsilon$, achieving a temperature-dependent sensitivity of 0.53 pm/°C and 0.31 pm/°C for strain-independent temperature measurement with root mean square errors of 2.4°C and 4.1°C at 25°C and 300°C respectively.

6.5.1. Background of the work

Reliable, accurate and simultaneous measurement of strain and temperature, and both strain-independent temperature measurement [205] and temperature-independent strain measurements by using fibre Bragg gratings (FBGs) are of significant interest for various applications. Improved measurements of these parameters are important for such industrial uses to achieve enhanced safety and reliability and lower cost. However, the inherent response of FBGs to both strain and temperature results in an unwanted cross sensitivity, which creates several complications in FBG-based sensor schemes for the measurement of both parameters simultaneously. To overcome the problem of cross sensitivity, researchers have proposed and investigated several different methods as discussed in earlier sections.

In this section, a simple technique is proposed for strain-independent temperature measurement (demonstrated in this work up to 300°C, but capable of being used for measuring higher temperatures) by using a combination of a type I and a type IIA grating written in a specially fabricated high germanium doped fibre. This special fibre has been chosen because it shows high photosensitivity and thermal stability. The non-linear thermal response of the gratings [101],[102],[182],[193],[210] has also been considered in this work so that the error in the temperature measurement carried out over a significant measurement range, can be minimised.

6.5.2. Description of the sensor and the principle of operation

During the writing of the FBGs, the expected shift of the Bragg wavelength was observed [169],[170],[190],[211] together with the growth in reflectivity of the type I and type IIA gratings. Fig. 6.23 shows this phenomenon during the inscription of the gratings in the fibre used, when it was exposed to light from a 248 nm KrF excimer laser with an energy of 12 mJ and a pulse repetition frequency of 200 Hz. This observation allows the design of a dual-grating sensor scheme, which enables the optimum utilisation of the available optical bandwidth in a wavelength division multiplexing (WDM) configuration well suited to sensor multiplexing. A fibre with a high germanium content in the core was used in this work to achieve a very good photosensitivity for writing gratings into the fibre and stable thermal sensitivity for the gratings, accompanied by higher temperature sustainability. Fig. 6.24 represents a schematic of the sensor, which comprises a combination of a type I and a type IIA grating, each of length of ~ 6.5 mm, inscribed 2 mm apart in the same fibre without the use of hydrogen-loading, leading to a total length of the sensor of ~ 15 mm. The fibre thus did not contain a splice, avoiding the mechanical weakness and splicing losses that can arise as a result.

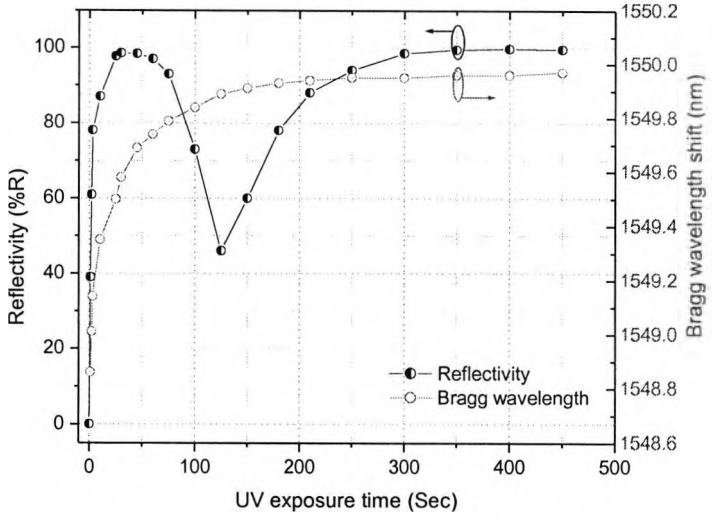

Fig. 6.23: Growth of a type I and a type IIA gratings and the shift of the Bragg wavelength during grating inscription in a high germanium doped fibre. A 248 nm KrF excimer laser was used with energy of 12 mJ with a pulse repetition frequency of 200 Hz for this grating inscription.

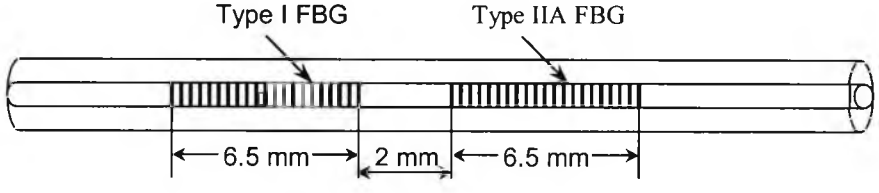

Fig. 6.24: A schematic diagram of the dual-grating sensor, the combination of a type I and a type IIA grating, separated by a distance of 2 mm.

Taking into account both the non-linear thermal response [101],[102],[182],[193] and the linear strain response of the gratings, the combined shift of the Bragg wavelength for grating i, for any applied temperature with any strain applied can be expressed as

$$\Delta\lambda_i(\varepsilon,T) = k_{i\varepsilon}\cdot\Delta\varepsilon + \Sigma k_{ijT}\cdot(\Delta T)^j \; ; \; i = 1, 2; \; j \geq 1 \qquad (6.13)$$

where $\Delta\lambda_i$ is the Bragg wavelength shift, and $k_{i\varepsilon}$ and k_{ijT} are the strain and temperature coefficients for the type I and type IIA gratings with the best order of non-linear polynomial considered to fit to the grating thermal response, j. As the gratings were inscribed very close to each other in the same fibre with a very small difference in the central peak wavelengths of the type I and type IIA gratings, the strain coefficients can reasonably be assumed to be exactly the same, as this parameter depends mainly on the fibre dimensions and the characteristics of the fibre material. So the strain-independent temperature can directly and simply be measured from the difference of the Bragg wavelengths of the two gratings as

$$\Delta\lambda_1(T) - \Delta\lambda_2(T) = \Sigma k_{1jT}\cdot(\Delta T)^j - \Sigma k_{2jT}\cdot(\Delta T)^j \; ; \; j \gtrsim 1 \qquad (6.14)$$

However, a simultaneous measurement of strain and temperature can also be obtained in the above scheme by measuring the temperature directly from the difference of the Bragg wavelengths and a measurement of strain can be achieved by eliminating the temperature effect from the total shift in the Bragg wavelength for either one of the gratings.

In comparison to the above scheme, assuming a linear approximation over the thermal and strain response of the gratings, the variation in the Bragg wavelengths of the type I and type IIA grating can be written in a similar way as expressed in Eq. (2.62) and the absolute values of the unknown parameters can be determined by Eq. (2.63). However, the limitations of this scheme are discussed in detail in the next section, in support of the experimental data obtained.

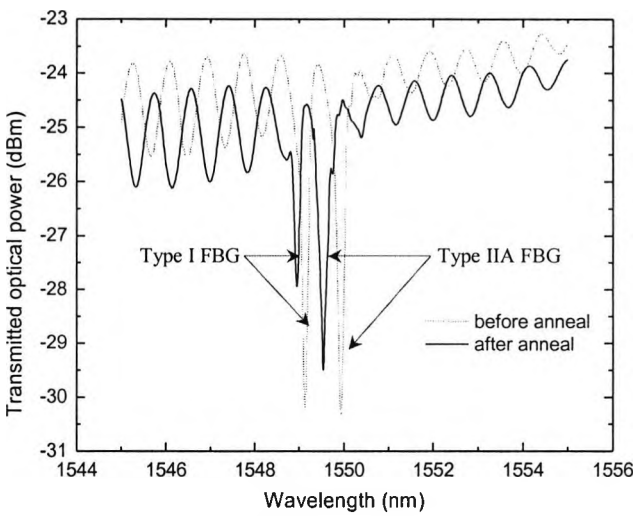

Fig. 6.25: Transmitted spectra of the dual-grating sensor at room temperature under zero axial strain. Dotted line represents the spectrum before annealing, whereas the solid line shows the spectrum after annealing at 320 °C for 10 hours.

6.5.3. Testing, calibration and measurements

The gratings used in this experiment were inscribed in a specially fabricated high germanium doped fibre (fibre type: A021, specification: mentioned in Table-3.2) using the same technique of ultra violet exposure through a phase mask. The *in-situ* grating spectra created during the grating inscription were monitored in a similar way as discussed earlier sections, by using a HP86140A OSA and illuminating the gratings with light from a broadband amplified spontaneous emission (ASE) light source. The fibre was exposed to the laser light for ~ 9 minutes to write the type IIA grating of reflectivity ~ 80 % (corresponding refractive index modulation of ~ 4.6×10^{-5}), whereas almost the same degree of growth in the reflectivity for the type I grating was achieved within a much shorter time of only 10 seconds with a laser energy of 12 mJ and a pulse

repetition frequency of 100 Hz. The transmission spectral characteristics of the dual-grating sensor at room temperature are shown in Fig. 6.25, where the dotted line represents the spectrum before annealing and the solid line shows the spectrum after annealing the sample at 320 °C for 10 hours. For both gratings, a blue shift due to the annealing process was observed. This research, and our previous work with fibres of this type [175],[182],[193] has shown how important it is to undertake an effective thermal annealing process at a temperature higher than the maximum operating temperature *before* incorporating the FBGs into sensor systems, to achieve a high repeatability in the response of the device. The Bragg wavelengths of the FBGs were observed to be 1548.93 nm (for type I) and 1549.52 nm (for type IIA) at room temperature (~ 25 °C) after the annealing process was complete. The reflectivities of both the gratings were measured to have a value of greater than 50% after the annealing process was completed, so that the Bragg wavelengths could be easily identified. At the same time, the full width half maximum (FWHM) bandwidths of the gratings were observed to be ~ 0.15 nm, which are good enough to achieve an acceptable level of precision in the measurement.

The sensor response was tested and to achieve a reliable and stable calibration of the device, the sensor containing a length of uncoated fibre was placed inside a well-calibrated CARBOLITE tube oven (Type: MTF 12/38/400) under zero axial strain for the temperature test and a micrometer-driven translation stage was mounted to allow the strain measurements to be made. The shifts of the Bragg wavelengths in all the experiments carried out were measured by using the OSA, with a resolution bandwidth of 0.05 nm (the resolution available for the peak/dip wavelength determination was 0.005 nm).

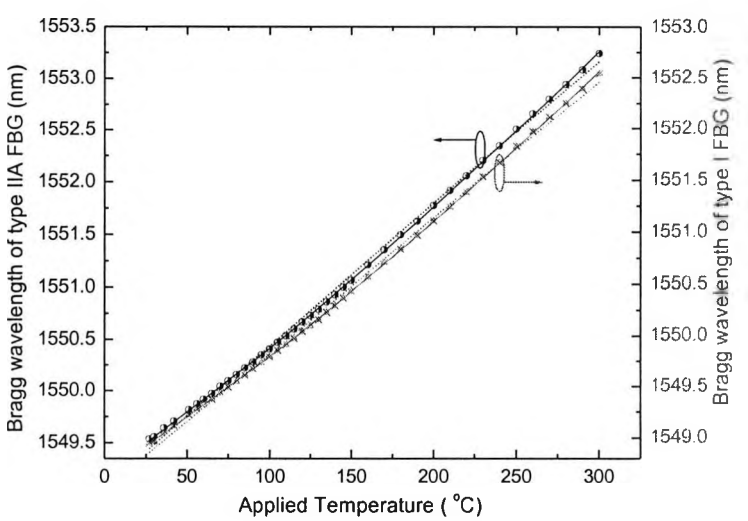

Fig. 6.26: Variation of Bragg wavelength of the dual-grating sensor with the applied temperature under zero axial strain. Solid lines represent the best polynomial (2^{nd} order) regression over the measurement range, whereas the linear regression is represented by the dotted lines.

Fig. 6.26 shows the variation of the Bragg wavelength of the gratings with the applied temperature (up to 300 °C starting from the room temperature), using 10 °C increments. A settling time of 15 minutes was allowed at each temperature to achieve thermal equilibrium between the grating and the oven before recording data for several cycles of both ascending and descending temperatures. The measured data for these temperature cycles, in terms of the Bragg wavelength change with temperature for the gratings tested, were observed to be highly consistent over a number of repeated measurement, showing a wavelength uncertainty of ± 0.005 nm. The solid lines on the graph represent the best polynomial (2^{nd} order) regression for the calibrations for both the gratings, and they can be expressed as

$$\lambda_{b1T}(T) = 1548.64 + 10.75\times10^{-3}\,T + 7.68\times10^{-6}\,T^2 \qquad \text{(for type I FBG)} \qquad (6.15a)$$

$$\lambda_{b2T}(T) = 1549.21 + 11.30\times10^{-3}\,T + 7.27\times10^{-6}\,T^2 \qquad \text{(for type IIA FBG)} \qquad (6.15b)$$

where λ_{b1T} and λ_{b2T} are the corresponding Bragg wavelengths for the type I and the type IIA gratings used at temperature, T °C, under zero axial strain. The coefficients of determination (R^2), a common statistical parameter to evaluate the quality of regression, were found to be 0.99994 and 0.99994 for the above two regressions, which are much better when compared to the values found for the linear fitting (0.99812 and 0.99840).

In the next stage of the experiment, the gratings were tested under a known applied strain at room temperature, using both increasing and decreasing strain, up to a maximum of 500 με. In this test, no evidence of hysteresis was observed with highly repeatable experimental data being obtained. Fig. 6.27 shows the strain response of the type I and type IIA gratings at room temperature. Using a linear regression, the variation of the Bragg wavelength for the gratings with the applied strain can be written as

$$\lambda_{b1\varepsilon}(\varepsilon) = 1548.95 + 1.23\times10^{-3}\,\varepsilon \qquad \text{(for type I FBG)} \qquad (6.16a)$$

$$\lambda_{b2\varepsilon}(\varepsilon) = 1549.53 + 1.23\times10^{-3}\,\varepsilon \qquad \text{(for type IIA FBG)} \qquad (6.16b)$$

where $\lambda_{b1\varepsilon}$ and $\lambda_{b2\varepsilon}$ are the Bragg wavelengths for the type I and type IIA FBGs with strain, ε, at room temperature (~ 25 °C). The set of Eqs. (6.16a) and (6.16b) confirms that the strain coefficient for both the FBGs are the same (1.23 pm/με) at room temperature (with R^2 values of 0.99915 and 0.99934 respectively) and similar results were demonstrated over the measured temperature range.

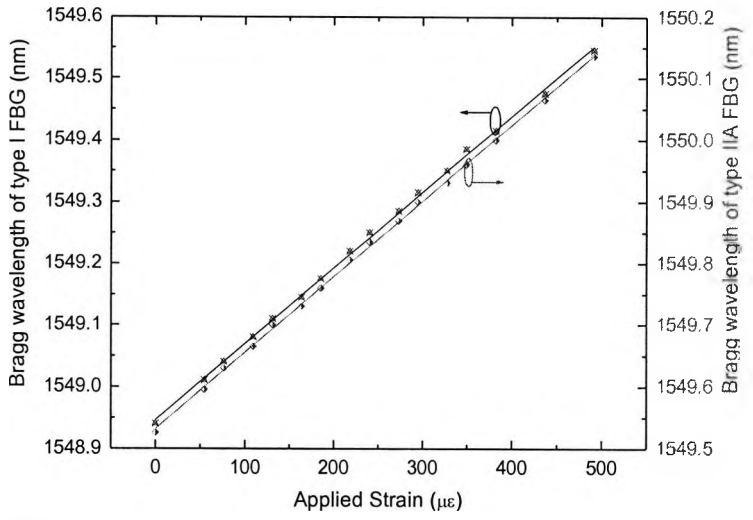

Fig. 6.27: Bragg wavelength shift with the applied strain at room temperature (~ 25°C) along with the linear regression.

From the above condition, where the strain coefficients of both gratings used in the experiment are exactly the same, the strain-independent temperature can simply be measured from the calibration formulated by subtracting Eq. (6.15a) from Eq. (6.15b). The resulting calibration graph for the above measurement is shown in Fig. 6.28, where the regression of that graph can be described by

$$\Delta\lambda_b(T) = 0.5679 + 5.50\times10^{-4}\,T - 4.07\times10^{-7}\,T^2 \qquad (6.17)$$

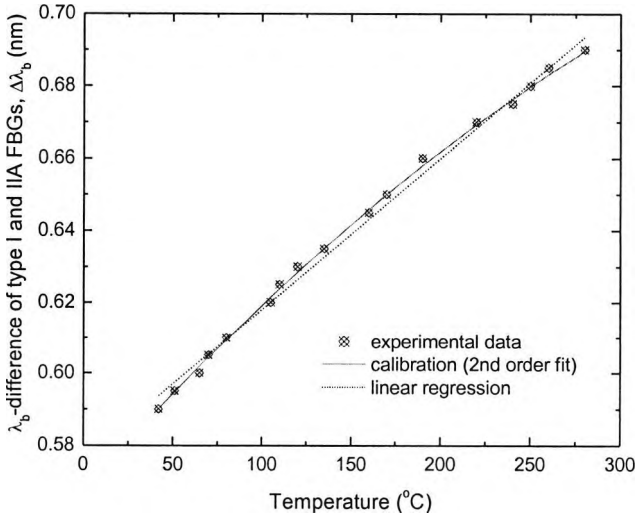

Fig. 6.28: Calibration graph for direct measurement of the strain independent temperature over the range of 25 – 300 °C. Solid and dotted lines represent the best polynomial (2nd order) and the linear regression respectively.

The temperature-dependent sensitivity for this measurement can be determined from Eq. (6.17), yielding values of 0.53 pm/°C and 0.31 pm/°C at room temperature (~ 25°C) and at 300°C, respectively. This regression fits very well (R^2 = 0.99894) with the experimental data compared to the results of the linear fit (R^2 = 0.99389). The root mean square (rms) uncertainties in this strain-independent temperature measurement were found to be 2.4°C and 4.1°C respectively for these two different temperatures mentioned above, over the temperature range studied of 25 – 300°C. With annealing of the sample gratings at higher temperatures, the range could be expected to be in excess of 500°C [182],[193] by measuring the detectable central peak wavelengths of the gratings from the reflection spectra.

The same scheme can also be exploited for the simultaneous measurement of strain and temperature. This is done by initially determining the temperature using Eq. (6.17) and then evaluating the applied strain using either the set of Eqs. (6.15a) and (6.16a) or the set of Eqs. (6.15b) and (6.16b). Using this approach, a preliminary investigation of the simultaneous measurement of both these parameters was conducted, over a temperature range of 25 – 300°C and a strain range of 0 – 500 με. In the experiments carried out, the rms uncertainties were determined to be 5.6°C for temperature and 50 με for strain. These values could be improved by more precise measurement of the grating wavelength change by using one or either of the various sophisticated signal-processing techniques, which have been discussed in the literature [10],[196].

6.5.4. Comparison of this approach with the conventional technique

In the conventional method of matrix-inversion analysis, assuming a linear regression for both the parameters of temperature and strain, the temperature and strain coefficients can be determined by solving the Eq. (2.63), which yields the values of

$$\left.\begin{aligned} k_{1T} &= 13.19 \text{ pm/°C}, \\ k_{2T} &= 13.62 \text{ pm/°C}, \\ k_{1\varepsilon} &= k_{2\varepsilon} = 1.23 \text{ pm/με}. \end{aligned}\right\} \quad (6.18)$$

The overall sensitivity for the strain-independent temperature measurement can be found 0.43 pm/°C over the measurement range of 25-300°C, with a root mean square uncertainty of 6.6°C. A comparison of the results of the above two schemes has been shown in Table 6.2.

Table 6.2: Comparison of sensitivity and RMS errors for the strain-independent temperature measurement for two analyses undertaken.

Response of type I and type IIA gratings considered over		Strain-independent temperature range: (25-300 °C)	
Temperature	Strain	Sensitivity	RMS error
Linear	Linear	0.43 pm/°C	6.6 °C
Polynomial (2^{nd} order)	Linear	0.53 pm/°C (at 25 °C) 0.31 pm/°C (at 300 °C)	2.4 °C (at 25 °C) 4.1 °C (at 300 °C)

6.6. Discussion

Various aspects of the schemes demonstrated for simultaneous measurement of strain and temperature and strain-independent temperature measurement, including significant advantages and limitations of the schemes and the procedure of the error-analysis have been discussed in this section.

6.6.1. Advantages and disadvantages of the scheme

The scheme demonstrated in the previous sections for simultaneous measurement of strain and temperature has several significant advantages over the conventional techniques used for this purpose. These are:

- Measurement of both parameters over a wide range is possible (for example, temperature: up to 600°C and strain: up to 2000$\mu\varepsilon$), with an acceptable measurement-errors.
- Power/intensity fluctuation problems of the signal can be overcome by introducing the FPPR scheme (i.e., considering the ratio of the ASE spectral intensity at two particular wavelengths of 1535 nm and 1552 nm).
- Very small length of the sensor device (10 cm) results in a convenient system to use.
- The sensitivity of the system can be improved and/or the length of the sensor device can be optimised by using a photosensitive fibre with higher concentration of Er^{3+}-doping.
- Writing of a single FBG makes the system relatively simple.
- The non-linearity in grating thermal response has been taken into account in the system calibration to minimise the deviation of the Bragg wavelength from its regression.

There are a few limitations of the scheme, which may be listed as

- The sensitivity of the system achieved was limited and that is mainly dependent on the dynamic range of the FPPR with the variation of temperature. However, this can be improved by using a photosensitive fibre with higher concentration of Er^{3+}-doping.
- The FPPR-sensitivity was found to be dependent on temperature and under certain cercumstances decreases with the increase of temperature (as observed in case of Sb-Er-Ge doped fibre).
- The value of the temperature-dependent FPPR is determined by taking the ratio of the ASE-based fluorescence intensity at the wavelength of 1535 nm and 1552 nm. The fluorescence peak at 1535 nm is constant; however, the peak at 1552 nm shows a shift of +/- 0.2 nm, although the smoothness of this peak gives the variation of the value within the range of +/- 1%.
- Although the length of the sensor used in this scheme is ~ 10 cm, this length is larger by comparison to several other types of temperature sensor, such as the thermo-couple and may not be suitable for some special measurement applications, where a very small size sensor is needed.

For the scheme of strain-independent temperature measurement, the combination of a type I and a type IIA FBG written in a high germanium doped fibre was used which does not require hydrogen-loading. Similar strain coefficients and dissimilar temperature coefficients are the factors that are responsible for the success of this novel scheme. The same strain coefficient value of the above two gratings studied was validated experimentally. Even if any slight variation (of the order of ~ $\pm$ 0.01 pm/$\mu\varepsilon$) in the strain coefficient values may be observed as a result of the regression approach, this would result in a negligible error. Even though the correction of this minor error can be made possible by means of a sophisticated technique, it has not been considered in this work, as a compromise in this scheme in order to avoid a more complicated signal processing for the system calibration. The particular value of the scheme used is the simplicity of the signal processing, even though the non-linear thermal response of the gratings has been taken into account to allow the coverage of a wider operational range of calibrated measurement. The same scheme can also be exploited for the simultaneous measurement of strain and temperature. The presence of any significant departure from the linear variation in the thermal response of the FBGs will represent a limitation in the use of the matrix inversion technique to determine the coefficients for strain and temperature: however, it will increase the dynamic range of the system to allow temperature measurement with higher level of precision. The result obtained in this scheme has been compared with that from the conventional approach adopted (the matrix inversion technique) to determine the parameters and its superiority has been reflected in the analyses of the system errors presented. In addition, it is important to note that, the scheme is compatible with multi-grating multiplexed sensor systems because a dual-

grating sensor system of this type can be configured to take the full advantage of multiplexing of a wide number of sensors using WDM techniques. Measurement of even higher temperatures can be explored with a range of different fibres specially fabricated for this type of work.

6.6.2. Error analysis

Consideration and analysis of errors are of particular importance for any single or multi-parameter measurements, especially in the area of measurement of strain and temperature individually or simultaneously. Typically a temperature change of 1°C has the same influence as an applied strain change of 10με. When strain-temperature recovery process is usually determined by the matrix-inversion process, the errors due to the individual and simultaneous measurements of the parameters can be expressed as written in Eqs. (6.3) and (6.4) [3],[127], as discussed in a previous section. However, these errors were estimated mainly from the limited resolution of the detection system used in this experiment regardless of the effect arising from the non-linearities and cross-sensitivity.

It is also important to be aware of resolution, reading, calibration uncertainties and the precision of the system, as no instrument exists that can measure a quantity to infinitely fine resolution. In general, the resolution limit of an instrument represents the smallest uncertainty that can be quoted in a single measurement. Reading uncertainties can be overcome presently by using any digital read-out devices, provided that instrument is well calibrated at some time against a standard. An uncalibrated, or poorly calibrated instrument, may lead to a systematic uncertainties. All such uncertainties exist whenever a measurement is made in an experiment. However, to be able to get a real value for the variable in a measurement, more than one measurement should be made for each quantity and to quantify the measurement uncertainties, some statistical analysis can be used. In general, all measurements discussed in the previous sections, a number of repeated measurements have been made for each cycle and the calibration curves were obtained based on these data. The deviations at each point are measured from the difference between the average of the measured values and the corresponding calibrated values. Finally, the uncertainty in the experimental measurements can be quantified by the square root of the mean of the squares of the deviations, named as, *root mean square (RMS)* deviation/error, which can be expressed as

$$Error_{RMS} = \{\sum(x_{cal} - \underline{x})^2]/n\}^{1/2} \qquad (6.21)$$

where x_{cal} is the calibrated value and $\underline{x}$ is the average of the measured value of the variable after repeating the measurements for n number of times.

6.7. Summary

A fibre-optic sensing scheme, based on a combination of the properties of the fibre Bragg grating (FBG) and the fluorescence from a rare-earth-doped photosensitive fibre, has been demonstrated for the simultaneous measurement of a wide range of both strain and temperatures. The temperature-dependent fluorescence peak power ratio (FPPR) of the two peaks occurring around 1535 nm and 1552 nm from the amplified spontaneous emission due to the $^4I_{13/2} \leftrightarrow {}^4I_{15/2}$ transitions in Er^{3+}-doped fibres, with 980 nm pumping along with the dual functionality of the FBG were exploited in this scheme. Tin-erbium-germanosilicate and antimony-erbium-germanosilicate specially fabricated fibres were used in this scheme for two separate sets of experiments with a single FBG written in a small length (~10 cm) of the above fibres. Simultaneous measurement of strain and temperature over ranges of 0–1150 με and 22–500 °C, with rms errors of 36 με and 6 °C respectively, can be achieved for Sn-Er-Ge doped fibre. The operational range was found to be enhanced by writing a strong FBG (high reflectivity) in a Sb-Er-Ge doped fibre, over ranges of 0–2000 με strain and 20–600 °C temperature, with rms errors of 36 με and 2.8 °C, respectively. In addition, a simple and effective scheme for strain-independent temperature measurement has also been demonstrated by writing both type I and type IIA FBGs in 2 mm separation in the same fibre (Er-High Ge doped fibre), which may alternatively be used to monitor strain and temperature simultaneously. The non-linear thermal response of the FBGs was included in all the schemes demonstrated to achieve a better precision in the temperature measurement over a wide range.

Chapter 7

Conclusions and future scope of the work

7.1. Conclusions on the work carried out

The main purpose of the work as a whole has been to carry out research on fibre Bragg grating-based schemes, especially for sensing applications and to extend the FBG-based research further towards various high-temperature sensing applications through writing gratings into various specialised photosensitive optical fibres. Several specific achievements have resulted from this work, these being summarised below and based on these specific results, conclusions are drawn.

- A brief yet comprehensive review on the research carried out in the field of fibre Bragg gratings has been made in Chapter 2, using a large number of references, which provides a background of this work and discusses various applications related to Bragg gratings in sensor systems.

- Based on the review of the FBG-based work, it has been seen that relatively little research had been undertaken prior to this research on high temperature sensing applications using FBGs. Hence, attention has been focused on the writing of Bragg gratings into several different specially fabricated photosensitive optical fibres and testing their performance through monitoring their high temperature sustainability. Chapter 3 reports on this subject in detail by considering various photosensitive fibres. Gratings written in tin and antimony doped photosensitive fibres were found to be very high temperature sustainable (up to ~ 850°C), making them almost comparable to the performance of a specially fabricated chemical composition grating (CCG) in a fluorine-doped fibre (which survives up to 1000°C). The introduction of erbium-ions into these fibres during fabrication makes the fibres more useful when using their combined properties of photosensitivity and fluorescence.

- Prior to use of the FBGs for high temperature measurement, the decay of the refractive index modulation (which is related to the grating reflectivity) and the decay of the effective refractive index (which is related to the shift in the Bragg wavelength of the grating) were tested over an extended period of time at various elevated temperatures. Both of these

decays were analysed for the most photosensitive fibre (boron-germanium doped fibre) and for the most useful fibre (tin-erbium-germanium doped fibre) among the fibres studied, in detail in Chapter 4, by estimating the activation energies associated to the trap-sites in the glass-structures of the fibres with the use of the *power-law*, *master-aging curve* and the *accelerated-aging* testing approaches.

- Temperature-induced reversible and irreversible changes in the grating spectra were observed in terms of the changes in the reflectivity and the Bragg wavelength of gratings. These effects were considered in the analysis of the thermal stability of the gratings in Chapter 4. In order to avoid irreversible changes in the Bragg wavelength, appropriate thermal annealing of the gratings at a temperature above the maximum operating temperature is very important, this being essential to achieve a reliable performance of the grating as a temperature sensor by producing reproducible data. For all of the pre-annealed gratings studied, a non-linear thermal response was observed. Non-linear regressions were compared to the linear regressions in terms of the thermal response of the gratings and a calibration according to the best-fitted non-linear regression was considered for each grating, before any temperature measurement, to achieve a smaller deviation between the regression and the experimental data. These issues were discussed in detail in Chapter 5.

- Simultaneous measurement of strain and temperature over a wider range has been demonstrated by writing a single grating in a piece of erbium doped photosensitive fibre, and the results are reported in Chapter 6. This is based on the temperature dependence of the fluorescence peak power at two distinct wavelengths and the dual functionality of the grating in its combined response to both strain and temperature. Specially fabricated tin-erbium-germanium doped and antimony-erbium-germanium doped fibres are used in two separate schemes to demonstrate these measurements over the ranges of 0-500/600°C and 0-1150/2000$\mu\varepsilon$ for temperature and strain determination, respectively. The limitation of the conventional matrix-inversion technique, generally used for simultaneous measurement of strain and temperature, has been discussed, and this may be overcome by using this scheme. In addition, the non-linear thermal response of the gratings is considered in this scheme to avoid what are more than acceptable deviations in the measurements.

- Strain-independent temperature measurement is an important requirement in industry, and one approach to this has been demonstrated in Chapter 6, by writing type I and type IIA gratings in a close proximity to each other in the same photosensitive fibre. Similar strain coefficients and dis-similar temperature coefficients of these two types of gratings are the basis of the measurement scheme discussed in this work.

7.2. Future directions

As a result of the work carried out and based on the conclusions arising from this research, the future direction of the grating-based work and its development, in relation to various specific applications, can be suggested. These include

- An improvement of the detection system, specifically for strain measurement and the simultaneous measurement of strain and temperature, to extend the applications further, with a better precision in the measurements. A Fabry-Perot tuneable filter with high resolution, in combination with a photo-detector (of appropriate operating wavelength region) may be designed, for example, and a data acquisition system interfaced with a PC, can be used as an improved alternative to an OSA. A sophisticated Hilbert transformation signal processing unit could also be developed, which can be incorporated within the detection system to achieve better resolution.

- The design and fabrication of a range of special photosensitive fibres, depending on the choice and the concentration of the doping ions in the core of fibre, (for example, bismuth, indium-doped fibres) to create ultra-high thermally stable FBGs [225],[226]. The absorption loss for these types of dopings can be measured to explore their suitability in long or short-haul communication or in sensor applications. This will require the continuation of a close cooperation with the partners at the University of Nice, France and in China, to achieve a satisfactory newly designed fibres.

- The fabrication of FBGs and LPGs after hydrogen-loading of the special photosensitive fibres and comparison of their photosensitivity, thermal stability and the thermal sensitivity [227] with those of the gratings written in the same unloaded fibres.

- The fabrication of chirped gratings to cover the full chirp range of the phase-mask can be realised by modifying the grating-writing system set-up, so that in contrast to the approach operated, only one chirped grating can be used in combination with various uniform gratings (of wavelengths within the range of the chirped grating) for the development of a multiplexed strain and/or temperature sensing system.

- The fabrication of long-length fibre Bragg gratings by slightly modifying the set-up including a translation stage is a further step to extend the "quasi-distributed" temperature sensing system towards a "distributed" system and to improve the resolution of the measuring region.

- To extend the FBG-based distributed system to potential new applications for different industries for smart material and smart structure designs [228] is also possible.

- The use of various polymer coated FBGs for the measurement of relative humidity [229],[230], which is being explored presently through a current project within the group.

- The fabrication of gratings in a birefringent photosensitive fibre and their utilisation can be explored for measuring various physical parameters (e.g., strain, temperature, pressure etc.) independently and simultaneously.

- The fabrication of long period gratings (LPGs) [52],[57],[231],[232] through the amplitude-mask technique in various photosensitive fibres would represent a new direction from the present knowledge base, building upon the success in high thermal stability of FBGs.

- The comparison of various modes of LPGs in terms of the thermal stability, strain and temperature sensitivities [233],[234] and the use of LPGs for various sensing applications [235],[236] may have significant potential to carry forward this research, to optimise the design of an LPG-based system for sensing several specific physical and/or chemical parameters building upon recently reported within the literature.

References

1. K. T. V. Grattan and B. T. Meggitt (Eds.), *Optical Fiber Sensor Technology*, Chapman & Hall, London, 1995.

2. K. T. V. Grattan and B. T. Meggitt (Eds.), *Optical Fiber Sensor Technology*, Vols. 2-5, Kluwer Academy, Boston, 1997-2000.

3. J. P. Dakin and B. Culshaw, *Optical Fiber Sensors: Principles and Components*, Artech House, Boston, 1998.

4. K. O. Hill, Y. Fujii, D. C. Johnson and B. S. Kawasaki, "Photosensitivity in optical fiber waveguides: Application to reflection filter fabrication," Appl. Phys. Lett., Vol. 32, pp. 647-649, 1978.

5. G. Meltz, W. W. Morey and W. H. Glenn, "Formation of Bragg gratings in optical fibers by a transverse holographic method," Opt. Lett., Vol. 14, pp. 823-825, 1989.

6. A. Othonos and K. Kalli, *Fiber Bragg Gratings: Fundamentals and Applications in Telecommunication and Sensing*, Artech House, Boston, 1999.

7. R. Kashyap, *Fiber Bragg Gratings*, Academic Press, San Diego, 1999.

8. K. O. Hill and G. Meltz, "Fiber Bragg grating technology fundamentals and overview," IEEE J. Lightwave Technol., Vol. 15, pp. 1263-1276, 1997.

9. A. Othonos, "Fiber Bragg gratings," Rev. Sci. Instrum., Vol. 68, pp. 4309-4341, 1997.

10. A. D. Kersey, M. A. Davis, H. J. Patrick, M. LeBlanc, K. P. Koo, C. G. Askins, M. A. Putnam and E. J. Friebele, "Fiber grating sensors," IEEE J. Lightwave Technol., Vol. 15, No. 8, pp. 1442-1463, Aug 1997.

11. Y. J. Rao, "In-fibre Bragg grating sensors," Meas. Sci. Technol., Vol. 8, pp. 355-375, 1997.

12. T. Sun, "Fluorescence-based fibre optic sensor systems for temperature and strain measurement," PhD Thesis (City University, London), 1999.

13. M. J. F. Digonnet (Ed.), *Rare Earth Doped Fiber Lasers and Amplifiers*, Marcel Dekker, New York, 1993.

14. P. C. Becker, N. A. Olsson and J. R. Simpson, *Erbium-Doped Fiber Amplifiers: Fundamentals and Technology*, Academic Press, San Diego, 1999.

15. D. P. Hand and P. St. J. Russell, "Photoinduced refractive-index changes in germanosilicate fibers," Opt. Lett., Vol. 15, pp. 102-104, 1990.

16. R. M. Atkins and V. Mizhari, "Observations of changes in UV absorption bands of single mode germanosilicate core optical fibres on writing and thermally erasing refractive index gratings," Electron. Lett., Vol. 28, pp. 1743-1744, 1992.

17. R. M. Atkins, V. Mizhari and T. Erdogan, "248-nm induced vacuum UV spectral changes in optical fibre perform cores: Support for a colour centre model of photosensitivity," Electron. Lett., Vol. 29, pp. 385-387, 1993.

18. L. Dong, J. L. Archambault, L. Reekie, P. St. J. Russell and D. N. Payne, "Photoinduced absorption changes in germanosilicate preforms: evidence for the color-center model of photosensitivity," Appl. Opt., Vol. 34, pp. 3436-3440, 1995.

19. P. Niay, P. Bernage, S. Legoubin, M. Douay, W. X. Xie, J. F. Bayon, T. Georges, M. Monerie and B. Poumellec, "Behaviour of spectral transmissions of Bragg gratings written in germania-doped fibers: Writing and erasing experiments using pulsed or CW UV exposure," Opt. Commn., Vol. 113, pp. 176-192, 1994.

20. W. X. Xie, P. Niay, P. Bernage, M. Douay, J. F. Bayon,, T. Georges, M. Monerie and B. Poumellec, "Experimental evidence of two types of photorefractive effects occuring during photoinscriptions of Bragg gratings written within germanosilicate fibres," Opt. Commn., Vol. 104, pp. 185-195, 1993.

21. D. L. Williams, B. J. Ainslie, R. Kashyap, G. D. Maxwell, J. R. Armitage, R. J. Campbell and R. Wyatt, "Photosensitive index changes in germania doped silica fibers and waveguides," Photosensitivity and Self-Organization in Optical Fibers and Waveguides, Proc. SPIE, Vol. 2044, pp. 55-68, 1993.

22. C. Foiri and R. A. B. Devine, "Evidence for a wide continuum of polymorphs in a-SiO_2," Phys. Rev. B, Vol. 33, pp. 2972-2974, 1986.

23. B. Poumellec, P. Guenot, I. Riant, P Sansonetti, P. Niay, P. Barnage and J. F. Bayon, "UV induced densification during Bragg grating inscription in Ge:SiO_2 preforms: Interferometric microscopy investigations," Optical Materials, Vol. 4, pp. 404-409, 1995.

24. M. Douay, W. X. Xie, T. Taunay, P. Bernage, P. Niay, P. Cordier, B. Poumellec, L. Dong, J. F. Bayon, H. Poignant and E. Delevaque, "Densification involved in the UV-based photosensitivity of silica glasses and optical fibers," IEEE J. Lightwave Technol., Vol. 15, pp. 1329-1342, 1997.

25. M. G. Sceats, G. R. Atkins and S. B. Poole, "Photo-induced index changes in optical fibers," Annual Reviews in Material Science, Vol. 23, pp. 381-410, 1993.

26. P. Y. Fonjallaz, H. G. Limberger, R. P. Salathe, F. Cochet and B. Leuenberger, "Tension increase correlated to refractive-index change in fibers containing UV-written Bragg gratings," Opt. Lett., Vol. 20, pp. 1346-1348, 1995.

27. P. J. Lemaire, R. M. Atkins, V. Mizrahi and W. A. Reed, "High pressure H_2 loading as a technique for achieving ultrahigh UV photosensitivity and thermal sensitivity in GeO_2 doped optical fibres," Electron. Lett., Vol. 29, pp.1191-1193, 1993.

28. B. Malo, J. Albert, K. O. Hill, F. Bilodeau and D. C. Johnson, "Effective index drift from molecular hydrogen diffusion in hydrogen-loaded optical fibres and its effect on Bragg grating fabrication," Electron. Lett., Vol. 30, pp. 442-443, 1994.

29. F. Bilodeau, B. Malo, J. Albert, D. C. Johnson, K. o. Hill, Y. Hibino, M. Abe and M. Kawachi, "Photosensitization of optical fiber and silica-on-silicon/silica waveguides," Opt. Lett., Vol. 18, pp. 953-955, 1993.

30. D. L. Williams, B. J. Ainslie, J. R. Armitage, R. Kashyap and R. Campbell, "Enhanced UV photosensitivity in boron codoped germanosilicate fibres," Electron. Lett., Vol. 29, pp. 45-47, 1993.

31. J. Albert, B. Malo, F. Bilodeau, D. C. Johnson, K. O. Hill, Y. Hibino and M. Kawachi, "Photosensitivity in Ge-doped silica optical waveguides and fibers with 193-nm light from an ArF excimer laser," Opt. Lett., Vol. 19, pp.387-389, 1994.

32. K. O. Hill, B. Malo, F. Bilodeau, D. C. Johnson and J. Albert, "Bragg gratings fabricated in monomode photosensitive optical fiber by UV exposure through a phase mask," Appl. Phys. Lett., Vol. 62, pp. 1035-1037, 1993.

33. D. Z. Anderson, V. Mizrahi, T. Erdogan and A. E. White, "Production of in-fibre gratings using a diffractive optical element," Electron. Lett., Vol. 29, pp. 566-568, 1993.

34. A. Othonos and X. Lee, "Novel and improved methods of writing Bragg gratings with phase-masks," IEEE Photon. Technol. Lett., Vol. 7, pp. 1183-1185, 1995.

35. R. Kashyap, J. R. Armitage, J. R. Campbell, D. L. Williams, G. D. Maxwell, B. J. Ainslie and C. A. Millar, "Light-sensitive optical fibres and planar waveguides," BT Technol. J., Vol. 11, No. 2, pp. 150-160, 1993.

36. P. E. Dyer, R. J. Farley and R. Giedl, "Analysis and application of a 0/1 order Talbot interferometer for 193 nm laser grating formation," Opt. Commn., Vol. 129, pp. 98-108, 1996.

37. J. D. Prohaska, E. Snitzer, S. Rishton and V. Boegli, "Magnification of mask fabricated fiber Bragg gratings," Electron. Lett., Vol. 29, pp.1614-1616, 1993.

38. Q. Zhang, D. A. Brown, L. Reinhart, T. F. Morse, J. Q. Wang and G. Xiao, "Tuning Bragg wavelength by writing gratings on prestrained fibers," IEEE Photon. Technol. Lett., Vol. 6, pp. 839-842, 1994.

39. B. Malo, K. O. Hill, F. Bilodeau, D. C. Johnson and J. Albert, "Point-by-point fabrication of micro-Bragg gratings in photosensitive fibre using single excimer pulse refractive index modulation techniques," Electron. Lett., Vol. 29, pp. 1668-1669, 1993.

40. C. G. Askins, T. E. Tsai, G. M. Williams, M. A. Putnam, M. Bashkausky and E. J. Friebele, "Fiber Bragg reflectors prepared by a single excimer pulse," Opt. Lett., Vol. 17, pp. 833-835, 1992.

41. J. L. Archambault, L. Reekie and P. St. J. Russel, "High reflectivity and narrow bandwidth fibre gratings written by single excimer pulse," Electron. Lett., Vol. 29, pp. 28-29, 1993.

42. J. L. Archambault, L. Reekie and P. St. J. Russel, "100% reflectivity Bragg reflectors produced in optical fibres by single excimer laser pulses," Electron. Lett., Vol. 29, pp. 453-454, 1993.

43. L. Dong, J. L. Archambault, L. Reekie, P. St. J. Russell and D. N. Payne, "Single pulse Bragg gratings written during fibre drawing," Electron. Lett., Vol. 29, pp. 1577-1578, 1993.

44. D. S. Starodubov, V. Grubsky, J. Feinberg, B. Kobrin and S. Juma, "Bragg grating fabrication in germanosilicate fibers by use of near-UV light: a new pathway for refractive index changes," Opt. Lett., Vol. 22, pp. 1086-1088, 1997.

45. A. Asseh, H. Storoy, B. E. Sahlgren, S. Sandgren and R. A. H. Stubbe, "A writing technique for long fiber Bragg gratings with complex reflectivity profiles," IEEE J. Lightwave Technol., Vol. 15, pp. 1419-1423, 1997.

46. W. H. Loh, M. J. Cole, M. N. Zervas, S. Barcelos and R. I. Laming, "Complex grating structures with uniform phase masks based on the moving fiber-scanning beam technique," Opt. Lett., Vol. 20, pp. 2051-2053, 1995.

47. K. C. Byron, K. Sugden, T. Bircheno and I. Bennion, "Fabrication of chirped Bragg gratings in photosensitive fibres," Electron. Lett., Vol. 29, pp. 1659-1660, 1993.

48. R. Kashyap, P. F. McKee, R. J. Campbell and D. L. Williams, "A novel method of writing photo-induced chirped Bragg gratings in optical fibres," Electron. Lett., Vol. 12, pp. 996-997, 1994.

49. R. Kashyap, "Design of step-chirped fibre Bragg gratings," Opt. Commn., Vol. 136, pp. 461-469, 1997.

50. R. Kashyap, H-G. Froehlich, A. Swanton and D. J. Armes, "Super-step-chirped fibre Bragg gratings," Electron. Lett., Vol. 32, pp. 1394-1396, 1996.

51. R. Kashyap, H-G. Froehlich, A. Swanton and D. J. Armes, "1.3 m long super-step-chirped fibre Bragg grating with a continuous delay of 13.5 ns and bandwidth 10 nm for broadband dispersion compensation," Electron. Lett., Vol. 32, pp. 1807-1809, 1996.

52. A. M. Vengsarkar, P. J. Lemaire, J. B. Judkins, V. Bhatia, T. Erdogan and J. E. Sipe, "Long period fiber gratings as band rejection filters," IEEE J. Lightwave Technol, Vol. 14, pp. 58-64, 1996.

53. B. J. Eggleton, P. A. Krug, L. Poladin and F. Ouellette, "Long period super-structure Bragg gratings in optical fibres," Electron. Lett., Vol. 30, pp. 1620-1621, 1994.

54. A. Yariv, *Optical electronics*, Harcourt Brace Jovanovich, Orlando, 4th Ed, 1991.

55. D. K. W. Lam and B. K. Garside, "Characterization of single-mode optical fiber filters," Appl. Opt., Vol. 20, pp. 440-445, 1981.

56. T. Erdogan, "Fiber grating spectra," IEEE J. Lightwave Technol., Vol. 15, pp. 1277-1294, 1997.

57. T. Erdogan, "Cladding-mode resonances in short- and long-period fiber grating filters," J. Opt. Soc. Am. A, Vol. 14, pp. 1760-1773, 1997.

58. V. Mizrahi and J. E. Sipe, "Optical properties of photosensitive fiber phase gratings," IEEE J. Lightwave Technol., Vol. 11, pp. 1513-1517, 1993.

59. L. Dong, L. Reekie, J. L. Cruz, J. E. Caplen, J. P. de Sandro and D. N. Payne, "Optical fibers with depressed claddings for suppression of coupling into cladding modes in fiber Bragg gratings," IEEE Photon. Technol. Lett., Vol. 9, pp.64-66, 1997.

60. W. W. Morey, G. Meltz, J. D. Love and S. J. Hewlett, "Mode-coupling characteristics of UV-written Bragg gratings in depressed-cladding fibre," Electron. Lett., Vol. 30, pp. 730-732, 1994.

61. J. Albert, K. O. Hill, B. Malo, S. Theriault, F. Bilodeau, D. C. Johnson and L. E. Erickson, "Apodisation of the spectral response of fibre Bragg gratings using a phase mask with variable diffraction efficiency," Electron. Lett., Vol. 31, pp. 222-223, 1995.

62. B. Malo, S. Theriault, D. C. Johnson, F. Bilodeau, J. Albert and K. O. Hill, "Apodised in-fibre Bragg grating reflectors photoimprinted using a phase mask," Electron. Lett., Vol. 31, pp. 223-225, 1995.

63. R. Kashyap, A. Swanton and D. J. Armes, "Simple technique for apodising chirped and unchirped fibre Bragg gratings," Electron. Lett., Vol. 32, pp. 1226-1228, 1996.

64. W. W. Morey, G. Meltz, J. D. Love and S. J. Hewlett, "Mode-coupling characteristics of UV-written Bragg gratings in depressed-cladding fibre," Electron. Lett., Vol. 30, pp. 730-731, 1994.

65. K. O. Hill, B. Malo, K. A. Vineberg, F. Bilodeau, D. C. Johnson and I. Skinner, "Efficient mode conversion in telecommunication fiber using externally written gratings," Electron. Lett., Vol. 26, pp. 1270-1272, 1990.

66. K. O. Hill, F. Bilodeau, B. Malo and D. C. Johnson, "Birefringent photosensitivity in monomode optical fibre: Application to the external writing of rocking filters," Electron. Lett., Vol. 27, pp. 1548-1550, 1991.

67. I. Riant and F. Haller, "Study of the photosensitivity at 193 nm and comparison with photosensitivity at 240 nm influence of fiber tension: Type IIA aging," IEEE J. Lightwave Technol, Vol. 15, pp. 1464-1469, 1997.

68. L. Dong and W. F. Liu, "Thermal decay of fiber Bragg gratings of positive and negative index changes formed at 193 nm in a boron-codoped germanosilicate fiber," Appl. Opt., Vol. 36, pp. 8222-8226, 1997.

69. T. Erdogan, V. Mizrahi, P. J. Lemaire and D. Monoroe, "Decay of ultraviolet-induced fiber Bragg gratings," J. Appl. Phys., Vol. 76, pp. 73-80, 1994.

70. S. R. Baker, H. N. Rourke, V. Baker and D. Goodchild, "Thermal decay of fiber Bragg gratings written in boron and germanium codoped silica fibers," IEEE J. Lightwave Technol., Vol. 15, pp. 1470-1477, 1997.

71. S. Kannan, J. Z. Y. Guo and P. J. Lemaire, "Thermal stability analysis of uv-induced fiber Bragg gratings," IEEE J. Lightwave Technol., Vol. 15, pp. 1478-1483, 1997.

72. H. Patrick, S. L. Gilbert, A. Lidgard and M. D. Gallagher, "Annealing of Bragg gratings in hydrogen-loaded optical fiber," J. Appl. Phys., Vol. 78, pp. 2940-2945, 1995.

73. I. Riant and B. Poumellec, "Thermal decay of gratings written in hydrogen-loaded germanosilicate fibres," Electron. Lett., Vol. 34, pp. 1603-1604, 1998.

74. D. L. Williams and R. P. Smith, "Accelerated lifetime tests on uv written intra-core gratings in boron germania codoped silica fibres," Electron. Lett., Vol. 31, pp. 2120-2121, 1995.

75. R. Feced, M. P. RoeEdwards, S. E. Kanellopoulos, N. H. Taylor and V. A. Handerek, "Mechanical strength degradationof UV-exposed optical fibres," Electron. Lett., Vol. 33, pp. 157-159, 1997.

76. D. Varelas, H. G. Limberger, R. P. Salathe and C. Kotrotsios, "UV-induced mechanical degradation of optical fibres," Electron. Lett., Vol. 33, pp. 804-806, 1997.

77. K. Imamura, T. Nakai, Y. Sudo and Y. Imada, "High reliability tin-codoped germanosilicate fibre Bragg gratings fabricated by direct writing method," Electron. Lett., Vol. 34, pp. 1772-1773, 1998.

78. K. A. Winick, "Effective-index method and coupled-mode theory for almost periodic waveguide gratings: A comparison," Appl. Opt., Vol. 31, pp. 757-764, 1992.

79. M. Yamada and K. Sakuda, "Analysis of almost-periodic distributed feedback slab waveguide via a fundamental matrix approach," Appl. Opt., Vol. 26, pp. 3474-3478, 1987.

80. L. A. Weller-Brophy and D. G. Hall, "Analysis of waveguide gratings: a comparison of the results of Rouard's method and coupled-mode theory," J. Opt. Soc. Am. A, Vol. 4, pp. 60-65, 1987.

81. E. Peral and J. Capmany, "Generalized Bloch wave analysis for fiber Bragg and waveguide gratings," IEEE J. Lightwave Technol., Vo. 15, pp. 1295-1302, 1997.

82. D. M. Bird, J. R. Armitage, R. Kashyap, R. M. A. Fatah and K. H. Cameron, "Narrow line semiconductor laser using fibre grating," Electron. Lett., Vol. 27, pp. 1115-1116, 1991.

83. G. A. Ball and W. H. Glenn, "Design of a single-mode linear-cavity erbium fiber laser utilizing Bragg reflector," IEEE J. Lightwave Technol., Vol. 10, pp. 1338-1343, 1992.

84. G. A. Ball, G. H. Glenn, W. W. Morey and P. K. Cheo, "Modeling of short, single-frequency fiber laser in high-gain fiber," IEEE Photon. Technol. Lett., Vol. 5, pp. 649-651, 1993.

85. V. Mizrahi, D. J. DiGiovanni, R. M. Atkins, S. G. Grubb, Y. K. Park and J. M. P. Delavaux, "Stable single-mode erbium fiber-grating laser for digital communications," IEEE J. Lightwave Technol., Vol. 11, pp. 2021-2025, 1993.

86. A. Othonos, X. Lee and D. P. Tsai, "Spectrally broadband Bragg grating mirror for an erbium-doped fiber laser," Opt. Eng., Vol. 35, pp. 1088-1092, 1996.

87. R. P. Davey, R. P. E. Fleming, K. Smith, R. Kashyap and J. R. Armitage, "Mode-locked erbium fibre laser with wavelength selection by means of fibre Bragg grating reflector," Electron. Lett., Vol. 27, pp. 2087-2088, 1991.

88. P. N. Kean, J. W. D. Gray, I. Bennion and N. J. Doran, "Dispersion-modified actively mode-locked erbium fibre laser using a chirped fibre grating," Electron. Lett., Vol. 30, pp. 2133-2135, 1994.

89. K. O. Hill, D. C. Johnson, F. Bilodeau and S. Faucher, "Narrow-bandwidth optical waveguide transmission filters: A new design concept and applications to optical fibre communications," Electron. Lett., Vol. 23, pp. 464-465, 1987.

90. D. C. Johnson, K. O. Hill, F. Bilodeau and S. Faucher, "New design concept for a narrowband wavelength-selective optical tap and combiner," Electron. Lett., Vol. 23, pp. 668-669, 1987.

91. G. E. Town, K. Sugden, J. A. R. Williams, I. Bennion and S. B. Poole, "Wide-band Febry-Perot-like filters in optical fiber," IEEE Photon. Technol. Lett., Vol. 7, pp. 78-80, 1995.

92. A. Othonos, X. Lee and R. M. Measures, "Superimposed multi Bragg gratings," Electron. Lett., Vol. 30, pp. 1972-1973, 1994.

93. V. Mizrahi, T. Erdogan, D. J. Digiovanni, P. J. Lamaire, W. M. MacDonald, S. G. Kosinski, S. Cabot and J. E. Sipe, "Four channel fibre grating demultiplexer," Electron. Lett., Vol. 30, pp. 780-781, 1994.

94. F. Bilodeau, D. C. Johnson, S. Theriault, B. Malo, J. Albert and K. O. Hill, "All in-fiber dense-wavelength-division multiplexer/demultiplexer using photo-imprinted Bragg gratings," IEEE Photon. Technol. Lett., Vol. 7, pp. 388-390, 1995.

95. J. A. R. William, I. Bennion, K. Sugden and N. J. Doran, "Fibre dispersion compensation using a chirped in fibre Bragg grating," Electron. Lett., Vol. 30, pp. 985-987, 1994.

96. R. Kashyap, S. V. Chernikov, P. F. Mckee and J. R. Taylor, "30ps chromatic dispersion compensation of 400fs pulses at 100Gbit/s in optical fibres using an all fibre photoinduced chirped reflection grating," Electron. Lett., Vol. 30, pp. 1078-1080, 1994.

97. P. A. Krug, T. Stephens, G. Yoffe, F. Ouellette, P. Hill and G. Dhosi, "Dispersion compensation over 270km at 10Gbit/s using an offset-core chirped fibre Bragg grating," Electron. Lett., Vol. 31, pp.1091-1093, 1995.

98. W. H. Loh, R. I. Laming, N. Robinson, A. Cavaciuti, F. Vaninetti, C. J. Anderson, M. N. Zervas and M. J. Cole, "Dispersion compensation over distances in excess of 500km for 10Gbit/s systems using chirped fiber gratings," IEEE Photon. Technol. Lett., Vol. 8, pp. 944-946, 1996.

99. B. J. Eggleton, T. Stephens, P. A. Krug, G. Dhosi, Z. Brodzeli and F. Ouellette, "Dispersion compensation using a fibre grating in transmission," Electron. Lett., Vol. 32, pp. 1610-1611, 1996.

100. B. J. Eggleton, G. Leng, N. Litchinitser, D. B. Patterson and R. E. Slusher, "Implications of fiber grating dispersion for WDM communication systems," IEEE Photon. Technol. Lett, Vol. 9, pp. 1403-1405, 1997.

101. G. M. H. Flockhart, W. N. MacPherson, J. S. Barton, J. D. C. Jones, L. Zhang and I. Bennion, "Departure from linearity of fibre Bragg grating temperature coefficients," Proc. 15th International Conference on Optical Fiber Sensors, Technical Digest, Portland, USA, 6-10 May, 2002, pp.75-78.

102. G. M. H. Flockhart, R. R. J. Maier, J. S. Barton, W. N. MacPherson, J. D. C. Jones, K. E. Chisholm, L. Zhang, I. Bennion, I. Read and P. D. Foote, "Quadratic behavior of fibre Bragg grating temperature coefficients," Appl. Opt., Vol. 43, pp. 2744-2751, 2004.

103. G. Ghosh, "Model for the thermo-optic coefficients of some standard optical glasses," J. Non-Cryst. Solids, Vol. 189, pp. 191-196, 1995.

104. S. Gupta, T. Mizunami, T. Yamao and T. Shimomura, "Fiber Bragg grating cryogenic temperature sensors," Appl. Opt., Vol. 35, pp. 5202-5205, 1996.

105. T. Mizunami, H. Tatehata and H. Kawashima, "High-sensitivity cryogenic fibre-Bragg-grating temperature sensors using teflon substrates," Meas. Sci. Technol., Vol. 12, pp. 914-917, 2001.

106. M. B. Reid and M. Ozcan, "Temperature dependence of fiber optic Bragg gratings at low temperatures," Opt. Eng., Vol. 37, pp. 237-240, 1998.

107. S. W. James, R. P. tatam, A. Twin, M. Morgan and P Noonan, "Strain response of fibre Bragg grating sensors at cryogenic temperatures," Meas. Sci. Technol., Vol. 13, pp. 1535-1539, 2002.

108. S. M. Melle, K. Liu and R. M. Measures, "A passive wavelength demodulation system for guided-wave Bragg grating sensors," IEEE Photon. Technol. Lett., Vol. 4, pp. 516-518, 1992.

109. M. A. Davis and A. D. Kersey, "All fibre Bragg grating strain sensor demodulation technique using a wavelength division coupler," Electron. Lett., Vol. 30, pp. 75-76, 1994.

110. M. A. Davis and A. D. Kersey, "Matched-filter interrogation technique for fibre Bragg grating arrays," Electron. Lett., Vol. 31, pp. 822-823, 1995.

111. M. G. Xu, J.-L. Archambault, L. Reekie and J. P. Dakin, "Discrimination between strain and temperature effects using dual-wavelength fibre grating sensors," Electron. Lett., Vol. 30, pp. 1085-1087, 1994.

112. S. W. James, M. L. Dockney and R. P. Tatam, "Simultaneous independent temperature and strain measurement using in-fibre Bragg grating sensors," Electron. Lett., Vol. 32, pp. 1133-1134, 1996.

113. P. M. Cavaleiro, F. M. Araujo, L. A. Ferreira, J. L. Santos and F. Farahi, "Simultaneous measurement of strain and temperature using Bragg gratings written in germanosilicate and boron-codoped germanosilicate fibers," IEEE Photon. Technol. Lett., Vol. 11, pp. 1635-1637, 1999.

114. H. J. Patrick, G. M. Williams, A. D. Kersey, J. R. Pedrazzani and A. M. Vengsarkar, "Hybrid fiber Bragg grating/long period fiber grating sensor for strain/temperature discrimination," IEEE Photon. Technol. Lett., Vol. 8, pp. 1223-1225, 1996.

115. V. Bhatia, D. Campbell, R. O. Claus and A. M. Vengsarkar, "Simultaneous strain and temperature measurement with long-period gratings," Opt. Lett., Vol. 22, pp. 648-650, 1997.

116. J. Jung, H. Nam, J. H. Lee, N. Park and B. Lee, "Simultaneous measurement of strain and temperature by use of a single-fiber Bragg grating and an erbium-doped fiber amplifier," Appl. Opt., Vol. 38, pp. 2749-2751, 1999.

117. J. Jung, N. Park and B. Lee, "Simultaneous measurement of strain and temperature by use of a single fiber Bragg grating written in an erbium: ytterbium-doped fiber," Appl. Opt., Vol. 39, pp. 1118-1120, 2000.

118. B. O. Guan, H. Y. tam, S. L. Ho, W. H. Chung and X. Y. Dong, "Simultaneous strain and temperature measurement using a single fibre Bragg grating," Electron. Lett., Vol. 36, pp. 1018-1019, 2000.

119. W. C. Du, X. M. tao and H. Y. Tam, "Fiber Bragg grating cavity sensor for simultaneous measurement of strain and temperature," IEEE Photon. Technol. Lett., Vol. 11, pp. 105-107, 1999.

120. B. O. Guan, H. Y. Tam, X. M. Tao and X. Y. Dong, "Simultaneous strain and temperature measurement using a superstructure fiber Bragg grating," IEEE Photon. Technol. Lett., Vol. 12, pp. 675-677, 2000.

121. G. P. Brady, K. Kalli, D. J. webb, D. A. Jackson, L. Reekie and J. L. Archambault, "Simultaneous measurement of strain and temperature using the first- and second-order diffraction wavelengths of Bragg gratings," IEE Proc. – Optoelectron., Vol. 144, pp. 157-161, 1997.

122. J. Echevarria, A. Quintela, C. Jauregui and J. M. Lopez-Higuera, "Uniform fiber Bragg grating first- and second-order diffraction wavelength experimental characterization for strain-temperature discrimination," IEEE Photon. Technol. Lett, Vol. 13, pp. 696-698, 2001.

123. M. A. Davis and A. D. Kersey, "Simultaneous measurement of temperature and strain using fibre Bragg gratings and Brillouin scattering," IEE Proc. – Optoelectron., Vol. 144, pp. 151-155, 1997.

124. O. Frazao, R. Romero, G. Rego, P. V. S. Marques, H. M. Salgado and J. L. santos, "Sampled fibre Bragg grating sensors for simultaneous strain and temperature measurement," Electron. Lett., Vol. 38, pp. 693-695, 2002.

125. X. Shu, Y. Lu, D. Zhao, B. Gwandu, F. Floreani, L. Zhang and I Bennion, "Dependence of temperature and strain coefficients on fiber grating type and its application to simultaneous temperature and strain measurement," Opt. Lett., Vol. 27, pp. 701-703, 2002.

126. F. Farahi, D. J. Webb, J. D. C. Jones and D. A. Jackson, "Simultaneous measurement of temperature and strain: cross-sensitivity considerations," IEEE J. Lightwave Technol., Vol. 8, pp. 138-142, 1990.

127. W. Jin, W. C. Michie, G. Thursby, M. Konstantaki and B. Culshaw, "Simultaneous measurement of strain and temperature: error analysis," Opt. Eng., Vol. 36, pp. 598-609, 1997.

128. R. S. Weis, A. D. Kersey and T. A. Berkoff, "A four-element fiber grating sensor array with phase-sensitive detection," IEEE Photon. Technol. Lett., Vol. 6, pp. 1469-1471, 1994.

129. K. Kalli, G. P. Brady, D. J. Webb, D. A. Jackson, L. Zhang and I. Bennion, "Wavelength division and spatial multiplexing using tandem inetrferometers for Bragg grating sensor networks," Opt. Lett., Vol. 20, pp. 2544-2546, 1995.

130. Y. J. Rao, K. Kalli, G. Brady, D. J. Webb, D. A. Jackson, L. Zhang and I Bennion, "Spatially-multiplexed fibre-optic Bragg grating strain and temperature sensor based on interferometric wavelength-shift detection," Electron. Lett., Vol. 31, pp. 1009-1010, 1995.

131. Y. J. Rao, A. B. L. Ribeiro, D. A. Jackson, L. Zhang and I. Bennion, "Combined spatial- and time-division-multiplexing scheme for fibre grating sensors with drift compensated phase sensitive detection," Opt. Lett., Vol. 20, pp. 2149-2151, 1995.

132. Y. J. Rao, A. B. L. Ribeiro, D. A. Jackson, L. Zhang and I. Bennion, "Simultaneous spatial, time and wavelength division multiplexed in-fibre grating sensor network," Opt. Comm., Vol. 125, pp. 53-58, 1996.

133. G. A. Ball, G. Hullallen, C. Holton and W. W. Morey, "Low noise single frequency linear fibre laser," Electron. Lett., Vol. 29, pp. 1623-1625, 1993.

134. G. A. Ball and W. W. Morey, "Compression tuned single frequency Bragg grating fiber laser," Opt. Lett., Vol. 19, pp. 1979-1981, 1994.

135. G. A. Ball, W. W. Morey and P. K. Cheo, "Single and multipoint fiber laser sensors," IEEE Photon. Technol. Lett., Vol. 5, pp. 267-270, 1993.

136. S. M. Melle, A. T. Alavie, S. Karr, T. Coroy, K. X. Liu and R. M. Measures, "A Bragg grating tuned fiber laser strain sensor system," IEEE Photn. Technol. Lett., Vol. 5, pp. 263-266, 1993.

137. A. Wilson, S. W. James and R. P. Tatam, "Time-division-multiplexed interrogation of fibre Bragg grating sensors using laser diodes," Meas. Sci. Technol., Vol. 12, pp. 181-187, 2001.

138. A. D. Kersey and W. W. Morey, "Multiplexed Bragg grating fibre laser strain sensor system with mode-locked interrogation," Electron. Lett., Vol. 29, pp. 112-114, 1993.

139. G. A. Ball, G. Meltz and W. W. Morey, "Polarimetric heterodyning Bragg grating fiber laser sensor," Opt. Lett., Vol. 18, pp. 1976-1978, 1993.

140. A. D. Kersey and W. W. Morey, "Multi-element Bragg grating based fibre laser strain sensor," Electron. Lett., Vol. 29, pp. 964-966, 1993.

141. A. T. Alavie, S. E. Karr, A. Othonos and R. M. Measures, "A multiplexed Bragg grating fiber laser system," IEEE Photon. Technol. Lett., Vol. 5, pp. 1112-1114, 1993.

142. K. P. Koo and A. D. Kersey, "Bragg grating based laser sensor systems with interferometric interrogation and wavelength division multiplexing," IEEE J. Lightwave Technol., Vol. 13, pp. 1243-1249, 1995.

143. E. J. Friebele, C. G. Askins, M. A. Putnam, A. A. Fosha, J. Florio, R. P. Donti and R. G. Blosser, "Distributed strain sensing with fibre Bragg grating arrays embedded in CRTM composites," Electron. Lett., Vol. 30, pp. 1783-1784, 1994.

144. V. M. Murukeshan, P. Y. Chan, L. S. Ong and A. Asundi, "Intra-core FBG for strain measurement in embedded composite structures," Appl. Opt., Vol. 40, pp. 145-149, 2001.

145. M. J. O'Dwyer, G. M. Maistros, S. W. james, R. P. Tatam and I. K. Partridge, "Relating the state of cure to the real-time internal strain development in a curing composite using in-fibre Bragg gratings and dielectric sensors," Meas. Sci. Technol., Vol. 9, pp. 1153-1158, 1998.

146. E. J. Friebele et al., "Fiber Bragg grating strain sensors: present and future applications in smart structures," Optics and Photonics News, Vol. 9, pp. 33-37, 1998.

147. D. R. Hjelme, L. Bjerkan, S. Neegard, J. S. rambech and J. V. Aarsnes, "Application of Bragg grating sensors in the characterization of scaled marine vehicle models," Appl. Opt., Vol. 36, pp. 328-336, 1997.

148. G. Wang et al., "Digital demodulation and signal processing applied to fiber Bragg grating strain sensor arrays in monitoring transient loading effects on ship hulls," Proc. Int. Conference Optical Fiber Sensor (OFS-12), Williamsburg, USA, 28-31 Oct., 1997, pp. 66-71.

149. Y. M. Gebremichael, W. Li, B. T. Meggitt, W. J. O. Boyle, K. T. V. Grattan, B. McKinley, G. F. Fernando, G. Kister, D. Winter, L. Cunning and S. Luke, "Structurally embedded fibre Bragg grating sensor arrays for design evaluation assessment in Europe's first all-fibre reinforced polymer composite public road Bridge," Proc. Int. Conference on Optical Fibre Sensor (OFS-16), Nara, Japan, 13-17 Oct., 2003, pp. 376-379.

150. Y. M. Gebremichael, W. Li, B. T. Meggitt, W. J. O. Boyle, K. T. V. Grattan, B. McKinley, L. F. Boswell, K. A. Aarnes, S. E. Aasen, B. Tynes, P. Y. Fonjallaz and T. Triantafillou, "A field deployable, multiplexed Bragg grating sensor system used in an extensive highway bridge monitoring evaluation tests," IEEE Sensors (Accepted for publication).

151. Y. J. Rao, D. J. Webb, D. A. Jackson, L. Zhang and I. Bennion, "In-fiber Bragg-grating temperature sensor system for medical applications," IEEE J. Lightwave Technol., Vol. 15, pp. 779-785, 1997.

152. Y. J. Rao et al., "In-situ temperature monitoring in NMR machines with a prototype in-fiber Bragg grating sensors system," Proc. Int. Conference Optical Fiber Sensor (OFS-12), Williamsburg, USA, 28-31 Oct., 1997, pp. 646-649.

153. Y. J. Rao et al., "In-fiber Bragg grating flow-directed thermodilution catheter for cardiac monitoring," Proc. Int. Conference Optical Fiber Sensor (OFS-12), Williamsburg, USA, 28-31 Oct., 1997, pp. 354-357.

154. L. Dong, J. L. Cruz, L. Reekie, M. G. Xu and D. N. Payne, "Enhanced photosensitivity in tin-codoped germanosilicate optical fibers," IEEE Photon. Technol. Lett., Vol. 7, pp. 1048-1050, 1995.

155. G. Brambilla, V. Pruneri and L. Reekie, "Photorefractive index gratings in SnO_2:SiO_2 optical fibers," Appl. Phys. Lett., Vol. 76, pp. 807-809, 2001.

156. G. Brambilla and V. Pruneri, "Enhanced photorefractivity in tin-doped silica optical fibers (Review)," IEEE J. Sel. Top. Quantum Electron., Vol. 7, pp. 403-408, 2001.

157. G. Brambilla and H. Rutt, "Fiber Bragg gratings with enhanced thermal stability," Appl. Phys. Lett., Vol. 80, pp. 3259-3261, 2002.

158. K. O. Hill, B. Malo, F. Bilodeau, D. C. Johnson and J. Albert, "Bragg gratings fabricated in monomode photosensitive optical fiber by UV exposure through a phase mask," Appl. Phys. Lett., Vol. 62, pp. 1035-1037, 1993.

159. L. Dong, W. F. Liu and L. Reekie, "Negative-index gratings formed by a 193-nm excimer laser," Opt. Lett., Vol. 21, pp. 2032-2034, 1996.

160. Q. Wang, A. Hidayat, P. Niay and M. Douay, "Influence of blanket postexposure on the thermal stability of the spectral characteristics of gratings written in a telecommunication fiber using a light at 193 nm," IEEE J. Lightwave Technol., Vol. 18, pp. 1078-1083, 2000.

161. B. O. Guan, H. Y. Tam, X. M. Tao and X. Y. Dong, "Highly stable fiber Bragg gratings written in hydrogen-loaded fiber," IEEE Photon. Technol. Lett., Vol. 12, pp. 1349-1351, 2000.

162. K. P. Chen and P. R. Herman, "Enhancement and tuning of fibre Bragg grating reflection by 157 nm F_2-laser post exposure," Electron. Lett., Vol. 37, pp. 822-823, 2001.

163. K. P. Chen, P. R. Herman and R. Tam, "Strong fiber Bragg grating fabrication by hybrid 157- and 248-nm laser exposure," IEEE Photon. Technol. Lett., Vol. 14, pp. 170-172, 2002.

164. C. J. Paddison, J. M. Dawes, D. J. W. Brown, M. J. Withford, R. I. Trickett and P. A. Krug, "Multiple fibre gratings fabricated using frequency-doubled copper vapour lasers," Electron. Lett., Vol. 34, pp. 2407-2408, 1998.

165. A. Dragomir, D. N. Nikogosyan, A. A. Ruth, K. A. Zagorul'ko and P. G. Kryukov, "Long-period fibre grating formation with 264 nm femtosecond radiation," Electron. Lett., Vol. 38, pp. 269-271, 2002.

166. S. J. Mihailov, C. W. Smelser, P. Lu, R. B. Walker, D. Grobnic and H. Ding, "Fiber Bragg gratings (FBG) made with a phase mask and 800 nm femtosecond radiation," Post deadline paper, Optical Fiber Communication Conference (OFC-2003), Atlanta, USA, 23-28 March, 2000.

167. D. D. Davis, T. K. Gaylord, E. N. Glytsis, S. G. Kosinski, S. C. Mettler and A. M. Vengsarkar, "Long-period grating fabrication with focused CO_2 laser pulses," Electron. Lett., Vol. 34, pp. 302-303, 1998.

168. Y. Shen, J. He, T. Sun and K. T. V. Grattan, "High temperature sustainability of strong fiber Bragg gratings written into Sb-Ge-codoped photosensitive fiber: decay mechanisms involved during annealing," Opt. Lett., Vol. 29, pp. 554-556, 2004.

169. S. Pal, J. Mandal, T. Sun and K. T. V. Grattan, "High temperature sensor potential of Bragg gratings fabricated in different photosensitive fibres," Proc. Applied Optics and Optoelectronics Conference (Photon02), Cardiff, UK, 2-5 Sept., 2002, pp. 49-50.

170. T. Sun, S. Pal, J. Mandal and K. T. V. Grattan, "Fibre Bragg grating fabrication using fluoride excimer laser for sensing and communication applications," Central Laser Facility Annual Report 2001/2002, pp. 147-149, Rutherford Appleton laboratory, Oxfordshire, UK, 2002.

171. L. Dong, V. N. Bagratashvili, S. I. Tsypina, Y. S. Zavorotny, A. O. Rybaltovskii, P. V. Chernov, S. S. Alimpiev and Y. O. Simanovskii, "One photon and two photon process in photo-decomposition of germanium oxygen deficient centres," Japanese J. Appl. Phys., Vol. 37, pp. 12-14, 1998.

172. P. L. Swart, M. G. Shlyagin, A. A. Chtcherbakov and V. V. Spirin, "Photosensitivity measurement in optical fibre with Bragg grating interferometers," Electron. Lett., Vol. 38, pp. 1508-1510, 2002.

173. J. Albert, B. Malo, K. O. Hill, F. Bilodeau, D. C. Johnson and S. Theriault, "Comparison of one-photon and two-photon effects in the photosensitivity of germanium-doped silica optical fibers exposed to intense ArF excimer laser pulses," Appl. Phys. Lett., Vol. 67, pp. 3529-3531, 1995.

174. W. X. Xie, M. Douay, P. Bernage, P. Niay, J. F. Bayon and T. Georges, "Second order diffraction efficiency of Bragg gratings written within germanosilicate fibers," Opt. Commn., Vol. 101, pp. 85-91, 1993.

175. S. Pal, J. Mandal, T. Sun, K. T. V. Grattan, M. Fokine, F. Carlsson, P. Y. Fonjallaz, S. A. Wade and S. F. Collins, "Characteristics of potential fibre Bragg grating sensor-based devices at elevated temperatures," Meas. Sci. Technol., Vol. 14, pp. 1131-1136, 2003.

176. M. Fokine, "Thermal stability of chemical composition gratings in fluorine-germanium-doped silica fibers," Opt. Lett., Vol. 27, pp. 1016-1018, 2002.

177. M A Fokine, B E Sahlgren, R Stubbe, "A novel approach to fabricate high-temperature resistant fiber Bragg gratings", Proceedings of Bragg Gratings, Photosensitivity, and Poling in Glass Fibers and Waveguides: Applications and Fundamentals, Vol. 17, pp. 58-60, 1997.

178. M Fokine, "Formation of thermally stable chemical composition gratings in optical fibers," J. Opt. Soc. Am. B, Vol. 19, pp. 1759-1765, 2002.

179. D. Razafimahatratra, P. Niay, M. Douay, B. Poumellec and I. Riant, "Comparison of isochronal and isothermal decays of Bragg gratings written through continuous-wave exposure of an unloaded germanosilicate fiber," Appl. Opt., Vol. 39, pp. 1924-1933, 2000.

180. K. E. Chisholm, K. Sugden and I. Bennion, "Effects of thermal annealing on Bragg fibre gratings in boron/germanium co-doped fibre," J. Phys. D: Appl. Phys., Vol. 31, pp. 61-64, 1998.

181. S. Pal, J. Mandal, T. Sun and K. T. V. Grattan, "Analysis of thermal decay and prediction of operational lifetime for a type I boron-germanium codoped fiber Bragg grating," Appl. Opt., Vol. 42, pp. 2188-2197, 2003.

182. S. Pal, T. Sun, K. T. V. Grattan, S. A. Wade, S. F. Collins, G. W. Baxter, B. Dussardier and G. Monnom, "Bragg grating performance in Er-Sn-doped germanosilicate fiber for simultaneous measurement of wide range temperature (to 500°C) and strain," Rev. Sci. Instrum., Vol. 74, pp.4858-4862, 2003.

183. Y. H. Shen, S. Pal, J. Mandal, T. Sun, K. T. V. Grattan, S. A. Wade, S. F. Collins, G. W. Baxter, B. Dussardier and G. Monnom, "Investigation of the photosensitivity, temperature sustainability and fluorescence characteristics of several Er-doped photosensitive fibers," Opt. Commn., Vol. 237, pp. 301-308, 2004.

184. A. Hidayat, Q. Wang, P. Niay, M. Douay, B. Poumellec and I. Riant, "Temperature-induced reversible changes in the spectral characteristics of fibre Bragg gratings," Appl. Opt., Vol. 40, pp. 2632-2641, 2002.

185. M. J. LuValle, L. R. Copeland, S. Kannan, J. B. Judkins and P. J. Lemaire, "A strategy for extrapolation in accelerated testing," Bell Labs. Tech. Jour., July-Sept., pp. 139-147, 1998.

186. B. Poumellec, "Links between writing and erase (or stability) of Bragg gratings in disordered media," J. Non-Cryst. Solids., Vol. 239, pp. 108-115, 1998.

187. Y. Imai and T. Hokazono, "Fluorescence-based temperature sensing using erbium-doped optical fibers with 1.48 μm pumping," Opt. Rev., Vol. 4, pp. 117-120, 1997.

188. S. A. Wade, D. I. Forsyth, Q. Guofu and K. T. V. Grattan, "Fiber optic sensor for dual measurement of temperature and strain using a combined fluorescent lifetime decay and fiber Bragg grating technique," Rev. Sci. Instrum., Vol. 72, pp. 3186-3190, 2001.

189. N. Chiodini, A. Paleari, G. Spinolo, A. Chiasera, M. Ferrari, G. Brambilla and E. R. Taylor, "Photosensitive erbium doped tin-silicate glass," J. Non-Cryst. Solids, Vol. 239, pp. 217-222, 2002.

190. S. Pal, T. Sun, K. T. V. Grattan, S. A. Wade, S. F. Collins, G. W. Baxter, B. Dussardier and G. Monnom, "Bragg gratings written in Sn-Er-Ge codoped silica fiber: investigation of photosensitivity, thermal stability and sensing potential," J. Opt. Soc. Am. A, Vol. 21, pp. 1503-1511, 2004

191. J. Rathje, M. Kristensen and J. E. Pedersen, "Continuous anneal method for characterizing the thermal stability of ultraviolet Bragg gratings," J. Appl. Phys., Vol. 88, pp. 1050-1055, 2000.

192. D. I. Forsyth, S. A. Wade, T. Sun, X. Chen and K. T. V. Grattan, "Dual temperature and strain measurement using the combined fluorescence lifetime and Bragg wavelength approach in doped optical fiber," Appl. Opt., Vol. 41, pp. 6585-6592, 2002.

193. S. Pal, T. Sun, K. T. V. Grattan, S. A. Wade, S. F. Collins, G. W. Baxter, B. Dussardier and G. Monnom, "Non-linear temperature dependence of Bragg gratings written in different fibres, optimised for sensor applications over a wide range of temperatures," Sensors and Actuators A: Physical, Vol. 112, pp. 211-219, 2004.

194. G. Ghosh, "Temperature dispersion of refractive-indexes in some silicate fiber glasses," IEEE Photon. Technol. Lett., Vol. 6, pp. 431-433, 1994.

195. J. Matsuoka, N. Kitamura, S. Fujinaga, T. Kitaoka and H. Yamahita, "Temperature-dependence of refractive-index of SiO_2 glass," J. Non-Cryst. Solids., Vol. 135, pp.86-89, 1991.

196. G. M. H. Flockhart, R. McBride, W. N. MacPherson, J. D. C. Jones, K. E. Chisholm, L. Zhang, I. Bennion, I. Read and P. Foote, "Application of Hilbert transformations to high resolution strain and temperature characterisation of fibre Bragg grating sensors," Proc. SPIE, Int. Conference on Optical Fibre Sensor (OFS-14), Venice, Italy, 11-13 Oct., 2000, Vol. 4185, pp. 376-379.

197. S. Trpkovski, S. A. Wade, G. W. Baxter and S. F. Collins, "Dual temperature and strain sensor using a combined fiber Bragg grating and fluorescence intensity ratio technique in Er^{3+}-doped fiber," Rev. Sci. Instrum., Vol. 74, pp. 2880-2885, 2003.

198. Y. C. Lai, G. F. Qiu, W. Zhang, L. Zhang, I. Bennion and K. T. V. Grattan, "Amplified spontaneous emission-based technique for simultaneous measurement of temperature and strain by combining active fiber with fiber gratings," Rev. Sci. Instrum., Vol. 73, pp. 3369-3372, 2002.

199. S. A. Wade, G. W. Baxter, S. F. Collins, K. T. V. Grattan and T. Sun, "Simultaneous strain-temperature measurement using fluorescence from Yb-doped silica fiber," Rev. Sci. Instrum., Vol. 71, pp. 2267-2269, 2000.

200. S. E. Kanellopoulos, V. A. Handerek and A. J. Rogers, "Simultaneous strain and temperature sensing with photogenerated in-fiber gratings," Opt. Lett., Vol. 20, pp. 333-335, 1995.

201. W. C. Du, X. M. Tao, H. Y. Tam, "Fiber Bragg grating cavity sensor for simultaneous measurement of strain and temperature," IEEE Photon. Technol. Lett., Vol. 11, pp. 105-107, 1999.

202. M. A. Davis and A. D. Kersey, "Simultaneous measurement of temperature and strain using fibre Bragg gratings and Brillouin scattering," IEE Proc.-Optoelectron., Vol. 144, pp. 151-155, 1997.

203. O. Frazao, M. J. N. Lima and J. L. Santos, "Simultaneous measurement of strain and temperature using type I and type IIA fibre Bragg grating," J. Opt. A: Pure Appl. Opt., Vol. 5, pp. 183-185, 2003.

204. Y. H. Shen, T. Sun, K. T. V. Grattan and M. Sun, "Highly photosensitive Sb/Er/Ge-codoped silica fiber for writing fiber Bragg gratings with strong high-temperature sustainability," Opt. Lett., Vol. 28, pp. 2025-2027, 2003.

205. S. A. Wade, S. F. Collins, K. T. V. Grattan and G. W. Baxter, "Strain-independent temperature measurement by use of a fluorescence intensity ratio technique in optical fiber," Appl. Opt., Vol. 39, pp. 3050-3052, 2000.

206. S. A. Wade, S. F. Collins, G. W. Baxter and G. Monnom, "Effect of strain on temperature measurements using fluorescence intensity ratio technique (with Nd^{3+}- and Yb^{3+}-doped silica fibers), ", Rev. Sci. Instrum., Vol. 72, pp. 3180-3185, 2001.

207. E. Maurice, S. A. Wade, S. F. Collins, G. Monnom and G. W. Baxter, "Self-referenced point temperature sensor based on a fluorescence intensity ratio in Yb^{3+}-doped silica fiber," Appl. Opt., Vol. 36, pp. 8264-8269, 1997.

208. E. Desurvire and J. R. Simpson, "Evaluation of $^4I_{15/2}$ and $^4I_{13/2}$ Stark-level energies in erbium-doped aluminosilicate glass fibers," Opt. Lett., Vol. 15, pp. 547-549, 1990.

209. P. A. Krug, M. G. Sceats, G. R. Atkins, S. C. Guy and S. B. Poole, "Intermediate excited-state absorption in erbium-doped fiber strongly pumped at 980-nm," Opt. Lett., Vol. 16, pp. 1976-1978, 1991.

210. S. Pal, Y. H. Shen, J. Mandal, T. Sun and K. T. V. Grattan, "Simultaneous measurement of strain (to 2000 με) and temperature (to 600°C) using a combined fluorescence and grating-based technique," IEEE Sensors (Accepted for publication).

211. S. Pal, T. Sun, K. T. V. Grattan, S. A. Wade, S. F. Collins, G. W. Baxter, B. Dussardier and G. Monnom, "Strain-independent temperature measurement using a type-I and type-IIA optical fiber Bragg grating combination," Rev. Sci. Instrum., Vol. 75, pp.1327-1331, 2004.

212. W. J. Miniscalco, "Erbium-doped glasses for fiber amplifiers at 1500 nm," IEEE J. Lightwave Technol., Vol. 9, pp. 234-250, 1991.

213. G. A. Ball, W. W. Morey and W. H. Glenn, "Standing-wave monomode erbium fiber laser," IEEE Photon Technol. Lett., Vol. 3, pp. 613-615, 1991.

214. S. L. Gilbert, "Frequency stabilization of a tunable erbium-doped fiber laser," Opt. Lett., Vol. 16, pp. 150-152, 1991.

215. P. Barnsley, P. Urquhart, C. Millar and M. Brierley, " Fiber Fox-Smith resonator: application to single-longitudinal-mode operations of fiber lasers," J. Opt. Soc. Am. A, Vol. 5, pp. 1339-1346, 1988.

216. G. J. Cowle, D. N. Payne and D. Reid, "Single-frequency travelling-wave erbium-doped fiber loop laser," Electron. Lett., Vol. 27, pp. 229-230, 1991.

217. B. Y. Kim, "Fiber lasers in optical sensors," in Optical fiber technology, Vol. 2: Devices and technology, Eds. K. T. V. Grattan and B. T. Meggitt, Chapman and Hall, London, UK, pp.99-115, 1998.

218. J. Mandal, S. Pal, T. Sun, K. T. V. Grattan and A. T. Augousti, "Optimization of erbium-doped fibre lasers and their sensor applications," Proc. Sensors and Applications XII, 2-4 Sept., 2003, University of Limerick, Ireland, pp. 271-278.

219. Z. Y. Zhang, K. T. V. Grattan, A. W. Palmer, B. T. Meggitt and T. Sun, "Characterization of erbium-doped intrinsic optical fiber sensor probes at high temperatures," Rev. Sci. Instrum., Vol. 69, pp. 2924-2929, 1998.

220. S. Kim, J. Kwon, S. Kim and B. Lee, "Temperature-independent strain sensor using a chirped grating partially embedded in a glass tube," IEEE Photon. Technol. Lett., Vol. 12, pp. 678-680, 2000.

221. J. Mandal, S. Pal, T. Sun, K. T. V. Grattan, A. T. Augousti and S. A. Wade, "Bragg grating-based fibre optic laser probe for temperature sensing," IEEE Photon. Technol. Lett., Vol. 16, pp. 218-220, 2004.

222. J. Mandal, S. Pal, W. Zhao, T. Sun, K. T. V. Grattan and S. A. Wade, "A novel high temperature sensor based on a compact rare earth fibre laser approach," Tech. Digest: International Conference on Optical Fiber Sensors (OFS-16), 13-17 Oct., 2003, Nara, Japan, pp. 200-203.

223. J. Mandal, T. Sun, K. T. V. Grattan, A. T. Augousti, S. A. Wade, S. F. Collins, G. W. Baxter, B. Dussardier and G. Monnom, "A wide temperature tunable fibre laser using a

chirped grating and a type IIA fibre Bragg grating," Meas. Sci. Technol., Vol. 15, pp. 1113-1119, 2004.

224. J. Mandal, Y. H. Shen, S. Pal, T. Sun, K. T. V. Grattan and A. T. Augousti, "Wide range temperature and strain measurement using Bragg grating based fibre laser approach," Proc. Second European Workshop on Optical Fibre Sensors (EWOFS'04), 9-11 June, 2004, Santander, Spain, pp. 156-159.

225. Y. H. Shen, J. Xia, T. Sun and K. T. V. Grattan, "Photosensitive indium-doped germano-silica fiber for strong FBGs with high temperature sustainability," IEEE Photon. Technol. Lett., Vol. 16, pp. 1319-1321, 2004.

226. O. V. Butov, K. M. Golant and I. V. Nikolin, "Ultra-thermo-resistant Bragg gratings written in nitrogen-doped silica fibres," Electron. Lett., Vol. 38, pp. 523-525, 2002.

227. X. Shu, T. Allsop, B. Gwandu, L. Zhang and I. Bennion, "High-temperature sensitivity of long-period gratings in B-Ge codoped fibers," IEEE Photon. Technol. Lett., Vol. 13, pp. 818-820, 2001.

228. K. Hotate, "Trends and prospects for optical distributed sensing: fibre optic nurve systems for smart materials and smart structures," Proc. Second European Workshop on Optical Fibre Sensors (EWOFS'04), 9-11 June, 2004, Santander, Spain, SPIE Vol. 5502, pp. 51-58.

229. T. L. Yeo, T. Sun, K. T. V. Grattan, D. Parry, R. Lade and B. D. Powell, "Polymer-coated fiber Bragg grating for relative humidity sensing," IEEE Sensors (Accepted)

230. T. L. Yeo, T. Sun, K. T. V. Grattan, D. Parry, R. Lade and B. D. Powell, "Characterisation of a fibre Bragg grating based relative humidity sensor," Photon04 (Accepted for presentation).

231. S. W. James and R. P. Tatam, "Optical fibre long-period grating sensors: characteristics and application," (Review article), Meas. Sci. Technol., Vol. 14, pp. R49-R61, 2003.

232. P. Palai, M. N. Satyanarayan, M. Das, K. Thyagarajan and B. P. Pal, "Characterisation and simulation of long period gratings fabricated using electric discharge," Opt. Commn, Vol. 193, pp. 181-185, 2001.

233. X. Shu, T. Allsop, B. Gwandu, L. Zhang and I. Bennion, "High temperature sensitivity of long-period gratings in B-Ge codoped fiber," IEEE Photon. Technol. Lett., Vol. 13, pp. 818-820, 2001.

234. S. Khaliq, S. W. James and R. P. Tatam, "Enhanced photosensitivity fibre optic long period gratingh temperature sensor, " Meas. Sci. Technol., Vol. 13, pp. 792-795, 2002.

235. V. Bhatia and A. M. Vengsarkar, "Optical fiber long-period grating sensors," Opt. Lett., Vol. 21, pp. 692-694, 1996.

236. H. J. Patrick, A. D. Kersey and F. Bucholtz, "Analysis of the response of long period fiber gratings to external index of refraction," IEEE J. Lightwave Technol., Vol. 16, pp. 1606-1612, 1998.

Appendix I

Guided wave propagation and the coupled mode theory

A1.1. Guided wave propagation

The theory of FBGs may be developed by considering the propagation of modes in an optical fibre. The relationship between the modes and the refractive index perturbation in a grating plays an important role on the overall efficiency. Before discussing the coupled-mode theory, the fundamentals of the guided wave propagation are discussed briefly in this section.

For an optical waveguide (assuming the material is non-ferromagnetic and source-free dielectric), Maxwell's equations can be written as

$$\nabla \cdot \mathbf{B} = 0 \tag{A1.1}$$

$$\nabla \cdot \mathbf{D} = 0 \tag{A1.2}$$

$$\nabla \times \mathbf{E} = -\partial \mathbf{B}/\partial t \tag{A1.3}$$

$$\nabla \times \mathbf{H} = \mathbf{J} + \partial \mathbf{D}/\partial t \tag{A1.4}$$

with the constitutive relations

$$\mathbf{D} = \varepsilon_o \mathbf{E} + \mathbf{P} \tag{A1.5}$$

$$\mathbf{B} = \mu_o \mathbf{H} \tag{A1.6}$$

where **B** and **H** are the magnetic flux and field vectors, respectively; ε_o is the dielectric constant and μ_o is the magnetic permeability; **D** is the electric displacement vector; **E** is the electric field vector; **J** is the conduction current and **P** is the induced polarisation vector, which may be expressed as

$$\mathbf{P} = \varepsilon_o \chi_{ij} \mathbf{E} \tag{A1.7}$$

where the linear susceptibility, χ_{ij}, is related to the permittivity tensor, ε_{ij}, through the equation

$$\varepsilon_{ij} = 1 + \chi_{ij} \tag{A1.8}$$

Assuming the conduction current (J) in the optical waveguide is zero and using Eq. (A1.5), in Eq. (A1.4)

$$\nabla \times \mathbf{H} = \partial/\partial t[\varepsilon_o \mathbf{E} + \mathbf{P}] \tag{A1.9}$$

Now, taking the '**curl**' of Eq.(A1.3), and using Eqs.(A1.1), (A1.6) and (A1.9)

$$\nabla \times \nabla \times \mathbf{E} = -\partial/\partial t[\nabla \times \mathbf{B}]$$

or, $\text{grad}(\nabla \cdot \mathbf{E}) - \nabla^2\mathbf{E} = -\mu_o \partial/\partial t[\nabla \times \mathbf{H}]$

or, $\nabla^2\mathbf{E} = \mu_o \partial^2/\partial t^2[\varepsilon_o\mathbf{E} + \mathbf{P}]$

or, $\nabla^2\mathbf{E} = \mu_o \varepsilon_o \partial^2\mathbf{E}/\partial t^2 + \mu_o \partial^2\mathbf{P}/\partial t^2$ (A1.10)

Eq.(A1.10) can be rewritten, using Eqs.(A1.7) and (A1.8), as

$$\nabla^2\mathbf{E} = \mu_o \varepsilon_o \partial^2\mathbf{E}/\partial t^2 + \varepsilon_o \mu_o \chi_{ij} \partial^2\mathbf{E}/\partial t^2$$

or, $\nabla^2\mathbf{E} = \mu_o \varepsilon_o \varepsilon_{ij} \partial^2\mathbf{E}/\partial t^2$ (A1.11)

which is commonly known as the 'wave equation'.

In the ideal-mode approximation, the transverse component of the electric field can be written as a superposition of the ideal modes labelled, j, such that

$$\mathbf{E}_t(x, y, z, t) = \sum [A_j(z)\exp(i\beta_j z) + B_j(z)\exp(-i\beta_j z)]\cdot\mathbf{e}_{jt}(x, y)\exp(-i\omega t) \quad \text{(A1.12)}$$

where $A_j(z)$ and $B_j(z)$ are the slowly varying amplitudes of the j-th mode travelling in the +z and –z directions, respectively. The transverse mode fields, $\mathbf{e}_{jt}(x, y)$, might describe the core-modes or the radiation LP-modes or the cladding-modes [56].

The fields (as expressed in Eq. (A1.12)) satisfy the same wave equation, Eq. (A1.11), as well as being bounded by the waveguide. The mode fields in the core are J-Bessel functions and in the claddings are K-Bessel functions. In general, the solutions of each of these functions are two sets of orthogonally polarised modes. The transverse fields for μ-th x-polarised mode in the core that satisfy the wave equation, are given by [7]

$$\xi_x = \mathbf{C}_\mu \mathbf{J}_\mu(ur/a)\{\cos(\mu\phi)\} \quad \text{(A1.13)}$$
$$\{\sin(\mu\phi)\}$$

$$\mathbf{H}_y = n_{eff}\,(\varepsilon_o\mu_o)^{1/2}\,\xi_x \quad \text{(A1.14)}$$

The corresponding fields in the cladding are

$$\xi_x = \mathbf{C}_\mu [\mathbf{J}_\mu(u)/\mathbf{K}_\mu(w)]\mathbf{K}_\mu(wr/a)\{\cos(\mu\phi)\} \quad \text{(A1.15)}$$
$$\{\sin(\mu\phi)\}$$

$$\mathbf{H}_y = n_{eff}\,(\varepsilon_o\mu_o)^{1/2}\,\xi_x \quad \text{(A1.16)}$$

where the used normalised parameters in the above equations are

$$v = (2\pi a/\lambda)\,(n_{co}^2 - n_{cl}^2)^{1/2} \quad \text{(A1.17)}$$

$$u = (2\pi a/\lambda)\,(n_{co}^2 - n_{eff}^2)^{1/2} \quad \text{(A1.18)}$$

$$w = (v^2 - u^2)^{1/2} \quad \text{(A1.19)}$$

where a is the radius of the fibre core and

$$n_{eff} = n_{cl}\{b[(n_{co} - n_{cl})/n_{cl}] + 1\} \quad \text{(A1.20)}$$

where n_{eff} is the effective index of the mode and the normalised parameter, b, can be expressed as

$$b = w^2/u^2 \qquad \text{(A1.21)}$$

Assuming only a single polarisation for a perfectly circular non-birefringent fibres, the power carried in the mode can be evaluated from the Poynting's vector relationship (i.e., $|A_\mu|^2$) and the normalisation constant, $\mathbf{C}_\mu$, can be expressed as [7]

$$\mathbf{C}_\mu = (2w/av)\ \{(\mu_o/\varepsilon_o)^{1/2}/[n_{eff}\,\pi e_\mu\,|\,\mathbf{J}_{\mu-1}(u)\,\mathbf{J}_{\mu+1}(u)\,|\,]\}^{1/2} \qquad \text{(A1.22)}$$

where $e_\mu = 2$ for fundamental mode ($\mu = 0$) and $e_\mu = 1$ for other higher order modes ($\mu \neq 0$). Matching the fields at the core-cladding boundary, for the LP modes, results in the waveguide characteristic eigen-value equation as

$$u\,[\mathbf{J}_{\mu\pm1}(u)/\mathbf{J}_\mu(u)] = \pm\, w\,[\mathbf{K}_{\mu\pm1}(w)/\mathbf{K}_\mu(w)] \qquad \text{(A1.23)}$$

which may be solved to calculate the values of the propagation constants of various modes.

2.5.3. Coupled-mode theory

A quantitative analysis of a fibre grating in terms of diffraction efficiency and spectral response can be done by using the coupled-mode theory. The analysis may be started with the equation for the transverse component of the electric field as a superposition of ideal modes, which has been expressed by Eq. (A1.12). While the modes are orthogonal in an ideal waveguide, they do not exchange energy. However, the presence of a dielectric perturbation creates the modes to be coupled to each other so that the amplitudes A_j and B_j of the j-th mode evolve along the length of fibre axis (z-axis) according to [56]

$$dA_j/dz = i\,\sum A_k(K^t_{kj} + K^z_{kj})\,\exp[i(\beta_k - \beta_j)z]$$

$$+\, i\,\sum B_k(K^t_{kj} - K^z_{kj})\,\exp[-i(\beta_k + \beta_j)z] \qquad \text{(A1.24)}$$

$$dB_j/dz = -i\,\sum A_k(K^t_{kj} - K^z_{kj})\,\exp[i(\beta_k + \beta_j)z]$$

$$-\, i\,\sum B_k(K^t_{kj} + K^z_{kj})\,\exp[-i(\beta_k - \beta_j)z] \qquad \text{(A1.25)}$$

The transverse coupling coefficient between modes j and k, in above two equations, is given by

$$K^t_{kj}(z) = (\omega/4)\iint_{\infty} dx\,dy\,\Delta\varepsilon(x, y, z)\,\mathbf{e}_{kt}(x, y)\cdot\mathbf{e}^*_{jt}(x, y) \qquad \text{(A1.26)}$$

where $\Delta\varepsilon$ is the perturbation in the permittivity, which is approximately equal to $2n\delta n$ for $\delta n << n$ (i.e., for weakly guided modes or LP modes). The longitudinal coefficient, $K^z_{kj}(z)$, can be defined in the similar way. However, $K^z_{kj}(z) << K^t_{kj}(z)$ for fibre modes, and thus is neglected.

In most of the photosensitive fibres, the UV-induced refractive index change, $\delta n(x, y, z)$, is almost uniform across the core and negligible in the cladding. With this assumption and defining two new coefficients

$$\sigma_{kj}(z) = (\omega n_{co}/2)\, \underline{\delta n}_{co}(z) \iint_{core} dx\, dy\, \mathbf{e}_{kt}(x, y) \cdot \mathbf{e}^{*}_{jt}(x, y) \qquad \text{(A1.27)}$$

$$\kappa_{kj}(z) = (v/2)\, \sigma_{kj}(z) \qquad \text{(A1.28)}$$

where κ is an "ac" component of the coupling coefficient, superimposed on a "dc" component of it, σ, with a visibility factor of v, the coupling coefficient can now be written as

$$K^{t}_{kj}(z) = \sigma_{kj}(z) + 2\kappa_{kj}(z) \cos[(2\pi/\Lambda) + \phi(z)] \qquad \text{(A1.29)}$$

For Bragg gratings, the wavelength for which reflection of a mode of amplitude, A(z), is coupled dominantly into an identical counter-propagating mode of amplitude, B(z), gives the Bragg resonance condition. Under such condition, Eqs.(A1.24) and (A1.25) may be simplified as [54],[56]

$$dR/dz = i\, \sigma'\, R(z) + i\, \kappa\, S(z) \qquad \text{(A1.30)}$$

$$dS/dz = -i\, \sigma'\, S(z) - i\, \kappa^{*}\, R(z) \qquad \text{(A1.31)}$$

where $R(z) = A(z) \exp(i\delta z - \phi/2)$ and $S(z) = B(z) \exp(-i\delta z + \phi/2)$. In these equations, κ is the "ac" coupling coefficient, and the "dc" self-coupling coefficient, σ, can be defined as

$$\sigma' = \delta + \sigma - (½)(d\phi/dz) \qquad \text{(A1.32)}$$

The de-tuning factor, δ, is independent of z and can be defined as

$$\delta = \beta - (\pi/\Lambda)$$
$$= 2\pi n_{eff}\, [(1/\lambda) - (1/\lambda_D)] \qquad \text{(A1.33)}$$

where $\lambda_D = 2n_{eff}\, \Lambda$, is the 'designed Bragg wavelength' for an infinitesimally weak grating ($\delta n_{eff} \rightarrow 0$). It may be noted that if $\delta = 0$, then $\lambda = 2n_{eff}\, \Lambda$, which satisfies the Bragg condition as predicted in the earlier section. The absorption loss in the grating can be described through a complex power loss coefficient, $\alpha = 2\, \mathrm{Im}(\sigma)$, and the derivative, $(1/2)(d\phi/dz)$, describes the possible chirp in the grating period.

For a single-mode FBG, the equations for the coupling coefficients can be simplified as

$$\sigma = (2\pi/\lambda)\, \underline{\delta n}_{eff} \qquad \text{(A1.34)}$$

$$\kappa = \kappa^{*}$$
$$= (\pi/\lambda)\, \underline{\delta n}_{eff} \qquad \text{(A1.35)}$$

For a uniform grating, $\underline{\delta n}_{eff}$ is constant and $(d\phi/dz) = 0$, and thus κ, σ and σ' are constants. These simplify the solutions for the Eqs. (A1.30) and (A1.31) with constant coefficients. The reflectivity of this uniform FBG of length, L, can be found by assuming a forward-propagating wave incident

from $z = -\infty$, while no backward-propagating wave exists for $z \geq L/2$ [i.e., $S(L/2) = 0$]. The amplitude, $\rho = S(-L/2)/R(-L/2)$ and the power reflection coefficient, $R = |\rho|^2$, can be expressed as [54],[56]

$$\rho = \{-\kappa \sinh[(\kappa^2 - \sigma'^2)^{1/2}L]\}/\{\sigma' \sinh[(\kappa^2 - \sigma'^2)^{1/2}L] + i(\kappa^2 - \sigma'^2)^{1/2} \cosh[(\kappa^2 - \sigma'^2)^{1/2}L]\} \quad \text{(A1.36)}$$

and

$$R = \sinh^2[(\kappa^2 - \sigma'^2)^{1/2}L]/\{\cosh^2[(\kappa^2 - \sigma'^2)^{1/2}L] - (\sigma'^2/\kappa^2)\} \quad \text{(A1.37)}$$

From Eq.(A1.37), the maximum achievable reflectivity of a uniform FBG can be obtained as

$$R_{max} = \tanh^2(\kappa L) \quad \text{(A1.38)}$$

when $\sigma' = 0$, from where the Bragg wavelength corresponding to this maximum reflectivity can be defined as

$$\lambda_{max} = [1 + (\delta n_{eff}/n_{eff})]\,\lambda_D \quad \text{(A1.39)}$$

Appendix II

1.3 Laser System Specifications

Table 1-1: Laser System Specifications

ExciStar S-200 / ExciStar S-500 *						
Laser Medium Wavelength	F_2 157 nm	ArF 193 nm	KrF 248 nm	XeCl 308 nm	XeCl long pulse 308 nm	XeF 351 nm
Tube Design	CeraTube™					
Pre-Ionization Technique	Corona Pre-Ionization					
Energy max.	1 mJ	8 mJ	18 mJ	8 mJ	6 mJ	8 mJ
Average Power max. • ExciStar S-200 • ExciStar S-500	 0.2 W 0.4 W	 1.2 W 3.5 W	 3 W 8 W	 1.5 W 3.5 W	 2.1 W 2.7 W	 1.5 W 3.5 W
Repetition. Rate max. • ExciStar S-200 • ExciStar S-500	 200 Hz 500 Hz					
Pulse Duration	15 ns (FWHM)	10 ns (FWHM)				
Energy Stability	σ < 2% stand. dev.					
Beam Dimensions	3 mm x 6 mm (FWHM)					
Beam Divergence	< 1 mrad x 2 mrad (FWHM)					
Gas Lifetime (without gas refill, 100 to 50 % values) • dynamic (pulses) • static	 2 Mio. 12 hours	 4 Mio. 2 days	 8 Mio. 4 days	 14 Mio. 10 days	 12 Mio. 10 days	 4 Mio. 4 days
Optics Service**(pulses)	50 Mio.	50 Mio.	70 Mio.	100 Mio.	100 Mio.	40 Mio.
Electrode Service**(pulses)	500 Mio.					
Cooling	Air cooled (water cooling optional)					
Gas pressure (absolute)	6000 hPa					
Laser Tube Volume	2.1 Liter					
Ambient Temperature	15 °C – 32 °C (59 °F – 90 °F), not condensing					
Electrical Specifications						
Voltage	100 V – 240 V AC					
Frequency	50 – 60 Hz					
Power	1000 W max. (10 A fuse), single phase					
Mechanical Specifications						
Dimensions (L x W x H)	650 mm x 460 mm x 270 mm					
Weight	55 kg					

*All specifications are typical data and subject to change without notice in order to provide the best product possible.

** Pulses between service intervals (replacement if required).

List of publications by the author

Journals:

1. **S. Pal**, J. Mandal, T. Sun and K. T. V. Grattan, "*Analysis of thermal decay and prediction of operational lifetime for a type I boron-germanium codoped fiber Bragg grating*," Appl. Opt., Vol.- 42, No.-12, pp. 2188-2197, 2003.

2. **S. Pal**, J. Mandal, T. Sun, K. T. V. Grattan, M. A. Fokine, F. Carlsson, P. Y. Fonjollaz, S. A. Wade and S. F. Collins, "*Characteristics of potential fibre Bragg grating sensor-based devices at elevated temperatures*," Meas. Sci. Technol., Vol.-14, No.- 7, pp. 1131-1136, 2003.

3. **S. Pal**, T. Sun, K. T. V. Grattan, S. A. Wade, S. F. Collins, G. W. Baxter, B. Dussardier and G. Monnom, "*Bragg grating performance in Er-Sn-doped germanosilicate fiber for simultaneous measurement of wide range temperature (to 500 ℃) and strain*," Rev. Sci. Instrum., Vol. 74, No. 11, pp. 4858-4862, 2003.

4. J. Mandal, **S. Pal**, T. Sun, K. T. V. Grattan, A. T. Augousti and S. A. Wade, "*Bragg grating-based fibre optic laser probe for temperature sensor,*" IEEE Photon. Technol. Lett., Vol. 16, No. 1, pp. 218-220, 2004.

5. **S. Pal**, T. Sun, K. T. V. Grattan, S. A. Wade, S. F. Collins, G. W. Baxter, B. Dussardier and G. Monnom, "*Non-linear temperature dependence of Bragg gratings written in different fibres, optimised for sensor applications over a wide range of temperatures,*" Sensors and Actuators A: Physical, Vol. 112, Issue 2-3, pp. 211-219, 2004.

6. **S. Pal**, T. Sun, K. T. V. Grattan, S. A. Wade, S. F. Collins, G. W. Baxter, B. Dussardier and G. Monnom, "*A fiber optic technique for strain-independent temperature measurement using type I and type IIA fiber Bragg grating combination,*" Rev. Sci. Instrum., Vol. 75, No. 5, pp. 1327-1331, 2004.

7. Y. H. Shen, **S. Pal**, J. Mandal, T. Sun, K. T. V. Grattan, S. A. Wade, S. F. Collins, G. W. Baxter, B. Dussardier and G. Monnom, "*Investigation of the photosensitivity, temperature sustainability and fluorescence characteristics of several Er-doped photosensitive fibers*," Opt. Commn., Vol. 237, Issue 4-6, pp. 301-308, 2004.

8. **S. Pal**, T. Sun, K. T. V. Grattan, S. A. Wade, S. F. Collins, G. W. Baxter, B. Dussardier and G. Monnom, "*Bragg gratings written in Sn-Er-Ge codoped fiber: investigation of photosensitivity, thermal sensitivity and sensing potential,*" Accepted for publication in J. Opt. Soc. Am. A, Vol. 21, pp. 1503-1511, 2004.

9. **S. Pal**, Y. Shen, J. Mandal, T. Sun and K. T. V. Grattan, "*Simultaneous measurement of strain (to 2000$\mu\varepsilon$) and temperature (to 600℃) using a combined Sb-Er-Ge codoped fiber-fluorescence and grating-based technique*," Accepted for publication in IEEE Sensors Journal.

10. J. Mandal, Y. Shen, **S. Pal**, T. Sun, K. T. V. Grattan and A. T. Augousti, "Bragg grating tuned fiber laser system for measurement of wider range temperature and strain," Submitted to Opt. Commn. Journal.

Conferences:

1. **S. Pal**, J. Mandal, T. Sun and K. T. V. Grattan, "*High temperature sensor potential of Bragg gratings fabricated in different photosensitive fibres*," Presented in the Applied Optics and Opto-Electronics Conference 2002 (Photon02), 02-05 September 2002, International Cardiff Arena, Cardiff, UK, Proceedings pp. 49-50.

2. **S. Pal**, J. Mandal, T. Sun, K. T. V. Grattan, M. A. Fokine, F. Carlsson and P. Y. Fonjollaz, "*High temperature performance of Bragg grating devices for potential sensor applications*," Presented at the meeting on Advanced sensors and Instrumentation systems for combustion processes conducted by the Institute of Physics, October 9, 2002, Rutherford Conference Centre, London.

3. T. Sun, D. I. Forsyth, S. A. Wade, **S. Pal**, J. Mandal, W. D. N. Pritchard, G. Garnham and K. T. V. Grattan, "*Fibre Bragg Grating coupled fluorescent optical fibre sensors*," Presented at the 1st International Conference on Optical and Laser Diagnostics (ICOLAD 2002), 16-20 December 2002, City University, London, UK, pp. 153-158.

4. **S. Pal**, T. Sun, K.T.V. Grattan, B. Dussardier, G. Monnom, S.A. Wade, G.W. Baxter and S. F. Collins, *"Use of a Bragg grating written into Er^{3+}-doped tin-germanosilicate fibre for simultaneous measurement of strain and a wide range of temperature,"* Proc. Conference on the Optical Internet 2003 and 28th Australian Conference on Optical Fibre Technology, Australia, 13-16 July, 2003, (ISBN 085825 739 4), pp. 407-410.

5. J. Mandal, **S. Pal**, T. Sun, K.T.V. Grattan and A.T. Augousti, "*Optimization of erbium-doped fibre lasers and their sensor applications,"* Presented at the conference on Sensors and their Applications XII, 2-4 Sept, 2003, Institute of Physics, University of Limerick, Ireland, pp. 271-278.

6. W. Zhao, Y.H. Shen, **S. Pal**, J. Mandal, T. Sun, K.T.V. Grattan and W.D.N. Pritchard, "*Optical fibre systems for measurements of high temperatures*," Presented in the Conference: On-line measurements for quality in the metal industries, Co-sponsored by Institute of Measurement and Control, London, UK, 7-8 October, 2003.

7. **S. Pal**, J. Mandal, Y.H. Shen, T. Sun, K.T.V. Grattan and M. Sun, "*Photorefractivity of Sb-Er-Ge codoped silica fibre for writing grating with high temperature stability*," Presented in the Conference: In-fibre gratings and special fibres (Photonex 03), Institute of Physics, Coventry, UK, 8-9 October, 2003.

8. **S. Pal**, T. Sun, K. T. V. Grattan, S. A. Wade, S. F. Collins, G. W. Baxter, B. Dussardier and G. Monnom, "*Simultaneous measurement of wide range temperature (to 500 °C) and strain using a fibre Bragg grating written into Er-doped tin-germanosilicate fibre,*" Proc. Technical digest: 16th International Conference on Optical Fiber Sensors (OFS-16), 13-17 October, 2003, Japan, IEICE, (ISBN 4-89114-036-4), pp. 42-45.

9. J. Mandal, **S. Pal**, W. Zhao, T. Sun, K. T. V. Grattan and S. A. Wade, "*A novel high temperature sensor based on a compact rare earth fibre laser approach,*" Proc. Technical digest: 16th International Conference on Optical Fiber Sensors (OFS-16), 13-17 October, 2003, Japan, IEICE, (ISBN 4-89114-036-4), pp. 200-203.

10. Y. H. Shen, **S. Pal**, J. Mandal, T. Sun, K. T. V. Grattan, B. Dussardier, G. Monnom, S. A. Wade, G. W. Baxter and S. F. Collins, "*Characteristics of some Er^{3+}-doped fibres for Bragg grating applications*," Book of Abstracts, Australian Conference on Optics, Lasers and Spectroscopy (ACOLS03), 1-4 December, 2003, University of Melbourne, Australia, pp. 183.

11. **S. Pal**, Y. H. Shen, J. Mandal, T. Sun and K. T. V. Grattan, "*Combined fluorescence and grating-based technique for wider range strain-temperature simultaneous measurement using Sb-Er doped fibre*," Proc. Second European Workshop on Optical Fibre Sensors (EWOFS'04), 9-11 June, 2004, Spain, SPIE Vol. 5502, pp. 160-163.

12. J. Mandal, Y. H. Shen, **S. Pal**, T. Sun and K. T. V. Grattan, "*Wide range temperature and strain measurement using Bragg grating based fibre laser approach*," Proc. Second European Workshop on Optical Fibre Sensors (EWOFS'04), 9-11 June, 2004, Spain, SPIE Vol. 5502, pp. 156-159.

13. **S. Pal**, Y. H. Shen, J. Mandal, T. Sun, K. T. V. Grattan, S. A. Wade, S. F. Collins, G. W. Baxter, B. Dussardier and G. Monnom, "*Comparison of Sn and Sb-doped specilized fluorescent fibres for grating-based wide range simultaneous strain-temperature measurement applications*," IoP Conference (Photon04), 6-9 Sept. 2004, Glasgow, UK, Abstract book pp. 58-59.

14. J. Mandal, Y. H. Shen, **S. Pal**, T. Sun, K. T. V. Grattan, A. T. Augousti, R. T. Zheng and Q. N. Ngo, "*Measurement of temperature and strain over a wide range using fibre optic laser-based sensor systems*," IoP Conference (Photon04), 6-9 Sept. 2004, Glasgow, UK, Abstract book pp. 10-11.

Reports:

1. T. Sun, **S. Pal**, J. Mandal and K. T. V. Grattan, "*Fibre Bragg grating fabrication using fluoride excimer laser for sensing and communication applications*," Lasers for Science Facility Programme - Physics, pp. 147-149, Central Laser Facility Annual Report 2001/2002, Rutherford Appleton Laboratory, Oxfordshire, UK.